Study of thermal and ground effects in atmospheric flows for wind turbine applications.

Ulysse Vigny

Thesis in order to obtain the degree of doctor in
Engineering Sciences and Technology

Jury

Supervisor:	Dr. Stéphanie Zeoli (UMONS)
Supervisor:	Dr. Pierre Bénard (CORIA - Rouen)
Supervisor:	Dr. Mostafa Safdari Shadloo (CORIA - Rouen)
President:	Prof. Grégory Coussement (UMONS)
Members:	Dr. Frédéric Blondel (IFPEN)
Members:	Prof. Laurent Bricteux (UMONS)
Members:	Prof. Isabelle Calmet (Centrale Nantes)
Members:	Dr. Vincent Moureau (CORIA - Rouen)

Mons, February 2025

Service Fluides-Machines
Fluids-Machines Unit

- Le vent. C'est le vent qui nous parle.
- Et qu'est-ce qu'il dit ?
- je ne sais pas. Je ne parle pas le vent.

L'Âge de glace

Abstract

Given today's energy and environmental challenges, increasing the electrical power generated by wind farms is of paramount importance. To this end, the size of wind turbines has increased significantly over the years, with rotors reaching hundreds of meters in diameter. At this size, they are under the influence of the atmospheric boundary layer. Although simulations of the neutral and convective boundary layer have been widely performed, accurate simulation of the stable boundary layer (SBL) remains a challenging task. Their smaller vorticies characteristic size calls for high-resolution large-eddy simulations. This doctoral thesis aims to study the impact of realistic atmospheric conditions on wind turbines.

An atmospheric solver framework is developed. The YALES2 constant density incompressible solver has been adapted. Thermal effects are modelled using the Boussinesq approximation for buoyancy-driven flows. The Coriolis force is taken into account using a source term in the momentum equation. Wall effects are represented using the Monin-Obukhov Similarity Theory wall model. The developed framework is capable of handling structured and unstructured meshes, necessary to represent complex terrain configurations. Validation of the framework has been performed on neutral, convective, and stable cases. In particular, the GABLS1 benchmark has been reproduced using both structured and unstructured grids, showing a good agreement with the literature results and enabling wind turbine simulations.

Wind turbine power production and fatigue loads strongly depend on incident wind turbulence or wake from upstream turbines. Thus, a critical physical phenomenon to study is the development of the turbulent vortical wake released downstream of a wind turbine. A fine enough mesh is required to capture the wind turbine wake. However, a compromise must be found between computational cost and accuracy. An adaptive mesh refinement strategy has been developed to this end. The wind turbine wake is flagged using a transported reactive scalar variable. Within, the grid is refined with an optimal mesh size. Reduced computational costs are achieved while maintaining high fidelity in the wake.

The impact of the atmospheric boundary layer on a wind turbine is studied on the basis of the SWiFT benchmark. Both neutral and stable atmospheric conditions are reproduced. Inflow turbulences are correctly reproduced using the precursor method even though the stability parameter is not reached in the stable condition. Wind turbine outputs and velocity deficit in the wake demonstrates the impact of the ABL. A stable boundary layer sustains a longer wake with a skewed shape due to increased shear. Finally, the study of complex terrain impact on wind turbine wakes is initiated. A methodology is developed to generate meshes that can follow complex terrains.

Keywords: Atmospheric boundary layer, Large-eddy simulations, Wind turbines, Stable boundary layer, Complex terrain, Adaptive mesh refinement, Wall model.

Remerciements

Il y a quelque temps, lors d'une discussion autour d'un café, le sujet des remerciements est venu. Qui remercier et comment ? La blague étant de ce la jouer Snoop Dogg: « I want to thank me for believing in me, I want to thank me for doing all this hard work. I wanna thank me for having no days off. I wanna thank me for never quitting. » Alors oui, ça en jette, mais ça serait mentir. Parce qu'une thèse, ça ne se fait pas seul.

Tout d'abord, je tiens à remercier les membres de mon jury qui m'ont suivi tout au long de cette thèse. Vos remarques, questions et commentaires ont toujours été bienveillants et constructifs. Interagir avec vous m'a poussé à réfléchir et à comprendre davantage. Pour cela, merci. En particulier, comment ne pas remercier mes promoteurs. Merci à toi Stéphanie de m'avoir accueilli à Mons et de m'avoir intégré à cette équipe. Merci pour ton encadrement et pour les discussions sur les écoulements atmosphériques, les éoliennes, l'écologie, le capitalisme... Merci à toi, Pierre, pour m'avoir supporté depuis maintenant six ans ! Eh oui, entre le PIE, le stage de fin d'étude et la thèse, ça commence à remonter. En plus de te remercier pour ton encadrement, ta rigueur, ta disponibilité et toutes tes autres qualités ô nombreuses, je tenais tout particulièrement à te remercier de m'avoir permis de faire ce stage. À cause de raisons administratives, il n'était pas censé pouvoir le faire. Mais tu as bataillé, rendant cela possible. Nul doute que sans cela, je n'aurais pas fait cette thèse.

Je tiens aussi à te remercier toi, Léa. Bien qu'officiellement, tu ne fasses pas partie de mon encadrement, pour moi, il n'y a aucun doute. Tu as été là pour débroussailler la littérature. Tu as été là pour développer. Tu as été là pour discuter. Tu as été là pour rédiger, relire, corriger. Tu as été là pour me remotiver dans les périodes de creux. Pour tout cela, un grand et sincère merci ! Un merci aussi à vous deux, Vincent et Ghislain, apparaissant tels des sauveurs capables de débloquer toutes situations. Merci Vincent pour les discussions. Je retiens tout particulièrement cette discussion sur la propagation d'erreurs numériques qui m'aura sortie d'une sacrée mélasse. Merci Ghislain pour ta disponibilité dès que le code ne compile plus, dès qu'il manque un package, dès que j'ai besoin d'une install sur un nouveau super-calculateur. J'espère ne pas t'avoir fait trop de frayeurs.

J'en viens maintenant à toutes les personnes avec qui j'ai pu interagir, que ça soit en conférence, lors de journées scientifiques ou lors de workshops. J'ai beaucoup appris autour de vous. Un merci tout particulier à toi, Erwan. Tu ne t'en es peut-être pas rendu compte, mais nos échanges par mail et lors du GDR m'ont beaucoup aidé, aiguillé et rassuré. Un grand merci aussi à toute la communauté YALES2. Je pense notamment à ces fameux Extrême CFD workshops, lieux d'échange, d'apprentissage, de fertilisation croisée, de synergie et d'enrichissement invraisemblables. Lieu aussi de 400m (Manu, j'aurai ma revanche !), d'ultimate, de bière, de consommation de bonbons en tout genre et de blagues Carambar. D'ailleurs, Félix, quel métier les chiens peuvent-ils exercer ? C'est aussi ça qui participe à cette ambiance si particulière, qui donne envie de revenir chaque année.

Un grand merci aussi à toute l'équipe du CORIA. Merci pour votre accueil toujours aussi chaleureux lors des différents séjours scientifiques. Merci à toi Félix pour ton aide, notamment les premières années. Des soudes à la colloc jusqu'au week-end à La Haye, j'en aurai des choses à raconter ! Merci Julien de m'avoir accueilli dans ton bureau. Heureusement que je n'étais pas là pour trois ans, sinon le bureau se serait vite transformé en salle de sport et en buanderie. Merci à toi, Antoine, et à ton canapé pour ces nombreuses nuits chez toi et ces séries devant l'ordinateur. D'ailleurs, il me semble qu'on n'a pas fini ! Merci aussi à vous Léa et Julien pour votre hébergement et vos tartes aux poireaux.

Enfin, merci à toutes ces personnes de Mons (et un peu d'ailleurs) qui ont rendu cette thèse bien agréable. Merci aux anciens, Kévin et Marion. Kévin, c'est toujours un plaisir de te croiser, de la guinguette au terrain d'ultimate, de Bruxelles à Rouen. Marion, merci pour ton accueil à Mons. Tu as largement contribué à rendre ce début de thèse fort sympathique. Ton implication et ta motivation m'auront largement inspiré. Et finalement, un grand merci au trio magique. Antoine, tous ces midis sur le mont Panisel ont largement contribué à trouver un équilibre, permettant de ne pas finir complètement fou. Maria, ces découvertes de villes belges ne sont pas terminées. Il en reste sur la liste. Patrick, cet espace de bienveillance et d'honnêteté qu'a été notre bureau a été essentiel pour moi. Merci à vous trois, c'était vraiment chouette de pouvoir s'épauler comme on l'a fait.

J'en arrive à ma famille. Merci pour les hébergements à Saint-Malo et Sartrouville lors des confinements successifs. Merci Alex et Sophie d'avoir été disponibles pour répondre à mes interrogations quand j'hésitais à me lancer dans cette thèse. Merci Elé et Rod d'avoir fait à manger à Lancieux pendant que je rédigeais ce manuscrit. Un deal est un deal ! Merci aussi à tous les participants de ces voyages à vélos (Thomas, Maxence, Etienne, Rod). Ces coupures annuelles ont été des moments fantastiques et inoubliables. Des bouffées d'oxygène pur et de fameuse rigolade. Des moments gravés à jamais. Bien que je sois toujours une brêle en descente, je compte bien continuer à essayer de vous suivre ! En particulier, merci à toi Maxence pour ce triathlon du lac de Paladru, qui m'aura permis de faire une super rencontre. Merci Valentine. Sans toi, cette thèse n'aurait pas été la même. C'est toujours avec beaucoup de joie que je pense à ces mercredis où je pars à Montpellier, avec ou sans vélo, pressé de te rejoindre. Merci pour tout ce que j'ai découvert à tes côtés et pour tout le soutien et le réconfort que tu m'as apporté.

Et finalement, last but not least, merci à la sncf et à ses salons grands voyageurs. Je n'ai jamais eu l'impression d'y être à ma place, mais toujours content d'y être. Une part non négligeable de ce manuscrit a été rédigée là-bas.

Nomenclature

Acronyms

ABL	Atmospheric Boundary Layer
ADM	Actuator Disk Method
ALM	Actuator Line Method
AMR	Adaptive Mesh Refinement
CBL	Convective Boundary Layer
CFD	Computational Fluid Dynamics
DNS	Direct Numerical Simulation
EROI	Energy Returned On energy Invested
GABLS	GEWEX Atmospheric Boundary Layer Study
GEWEX	Global Energy and Water Cycle Experiment
GWP	Global Warming Potential
HAWT	Horizontal-Axis Wind Turbine
HIT	Homogeneous Isotropic Turbulence
HPC	High-Performance Computing
IPCC	Intergovernmental Panel on Climate Change
LCA	Life Cycle Assessment
LCOE	Levelized Cost Of Energy
LES	Large-Eddy Simulations
MOST	Monin-Obukhov Similarity Theory
MPI	Message Passing Interface
NBL	Neutral Boundary Layer
NS	Navier-Stokes
PBL	Planetary Boundary Layer
PDF	Probability density function
RANS	Reynolds Average Navier-Stokes
SBL	Stable Boundary Layer

SGS	subgrid scale
SWiFT	Scaled Wind Farm Technology
TI	Turbulent Intensity
TKE	Turbulent Kinetic Energy
VAWT	Vertical-Axis Wind Turbine

Greek letters

α	Local angle of attack
β	Twist angle
γ	Pitch angle
Δ	Mesh cell size, m
ϵ	Dissipation rate of the turbulent kinetic energy, $m^2.s^{-3}$
ζ	Stability parameter
η	Smallest turbulent structure lengthscale, m
θ	Potential temperature, K
κ	Von Kármán constant
λ	Tip speed ratio
ν	Kinematic viscosity, m^2/s
ν_t	Subgrid scale turbulent viscosity, m^2/s
ρ	Density, $kg.m^{-3}$
σ	Standard deviation
τ_{ij}^R	Residual stress tensor, $kg.m^{-1}s^{-2}$
τ_w	Wall shear stress, $kg.m^{-1}s^{-2}$
ϕ	Flow angle
$\psi_{m/h}$	Correction functions
Ω	the Earth angular velocity, rad/s

Symbols

A	Swept rotor area, m^2
C_D	Drag coefficient
C_L	Lift coefficient
c_p	Specific heat of dry air, $m^2.s^{-2}.K^{-1}$
C_s	Smagorinsky constant
C_T	Thrust coefficient
D	Drag aerodynamic force, $kg.m.s^{-2}$
F_c	Coriolis force, $kg.m.s^{-2}$
f	Coriolis frequency, s^{-1}
g	Gravitational acceleration constant, $m.s^{-2}$
h	Boundary layer height, m
L	Monin-Obukhov length, m
N	Brunt-Väisälä frequency, s^{-1}
P	Pressure, $kg.m^{-1}.s^{-2}$
q_w	wall heat flux, $kg.s^{-3}$
R	Specific gas constant, $m^2.s^{-2}.K^{-1}$
Re	Reynolds number
R_O	Rossby number
T	Temperature, K
U	Streamwise velocity, $m.s^{-1}$
$U_{h,\infty}$	Streamwise velocity at hub height far from the wind turbine, $m.s^{-1}$
u_*	Friction velocity, $m.s^{-1}$
V	Tangential velocity, $m.s^{-1}$
V_{rel}	Relative velocity, $m.s^{-1}$
W	vertical velocity, $m.s^{-1}$
$\overline{w'\theta'}$	Kinematic vertical heat flux, $kg.s^{-3}$
z	Height, m
z_0	Roughness length, m

Contents

1 Context and objectives **17**

1.1 The global energy challenge . . . 18

1.1.1 Carbon emissions . . . 18

1.1.2 The downside of oil . . . 22

1.1.3 The future of energy . . . 24

1.2 Wind turbines: new scales and new physics . . . 28

1.2.1 Functioning . . . 30

1.2.2 Multi-scale problem . . . 31

1.2.3 Multi-physic problem . . . 33

1.3 Tools to address wind energy grand challenges . . . 36

1.3.1 Large eddy simulation for wind turbine modelling . . . 36

1.3.2 High resolution for stable boundary layer . . . 37

1.3.3 Unstructured grids for complex terrain . . . 39

1.4 Objectives . . . 40

1.5 Outlines . . . 41

2 The Atmospheric Boundary Layer **45**

2.1 Structure of the atmosphere . . . 46

2.1.1 The lowest layer . . . 47

2.1.2 Thermal stratification . . . 49

2.1.3 Coriolis force . . . 52

2.1.4 Geostrophic balance . . . 53

2.2 State of the art in atmospheric flow modelling . . . 54

2.2.1 Meso-scale modelling . . . 54

2.2.2 Micro-scale modelling . . . 57

2.2.3 Coupling the meso-and micro-scale . . . 62

2.2.4 Inflow turbulence generation . . . 63

2.2.5 Wind turbine and wind farm flow modelling . . . 68

2.2.6 Atmospheric flows solvers . . . 71

2.3 Conclusion . . . 72

3 Numerical methods and wind turbine modelling **75**

3.1 Numerical modelling for turbulent flows . . . 76

3.1.1 Navier-Stokes equations . . . 76

3.1.2 Turbulent flows . . . 76

3.1.3 Modelling approach . . . 78

3.1.4 LES equations . . . 80
3.1.5 Subgrid-scale modelling . . . 81
3.1.6 Meshing . . . 82
3.2 YALES2 platform . . . 84
3.2.1 Incompressible constant density solver . . . 85
3.2.2 Spatial discretisation . . . 86
3.2.3 Temporal discretisation . . . 87
3.2.4 Double-domain decomposition and parallelism . . . 88
3.2.5 Dynamic mesh adaptation . . . 89
3.3 Horizontal axis wind turbine modelling . . . 91
3.3.1 Actuator Disk Method . . . 91
3.3.2 Actuator Line Method . . . 93
3.3.3 Force mollification . . . 94
3.4 Conclusion . . . 95

4 Development and application of the atmospheric solver 97
4.1 Development of atmospheric models . . . 98
4.1.1 Coriolis force . . . 98
4.1.2 Boussinesq buoyancy approximation . . . 99
4.1.3 Wall model . . . 100
4.1.4 Wall law filtering . . . 101
4.2 Application to a Neutral Boundary Layer . . . 102
4.3 Application to a Convective Boundary Layer . . . 103
4.3.1 Numerical setup . . . 103
4.3.2 Results . . . 104
4.4 Application to a Stable Boundary Layer . . . 105
4.4.1 GABLS1 configuration . . . 107
4.4.2 Numerical set-up . . . 108
4.4.3 Results . . . 109
4.4.4 Conclusions of the GABLS1 study . . . 119
4.5 Conclusion . . . 120

5 A new adaptive mesh refinement strategy for wind turbine application 121
5.1 Introduction . . . 122
5.2 Methodology . . . 123
5.3 Application to yawed wind turbine wakes . . . 124
5.3.1 Context . . . 124
5.3.2 Framework . . . 124
5.3.3 Results . . . 127
5.4 Conclusion . . . 132

6 Realistic wind turbine studies 135

6.1 Atmospheric boundary layer impact on wind turbines . . . 136
6.1.1 Presentation of the SWiFT benchmark . . . 136
6.1.2 Methodology . . . 138
6.1.3 Numerical setup . . . 139
6.1.4 Neutral benchmark . . . 140
6.1.5 Stable benchmark . . . 149
6.1.6 Conclusion of the SWiFT benchmark . . . 158
6.2 Complex terrain impact on wind turbines wake . . . 160
6.2.1 Mesh generation . . . 160
6.2.2 Application setup . . . 162
6.2.3 Results . . . 163
6.2.4 Conclusion . . . 164

7 Conclusion and perspectives 167
7.1 Conclusion . . . 168
7.1.1 General background . . . 168
7.1.2 Development and validation of the atmospheric solver . . . 168
7.1.3 The adaptive mesh refinement strategy . . . 170
7.1.4 Application to realistic wind turbine studies . . . 171
7.2 Perspectives . . . 172
7.2.1 Optimisations and improvements of the atmospheric solver . . . 173
7.2.2 Improving the realistic inflow turbulence . . . 173
7.2.3 Enhance the adaptive mesh refinement strategy . . . 174
7.2.4 Long term perspectives . . . 175

Appendices 177
A YALES2 Scaling on LUMI supercomputer . . . 177
B TFV4A temporal discretization scheme . . . 179
C Newton-Raphson algorithm . . . 180
D GABLS1 source of errors . . . 181
E Determining the Geostrophic wind from frictional velocity. . . . 183

Figures index 188

Tables index 189

References 189

Chapter 1

Context and objectives

This chapter introduces the context, challenges, objectives, and main tools used in this work. The global energy challenge ahead is reviewed, as well as the development of wind energy as part of the solution. A brief introduction on how horizontal axis wind turbines work will lead to the associated multi-scale and multi-physics problems. To address these challenges, adequate tools for wind turbine simulation under a stable boundary layer and complex terrain influence are selected. The objective of this work is detailed.

Contents

1.1 The global energy challenge 18

1.1.1 Carbon emissions 18

1.1.2 The downside of oil 22

1.1.3 The future of energy 24

1.2 Wind turbines: new scales and new physics 28

1.2.1 Functioning 30

1.2.2 Multi-scale problem 31

1.2.3 Multi-physic problem 33

1.3 Tools to address wind energy grand challenges 36

1.3.1 Large eddy simulation for wind turbine modelling 36

1.3.2 High resolution for stable boundary layer 37

1.3.3 Unstructured grids for complex terrain 39

1.4 Objectives 40

1.5 Outlines 41

1.1 The global energy challenge

For the majority of human history, our forbears relied on very basic forms of energy: human muscle, animal muscle, and the combustion of biomass, such as wood and crops [1]. But the advent of a new energy resource has deeply transformed our society. The use of fossil fuels (coal, oil, and gas) triggered the Industrial Revolution and all the technological advances that followed. Since the beginning of the 20*th* century, the development of our Western societies has been based on the access to abundant fossil fuels [2]. Its use has been extensive and continues to grow, as shown in Fig. 1.1. Today, more than 80% of the world energy mix relies on fossil fuels. In Belgium, fossil fuels represent 67% of the energy mix. In France, a popular belief is that most of the energy comes from the nuclear fleet. But 50% of the energy mix still comes from fossil fuels [3]. To understand these figures, it is important to acknowledge the distinction between energy and electricity. Electricity is part of the energy mix, but not the only source. Most of the energy consumption comes from transport, heat and industry. Sectors that rely heavily on fossil fuels. In Belgium and France, electricity is produced mainly by nuclear power plants. However, it is only a small part of the energy mix: 17.3% in Belgium and 24.7% in France [3].

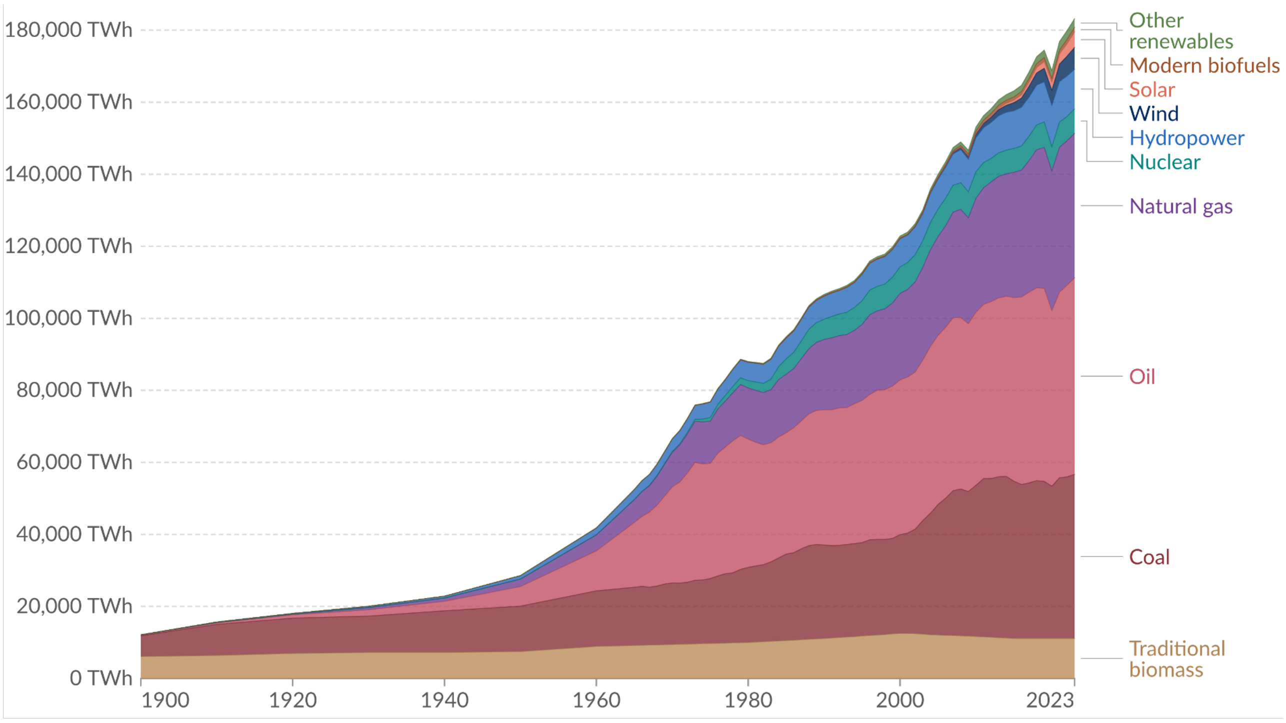

Figure 1.1: World primary energy consumption by source, from [2].

1.1.1 Carbon emissions

Despite being an immense source of energy, fossil fuels have a devastating impact on climate. When fossil fuels are burned, they release large amounts of gas into the atmosphere. The fuel gases are mainly nitrogen (N_2), water vapour (H_2O) and carbon dioxide (CO_2) and, in much smaller proportions, carbon monoxide (CO), hydrocarbons (C_xH_y) and nitrogen oxides (NO_x). Carbon monoxide, hydrocarbons, and nitrogen oxides are known to have poisonous effects, contributing to deterioration in air quality. Towards the end of the 2010s, fossil fuel-related air pollution is estimated to be responsible for 3.6 million deaths worldwide each year [4]. In Europe, the number of deaths in 2015 was estimated to be almost 500000. Of these, 47500 were in France and 9120 in Belgium [5]. Although this is an important issue, it is not the only one to consider. All gases also have a greenhouse effect.

Because the surface of the Sun is around 5700 K, the radiation wavelengths are much lower than the Earth, $\lambda_{sun} = 0.4$ μm compared to $\lambda_{earth} = 10$ μm. Due to this discrepancy, Sun radiation can go through the Earth's atmosphere. But once re-emitted by the Earth, at a much higher wavelength, part of the radiation is captured. By capturing part of the Sun's radiation at the Earth's surface, the atmosphere plays an essential role in life on earth, allowing an average temperature of 15°C at the Earth's surface. For comparison, the temperature on the surface of Mars, a planet without atmosphere, is −60°C. However, a surplus of greenhouse gases in the atmosphere generates a rise in temperature. According to their capacity to absorb these radiations and their lifetime in the atmosphere, some gases have a significant impact, while others are negligible. Their impacts are expressed by their global warming potential (GWP), i.e. their capacity to absorb radiation over a given time period. As carbon dioxide is used as a reference, its GWP is one. For comparison, the GWP of methane is between 27 and 30, while the water vapour has an estimated GWP between −0.001 and 0.0005.

In order to have a unified measurement tool, the carbon dioxide equivalent CO_2eq can be calculated. For any gas, it represents the mass of CO_2 that would have an equivalent warming impact. Using the previous examples, one tonne of methane is counted as 28 tonnes CO_2eq over 100 years. Anthropogenic CO_2eq emissions are the cause of what is known as global warming; the greatest challenge of the 21*st* century [6]. To prevent future catastrophes and, in the worst-case scenario, adapt to them, it is important to quantify the impact of rising temperature on the environment. With that in mind, in 2021, the Intergovernmental Panel on Climate Change (IPCC) has developed Shared Socioeconomic Pathways (SSP) scenarios [7] based on emissions profiles. SSP scenarios are expressed as SSP X − Y where X refers to the socio-economic scenario and Y refers to the increase in radiative forcing by 2100. Thus, a SSP X − Y scenario is a trajectory of CO_2eq emissions and associated warming. The main five IPCC scenarios are:

- SSP1 − 1.9: The most optimistic scenario. COP21 commitments are respected. Actions are being taken to mitigate climate change. By 2100, the radiative forcing will be 1.9 W/m^2 higher than in 1850. The global temperature rise should be contained below 1.5°C by 2100.

- SSP1 − 2.6: A low CO_2eq emissions scenario. CO_2eq emissions start to decline by 2020 and go to zero by 2100. By 2100, the radiative forcing will be 2.6 W/m^2 higher than in

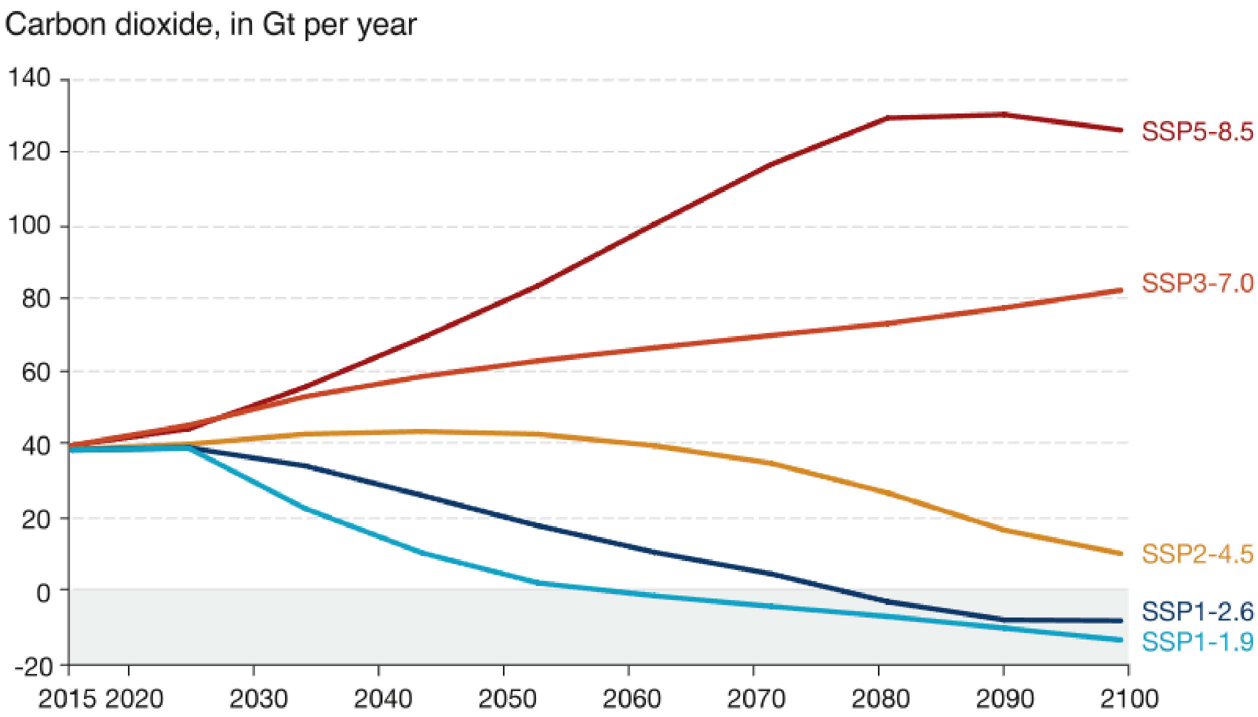

Figure 1.2: Projected annual global carbon emissions. From [7].

1850. The global temperature rise should be contained below 2°C by 2100.

- SSP2 – 4.5: An intermediate scenario. CO_2eq emissions have been curbed by 2050 and are halved between 2050 and 2100. By 2100, the radiative forcing will be 4.5 W/m^2 higher than in 1850. The rise in temperature should be between 2°C and 3°C by 2100. The mean increase in sea level is 35% higher than that of SSP1 – 2.6 [8]. Many plant and animal species will be unable to adapt to the effects of SSP2 – 4.5 and higher SSPs [9].

- SSP3 – 7: An intermediate, more negative, scenario in which the emissions peak around 2080. Technologies help stabilize radiative forcing after 2100. By 2100, the radiative forcing will be 6 W/m^2 higher than in 1850. The rise in temperature should be between 3°C and 4°C by 2100.

- SSP5 – 8.5: The most pessimistic scenario. No measures are being taken to mitigate climate change. Greenhouse gas emissions are constantly increasing. By 2100, the radiative forcing will be 8.5 W/m^2 higher than in 1850. The rise in temperature will exceed 4°C by 2100.

Fig. 1.2 shows the projected annual global carbon emissions and Fig. 1.3 shows the projected global temperature, in agreement with these five scenarios. As shown in these figures, CO_2eq emissions have increased and the temperature has already increased. However, five very

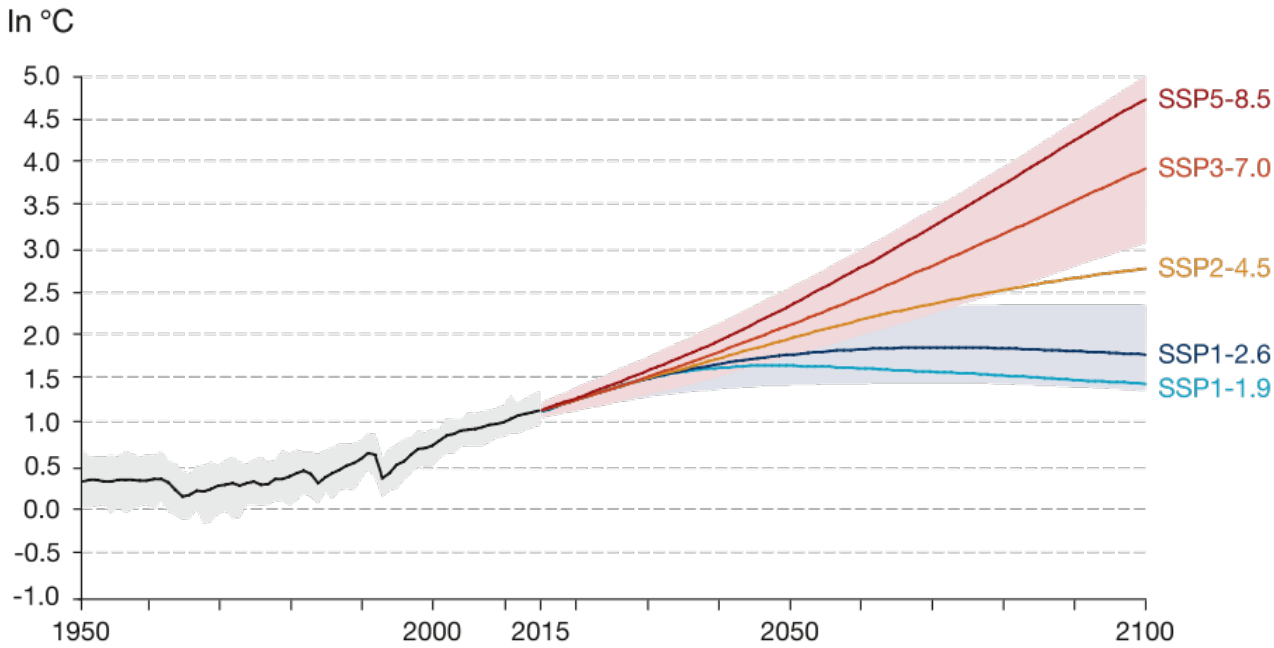

Figure 1.3: Projected global temperatures. From [7].

different futures can be considered. One thing that should be noted is that the temperature increase does not have linear consequences. A temperature rise of 1.5°C since pre-industrial times (before 1850) would have consequences such as: sea level rise, water stress, soil erosion, vegetation loss, food supply instability, increase in extreme weather events, etc. However, a temperature increase of 2°C would have a much greater impact [10]. Obviously, an even greater rise in temperature will have even greater consequences.

Keeping that in mind, in 2015, during COP21, most countries committed themselves to limit global warming to 1.5°C – 2°C, according to the recommendations of the IPCC [11]. The objective is to reach zero net emission by 2050 and then to continue towards negative emissions. To do so, a rapid reduction in CO_2eq emissions is mandatory worldwide. Although ambitious goals have been set during the COP21, it is worth mentioning that, for the moment, we are far from achieving its objectives. At the time of writing this dissertation, global warming has already reached 1.5°C and forecasts are not positive. A 2020 commentary described the SSP2 – 4.5 scenario as likely [12]. However, another study showed that the scenario SSP5 – 8.5 is the best match to the cumulative emissions from 2005 to 2020, in agreement with 1% [13]. They also state that it is the closest under current and stated policies. That said, we must not be discouraged from reducing global energy consumption and shifting energy production towards low-carbon emissions power plants. On the contrary, every degree counts.

To quantify the carbon emissions of power plants, a life cycle assessment (LCA) is performed. The aim is to quantify the effect that a product has on the environment throughout the entire life of the product, from the production of raw material to the decommissioning.

Energy source	Emissions (gCO_2eq/kWh)
Coal	800 – 1600
Oil	600 – 1100
Gas	300 – 900
Hydraulic	6 – 40
Nuclear	6 – 12
Photovoltaic	25 – 33
Wind	8 – 22

Table 1.1: CO_2eq emissions by type of power plant. Most data are from [14].

This footprint is reduced to the production of 1 KWh, allowing a fair comparison of power plants in terms of CO_2eq cost per KWh produced. As for each energy source the LCA depends on the technology, the methodology, the transport, the production sites, and otherwise there is a fairly wide range of results. In particular for renewable energies, because the development of these technologies is particularly intense, studies are rapidly outdated. Tab. 1.1 summarizes the value range for the main energy sources. Given the range of data for each energy source, it is difficult to provide an exact ranking of the energy sources. However, we can see that two distinct groups can be identified: low carbon emission power plants, such as renewable and nuclear and high carbon emission power plant, such as fossil fuels (coal, oil, gas). In light of this result, to achieve a zero net emission, fossil fuels should eventually be phased out. For that, it is essential to reduce global energy consumption and shift our energy production toward low carbon emissions power plants, such as wind energy.

1.1.2 The downside of oil

In addition to global warming and the issue of fossil fuel carbon emissions, other challenges require the shift of energy production. One is the finite quantity of fossil fuels. As we live in a finite world, infinite consumption of oil is by its nature impossible. But with a large stock, almost infinite, the problem could be postponed. However, this is not the case. To understand the problem, it is important to differentiate conventional and unconventional oil. Whether conventional or unconventional, oil is derived from the transformation of a rock that is rich in organic matter. Under high pressure and temperature, mostly due to sedimentation, organic matter breaks down into hydrocarbons. For conventional oil, the hydrocarbons formed in the bedrock migrate to a porous, permeable rock, called a reservoir. There, they accumulate and can be exploited simply by drilling. For unconventional oil, the hydrocarbons remain dispersed. They may be trapped in the bedrock and be known as shale oil. Because of the greater difficulty of exploiting unconventional oil, conventional oil was historically the first to be used. However, in 2006, conventional oil reached its maximum production, leading to 'peak oil' [15]. Fig. 1.4 shows the evolution of oil energy production depending on the oil source. It is possible to see that indeed, after 2006, conventional oil production, including field and offshore oil, started to decline. Unconventional oil, which regroups shale tight and sand oil, offsets this decline.

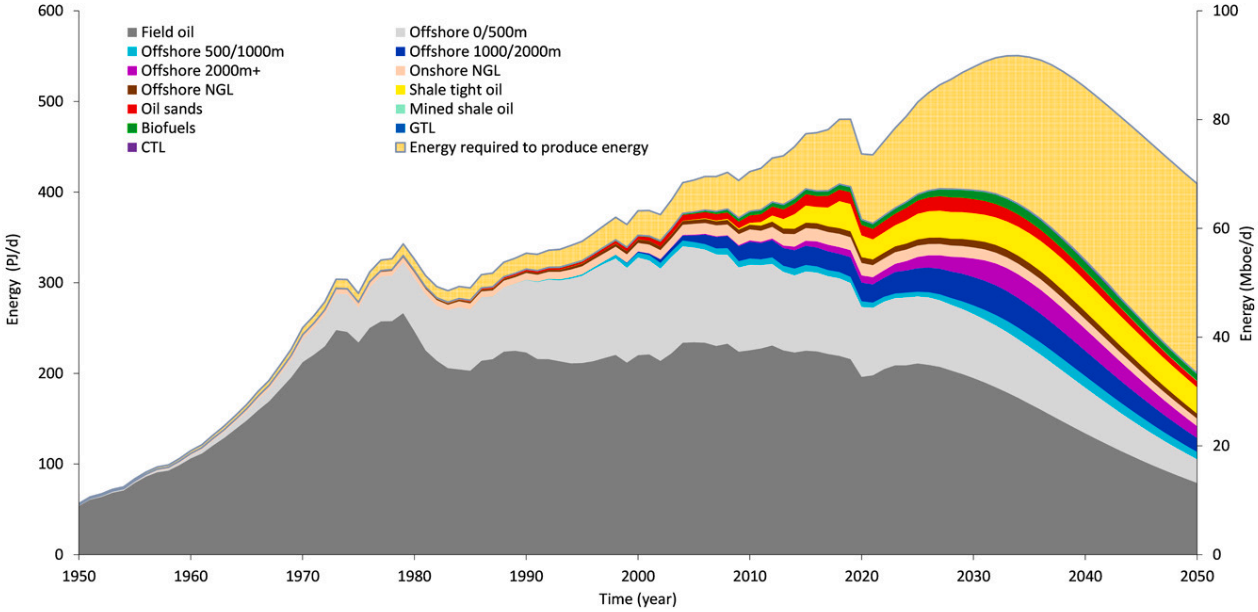

Figure 1.4: Average oil liquids net-energy production from 1950 to 2050, compared to the gross energy. From [15].

However, in its current form, by 2030, total oil production will decline. Therefore, limited oil resources are prompting us to change the way we produce energy.

As global oil reserves decrease, operators are increasingly focusing on deposits that are more and more complicated to exploit. A direct consequence is that the energy returned on energy invested (EROI) indicator decreases. The EROI indicator quantify the amount of energy required to extract energy. Simple at first glance, the indicator is highly dependent on the methodology [16]. Although research has tried to harmonize the methodology [17], comparing different sources of energy can be complex. However, for a fixed methodology, the indicator can be used to quantify the evolution of a single energy source. From 1940 to 2005, the EROI of conventional oil, based on the primary energy returned, has decreased from approximately 100 to 8. In 2005, 1 kWh was required to extract 8 kWh of primary energy. The EROI of shale oil is even lower, reaching approximately 2 [18]. This can be seen in Fig. 1.4, where the energy required to produce oil is constantly growing since 1950, with a sharp increase from 2010. The immediate consequences are an increase in the carbon footprint of oil and an increase in the levelized cost of energy (LCOE) presented afterwards. Another reason to shift our energy production.

Finally, another topic that must be highlighted is the notion of energy independence. France and Belgium are producing only a few percent of their oil consumption and therefore import almost everything. However, imports fluctuate with geopolitical and energy crises. The Russian crisis following the invasion of Ukraine is a perfect example. Between 2019 and 2023 in France, Russian oil imports have decreased from 12.7% to 0%, but other countries have

Location	Production [GWh]	Electricity mix [%]	Energy mix [%]
World	1,864,067	6.5	1.69
Europe	500,158	12	3.3
Belgium	11,971	12.6	1.97
France	38,064	8	1.8

Table 1.2: Wind energy production in 2022, From [3].

compensated for it. For example, Libyan oil imports have increased from 5.3% to 8.8% [19]. In Belgium, a similar scenario occurred. In 2019, 22% of the oil came from Russia. It has been replaced by Norwegian and US oil, which now represent 16% and 13% of oil importation [20]. Gas supplies has followed an equivalent trend. As we depend on oil and gas imports, we cannot simply stop importation from a country. It has to be replaced by another supplier. So we remain highly dependent on other countries. Thus, becoming less dependent on fossil fuel exporting countries is a major topic when evoking independence and self-sufficiency. Yet another reason to transform the way we produce energy.

1.1.3 The future of energy

Wind energy represents only a small part of the energy and electricity mix [3]. Tab. 1.2 presents the part of wind energy in electricity and energy mix worldwide, in Europe, in Belgium and in France in 2022. We can see that Europe and Belgium have a higher ratio of wind energy in their electricity mix compared to world-wide and France. France has less wind energy in its energy mix due to the high proportion of nuclear power plants. However, since electricity represents only 17.3% of the energy mix, having only 10% percent of the electricity mix and a few percent of the energy mix generated by wind energy is very low.

Unlike oil, the cost of wind energy is continuously decreasing [21]. To quantify it, the levelized cost of energy is used. Similar to the life cycle assessment which allows to compare the carbon footprint of each energy source, seen in Section 1.1.1, the LCOE allows to compare the cost of each energy source. For an energy source, it measures all costs of production, divided by the amount of energy generated. Once again, depending on the methodology, the results vary. However, general trends can be identified. Fig. 1.5 shows the evolution of LCOE per megawatt hour between 2009 and 2023 for different energy sources. We can see that in 14 years, the cost of each energy has varied. For fossil fuels and nuclear energy, costs have tended to increase in recent years. In contrast, for renewable energy sources such as wind energy, costs have tended to decrease. The main reason is attributed to the increasingly widespread implementation of renewable energy sources. Today, wind energy is amongst the most cost-effective forms of energy.

In addition to being cost-effective, wind energy is part of the energy source that emits the

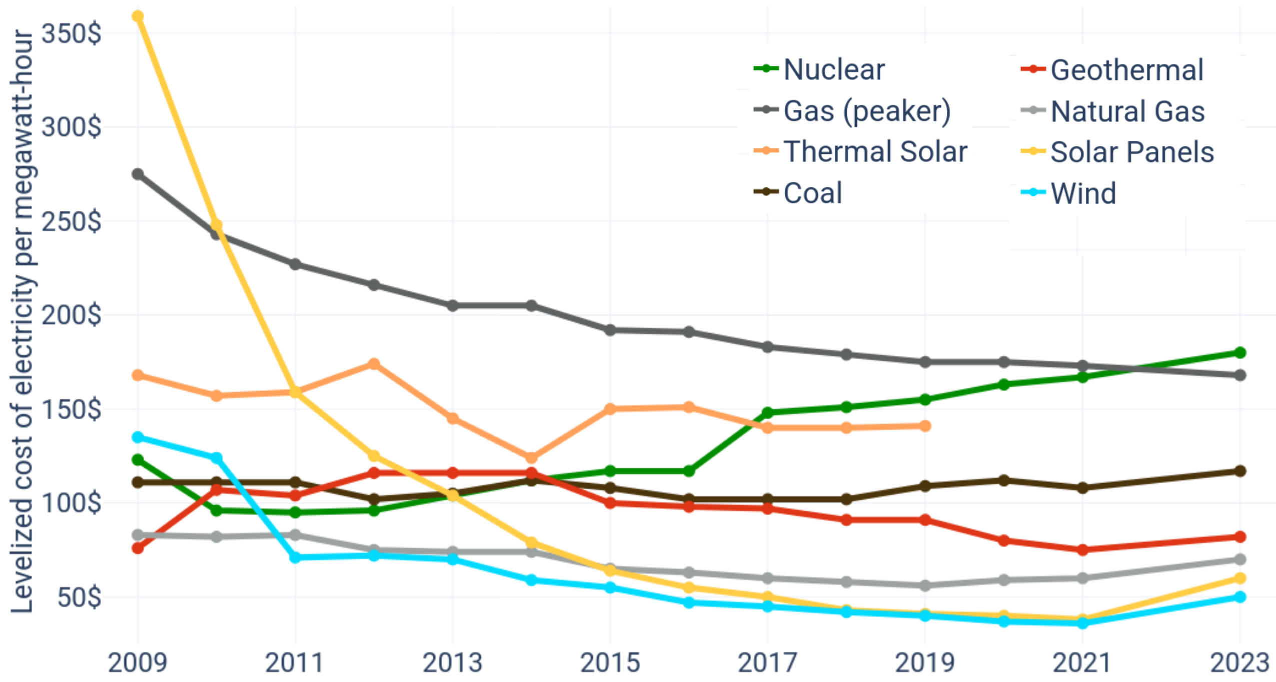

Figure 1.5: Levelized cost of energy per megawatt-hour evolution, from [21].

least CO_2eq per kWh, as seen in Tab. 1.1. The combination of these two arguments presents a compelling case for increased wind energy utilization. This is true for all greenhouse gases reduction scenarios, which gives a significant role to wind energy [22]. In this sense, in 2019, the International Renewable Energy Agency (IRENA) published a road-map to 2050 with two routes [23] focused on wind energy production. The first is an energy pathway established by current and planned policies. The second is a pathway to contain global warming below 2°C, in accordance with the SSP1 − 2.6 scenarios presented above [24]. Although ambitious, this scenario is designed to be achievable. But in order to do so, onshore and offshore wind power must be massively developed.

For onshore wind energy, the global cumulative installed capacity must triple by 2030 and increase ninefold by 2050. In absolute terms, this means going from 542 GW in 2018 to 1787 GW in 2030 and 5044 GW in 2050. For global offshore wind power, the global cumulative installed capacity must be increased almost tenfold by 2030 and multiplied by forty-three by 2050. This means going from 23 GW in 2018 to 228 GW in 2030 and 1000 GW in 2050. All these data are collected and shown in Fig. 1.6 and Fig. 1.7. They show the impressive wind energy growth required to match global warming below 2°C. In 2023, 946 GW of installed onshore wind turbines and 75 GW of installed offshore wind turbines have been reached, for a total of approximately 1 TW installed capacity. Although lower than the 1.2 TW advocated by the IRENA scenario [23], it is relatively close. The issue lies in the projected installed capacity, where current and planned policies are well below the recommended trajectory. As wind energy deployment and increased efficiency can greatly contribute to carbon dioxide emissions reductions, we need to properly define what a wind turbine is and how it works.

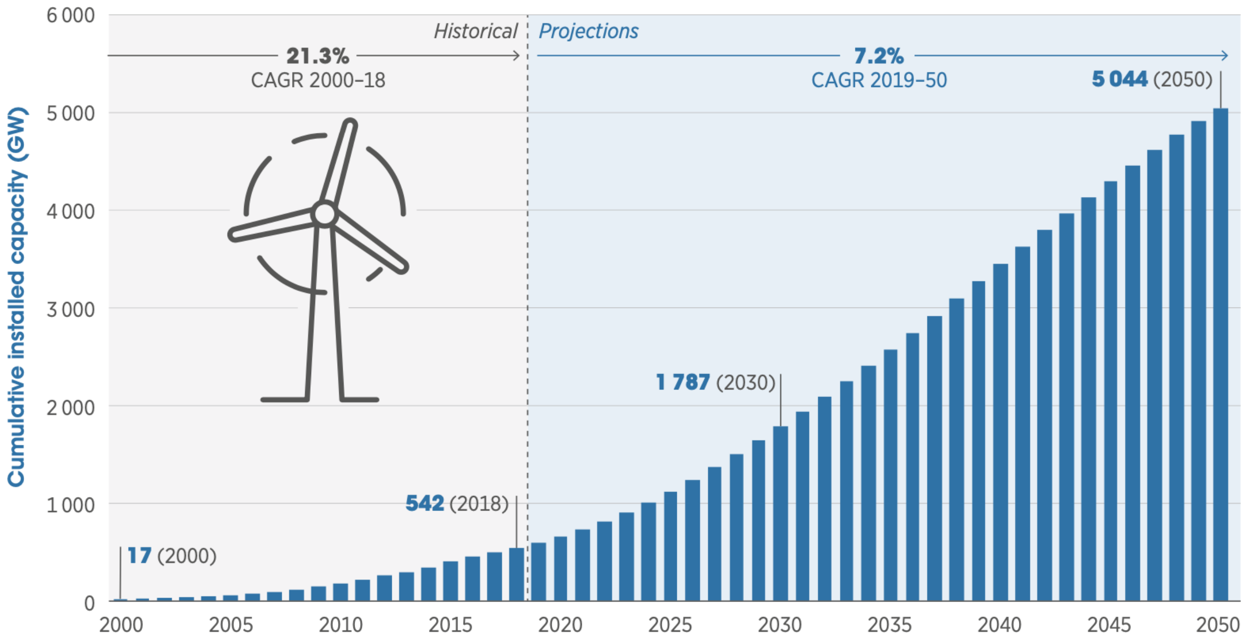

Figure 1.6: Onshore wind cumulative installed capacity projection, from [23].

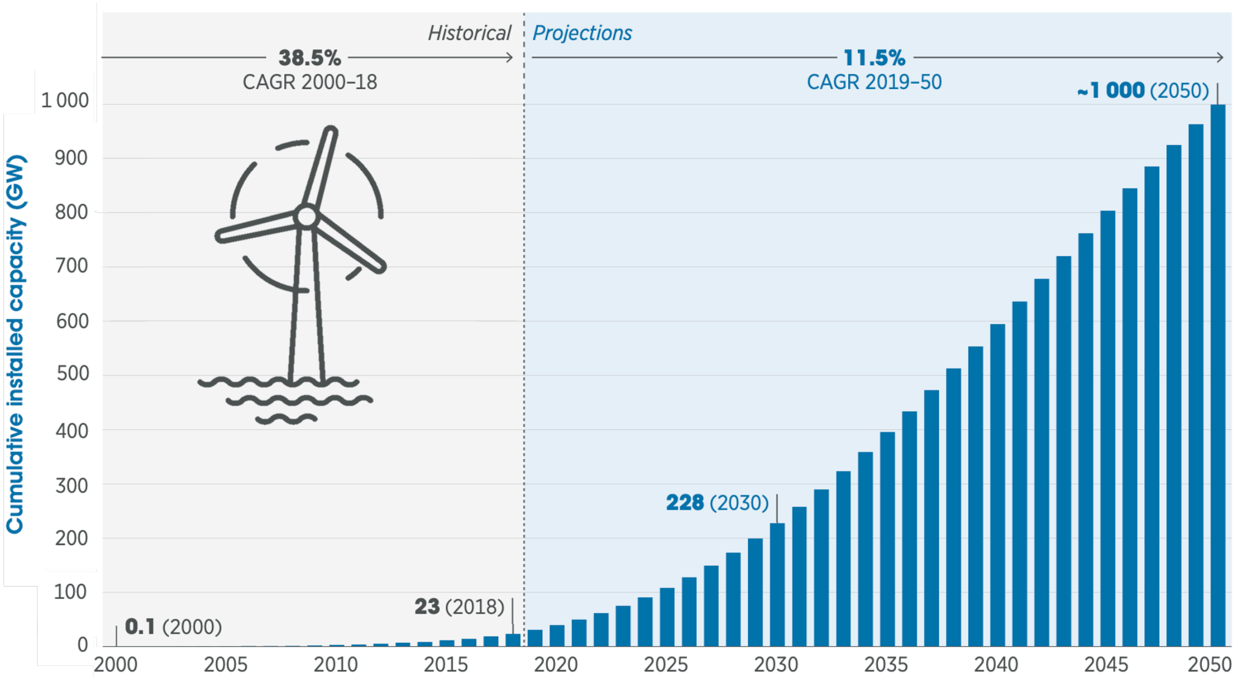

Figure 1.7: Offshore wind cumulative installed capacity projection, modified from [23].

Before continuing with a technical approach focused on wind turbines, it should be mentioned that while the energy challenge is at the centre of the climate change challenge, it is itself encompassed in a wider issue of the impact of human activity on the environment. Known as planetary boundaries, the 2009 study [25] identified nine planetary boundaries, pictured in Fig. 1.8, that quantify the impact of human activities on the Earth system. These boundaries are as follows.

1. **Climate change**: Trapped radiation causes an increase in global temperatures and alters climate patterns.

2. **Novel entities**: Novel entities released into the environment encompass synthetic chemicals substances such as microplastics but also human interventions in evolutionary processes such as genetically modified organisms.

3. **Stratospheric ozone depletion**: The stratospheric ozone layer protects life on Earth from ultraviolet radiation. The thinning of the layer is due to human-made chemicals and allows more harmful UV radiation to reach Earth's surface.

4. **Atmospheric aerosol loading**: Airborne particles from human activities influence the climate by altering temperature and precipitation patterns.

5. **Ocean acidification**: The phenomenon of increasing acidity in ocean water due to the absorption of atmospheric CO_2. This process impacts marine ecosystems, damages calcifying organisms, and reduces the efficiency of the ocean in acting as a carbon sink.

6. **Modification of biogeochemical flows**: The flow of phosphorus into the ocean and the industrial fixation of nitrogen disrupt the natural nutrient cycles that are crucial to supporting life and maintaining ecosystems.

7. **Freshwater change**: Human-induced disturbances of freshwater cycles, including rivers and soil moisture, impact natural functions such as carbon sequestration and biodiversity and can lead to changes in precipitation levels

8. **Land system change**: Deforestation and urbanization have reduced natural carbon sequestration, moisture recycling, and habitats for wildlife, which are crucial for the health of the Earth's system.

9. **Biosphere integrity**: The loss of genetic diversity such as living organisms and ecosystems threatens the ability of the biosphere to co-regulate the state of the planet by impacting the energy balance and chemical cycles on Earth.

These limits represent a threshold beyond which the environment may no longer be able

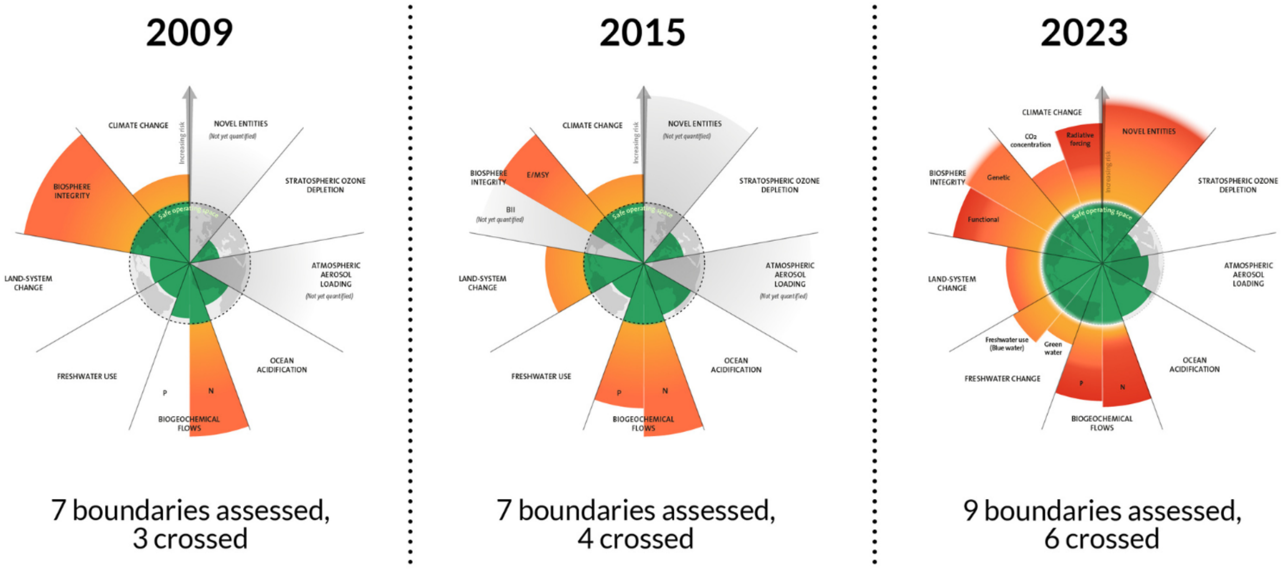

Figure 1.8: Evolution of the planetary boundaries between 2009 and 2023, based on [25–27].

to self-regulate. This would mean that the Earth system would leave the stability period of the Holocene, in which human society developed [25]. Transgressing one or more planetary boundaries may have catastrophic consequences due to the risk of exceeding thresholds that will trigger non-linear environmental change. Among the nine planetary boundaries, three were exceeded in 2009 [25], four in 2015 [26] and six in 2023 [27]. Although this work focuses on the first planetary boundary challenge, climate change, it is important to acknowledge that this challenge is merely one of the nine challenges that have been enumerated. The development of wind turbines as a means of reducing our carbon dioxide emissions does not address other planetary boundaries. Furthermore, in the literature, it has been shown that wind turbines could potentially have a negative impact on biodiversity due to habitat loss [28] or noise pollution [29]. Although these considerations are important in the balance of advantages and disadvantages of wind turbines, they are beyond the scope of this work, which focuses on the technical aspect of wind turbines.

1.2 Wind turbines: new scales and new physics

A wind turbine is a device that converts wind kinetic energy into electrical energy. Its existence goes back to ancient times, when it was called a windmill. Its first appearance in Persia dates back to 620 AD. It was followed by the wind pump, which appeared in what is now Afghanistan in the ninth century. The first electricity-generating wind turbine was installed by the Austrian Josef Friedländer at the Vienna International Electrical Exhibition in 1883. It consisted of a windmill that drove a dynamo that supplied electricity to a series of batteries. Since then, a great deal of progress has been made in optimizing wind turbines. Nowadays, wind turbines can be divided into two categories. Vertical-axis wind turbine (VAWT) and horizontal-axis wind turbine (HAWT). Wind turbines with different numbers of blades exist. Fig. 1.9 compares the

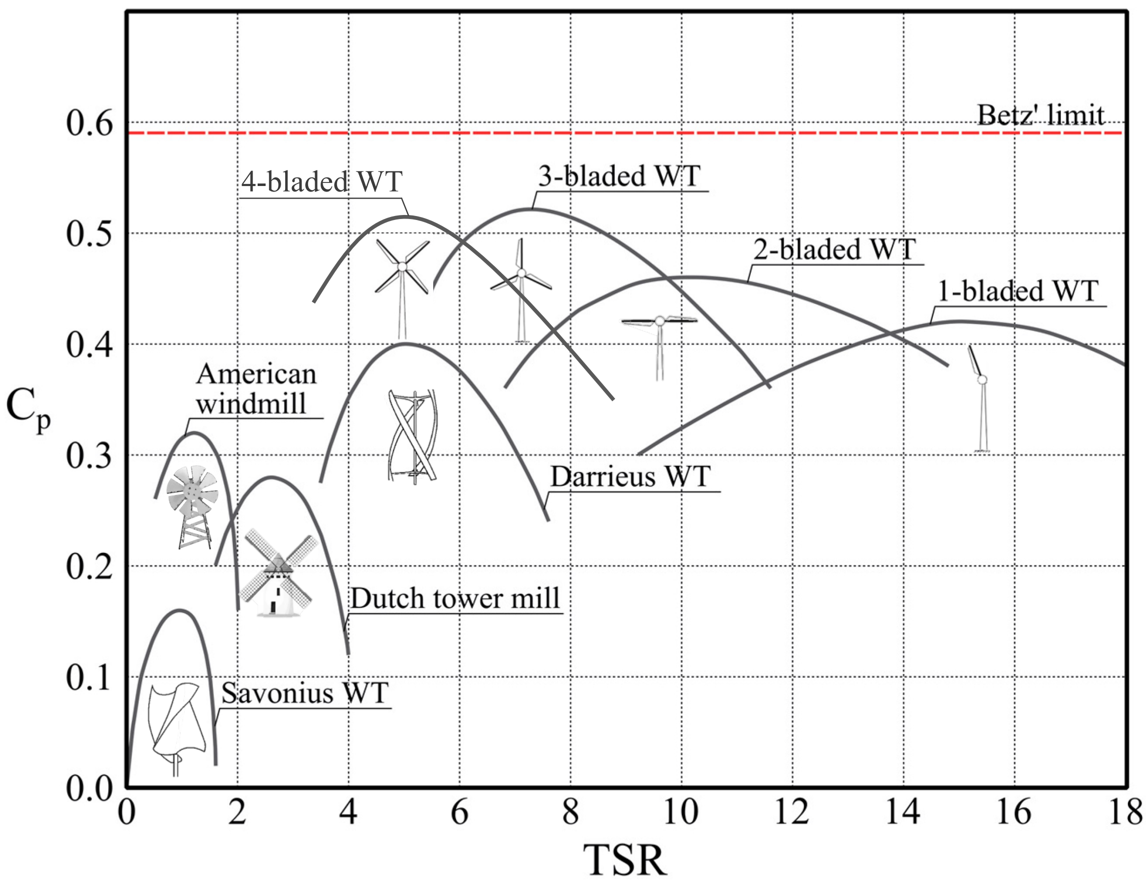

Figure 1.9: Aerodynamic efficiencies comparison for several types of wind turbines. Adapted from [30].

power coefficient of common types of wind turbines, depending on the tip-speed ratio (TSR), the ratio of the velocity at the tip of the blade and the wind speed.

The Betz limit [31] shown in the graph is developed in the following section. From this graph, we can understand why the most widely used wind turbine is the HAWT with three blades. It is the one with the highest power coefficient. In terms of structure, three blades give a constant angular momentum, allowing minimal constraint on the structure. Adding more blades does not generate more power output, but will be more expensive to produce, heavier, and thus less cost-effective. The main components of the three-blade horizontal axis wind turbine are shown in Fig. 1.10. The rotation of the wind turbine drives a gearbox that powers a generator. To connect to the grid, the electricity passes through a transformer, which increases the voltage, to be used on the network. In light of their efficiency and prevalence, these three-blade horizontal axis wind turbines are the most suitable for use in this project.

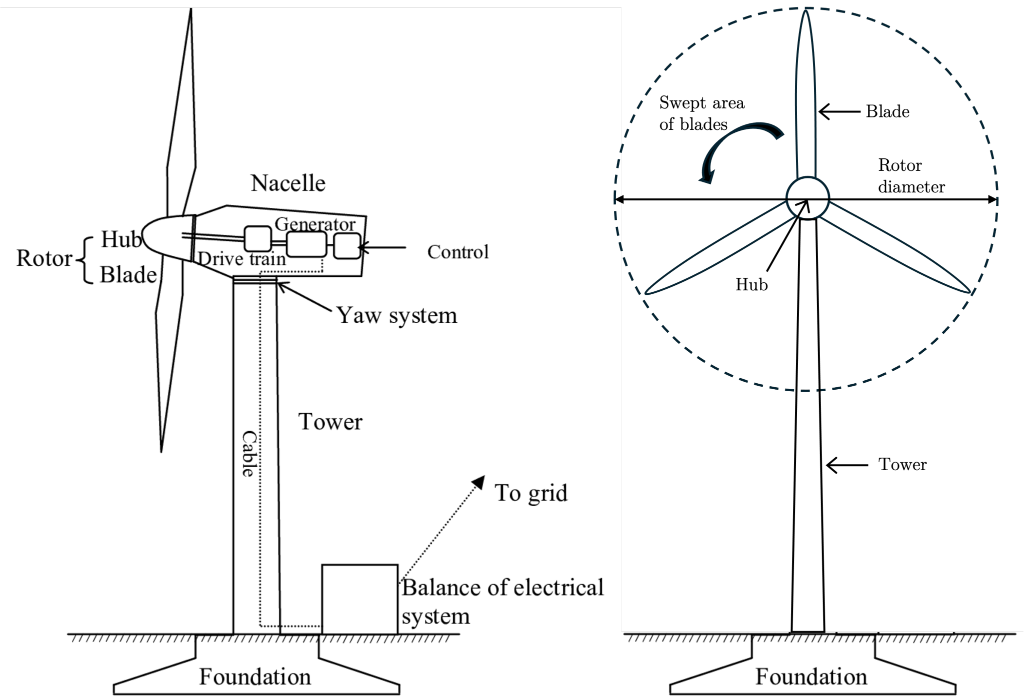

Figure 1.10: Main components of a 3 blades horizontal axis wind turbine.

1.2.1 Functioning

Conservation of mass requires that the amount of air entering and leaving a wind turbine be equal. Therefore, according to Betz's law [31], the maximum achievable extraction of wind energy by a wind turbine is 16/27 of the rate at which the kinetic energy of the air arrives at the turbine. The maximum theoretical power output P can be expressed as:

$$P = \frac{16}{27}\frac{1}{2}\rho v^3 A = \frac{8}{27}\rho v^3 A \tag{1.1}$$

where A is the blades sweep area, v the horizontal average wind velocity and ρ the air density.

Wind turbine performance can be controlled by the orientation of its blades through adjustment angles, shown in Fig. 1.11.

- **Yaw angle**: It corresponds to the angle between the direction of the incident wind and the axis of the rotor in the horizontal direction.

- **Tilt angle**: It corresponds to the angle between the direction of the incident wind and the axis of the rotor in the vertical direction.

- **Pitch angle**: It allows the blades to rotate around the radial axis to modify their surface area in the wind. Depending on the need, it can therefore maximize lift or act as a brake to limit the blade rotation speed.

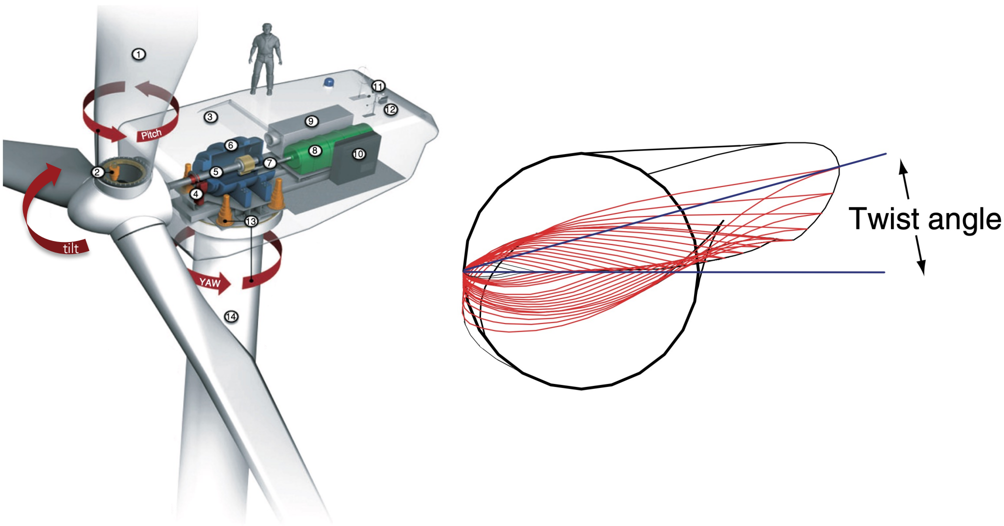

Figure 1.11: Left: pitch, yaw and tilt angle. Right: twist angle. Modified from [32].

- **Twist angle**: The twist is established when the blade is designed. The twist is used to vary the angle of attack (AOA) of the blade along its span. The optimum AOA of a blade is calculated in relation to a relative speed that depends on the incident flow velocity and the local rotational speed. As the rotation speed is directly proportional to the radius of the blade, the AOA increases with the distance from the centre of rotation.

1.2.2 Multi-scale problem

To further increase wind energy production, as illustrated in Fig. 1.6 and Fig. 1.7, projections are based on several factors.

- Installation of additional wind turbines. In addition to classical onshore wind turbines and offshore wind turbines as we know them, new technologies are being developed, such as floating wind turbines [23]. Floating wind turbines have the ability to take advantage of the abundant wind potential in deeper waters, increasing the surface area available to wind turbines.

- Increasing the efficiency of wind turbines. Efficiency can be increased by improving the blades. With optimized parameters such as power coefficient, blade mass and blade design, the cut-in speed and the rated speed can be reduced [33]. This consequently allows for a wider range of use, limiting the intermittency inherent in wind energy. The energy output will thus be increased.

- Increasing the production of wind farms. Wind turbines have a negative impact on each other in wind farms due to the wake effect [34]. Being in a wake of an upstream wind

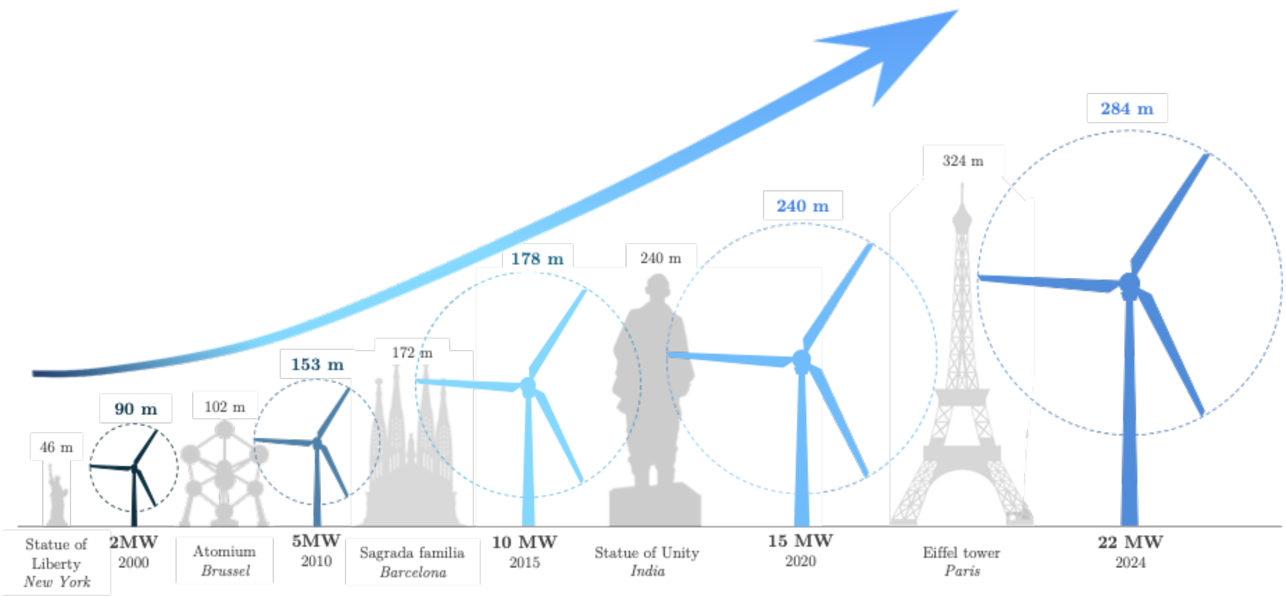

Figure 1.12: Evolution of wind turbine diameter and capacity growth, modified from [36].

turbine decreases the average inflow velocity but can also increase load variations. With new control strategies such as yaw misalignment [35] and individual pitch control [36] the global power output of a wind farm can be improved, even if it means reducing the power generated by a single turbine.

- Increasing the size of wind turbines.

As seen in Eq. 1.1, the power output directly depends on the area swept by the rotor. Therefore, increasing the size of the wind turbine directly increases the power output. In addition, the wind at altitude is less affected by the ground and is thus stronger and less turbulent. A bigger wind turbine will benefit from this. As a result, the size of wind turbines has increased dramatically. As shown in Fig. 1.12, in 2000, the wind turbines were about 90 m in diameter with a capacity of 2 MW. Today, offshore wind turbines can reached a diameters of 380 m and a capacity of 15 MW. This increase in size has implications for the flow physics around these wind turbines. Wind turbines are no longer affected solely by micro-scale wind flows. They are also affected by meso-scale processes. They are at the interface between the micro- and meso-scale [37].

In the context of atmospheric flows, micro-scale flows refer to processes that extend well below 1 km. This is referred to as the site effects. At the very bottom of this scale is the surface layer, i.e. the 100 meters at the bottom of the atmosphere. In the surface layer, processes such as ground roughness, surface temperature, and stability conditions directly impact ground velocity and temperature fluxes from the ground. These processes also influence the horizontal and vertical velocity gradients. In fact, complex terrain can induce flow separation, recirculation, and change in roughness. Urban canopies can act as obstacles, with isolated buildings or cities, but also as speeding areas with street canyons. Forest canopy behaves similarly, with shelterbelts, forests, and trees. Above the surface layer is the atmospheric boundary layer (ABL) that expends between 100 m and 1 km. In this layer, we find larger scale phenomena such as thermal stratification and Coriolis forcing. Thermal stratification is due to the sun's radiation heating the Earth's surface. It causes variations in air density, resulting in alterations to buoyancy forces and the emergence of thermal stratification. Coriolis forcing is a consequence of the Earth's rotation and the conservation of angular momentum. The inertial force deflects all moving objects and flows to the right in the northern hemisphere and to the left in the southern hemisphere. All these phenomena are further developed in Chapter 2.

Larger, meso-scale flows range from 5 to hundreds of kilometres in size. This is referred to as meteorological effects. Meso-scale forcing, which defines the global behaviour of the flow, is based on the geostrophic wind, which is induced by weather systems such as low-pressure and high-pressure areas. It is a determining factor in the ABL behaviour. In addition to large forcing forces, meteorological events can occur. Among these are the low-level jets, a fast-moving ribbon of air at low levels of the atmosphere. But also cold pools, a cold pocket of dense air, that form when rain evaporates during intense precipitation. This phenomenon can be observed beneath thunderstorm clouds or precipitating shallow clouds. Other examples include ramp, a large wind speed change, or a large wind direction change [38]. Although meso-scale flows operate at a larger scale than wind turbines, these phenomena impact the boundary layer development, and thus wind turbines.

Being at the interface between micro-scale and meso-scale flows, wind turbines are greatly impacted by the atmospheric boundary layer. It can be observed in the energy production, loads and fatigue [34] of a single wind turbine. However, effects are also visible on a wind farm scale. Upstream wind turbines have an impact on downstream wind turbines, due to their wakes. As atmospheric flows have an impact on wake recovery, velocity deficit and induced turbulence [34], interactions will be impacted. A finer comprehension of the involved physics is required to better predict the behaviour of wind turbines and wind farms in these configurations. However, because a wide range of scales are involved, having accurate analyses is extremely complicated. In particular, the micro and meso-scale are numerically modelled in fundamentally different ways. In this regard, the subject has become one of the grand challenges in wind energy research [37]. This work aims to meet this multi-scale challenge.

1.2.3 Multi-physic problem

Wind turbines growth is not the only grand challenge in wind energy research. Various physical phenomena are involved and are being studied. They are frequently classified into three categories: the physics of flows, the wind turbine structural dynamics and the integration into electricity grid [37]. Fig. 1.13 illustrates this classification. In the diagram, the three categories are highlighted in red, blue, and green. These grand challenges in wind energy research can be

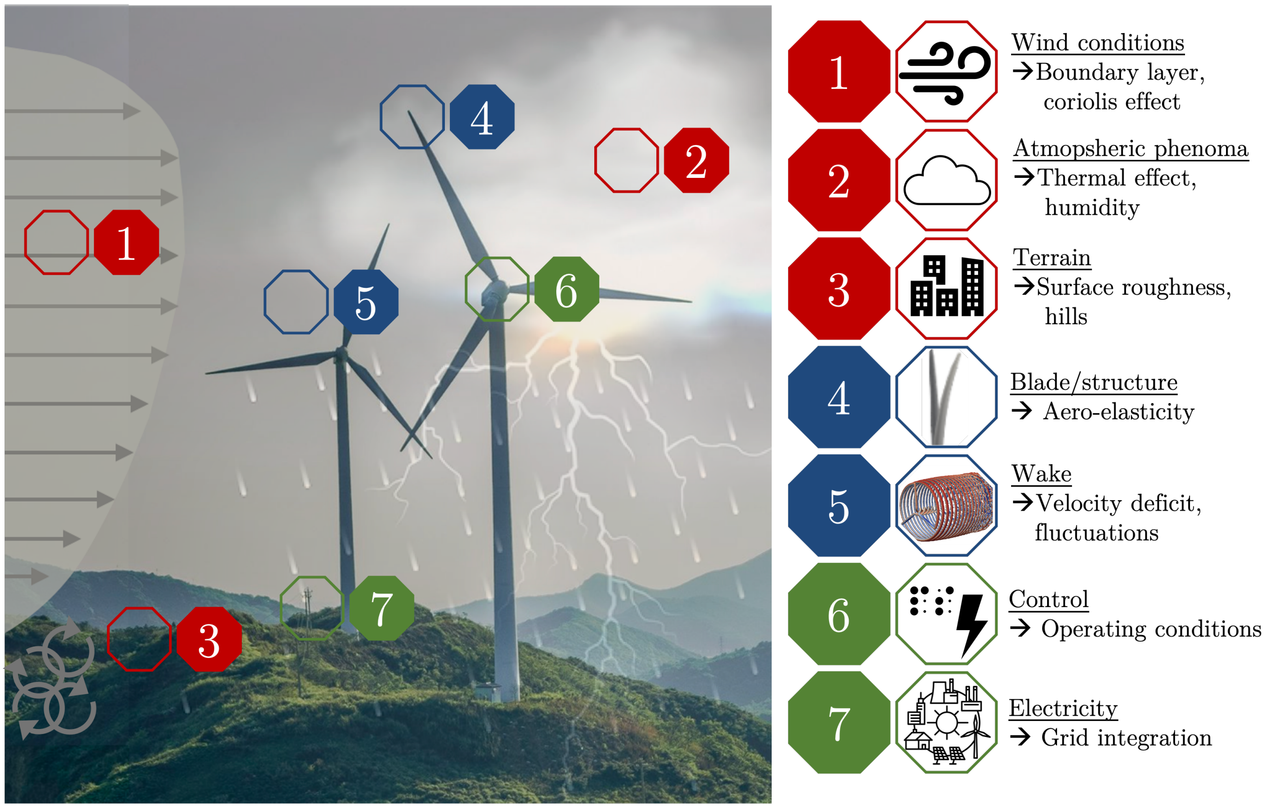

Figure 1.13: Representation of various physical phenomena involved in wind energy.

summarised as follows:

- 1^{st} grand challenge: "**improved understanding of atmospheric and wind power plant flow physics**". This challenge aims to better understand micro- and meso-scales processes and their impact on wind turbines. As mentioned above, a wide range of scales are involved, making the study arduous. This thesis is in the scope of this first grand challenge and aims to make a contribution to this field of study.

- 2^{nd} grand challenge: "**Aerodynamics, structural dynamics, and offshore wind hydrodynamics of enlarged wind turbines**". Operating wind turbine blades, while seemingly still, are in constant motion due to dynamic forces. Advances in numerical simulation have allowed the wind industry to design efficient turbines, with blade lengths nearing 150 meters and tower heights exceeding 200 meters, that can withstand extreme weather. But as even larger turbines are planned, new research questions about turbine dynamics must be addressed. These include understanding atmospheric interactions, wake effects, and the aeroelastic behaviour of large turbines. As turbines operate partly above the surface layer, they face substantial variation in inflow conditions, such as shear, a variation of wind speed with height, and veer, a rotation of the flow with height. Understanding these phenomena is essential for optimizing power generation and ensuring structural safety [39].

Advancements in materials and manufacturing are essential for developing reliable, cost-effective structures. While the wind energy sector has seen innovations in materials like fiber-reinforced composite, it remains a pressing need for improved material performance in harsh environments. In particular, the blades are required to be stiff yet flexible to adapt to changing wind conditions, durable and erosion-resistant while being not too expensive to be produced at scale. Innovations in resin matrices, fiber reinforcements, and recyclability are necessary for future designs [40].

At the same time, current aerodynamic assumptions are being challenged by the interaction of flexible blades with highly variable inflow. Fundamental lift and drag characteristics of the airfoil are affected [41]. The elastic behaviour of increasingly large and flexible blades complicates aerodynamics, as blades interact with their own vorticity. This may require a reassessment of design models. Moreover, on specific cases such as offshore wind power plants, aerodynamic forces are being affected by hydrodynamic forces. Analysis of the interactions between these two forces is critical for wind energy. In particular, floating offshore systems introduce additional complexities as they have additional degrees of freedom in the motion of the turbine [42]. Their movement can significantly affect rotor dynamics and wake interactions, which complicate existing hydrodynamic theories.

- 3^{rd} grand challenge: "**Systems science for integration of wind power plants into the future electricity grid**". The global electricity system operates on multiple timescales, ranging from sub-second to decades, to ensure grid stability and reliability. Power plants must provide protection against sub-second perturbation such as lightning and surges voltage instabilities, but also to annual perturbation such as the intermittence [43]. As the reliance on traditional energy sources decreases, renewable energy sources like wind and solar are increasingly expected to provide predictable power and enhance grid reliability, necessitating advancements in their operational capabilities [44].

  Future wind power plants will require sophisticated control systems such as the individual pitch control (IPC) that can manage the dynamics of individual turbines. By optimizing the collective performance of wind plants, operators can maximize energy production while improving overall system efficiency [45]. Additionally, the future grid will rely heavily on real-time data management and advanced analytical techniques to address the uncertainties inherent in renewable energy generation and demand. New sensors and data sources will be critical for monitoring and managing the grid.

Over the past few decades, advances in numerical simulation techniques have allowed the wind industry to design larger and larger turbines, becoming the largest flexible rotating machines in the world [37]. These wind turbines can efficiently generate power for long periods while enduring extreme weather conditions. But as the industry seeks even larger turbines that access higher wind speeds, new challenges arise. Being at the interface between the micro- and the meso-scale, wind turbines are impacted by larger-scale turbulent and heterogeneous flow.

Various physical phenomena are involved in the flow, which impacts the behaviour of wind turbines. To provide meaningful insights to this multi-scale and multi-physic challenge, this work must be based on reliable and accurate prediction tools.

1.3 Tools to address wind energy grand challenges

To predict wind turbine power output, loads, and fatigue, various approaches can be employed. Field experiments have been carried out for decades to measure the flow around wind turbines under realistic conditions. Initially with anemometers [46], new technologies such as lidars [47] and radars [48] have provided new insights into atmospheric turbulence. Wind tunnel experiments have been performed to measure the flow around wind turbines in uniform inflow. Studies on turbulent boundary layer and wind turbine interactions have been conducted [49]. However, performing experimental studies often proves to be complex and costly. Studies are limited in terms of data that are being analysed as sensors are required. They are also limited in terms of studied physical phenomena, as they can hardly be isolated and study hardly be reproduced. Although experimental studies allow for a better understanding of complex phenomena, they do not provide a priori knowledge of a flow at a future wind farm location. For all these reasons, numerical simulations have been used increasingly [34]. However, it should be noted that experimental studies are valuable in providing knowledge about physics and validation scenarios, which are required when testing numerical models.

1.3.1 Large eddy simulation for wind turbine modelling

The Blade-Element Momentum (BEM) theory developed by Glauert in 1935 is the basis on which most wind turbine modelling codes are based [50]. Subsequently, improvements have been made to better predict aerodynamic loads [51]. Yet, various experimental campaigns have shown that BEM theory is not always accurate and reliable for predicting the aerodynamic load distributions on the wind turbine blades. One of the major limit is that the incoming flow must be known a priori. This knowledge is impossible to have when modelling the ABL, a turbulent, non-stationary, heterogeneous flow. This is also not possible when modelling wind farms as the wake of an upstream turbine affects the inflow of a downstream turbine. Modelling a wind turbine in the ABL or a wind farms using the BEM theory becomes inaccurate.

Analytical models have been proposed to predict the average velocity deficit in wind turbine wakes [52], infinite wind farms [53], and their impact on weather models [54]. Based on the mass, momentum, and energy conservation equation, they are more accurate than simpler models, with yet a low computational cost compared to more complex modelling tools. However, they are less accurate than numerical tools for resolving turbulence. This limitation is particularly acute in complex scenarios, when wind turbines are impacted by ABLs, thermal effects, complex terrains, and more. They are tailored for optimization and control purposes that require numerous simulations. This major limitation prevents their use in addressing the multi-scale and multi-physics challenges.

Computational Fluid Dynamics (CFD) is a modelling approach that consists of studying a fluid motion and its effects by numerically solving the fluid governing equations: the Navier-Stokes (NS) equations. This technique allows to model complex flows such as atmospheric boundary layer and then study their interactions with wind turbines. However, since no analytical solution exists, three main approaches are used to model the flow. The key points are developed here, but more details can be found in Sec.3.1.2.

- **The Reynolds Average Navier-Stokes (RANS)** equations approach consists of applying an averaging operation to the NS equations to obtain the mean equations of the fluid flow. The turbulence is then exclusively modelled through the turbulence model. This method is the less expensive CFD method, but also the less accurate as it heavily relies on the turbulence model to predict fluctuations. Although capable of solving the global flow behaviour, this method is inadequate to precisely study wind turbine wake fluctuations, power output variations, loads, and fatigue.

- **The Direct Numerical Simulation (DNS)** approach consists of resolving the entire range of the turbulence length scales. It is the most accurate, as it resolves all fluctuations. Yet, it is also the most expensive, as resolving small scales can become incredibly expensive for large-scale problems. This method is thus inoperable on wind turbine / wind farm scales.

- **The Large Eddy Simulation (LES)** technique is the intermediate approach in terms of precision and cost. It consists of resolving the large scales of the flow while modelling the small ones through a subgrid scale (SGS) model. Due to the nature of turbulence, large scales are the most energetic and thus the ones defining the global behaviour of the flow. Resolving the large scales of the flow provides greater accuracy than the RANS approach, while modelling the small scales reduces the computational costs compared with the DNS approach.

Due to the improvement in computational power, the LES technique has become a viable option in wind turbine applications [55]. Validation studies have demonstrated the reliability and the accuracy of this method to reproduce and simulate turbulent boundary layer flow around wind turbines and wind farms [56]. To tackle the multi-scale and multi-physics challenges presented above, a solver that can perform LES will be used in this work.

1.3.2 High resolution for stable boundary layer

The LES technique was first used for atmospheric sciences in 1963 and 1967 by Smagorinsky [57]. Since then, this method has been increasingly used, becoming one of the dominant numerical techniques for modelling the atmospheric boundary layer [58]. Numerous studies have investigated the impact of ABL on wind turbines and wind farms using LES [59,60]. It is well established that wind turbine performance is significantly influenced by wind shear, with implications on wake recovery, velocity deficit, induced turbulence, energy production, loads, and fatigue. One of the main mechanisms generating wind shear is thermal stratification [34]. There are three main ABLs depending on the thermal gradient: neutral, convective, and stable. The neutral boundary layer (NBL) is the state in which there is no heating or cooling at the surface. The temperature gradient is zero. This ABL is often found in transitional periods. The convective boundary layer (CBL) is formed when there is a lower temperature gradient than that naturally present in the atmosphere. Hot air is at the bottom and cold air is at the top. This ABL is often found during days, or in tropical regions, when the sun is heating the surface. The stable boundary layer (SBL) is the case when there is a higher temperature gradient than that naturally present in the atmosphere (often positive). Hot air is at the top and cold air is at the bottom. This ABL is often found during the night or in polar regions, when the surface cools. The temperature gradient modifies the ABL structure.

CBLs are driven by large convection vortices that generate further turbulence. Reaching a height of $O(1\text{ km})$, the eddies are usually larger. In contrast, SBLs exhibit lower levels of turbulence. In this respect, they can only be propelled through geostrophic wind. Reaching a height of $O(100\text{ m})$, the eddies are smaller. As a result of the SBL reduced turbulence and height, its vorticies characteristic sizes are also smaller. These differences can be seen in the behaviour of the wind turbine wakes. They recover quickly in a CBL because of its higher turbulence level, while they tend to propagate longer in an SBL. These discrepancies in the ABLs type are also impacting the boundary layer modelling. The main difficulty lies in the capture of characteristic vortices, large for a CBL and small for an SBL. To accurately capture small vortices, high spatial resolution is required. However, this resolution comes at the expense of an increase in computational cost. Although CBLs have been widely modelled, accurate and reliable simulation of SBLs remains a challenging task [58].

To enhance comprehension of SBLs by LES, the Global Energy and Water Cycle Experiment (GEWEX) initiated the GEWEX Atmospheric Boundary Layer Study (GABLS) in 2001. The focus of GABLS has been on stable boundary layer over land and on the representation of the diurnal cycle under clear skies. Four benchmarks have been set. An overview was provided by Holtslag et al. [61]. The general conclusions were that moderate stratification could be successfully represented by LES, as long as the resolution was sufficient to properly capture the vortices of SBL [62]. As it is possible to model SBL using the LES technique, this method is increasingly being used to examine more complex scenarios, such as the impact of SBL on wind turbines [63–65]. Although feasible, simulations of the SBL are always at the expense of a very high spatial resolution and therefore a high computational cost [58].

To perform accurate simulations of stable boundary layers and quantify their impact on wind turbines, this work will use a high spatial resolution, based on literature recommendations. For that reason, high-performance computing (HPC) will be used. An LES solver capable of handling massively parallel computations while maintaining good performance will be used.

1.3.3 Unstructured grids for complex terrain

Offshore is the best location for wind power generation. The average wind speed is higher, more consistent, and less turbulent than onshore's. However, the complexity of integrating an offshore wind farm into the electricity grid, coupled with the high maintenance costs [66], has resulted in onshore wind energy being the most used option, as seen in Figs. 1.6 and 1.7. Theoretically, coastal wind energy represents the optimal location for installation. However, acceptance issues frequently impede the implementation of wind energy projects [67]. For these reasons, onshore inland wind energy is the most used at the time. But inland, the terrain is often complex. The heterogeneity of the site influences the horizontal and vertical velocity and temperature gradients, as developed in Section 1.2.2. All micro-scale effects interact with the ABL, making it more challenging to model [68].

A finer comprehension of the physics underlying the previously described phenomena is required to better predict the behaviour of wind turbines in complex environments. However, performing LES on such terrain can be arduous. One of the difficulties lies in representing a very complex boundary based on the topography onto the mesh. Structured meshes, widely used in atmospheric flow simulations, have difficulties following complex geometries. Simple topology might be meshed using a C-shape method [69] but complex terrain, such as Askervein hill [70], Bolund hill [71], Perdigao double hill [72] or Alaiz mountain [73] makes it impossible. Alternatives such as Immersed Boundary methods exist, but also have difficulties in well discretizing the boundary layer. The use of an unstructured grid, able to faithfully represent complex geometries, is therefore very appealing.

However, unstructured grids tend to generate more numerical errors than structured grids. Indeed, for structured grids, parts of the errors made at opposite cell faces when discretizing diffusion terms partially cancel. For unstructured grids, as cells are often distorted, the error does not cancel, and the numerical diffusion is higher. In addition, near the wall, cells must be fine to capture the boundary layer in the direction normal to the surface. In other directions, the discretization can be coarser to circumvent the creation of an excessively large mesh. For unstructured grids, this requirement leads to long thin tetrahedra, which generates more numerical errors when approximating diffusive fluxes. In order to offset these discrepancies, high-order interpolation and diffusion schemes should be employed, reducing numerical errors to a lower order. However, the complexity of developing high-order flow solvers for unstructured meshes has limited their use in real atmospheric studies.

To perform complex terrain simulations, its interaction with atmospheric boundary layer, and the impact on wind turbines, this work will use a solver that can handle unstructured grids, using high-order numerical schemes.

1.4 Objectives

Previous sections have introduced the context of this thesis and the grand challenges of wind energy. Specific tools are required to perform stable boundary layer simulations, to consider the interaction of the terrain with the flow, and to quantify their impact on wind turbines. To achieve this, the solver must:

1. Perform Large-Eddy Simulations,
2. Handle massively parallel computations,
3. Manage unstructured grids,
4. Use high-order numerical schemes.

To the author's knowledge, there is no solver in the atmospheric flow community that meets these criteria. Therefore, a solver that has not yet been used for atmospheric flow simulations but meets these demands will be employed: the YALES2 library [74]. As this solver has already been used multiple times for wind turbines simulations [35, 75–77], the initial objective is to develop an atmospheric solver framework, necessary for such simulations. Subsequently, numerical studies may be conducted. These are the questions addressed in this work.

- Can unstructured meshes be used for the Large-Eddy Simulation of stable atmospheric boundary layers? How does mesh resolution impact the boundary layer? Does the required mesh size be similar to that of structured meshes?

- How to use adaptive mesh refinement to optimize computational cost in wind turbine simulations? How to track the wind turbine wake at a low computational cost? Is adaptive mesh refinement useful for wind turbine simulations?

- How to properly generate an atmospheric inflow for wind turbine simulations? Is the precursor method suited for non-neutral atmospheric boundary layers?

- Would a complex terrain affect the power output and wakes of wind farms? How to accurately mesh the terrain?

- When applied to a realistic wind turbine study, what is the impact of a stable boundary layer on a wind turbine power, loads, and wake, and how does it differ from a neutral boundary layer case?

1.5 Outlines

The goal of the present dissertation is to answer these questions or at least make a substantial contribution. To do so, this work is based on a high-order Large-Eddy Simulation solver (YALES2) using unstructured grids. It focuses on the stable boundary layer modelling and its impact on a wind turbine. The manuscript is organized as follows. Fig. 1.14 summarizes the different chapters and highlights their connections and dependence.

Chapter 2: The Atmospheric Boundary Layer
Chapter 2 presents a review of the functioning of the atmospheric boundary layer and an overview of the current state-of-the-art in its modelling. The first section gives an insight into how the dynamics of the atmosphere works. It reviews its functioning and behaviour. The main physical phenomena involved, such as thermal stratification and Coriolis force, are further developed. The second section presents the state-of-the-art in ABL modelling. Starting with meso-scale modelling, the review then focuses on micro-scale modelling, as well as the coupling between the two scales. The most significant points are developed, such as the free-atmosphere impact, the subgrid-scale modelling and the wall model approach. As this work does not uses meso-scale solver, the inflow turbulence generation methods are reviewed. Finally, wind turbine and wind farm flow modelling are discussed. The existing atmospheric flow solvers for wind turbine applications are reviewed, resulting in the need to use the YALES2 library.

Chapter 3: Numerical methods and wind turbine modelling
Chapter 3 describes the methodology, outlines the theoretical background of fluid dynamics used in this work, and lays out the tools used for the Large-Eddy Simulation of wind turbines. The first section covers the numerical modelling of turbulent flows. Then numerical methods for simulating turbulent flows are presented with a focus on the Large-Eddy Simulation approach. The YALES2 CFD platform is presented in the second section. The incompressible constant density solver is described in detail. The third section deals with the modelling of horizontal axis wind turbines. Both actuator disk and actuator line methods are used and thus presented.

Chapter 4: Development and application of the atmospheric solver
Chapter 4 describes the elaboration of the atmospheric solver, based on the YALES2 library. The several fundamental components of its development are detailed. It encompasses the Coriolis force, the Boussinesq buoyancy approximation and the wall modelling using the Monin-Obukhov Similarity Theory. The solver is then applied against numerical studies with varying stability configurations. The following sections present simulations of a neutral, convective and stable boundary layer. These studies enable the validation of the implementation of the Coriolis force, the Monin-Obukhov similarity theory, and the Boussinesq buoyancy approximation. The stable boundary layer is performed on both structured and unstructured grids, using different grid resolutions. This work has been the subject of a publication [78]. Conclusions are detailed in the last section.

Chapter 5: A new adaptive mesh refinement strategy for wind turbine application
Large-eddy simulation is an expensive technique for studying wind turbines. To accurately predict the flow behaviour most of the turbulence has to be resolved. To do so, the grid is refined. However, refinement comes at the expense of an increase in computational cost. A cost-fidelity trade-off is to be found. Its optimisation is of importance. In Section 5.2, a methodology is developed to decrease the simulation cost while maintaining the same physical precision. The tracking of the wind turbine wake is performed using a progress variable with a source term in the rotor region. Adaptive mesh refinement is used to refine the mesh within the wake to capture smaller vorticies and improve the accuracy of the simulation. The AMR strategy is compared to a reference case with uniform cell size in a coarsely defined wake region. The results of the study are detailed in Section 5.3.3. Finally, the conclusions and the remaining work are detailed in Section 5.4. This work has been presented at the 2022 TORQUE conference and is the subject of a publication [76].

Chapter 6: Realistic wind turbine studies
In Chapter 4, the modelling of atmospheric boundary layers under the three thermal configurations has been validated. In Chapter 5, a new adaptive mesh refinement strategy has been developed for wind turbine simulation, enabling the optimisation of the computational cost for such simulation. This chapter assembles both previous work to enable the study of wind turbines in realistic environments. First, Section 6.1 covers the study of a wind turbine under realistic atmospheric conditions. Based on the experimental and numerical benchmark named SWiFT, both neutral and stable configurations are studied. Finally, as an opening, Section 6.2 deals with the topic of complex terrain. The tools and methodology used to generate complex terrains are presented.

Chapter 7: Conclusion and Perspectives
In the final chapter, general conclusions of this thesis are drawn and perspectives for future investigations are discussed in the field of atmospheric boundary layer and complex terrain impact on wind turbines.

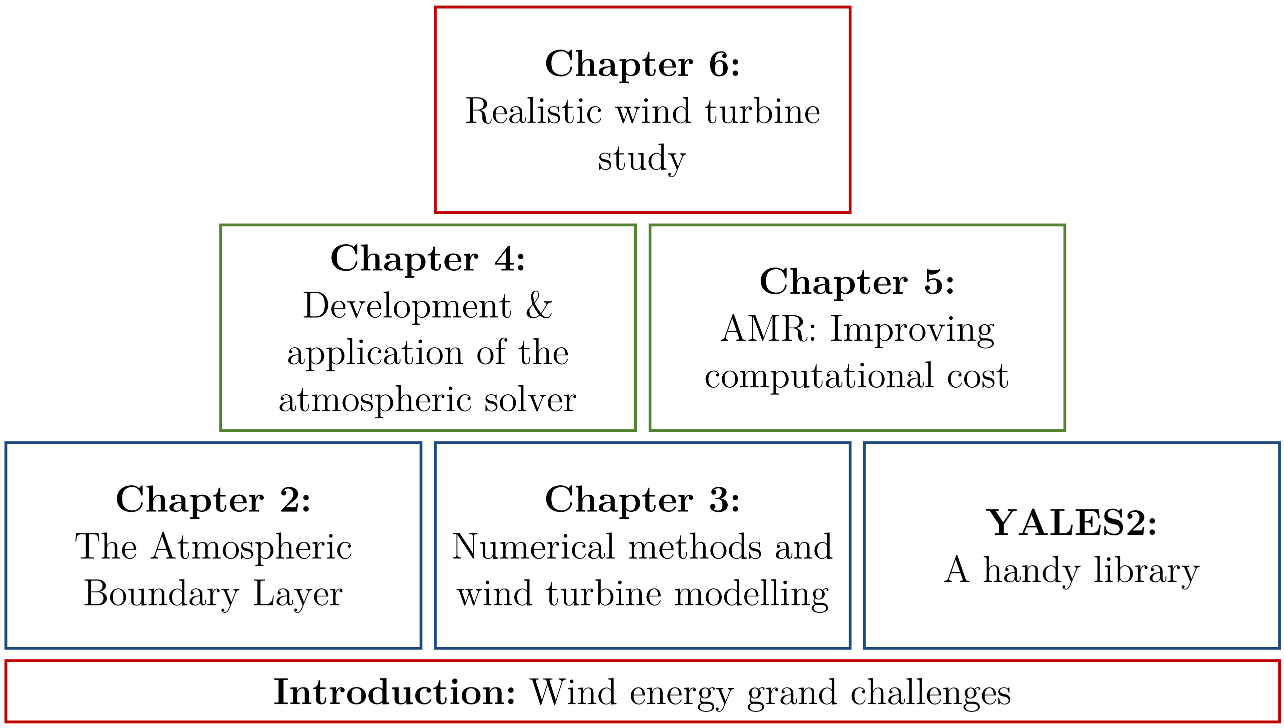

Figure 1.14: Outline of the different chapters, their links and the organisation of this work.

Chapter 2

The Atmospheric Boundary Layer

Chapter 2 presents a review of the functioning of the atmospheric boundary layer and an overview of the current state-of-the-art in its modelling. The first section gives an insight into how the dynamics of the atmosphere works. It reviews its functioning and behaviour. The main physical phenomena involved, such as thermal stratification and Coriolis force, are further developed. The second section presents the state-of-the-art in ABL modelling. Starting with meso-scale modelling, the review then focuses on micro-scale modelling, as well as the coupling between the two scales. The most significant points are developed, such as the free-atmosphere impact, the subgrid-scale modelling and the wall model approach. As this work does not uses meso-scale solver, the inflow turbulence generation methods are reviewed. Finally, wind turbine and wind farm flow modelling are discussed. The existing atmospheric flow solvers for wind turbine applications are reviewed, resulting in the need to use the YALES2 library.

Contents

2.1 Structure of the atmosphere 46

2.1.1 The lowest layer 47

2.1.2 Thermal stratification 49

2.1.3 Coriolis force 52

2.1.4 Geostrophic balance 53

2.2 State of the art in atmospheric flow modelling 54

2.2.1 Meso-scale modelling 54

2.2.2 Micro-scale modelling 57

2.2.3 Coupling the meso-and micro-scale 62

2.2.4 Inflow turbulence generation 63

2.2.5 Wind turbine and wind farm flow modelling 68

2.2.6 Atmospheric flows solvers 71

2.3 Conclusion 72

2.1 Structure of the atmosphere

The atmosphere is an air layer that surrounds the Earth surface. This air is retained because of Earth's gravity. Further from Earth, gravity effects weaken, air density becomes negligible, and the atmosphere gives way to outer space. The atmosphere expends for approximately 100 km, even though there is no definite boundary between the atmosphere and the outer space. As gravity effects decrease with height, most of the mass of the atmosphere is within the first 10 km. It becomes thinner with increasing altitude. The atmosphere is of paramount importance for Earth survivability as it operates as a protective buffer between the outer space and the Earth surface. It shields the surface from meteoroids and solar radiation, regulates temperature, and redistributes heat and moisture via air current. Atmosphere is not sufficient for life to exist, but necessary. Quantities such as temperature and density vary with altitude, but not always in a linear, continuous way. It provides a useful metric to divide the atmosphere into layers, with different physics and behaviour. A summary of these layers and major quantities variation are pictures in Fig. 2.1. Temperature evolves in a complex way and is detailed below. The speed of sound depends only on temperature and thus have a similar behaviour. Density and pressure decrease with altitude. The layers in the atmosphere are the following.

- At the highest altitude is the exosphere, which expends from an ill-defined boundary with the outer space to the thermopause, the boundary with the thermosphere. Thermopause altitude varies from 500 km to 1000 km, due to solar activity. As the exosphere is far from the Earth's surface, meteorological phenomena are non-existent.

- Below is the thermosphere, which expends from the thermopause to the mesopause, the boundary with the mesosphere. The mesopause is found around 80 km altitude. Within this layer, at approximately 100 km altitude, is the Kármán line. Although not universally accepted, this line is often referred to as the edge of space. The temperature in the thermosphere gradually increases with height and can reach 1500°C. But because this layer is far from Earth, the density and pressure are almost zero. In this layer occurs aurora borealis and australis. It is also the layer in which the International Space Station and most satellites are present.

- Between the mesopause (~ 80 km) and the stratopause (~ 50 km) is the mesosphere. In this layer, the temperature decreases with altitude and can reach -100°C. The temperature drop is a result of the decreasing absorption of solar radiation due to the rarefied ozone concentration. Indeed, for ultraviolet wavelengths that have not been absorbed within the thermosphere, ozone is the main absorber. In addition, the mesosphere is the layer in which most meteors burn.

- Below the mesosphere is the stratosphere, which extends from the stratopause to the tropopause, a boundary at approximately 12 km altitude. The ozone layer is within the stratosphere. Consequently, in this layer, the temperature increases with altitude, reaching −60°C at the tropopause and 0°C at the stratopause. This very stable condition leads to almost zero turbulence.

- Finally, the lowest layer in the atmosphere and the one of interest for wind turbine study is the troposphere. This layer expends from the Earth surface to the tropopause (∼ 12 km). Temperature tends to decrease with altitude as the troposphere is mainly heated from the surface. This unstable condition is favourable for vertical mixing in its lowest part. The friction of the troposphere with the Earth's surface forms the atmospheric boundary layer.

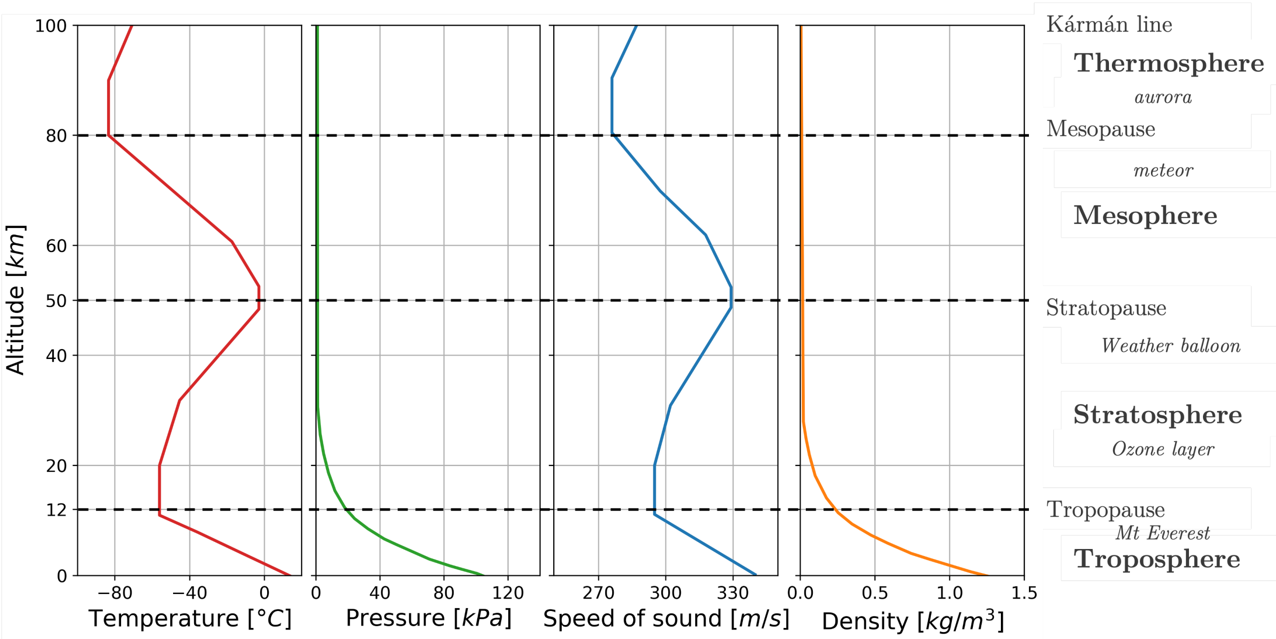

Figure 2.1: Physical quantities variation with the altitude in the Atmosphere. From left to right: Temperature, pressure, speed of sound, density.

2.1.1 The lowest layer

The troposphere is generally decomposed into two sublayers: the free atmosphere and the atmospheric boundary layer. The highest is the free atmosphere. In this region, the influence of the Earth surface is negligible, leading to a steady, mainly horizontal flow. This flow is determined by horizontal pressure gradients and is often called geostrophic wind. Horizontal pressure gradients are driven by large-scale movement of the air, known as global atmospheric circulation. The atmospheric circulation of the Earth can vary with time, but remains fairly constant in the long term. Due to the heat of the sun, the circulation is organised in three convection cells, symmetric between the two hemispheres. These cells are represented in Fig. 2.2.

The three convection cells are the Hadley, the Ferrel, and the Polar cell. The Hadley cells start at the equator, where moist air is warmed by the Earth's surface. As the air becomes warmer, the lower its density, this hot air rises, producing a low-pressure zone near the equator.

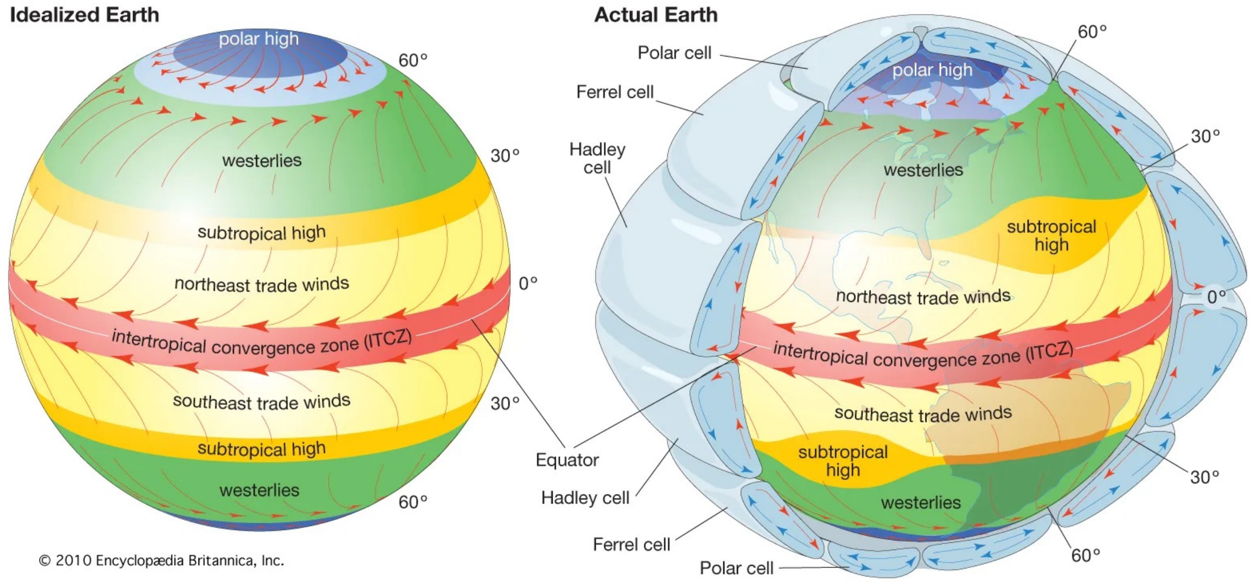

Figure 2.2: Three-dimensional representation of the atmospheric circulation. From [79]

Air from the tropics is attracted, and with the addition of the Coriolis force, which will be detailed hereafter, this generates the well-known "trade winds" on each hemisphere. As the hot air on top moves polewards, it cools down. The density increases back and the air descends near the tropics, causing a high-pressure area. Polar cells operate in a similar way, where cold air at the pole is cold and goes near the Earth surface toward the $60th$ parallel. As the air is warmed by the Earth's surface, density increases, the air rises, and so on. Between these two cells is the Ferrel cell, which can be seen as a gear wheel. The Ferrel cell isn't self-propelled, but mostly driven by the Hadley and the Polar cells. Depending on the season, these cells do not always centre on the equator. However, the functioning remains the same. Within the atmospheric circulation, smaller-scale weather systems, such as depressions or high-pressure systems, occur chaotically. Together they form the geostrophic wind.

Below the free atmosphere is the atmospheric boundary layer, the region directly influenced by the surface. The wind is slowed by the friction of the air on the surface of the Earth. This interaction leads to a complex, three-dimensional, turbulent flow, which can once again be subdivided into two layers:

- **The Surface layer**. This layer corresponds to the lower part of the ABL, accounting for approximately 10% of the total height. In this layer, air friction on the surface is predominant. The direction of the wind at all altitudes is near constant, but the velocity increases with height. The decay is logarithmic similarly to any turbulent boundary layer.
- **The Ekman layer**. This layer goes from the surface layer to the free atmosphere, the upper part of the ABL. In this region, the surface friction is balanced by the Coriolis force

which becomes predominant with height. Due to the Coriolis force, the wind direction is rotating with altitude. The balance between the geostrophic wind, the Coriolis force, and the surface friction forms the Ekman spiral. Instead of having a standard boundary layer, the flow does not only accelerate with height, it also rotates.

A representation of these two layers is shown in Fig. 2.3. The total height of the atmospheric boundary layer varies from 100 m to 3 km, depending on wind shear but also buoyancy forces, which can produce or dissipate turbulent energy. As buoyancy forces depend on thermal stratification, the structure and depth of the ABL are closely related to the thermal stability of the atmosphere.

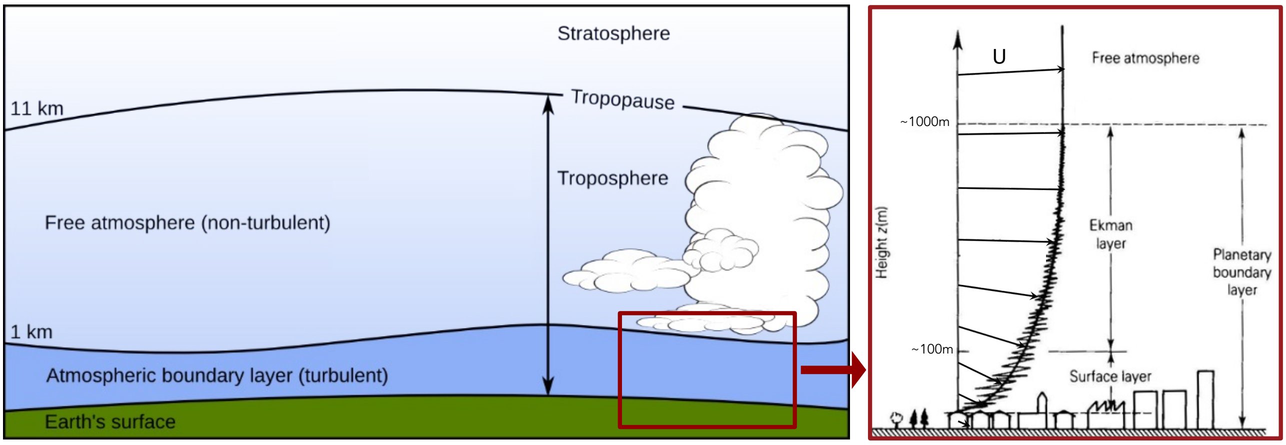

Figure 2.3: Planetary boundary layer representation. Adapted from [80] and [81].

2.1.2 Thermal stratification

The atmosphere boundary layer is different between days and nights. Depending on the vertical temperature gradient and hence the buoyancy flux, three types of ABL exist. As detailed above in Section 1.3.2, the ABL can be neutral, convective, or stable. These boundary layers depend on the vertical thermal gradient. It is important to note that air is considered to be an ideal gas and therefore follows the ideal gas law. In meteorology, the ideal gas law is can be written as:

$$P = \rho_{air} R_s T \tag{2.1}$$

Where P is the atmospheric pressure, ρ_{air} is the air density, R_s the air specific gas constant and T the temperature. Following this law, as the density decreases with altitude, the temperature also decreases. A neutral boundary layer is thus when temperature decrease at the same rate as the background temperature:

$$g/c_p = 9.8 \text{ K/km} \tag{2.2}$$

Where g is the gravitational acceleration constant and c_p the specific heat of dry air at constant pressure. Unstable or convective conditions occur when the temperature decreases at a faster rate than adiabatically. In contrast, stable conditions occur when the temperature decreases (or increases) at a lower rate than adiabatically. In this context, it is convenient to define a potential temperature θ, which accounts for the temperature that results after reducing the pressure to a reference pressure adiabatically:

$$\theta = T\left[\frac{P}{P_{ref}}\right]^{-R_s/c_p} \tag{2.3}$$

Potential temperature is widely used in atmospheric studies because it removes temperature variations caused by altitude-induced pressure variation. It simplifies the description of the boundary layer stratification, where the potential temperature gradient is negative, zero, or positive for unstable, neutral, and stable conditions, respectively. A representation of temperature and potential temperature gradient on neutral, unstable and stable configurations is showcased in Fig. 2.4.

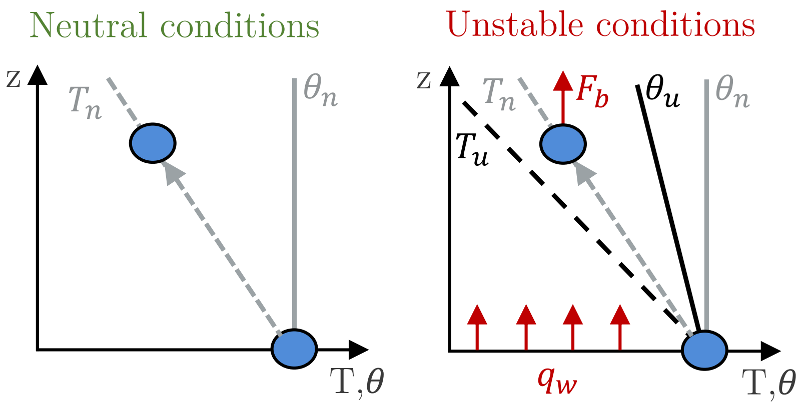

Figure 2.4: Temperature (- - -) and potential temperature (—) vertical profiles for neutral, unstable and stable configurations, illustrating the buoyancy effect on a air parcel (blue circle) that is moving upwards. F_b represents the buoyancy force. Inspired from [82].

As in mid-latitudes CBL occurs during the day and SBL during the night, they usually follow each other on a diurnal cycle. On top of atmospheric boundary layers is a capping layer. This layer acts as a buffer region between the turbulent ABL and the non-turbulent free atmosphere, limiting the penetration of turbulent gusts. The mixing process in this region directly influence the boundary layer height. In the CBL context, moist air stagnates in this region due to the boundary layer effect. Clouds are often capped. This layer is called entrainment zone. In the SBL context, in addition to the capping layer, a residual zone is present. At sunset, the solar heat flux stops, leading to a rapid decrease of buoyancy-driven turbulent mixing. As the SBL develops from the surface, the CBLs leave a residual layer above. The representation of the diurnal cycle is shown in Fig. 2.5.

To quantify the thermal stratification of the atmosphere, the stability parameter is used [83]. This number ζ is defined as:

$$\zeta = \frac{z}{L} \tag{2.4}$$

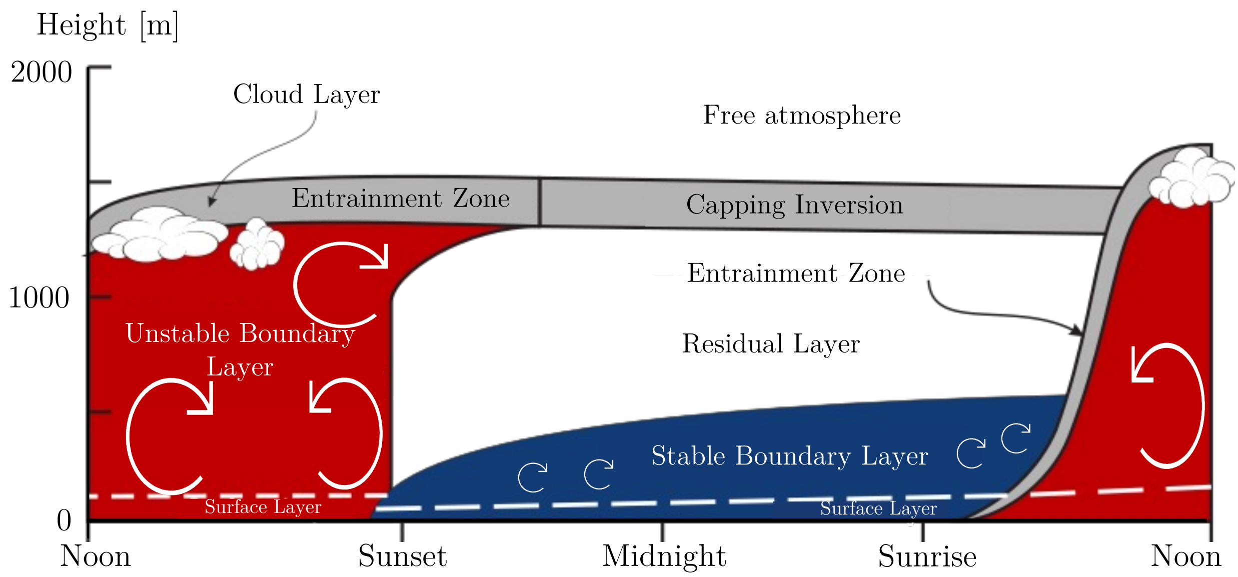

Figure 2.5: Planetary boundary layer representation. Adapted from [80].

Where z refers to the height above ground and L is the Monin-Obukhov length which represents the height at which buoyancy forces and mechanical shear forces are of similar magnitude. The Monin-Obukhov length is defined as:

$$L = \frac{u_*^3\,\theta_0}{\kappa\,g\,\overline{w'\theta'}}\ , \tag{2.5}$$

where u_* is the friction velocity, θ_0 the reference potential temperature, κ the von Kármán constant, g is the Earth's gravity, and $\overline{w'\theta'}$ the kinematic vertical heat flux. The Monin-Obukhov length is highly related to the Monin-Obukhov Similarity Theory, further developed in Section 4.1.3. Atmospheric stability can be classified depending on the stability parameter:

- $\zeta < 0$: The ABL is unstable.
- $\zeta > 0$: The ABL is stable.
- $\zeta \approx 0$: The ABL is neutral.

The stability parameter is related to the friction velocity and thus the surface layer. It is often used in atmospheric boundary layer studies. This number will be used in Section 6.1. In addition to thermal stratification, the Coriolis effect must be taken into account to understand the functioning of an atmospheric boundary layer.

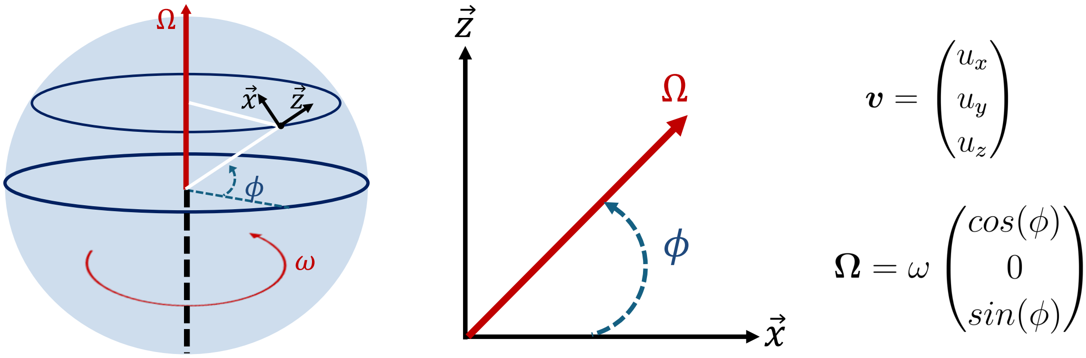

Figure 2.6: Coordinate system at latitude ϕ with x-axis north, y-axis west, and z-axis upward (i.e. radially outward from centre of sphere).

2.1.3 Coriolis force

The Coriolis force is an inertial force that acts on an object in motion in a rotating reference frame. It is the result of Newton's law of motion applied to a rotating frame. Applied on Earth, the equation becomes:

$$\boldsymbol{F_c} = -2 \cdot m \cdot \boldsymbol{\Omega} \times \boldsymbol{v} \ , \tag{2.6}$$

where m is the mass of the object, $\boldsymbol{\Omega}$ is the spin rate of the Earth and $\boldsymbol{v}$ the object velocity.

Consider a location at latitude ϕ. A local coordinate system is set up with the x-axis horizontally due north, the y-axis horizontally due west, and the z-axis vertically upward. Its representation is shown in Fig. 2.6.

The Coriolis force becomes:

$$\boldsymbol{F_c} = -2 \cdot m \cdot \omega \cdot \begin{pmatrix} cos(\phi) \\ 0 \\ sin(\phi) \end{pmatrix} \times \begin{pmatrix} u_x \\ u_y \\ u_z \end{pmatrix} \tag{2.7}$$

where ω is the norm of the spin rate of the Earth and u_x, u_y, u_z the object velocity in the local coordinate system. Thus:

$$\boldsymbol{F_c} = -2 \cdot m \cdot \omega \cdot \begin{pmatrix} sin(\phi) \cdot u_y \\ sin(\phi) \cdot u_x - cos(\phi) \cdot u_z \\ cos(\phi) \cdot u_y \end{pmatrix} \tag{2.8}$$

The vertical component of the Coriolis force is negligible compared to the gravity force. Similarly, the vertical velocity is small compared to the horizontal velocity. Thus, u_z is neglected. Finally, we obtain:

$$
\begin{aligned}
F_{cx} &= -2 \cdot m \cdot \omega \cdot sin(\phi) \cdot u_y \\
F_{cy} &= -2 \cdot m \cdot \omega \cdot sin(\phi) \cdot u_x
\end{aligned}
\tag{2.9}
$$

To simplify writing, we introduce the Coriolis parameter, analogous to a frequency, such that: $f = 2\ \omega\ sin(\phi)$.

Due to the negative cross product between the Earth rotation velocity and the velocity of the object, in the north hemisphere all moving objects are automatically deflected to the right. In the south hemisphere, they are deflected to the left. The vertical components of the cross-product is usually negligible compared to earth gravity. Although the horizontal Coriolis force component is maximal at the poles, it decreases as the equator approaches. To determine whether the Coriolis force is important, the Rossby number can be computed. It is the ratio of the velocity U of the object to the product of the Coriolis parameter f and the length scale L, of the motion:

$$
Ro = \frac{U}{fL} \ . \tag{2.10}
$$

Hence, it is the ratio of inertial forces to Coriolis forces. A small Rossby number indicates that the object is mostly affected by Coriolis forces, while a large Rossby number indicates that inertial forces are predominant. This is noticeable for trains, which in the northern hemisphere have a more worn rail on the right-hand side. But, above all, it has a major impact on atmospheric flows. As examples, an atmospheric system moving at $U = 10$ m/s with a characteristic size of $L = 1000$ km, has a Rossby number of approximately 0.1. Coriolis forces are predominant. It should be noted that for tornadoes or other very high-velocity systems, the Rossby number is large, and the Coriolis force has little impact. The centrifugal force balances the pressure.

2.1.4 Geostrophic balance

In a neutral boundary layer, only three forces intervene. The pressure gradient due to large-scale movement, the Coriolis force due to the rotation of the Earth, and the drag force due to surface roughness. The result of these forces determines the direction and intensity of the wind speed. In the free atmosphere, since surface friction is negligible, a balance is found between the Coriolis force and the pressure gradient. It is called geostrophic balance. An overview of these forces is shown in Fig. 2.7. For the free atmosphere, the pressure gradient equations are:

$$
\begin{aligned}
0 &= -\frac{1}{\rho}\frac{\partial P}{\partial x} + fV_g \\
0 &= -\frac{1}{\rho}\frac{\partial P}{\partial y} - fU_g
\end{aligned}
\tag{2.11}
$$

where V_g and U_g are the horizontal geostrophic wind components. As mentioned above, the vertical component is usually neglected because the order of magnitude of the Coriolis force in this direction is negligible compared to gravity.

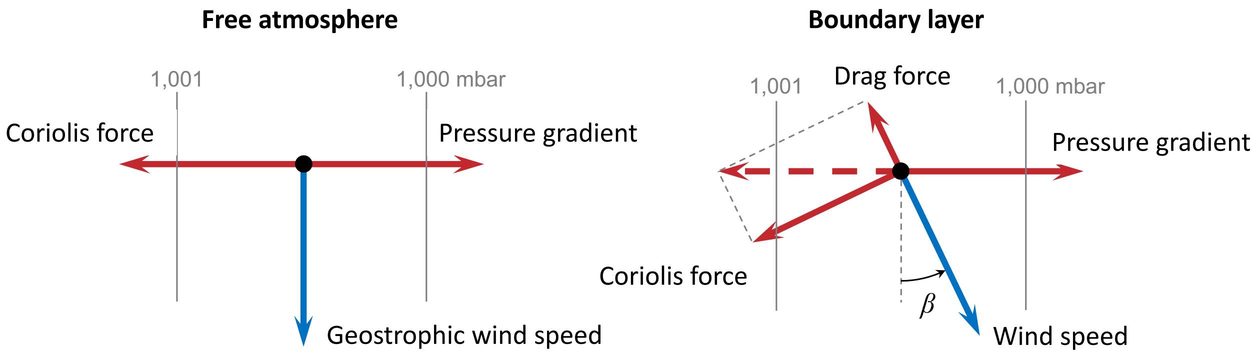

Figure 2.7: Geostrophic balance representation in the free atmosphere and in the ABL.

2.2 State of the art in atmospheric flow modelling

As the atmosphere is a complex non-homogeneous turbulent flow, the accurate modelling of its flow physics is a vast topic which involves a wide range of themes. Depending on the application, some areas of research are more significant than others. In that regard, this atmospheric flow state-of-the-art focuses on atmospheric flow modelling for wind turbine applications. Particular attention is paid to the difficulty of representing all the scales. Different methods and models have been developed over the years to address some physical or numerical issues. By reviewing the different flow solvers used in the literature, the objective is to demonstrate the distinctive characteristics of the solver developed in this work and its potential contributions to the scientific community, which justify this thesis.

2.2.1 Meso-scale modelling

Meso-scale modelling has become a cornerstone of wind energy research, offering insights into atmospheric dynamics at regional scales. These models bridge the gap between global climate models and micro-scale simulations, providing essential boundary conditions for understanding wind farm flows. Meso-scale models simulate atmospheric processes at scales ranging from a few kilometres to several hundred kilometres. The free atmosphere process is one of them. As mentioned above, the height of the boundary layer is influenced by the stratification of the free atmosphere aloft [84]. In order to classify ABLs, the surface heat flux is therefore not sufficient. Another parameter, depending on the free atmosphere, is often used, the Brunt-Väisälä frequency [85]. It is defined as:

$$N \equiv \sqrt{\frac{g}{\theta}\frac{d\theta}{dz}}\ , \tag{2.12}$$

where θ is the potential temperature, g the local acceleration of gravity and z geometric heigh. The Brunt-Väisälä frequency reflects the stability of the fluid to vertical displacements. It measures the frequency at which a vertically displaced parcel will oscillate within a stable environment. N^2 is used to determine whether the flow is stable or unstable. If $N^2 < 0$, the flow is unstable and the air parcel will continue to move away from its initial position. If $N^2 = 0$, the air parcel will not be entrained, neither toward its initial position nor away from it. Finally, if $N^2 > 0$, the flow is stable and the air parcel will be drawn back towards its initial position. In doing so, the air parcel will oscillate around its initial position, leading to a phenomenon called gravity waves [65].

From the surface heat flux and the free atmosphere Brunt-Väisälä frequency, we can distinguish different planetary boundary layer (PBL) types. As neutral boundary layers are defined by a zero surface heat flux, two types exist:

- **The True Neutral PBL (TN PBL)**: This boundary layer occurs when $q_w = 0$ and $N = 0$. Hess [86] analysed atmospheric data and concluded that the truly neutral ABL is an idealised case that "does not seem to exist in the atmosphere or is so rare that it has not been well observed.".

- **The Conventionally Neutral PBL (CN PBL):** This boundary layer occurs when $q_w = 0$ and $N > 0$. It represents a state at which the buoyancy flux at the surface is zero but the free atmosphere is strongly stratified. CN PBLs are usually encountered over sea or lands during the transition period between CBL and SBL [87].

For the stable boundary layer, unlike the NBL, the surface heat flux is negative. There are two types of SBL that correspond to two different physics.

- **The Nocturnal Stable PBL (NS PBL):** This boundary layer occurs when $q_w < 0$ and $N = 0$. It represents a boundary layer made stably stratified by flowing over a cooler surface.

- **The "Long-lived" Stable PBL (LS PBL):** This boundary layer occurs when $q_w < 0$ and $N > 0$. It represents a boundary layer made stably stratified by entrainment of warmer air aloft.

This classification is of importance, as it changes the atmospheric boundary layer dynamic. In particular, it changes the relation between the geostrophic wind and the frictional velocity. This relation is named the geostrophic drag law and is highly dependent on thermal stratification [88]. For unstable boundary layer, such classification is less important are they are self propelled and thus depends less of external factor such as the stratification of the free atmosphere. More details on how to compute the geostrophic wind from frictional velocity is given in **Appendix E**.

The free atmosphere is not the only meso-scale effect impacting wind turbines. The Coriolis effect also plays a major role in wind shear. As the wind speed increases with altitude, the Coriolis effect causes a change in the wind direction accordingly. It has been confirmed by numerous field observations [89–91]. This force creates a lateral shear, which is considerable for large-sized wind turbines. It has been shown in Lu and Porté-Agel [92] that the Coriolis force not only causes additional lateral shearing loads on wind turbines but also drives part of the turbulence energy away from the centre of the wind turbine wakes. In 2016, Tsai and Colonius [93] studied the Coriolis effect on a two-dimensional airfoil profile. It is found that at low tip-speed ratios, the Coriolis force induces a wake capturing phenomenon which leads to a lift decrease. In the light of these studies, the Coriolis force must be considered for wind turbine or wind farm simulations.

Other atmospheric effects such as moisture can also affect wind turbines and wind farms. One of the first studies dates from 2011. Roy studied the impact of a wind farms on local hydrometeorology [94]. The results showed that wind farms affect near-surface air temperature and humidity in an area up to 23 km downwind, depending on thermal stability. In 2018, Siedersleben et al. [95] investigated the marine boundary layer (MBL) taking into account both temperature and humidity. They found that offshore wind farms can impact the MBL. The temperature was increasing within the wake while the water vapor mixing ratio was decreasing, both impacting the wake. Additional work has been carried out on the protection of wind turbine blades against erosion. A recent review investigates the area of leading edge erosion of blades, anti-erosion coatings and new materials [96]. It is argued that humidity has potentially a strong effect on coating degradation. Although humidity effects could have been included in the framework by using the virtual potential temperature [80], the current work will always assume dry atmospheric conditions. It simplifies complex phenomena such as cloud formation and phase transitions, which are beyond the scope of this work, to focus on more important phenomena: the Coriolis force and the thermal stratification.

Meso-scale models, such as the Weather Research and Forecasting (WRF) model, are commonly used in wind energy applications because of their ability to resolve atmospheric dynamics across large spatial and temporal scales. These models allow a representation of regional wind climate, boundary layer dynamics, cloud processes, and wind variability [39]. Parametrizations of turbulence and surface interactions are crucial for meso-scale models to accurately predict wind farm performance. However, their ability to represent flows near the surface, especially in complex terrains, remains limited [97, 98]. In 2016, Shin and Dudhia [99] showed that for the WRF model, all the schemes that are designed for one feature do not necessarily perform well for other aspects. Wind farm parametrizations have also been directly used in meso-scale models. In 2013, Fitch et al. introduced a wind farm wake parametrization model into WRF to study large-scale impacts of wind farms on the local environment [100]. Jiménez et al. [101] used this wind farm parametrization to replicate the Horns Rev wind farm, using a horizontal resolution of 333 m. But they found that the model tends to underestimate the power deficit, attributing this effect to the mesh resolution, still too coarse. In fact, these meso-scale models often oversimplify turbulence and wake effects on wind turbine scales, leading to inaccuracies in wake predictions and power forecasts [39]. Thus, the integration of micro-scale models into meso-scales simulations is the best option for accurate wind farm modelling. Meso-scale models provide the background meteorological conditions, which are downscaled to resolve finer scales using high-resolution models like LES. This coupling allows to capture both the regional wind dynamics and the localized effects of terrain and turbine wakes [39].

2.2.2 Micro-scale modelling

Micro-scale modelling focuses on the detailed simulation of atmospheric flows at small scales, typically at the level of individual wind turbines or wind farms. These models resolve fine-scale turbulence and wake dynamics, capturing the interactions between turbines and the surrounding ABL. Micro-scale modelling is critical for understanding turbine performance, optimizing wind farm layouts, and mitigating wake-induced power losses, loads, and fatigue [39]. Micro-scale modelling addresses the gaps left by meso-scale models, which cannot fully resolve turbulence or wake interactions at turbine scales. The LES technique is the most widely used when modelling the micro-scale in wind energy applications, providing a high-fidelity approach. It enables a fine prediction of wake recovery and turbulence intensity downstream of wind turbines, both of which significantly influence wind farm performance [34]. Many studies have validated its application, the first being the one from Wu and Porté-Agel [102], in 2011, which demonstrated the ability of LES to accurately simulate turbine wakes and their interaction with the ABL.

Subgrid-scale model

Unlike RANS models, which rely entirely on turbulence parametrizations, LES resolves large-scale turbulent structures while modelling only the unresolved small scales. This modelling is performed using subgrid-scale (SGS) models. The first ABL study using LES was conducted by Mason and Derbyshire [103] in 1990. They showed that the flow behaviour was highly dependent on the SGS model. However, it should be noted that their mesh was less than eighty thousand elements, with a grid spacing for a maximum resolution of $\Delta = 12.5$ m. For a stable boundary layer, it is now known to be particularly coarse [62], meaning that much of the energy cascade is unresolved. The SGS model thus has a higher impact. In 2000, Kosovic and Curry [104] used a non-linear SGS model to reproduce an SBL, allowing a better insight of the SGS model. Their study based on the Beaufort Sea Arctic Stratus Experiment (BASE) is the one that led to the GABLS1 benchmark [62]. Various SGS models exist, each with its advantages and disadvantages. The most widely used are detailed below.

1. **Smagorinsky model.** Introduced by Smagorinsky in 1963 [57], the Smagorinsky model assumes that the equilibrium between the kinetic energy production rate and dissipation

rate at the LES filter size. The turbulent viscosity is expressed as:

$$\nu_{SGS} = C_s^2\,\Delta^2\,\bar{\mathcal{S}}\ , \tag{2.13}$$

where C_s is the model coefficient, usually taken between $0.1 - 0.2$. For atmospheric flow simulations, a commonly taken value is $C_s = 0.17$. Δ the grid size and $\bar{\mathcal{S}}$ the filtered rate of strain. Details can be found in Section 3.1.5. This model was first developed for atmospheric circulation, but have been extensively used in all research domains because of its simplicity, robustness, and affordable computational costs [58]. However, this model is limited. First, because the Smagorinsky constant is static and uniform, the model has one universal length scale to model all the eddies. The near-wall regions, where the size of the eddies reduces, are thus poorly modelled. Second, it assumes SGS stress isotropy, which is correct only for isotropic flow. It performs relatively well for neutral flows, but lacks precision for stable boundary layers, where the flow is anisotropic. In this scenario, the model overestimates dissipation leading to excessive energy loss.

2. **Dynamic Smagorinsky model (DSM).** Elaborated by Germano et al. in 1991 [105] and improved by Lilly in 1992 [106], the dynamic Smagorinsky model consists of dynamically determined the Smagorinsky constant, based on the resolved turbulence. Details can be found in Section 3.1.5. Do to this dynamic procedure, this model has several advantages. First, the model is universal. Unlike the classical Smagorinsky model, the DSM does not require manual tuning of C_s for different flows or grid resolutions. It can also adapt to weakly/strongly turbulent regions by locally reducing/increasing dissipation. However, this model has two drawbacks. First, by dynamically determining the Smagorinsky constant, the computational cost is increased. Second, this model is based on the same isotropy assumption as the classical Smagorinsky model, assuming that small scales are isotropic. In stratified atmosphere, this assumption is not entirely true.

3. **One-Equation Turbulent Kinetic Energy (TKE) Model.** Developed by Deardorff in 1970 [107], its application to boundary layers dates back to 1980 [108]. The TKE model solves an additional transport equation for SGS kinetic energy to compute eddy viscosity, expressed as:

$$\nu_{SGS} = C_k\, l_{SGS}\, \sqrt{e_{SGS}}\ , \tag{2.14}$$

where C_k is the model coefficient, e_{SGS} is the SGS kinetic energy. $l_{SGS} = \min(\Delta, l_e)$ with l_e denoting a stability-related length scale. The model thus takes into account buoyancy effects into the SGS stress formulation, which makes it suitable for moderately stable boundary layers. However, the model has a relatively high computational cost due to the additional equation to be solved, and it requires a careful calibration of the model parameters to ensure stability [58].

4. **Stability-Dependent Smagorinsky (SDS) Model.** Introduced by Mason and Der-

byshire in 1990 [103], this model extends the Smagorinsky model by incorporating stability corrections. The work has been extended by Stevens et al. in 2000 [109] by explicitly modifying the Smagorinsky constant and the Prandtl number, based on local stability conditions, i.e. the gradient Richardson number defined in Section 2.1.2. As this model does not solve an additional transport equation, its computational cost is affordable. However, as it is based on the gradient Richardson number, the model is turned off in the case of strongly stable boundary layers, assuming a strong turbulence decay and that the flow becomes laminar. However, as stated in Section 2.1.2, this assumption has been shown to be incorrect [110, 111].

5. **Wall-Adapting Local Eddy-Viscosity Model (WALE).** Developed by Nicoud and Ducros in 1999 [112], the WALE model extends the Smagorinsky model to better capture near-wall turbulence by accounting for both strain and rotating tensors. By reducing the turbulence near walls, this model does not require near-wall damping functions. Furthermore, the flow is not necessarily homogeneous. The WALE model is accurate in the near-wall region and can handle flow with strong shear or rotation. However, like the Smagorinsky model, this model is not tailored to capture the temperature profile [113].

6. **σ-model.** Developed by Nicoud et al. in 2011 [114], the σ-model relates the SGS to the singular values of the resolved velocity gradient tensor. The objective of this model was first to drain the proper amount of kinetic energy from the resolved velocity scales while remaining positive and evaluated locally. Also, the model is tailored to vanish for a two-dimensional or a two-component flow, such as pure shear or rotation cases. As for the WALE model, the σ-model has a cubic behaviour near walls, not requiring near-wall damping functions. The model can be used in a static or a dynamic form. In 2014 the model has been tested by Rieth et al. [115] which found that compared to a dynamic Smagorinsky model, the σ-model was more cost effective for similar results. But like the WALE model, the model is not suited for anisotropic SGS turbulence.

7. **Lagrangian-Averaged Scale-Dependent Model (LASD).** Elaborated by Meneveau and Katz in 2000 [116], the LASD model has been introduced to better manage heterogeneous flows, such as flows over complex terrains of wind farms. It incorporates a Lagrangian averaging procedure along the fluid pathlines, allowing three-dimensional variation of the SGS coefficients. The model has been improved using a dynamic procedure by Bou-zeid et al. in 2005 [117], renaming the model: LASDD. The main advantage of the model is to capture the anisotropy of the SGS stress tensor, which makes it accurate for stratified or heterogeneous flow. However, this model has the highest computational cost due to the required global filtering operations. It can cost up to 34% more than the classical Smagorinsky model [118]. In addition to the computational cost, the model requires the storage of time histories, which makes it hard to implement in most CFD codes and leads to higher memory overhead.

SGS model	Advantages	Disadvantages
Smago. [57]	Ease of implementation Robustness Cost effective	Near-wall region Isotropic flows Tuning coefficient
Dyn Smago [105, 106]	Tuning-free Adapt to local turbulence	Isotropic SGS turbulence
TKE [107, 108]	Buoyancy effects	High computational cost Tuning coefficient
SDS [103, 109]	No transport equation affordable cost	Turns-off in strongly stable scenarios
WALE [112]	Wall handling Ease of implementation Cost effective	Isotropic SGS turbulence Tuning coefficient
σ [114]	Wall handling Ease of implementation Cost effective	Isotropic SGS turbulence
LASD [116, 117]	Anisotropic flows	Very high computational cost Temporal data memory
AMD [119–121]	Anisotropic flows Cost effective	Tuning coefficient

Table 2.1: Summary of the advantages and disadvantages for the main SGS models in atmospheric flows for wind turbine application.

8. **Anisotropic Minimum Dissipation Model (AMD).** Dissipation models is a new class of SGS models which does not require additional filtering operations. The minimum dissipation is computed to balance the turbulence production at subgrid-scales. As the SGS energy cannot increase, the energy is upper bounded by the Poincaré inequality [118]. Initially developed for isotropic turbulence by Verstappen in 2011 [119], Rozema et al. [120] extended their use in 2015 to anisotropic turbulence. Furthermore, Abkar and Moin added buoyancy effects in the AMD model in 2017 [121]. Like the LASD model, the AMD model provides three-dimensional variation of the SGS coefficients, which allows a better reproduction of anisotropic flows. Although recent, the AMD model has shown promising results in a stable boundary layer context. With results similar to the LASD model, the computational cost is reduced by 15% [118] and does not require particular memory storage. One disadvantage of the AMD model is that the Poincaré constant must be tuned in complex scenarios such as wind farms. While attractive, the AMD model is still young and additional validation would be beneficial.

As all subgrid-scale models have pros and cons, choosing one is often a source of debate.

In order to clarify, Table 2.1 summarises the advantages and disadvantages of all the models presented above. For the computational cost, it should be mentioned that while the cost varies from one model to another, their cost is almost negligible compared to the cost of the whole computation. In addition, while SGS models impact the flow behaviour, their impact is often overestimated. In 1994, Mason [122] conducted a review of the SGS technique and showed that most results are not sensitive to SGS models. In 2006, Beare et al. [62] conducted a comparison of different codes, using different SGS models (classical Smagorinsky, dynamical Smagorinsky, TKE). All models were able to reproduce a stable boundary layer in good agreement. In 2015, Sarlak et al. [123] compared different SGS models based on prediction of flow structures for a wind turbine study. The results show that the choice of the SGS model is not a determining factor in the simulation accuracy, as long as the resolution is sufficient. Finally, in 2020, on the SWiFT benchmark (IEA wind task 31), one conclusion of the original comparison [124] was that the inflow turbulence characteristics had a greater impact than the SGS models. In light of these results, it was decided that the dynamic Smagorinsky model would be used in this work. Although not the most accurate in a strongly stratified configuration due to turbulence anisotropy, the model has been tested and validated for years. The computational cost is also affordable.

Law of the wall

Another difficulty in simulating the ABL is being able to accurately represent the turbulent flow in the region near the wall. Due to the high shear stress near the wall surface, very large velocity gradients are present, and the ability to accurately capture these effects is necessary to obtain realistic simulation results. When performing LES of wall-bounded flows, there are two options that can be used: wall-resolved LES and wall-modelled LES. Since the viscous sublayer has a length scale of the order of 1 mm, performing a wall-resolved LES of the ABL would require a spatial resolution of the same magnitude. Therefore, it is unrealistic with current computational resources.

An idealized vertical profile of the mean flow for a neutral boundary layer is the logarithmic wind profile. Derived from Prandtl's mixing length theory [125], which states that the horizontal component of mean flow is proportional to the logarithm of height, the velocity equation is:

$$u(z) = \frac{u_*}{k}\left[\ln\left(\frac{z}{z_0}\right)\right] \ , \tag{2.15}$$

where $u_* = \sqrt{\tau_w/\rho}$ is the friction velocity. τ_w refers to the local shear stress at the wall. ρ is the density of the fluid. κ the von Karman constant. z_0 the roughness length. Yet, this vertical profile is unrealistic for non-neutral conditions. Therefore, Monin and Obukhov further generalize the theory of mixing length [126].

The Monin-Obukhov similarity theory (MOST) [126,127] is the wall model used in nearly all the computational codes to represent the effect of the ground for non-neutral atmospheres.

Its popularity is due to its practical convenience and reliability [128]. This model can handle all three atmospheric thermal configurations. The theory is developed in Section 4.1.3, as this wall model has been implemented in the YALES2 library.

Basu and Lacser [129] indicate that repeatedly in the literature of very high-resolution LES the lowest grid level was located well within the roughness sublayer. However, this scenario is incompatible with the Monin-Obukhov similarity theory. Indeed, they recall that MOST can only be considered valid within the inertial sublayer (the upper part of the surface layer), but not in the roughness sublayer (below). In this region direct effects of single surface roughness elements are present. Therefore, they recommend using the lowest grid level z_1 at $z_1 > 50z_0$. Additionally, since wall models are derived from averaged Navier-Stokes equations, quantities such as velocity and temperature must be spatially filtered [130]. For structured meshes filtering quantity at the first grid node is straightforward. But for unstructured meshes, as the first grid node is not easily defined, the operation is much more arduous. In this thesis, wall-law filtering has been developed and is detailed in Section 4.1.4. Finally, as mentioned in [131], the MOST wall law is more reliable when prescribing the surface temperature instead of the surface heat flux as a boundary condition. However, this formulation leads to a two-unknown problem, where the frictional velocity and the wall heat flux must be determined. In this regard, it has been decided that both methodologies could be useful depending on the case and have thus been developed in YALES2.

Micro-scale models are the adequate tools for wind turbine and wind farm studies, allowing accurate simulation of the surrounding turbulence and the interaction between wind turbines and site topography. However, as stated before, such studies are only possible if inflow conditions are defined. For a realistic wind turbine study in the context of regional wind dynamics, the surrounding atmosphere is required, and micro-scale models are usually too limited for its modelling. In this context, the coupling between meso-scale and micro-scale models are appropriate.

2.2.3 Coupling the meso-and micro-scale

Meso- and micro-scale models perform well in two different areas. Meso-scale models enable the modelling of large-scale dynamics such as climate or atmospheric scales. Micro-scale models enable the accurate modelling of small scales such as near-wall region or wind turbine interactions. It is therefore appealing to combine the strengths of both to enable the modelling of regional wind flows and the response of wind farms.

However, coupling meso-scale and micro-scale is not as straightforward as it seems. As stated, micro-scale models are struggling with representing all the atmospheric scales, while meso-scale models are too coarse to resolve local turbulent structure. Therefore, both should be used in their range of use. However, these ranges do not overlap. In 2004, Wyngaards popularized a term: "The Terra incognita", referring to the intermediate scales between the meso- and the micro-scales, where turbulence is neither fully resolved nor adequately parametrized [132]. These scales are generally between 100 m and 2 km. At this range, meso-scale models rely on coarse parametrizations of turbulence that fail to capture localized dynamics, while micro-scale models are computationally constrained and cannot fully resolve all the scales. This modelling gap poses significant issues for applications like wind energy, where wake effects and near-surface turbulence often occur within this range. Efforts to address the Terra incognita have been made over the years, with various methods developed to couple the meso-scale and the micro-scale, also called downscaling methods. A fairly recent and exhaustive review of the matter has been completed by Sanz Rodrigo et al. [39] in 2016.

In the literature on atmospheric flow solver for wind turbine applications, some codes use internal coupling, while others have used external coupling. For the internal coupling, we often found meso-scale codes that have developed an internal LES solver for micro-scale flow modelling. In the WRF library [133], the Advanced Research WRF (ARW) has been developed for micro-scale simulations. In 2019, Prósper et al. [134] studied a wind farm on complex terrain. For the Meso-NH solver [135], grid nesting is also used since the 2000s [136]. Other codes, usually codes that are designed for micro-scale study, use external coupling with a meso-scale solver. In 2012, Wyszogrodzki et al. [137] uses the WRF model as meso-scale model and the EULAG LES model as CFD model. In 2020, Piroozmand et al. [138] coupled the Consortium for Small-scale Modeling (COSMO) meso-scale model with an Unsteady Reynolds Averaged Navier–Stokes (URANS) implementation of the OpenFOAM CFD model. In 2022, Vogel et al. [139] coupled WRF with PALM [140], a micro-scale flow solver. The major codes for atmospheric flow simulations are reviewed hereafter.

For large spatial- and temporal-scale studies, coupling a meso-scale to a micro-scale solver is mandatory. To study a wind turbine or a wind farm in the context of regional wind dynamics, a meso-scale model is required. However, for more local studies, stand-alone micro-scale models can performed well. Due to computational power increase, micro-scale models can study wind turbines in atmospheric boundary layers, as long as the spatial and temporal scales are limited. In particular, if they take into account meso-scale phenomena such as the Coriolis force, they can accurately simulate the atmospheric boundary layer. As this work will perform simulations with a maximum spatial scale of $O(1\text{km})$ and a time scale of $O(1\text{h})$, it does not require a meso-scale model. The coupling to a meso-scale flow solver could come at a later stage, but is beyond the scope of this work. As such, the inflow turbulence characteristics are not given by an external solver and must be adequately generated.

2.2.4 Inflow turbulence generation

To adequately study wind turbines in an atmospheric context, inflow turbulence must be realistic. Several turbulence generation methods exist. As inflow turbulence determines the flow behaviour, it has a major impact on the study [141]. Depending on the applications, different methods exist with a different cost-accuracy trade-off. The most widely used methods are

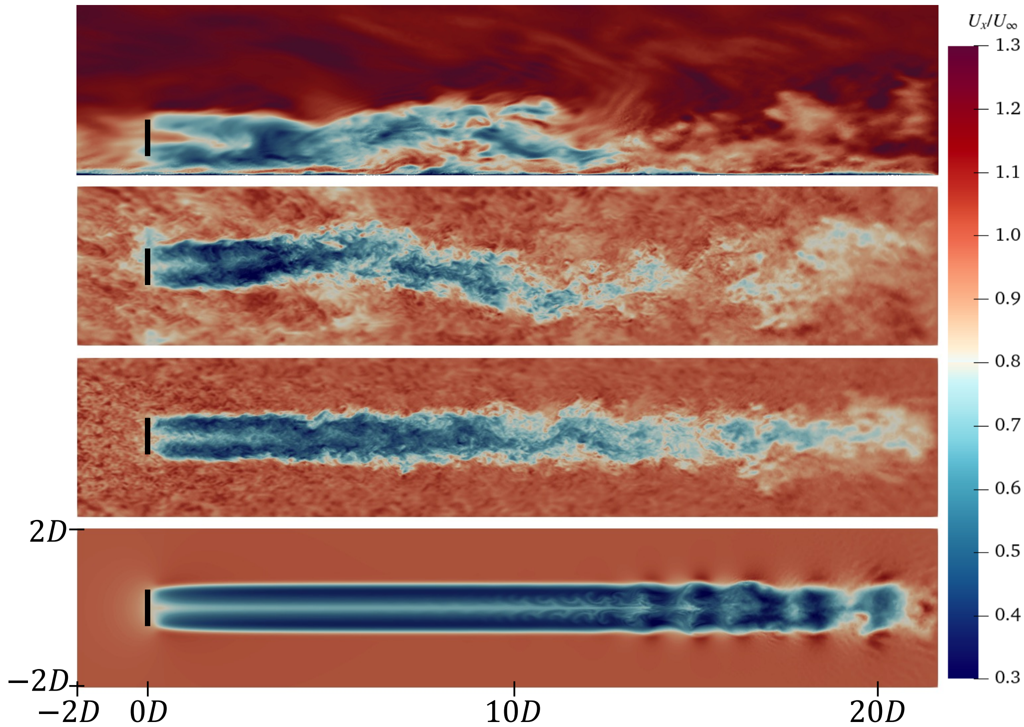

Figure 2.8: Velocity field. From top to bottom: Precursor method, Mann algorithm method, synthetic method: Homogeneous isotropic turbulence (HIT) and a constant velocity .

wind tunnel replication, synthetic methods, Mann algorithm, recycling method, and precursor method. Figs. 2.8 and 2.9 illustrate the impact of the turbulence injection method on a wind turbine wake. Fig. 2.8 shows an instantaneous velocity field while Fig. 2.9 shows the turbulent kinetic energy (TKE) field. The lower illustration shows the impact of a constant-velocity inflow. The TKE field exhibits very low fluctuation, which results in very little destabilisation of the wind turbine's wake, highlighted by the instantaneous velocity field. Above, the inflow turbulence is generated using a synthetic method, which generates homogeneous isotropic turbulence (HIT). The TKE field exhibits a higher level of turbulence, especially at the tip of the blade. The wind turbine wake is more destabilized; however, the instantaneous velocity field exhibits non-realistic atmospheric turbulent structure. Above, the inflow turbulence is generated using the Mann algorithm method. This method generates larger coherent structures. Finally, in the top, the precursor database method is used. The main difference from the Mann algorithm method is that the inflow can follow a logarithmic velocity profile that increases with height. Thus, the interaction with the ground can be studied. The aforementioned methods are developed hereafter.

The wind tunnel replication method is a straightforward method in which an exact replica of a wind tunnel is composed [142]. Thus, the approaching flow is also a replica of the experimental wind tunnel that contains temporal and spatially correlated structures. This method has been used by Paepe et al. [143] in a turbulent flow study and by Phuc et al. [144] and Capra et al. [145].This method has high accuracy, but is computationally expensive. It is also

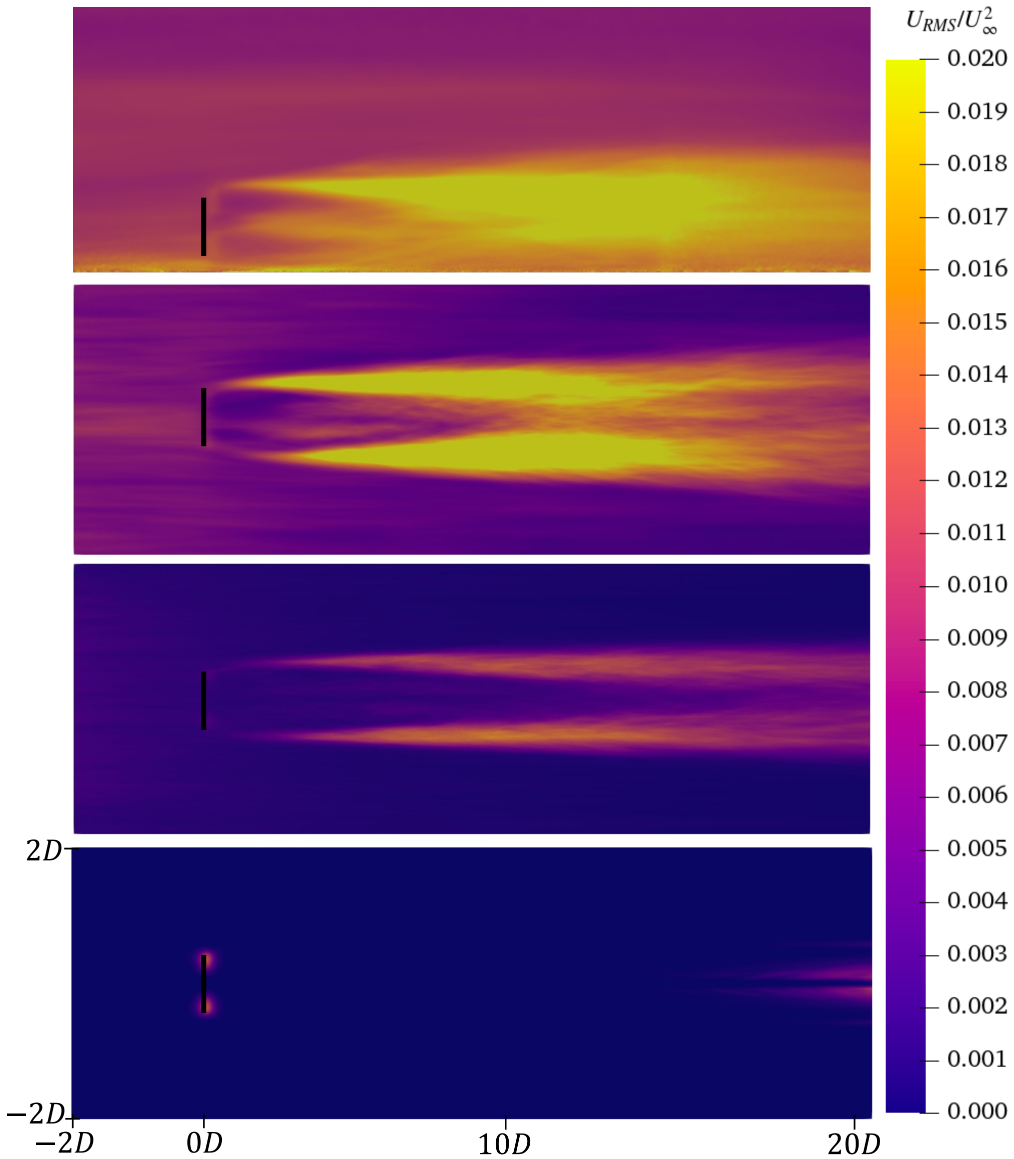

Figure 2.9: TKE field. From top to bottom: Precursor method, Mann algorithm method, synthetic method: Homogeneous isotropic turbulence (HIT) and a constant velocity profile with no fluctuations.

limited to a wind tunnel simulation, which is a good way to determine wind loads on complex structures, but not thermal stratification with all the turbulence effects that follow.

Synthetic inflow turbulence is the result of several methods [141]. The Fourier methods offer an approach in which the turbulence is generated through a summation of harmonic functions. For example, the random flow generation (RFG) method proposed by Smirnov et al. [146] is based on previous studies of synthesizing divergence-free vector fields from a sample of Fourier harmonics [147]. It allows to generate non-homogeneous anisotropic flow field representing turbulent velocity fluctuations. Huang et al. [148] modified the Smirnov method, so that any assigned energy spectrum could be reproduced; they termed this method the discretizing and synthesizing random flow generation method. However, this method shows limitations such as the underprediction of wind-induced forces and torsional moments as well as poor spectra fidelity. Improvements have been proposed by Castro et al. [149] with a focus on pressure and force coefficients. Aboshosha et al. [150] also proposed a modification, named consistent discrete random flow generation.

The digital filter whose aim is to generate velocity fluctuations starting from a set of random data using a digital filter based on a correlation function. In this method, correlations are imposed directly and not through a prescribed energy spectrum [151]. Some examples of digital filter methods are described by di Mare et al. [152], Klein et al. [153], Veloudis et al. [154], and Xie and Castro [155]. An improvement has been made by Kim et al. [156] so that the inflow is divergence-free. A Cholesky decompositions of turbulence flux tensor has been developed by Okaze and Mochida [157] based on the work of Xie and Castro [155], to generate turbulent fluctuations of both the velocity components and the scalar, with prescribed temporal and spatial correlations.

The vortex method imposes that fluctuations are generated through a synthesized vorticity field and superimposed on the mean velocity profile. It was originally proposed by Sergent [158] and modified by Mathey et al. [159]. The synthetic eddy method [160] generates inflow turbulence with prescribed mean velocity, turbulence length scales, and Reynolds stresses, through a sum of synthetic eddies that are convected through a virtual box that encloses the inlet plane of the computational domain. Both the vortex method and the synthetic eddy method are not divergence-free. However, a divergence-free modification has been proposed by Poletto et al. [161]. The literature has shown that the vortex method outperforms the RFG method [141]. Else, since synthetic methods do not require a precursor simulation, they are flexible and computationally not expensive. However, all of these methods are low in accuracy and are unable to properly reproduce an atmospheric boundary layer.

One of the most widely used methods to generate atmospheric inflow turbulence is the Mann algorithm [162, 163]. This method allows to pre-generate a turbulent inflow. Mann developed a model based on Rapid Distortion Theory. The model assumes that the velocity profile in the height interval of interest is approximately linear. The linearized Navier-Stokes equation, together with considerations of 'eddy' lifetimes, is then used to modify the spatial second-order structure of the turbulence. It also models the blocking by the surface in addition to the shear. The resulting model of the spectral velocity tensor contains only three adjustable parameters: a length scale describing the size of the largest energy-containing eddies, a non-dimensional number used in the parametrization of 'eddy' lifetime, and the third parameter is a measure of energy dissipation. The method is particularly efficient, not computationally expensive, and has a physical approach. Thus, it is currently used for load calculations in wind turbines [163]. However, a disadvantage of this technique is that the turbulence intensity fluctuation is independent of the height and therefore not suitable for the boundary layer. Also, a non-neutral boundary layer cannot be properly reproduced.

The recycling inflow turbulence method is based on a simple equation. The velocity at one selected streamwise position is used to prescribe the velocity field at the inlet. However, several limitations can be found. First, the geometry of the wall should be identical between the inlet and the recycling plane. In addition, Chung and Sung [164] noted that the grid resolution should be identical. More, the recycling method relies on the streamwise periodicity of the simulation between the inlet and the recycling plane. This limitation can lead to physically unrealistic streamwise-repetitive features. Nikitin [165] found that spurious periodicity can arise spontaneously. The recycling method, although more physical than synthetic methods, is less accurate than extracting inflow turbulence from a precursor simulation [166, 167].

Finally, the precursor method is the most used method for atmospheric boundary layer, especially in non-neutral boundary layer context. This method is used, for example, by the SOWFA library [168], presented hereafter. An effective method to obtain inflow data is to simulate a precursor domain with periodic boundary conditions. Once the flow is fully developed, the velocity data from the cross-sectional planes are sampled and stored in a database that is used as the inflow boundary conditions for the main simulation. A scheme of this method is shown in Fig. 2.10. For applications without geostrophic wind and Coriolis force, the flow is driven by a pressure gradient forcing term [141]. Otherwise, the geostrophic balance accounts for the pressure gradient forcing. This method, while accurate, can lead to memory overhead as the generated turbulence box can prove to be very large. One solution to limit the size of the box can be to generate a limited number of planes. Although the periodicity of the box is not a-priori valid, data can be manipulated [164] to obtain a box that can be repeated. Phase and amplitude jitter can be used [169]. However, these methods tend to be limited. The hypothesis used is found to be applicable for solenoidal motion, such as vorticity, but it is found to be invalid for purely compressible motion, such as dilatation. A method has been proposed [170] through which the velocities of the inner and outer layers are rescaled according to similarity laws and reintroduced at the inlet of the precursor domain. However, the most accurate method remains to store the data in a sufficiently large domain. The precursor tends to be the most suitable method for preserving the homogeneity of the flow in the streamwise direction [141]. In addition, only the recycling and the precursor method deal with a non-neutral

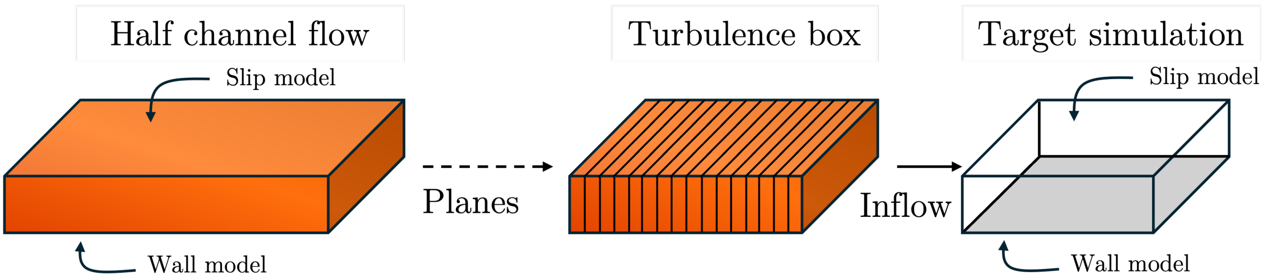

Figure 2.10: Schematic of the Precursor database method.

atmospheric boundary layer, generating temperature conditions at the boundary additionally to the velocity.

In the following work the turbulence injection is performed using the precursor database method. Enough data from the precursor domain are saved so that during the main simulation, the turbulence box does not need to be repeated. This solves the unrealistic streamwise-repetitive features issue.

2.2.5 Wind turbine and wind farm flow modelling

The growth in size of wind turbines has resulted in wind turbine being influenced by both meso- and micro-scale phenomena. Meso-scale phenomena include Coriolis force, thermal stratification, and free atmosphere stratification, and are thus dominant in the turbulence structure of the boundary layer [39]. Such phenomena can affect the internal boundary layer of a wind farm [171]. On the other hand, micro-scale phenomena include the site topography, urban canopies, and obstacles, which are also important in the boundary layer turbulence structure. In addition, they can induce flow separation and recirculation [172]. All of these phenomena impact wind turbines behaviour and wakes. Understanding and modelling these phenomena is relevant and offers a more accurate and precise representation of reality. Fig. 2.11 regroups all the scales mentioned above and the associated model chain framework. Depending on the modelling scale, different quantities are observable, leading to different applications. Various methods can be employed depending on the cost/fidelity trade-off.

The Large-Eddy Simulation technique has been increasingly used to simulate wind turbine wakes. This high-fidelity approach provides detailed results on wind turbine wake dynamic, which is crucial to predict energy losses and fatigue loads on downstream turbines [34]. As shown in Fig. 2.11, LES is the most accurate modelling tool for wind turbine and wind farm flow modelling. The first LES study goes back to 2009 when Ivanell [173] reproduced two rows of the Horns Rev I wind farm. Inflow turbulence was generated using a power-law profile and Mann turbulence [162, 163]. This simulation was intended to study a developing wind farm as the boundary layer evolves in the streamwise direction. Since then, other studies have performed developing wind farms. For example: Porté-Agel et al. in 2011 [63], Wu et

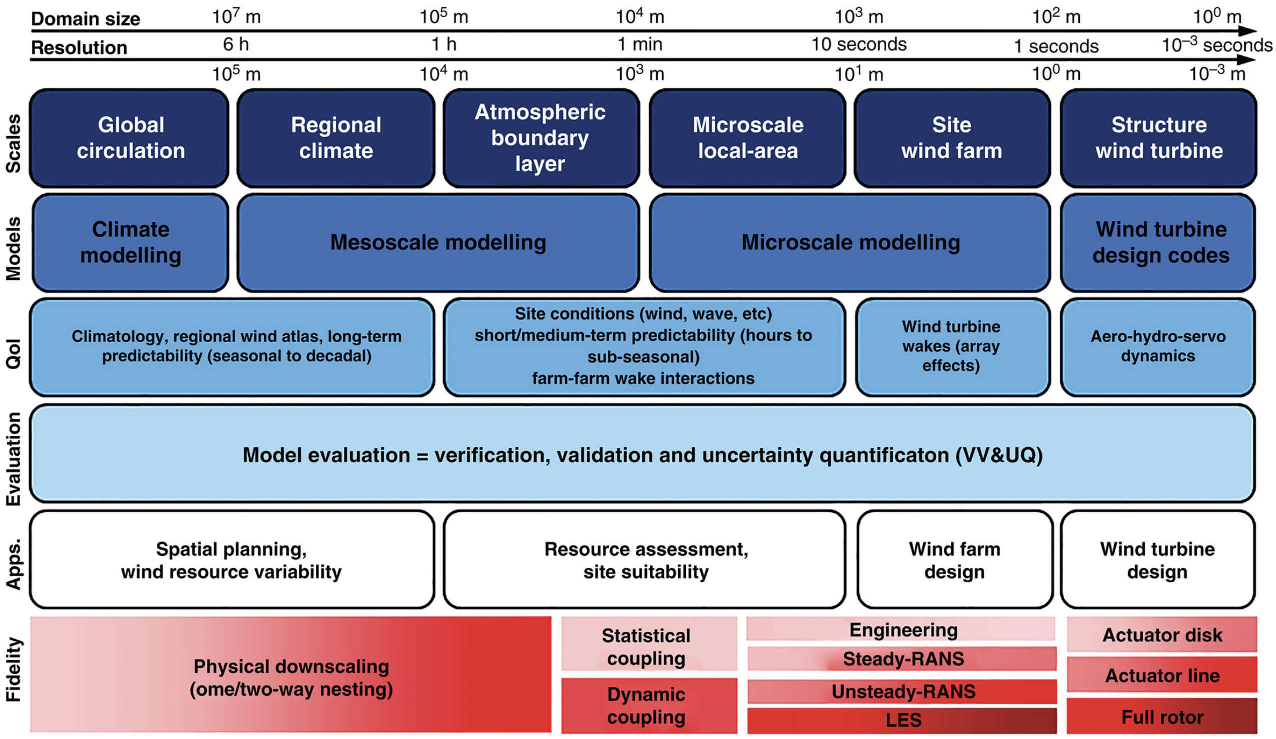

Figure 2.11: Model-chain for wind farm flow modelling. "QoI" stands for quantities of interest and "Apps." for application. Shading represents the accuracy. From [39].

al. in 2015 [174], Stevens et al. in 2017 [175], Abedi et al. in 2021 [176]. Other studies have investigated fully developed wind farms, also known as infinite wind farms. It occurs when the length of the wind farm is much greater than the height of the ABL. The turbulent boundary layer approaches a fully developed regime. These simulations are performed using periodic domains. The first study was conducted in 2010 by Calaf et al. [177]. Since then, other studies have focused on an infinite wind farm, for example: Verhulst and Meneveau in 2014 [178], Allaerts and Meyers in 2017 [87], Lanzilao and Meyers in 2024 [179]. But all of these studies focus on neutral pressure-driven boundary layers. Flow rotation and thermal stratification are absent. In these studies, the assumption of a high ABL height is made. If the wind turbines are located in the lower 10%-15% of the ABL, the height of the boundary layer and the Coriolis force do not affect the wind farm. But for shallower ABL, such as the stable boundary layer, this assumption does not stand [180].

More recent studies have focused on non-neutral atmospheric boundary layer, taking into account thermal stratification. For the convective boundary layer, in 2013, Zhang et al. studied a wind turbine wake based on a wind tunnel experiment [181]. Turbulence has been found to be 20% higher than in NBL. In 2015, Lu and Porté-Agel studied the impact of a wind farm on the CBL [182] and found that the height of the CBL increased. Stable boundary layer impact has also been studied. The first study dates from 2011 [92] where Lu and Porté-Agel modelled a single wind turbine, accounting for a wind farm, as the boundary conditions were periodic. In 2015 Dörenkämper et al. [64] compared wake effects between stable and unstable situations. In 2022, Strickland et al. studied the effect of wind farm blockage [183]. They showed that wind farm blockage increases with atmospheric stability, where a high-pressure region at the wind farm entrance is generated by a cold air flow. The impact of free-atmosphere stratification on wind farms has also been reviewed by Abkar and Porté-Agel in 2013 [53] and in 2014 [184]. The general conclusion was that as the stratification of the free atmosphere increases, the power output of the wind farm decreases, up to 35%. A major review on wind turbine and wind farm flows has been performed in 2020 by Porté-Agel et al. [34]. They emphasize on the impact of the ABL in wind turbine simulation. One of the conclusions is that further investigation and understanding of the effects of thermal stability and atmospheric turbulence on wind turbine wake dynamics and structure is required. This coincides with Veers et al. conclusion [37], that knowledge about wind flows under varying atmospheric stability conditions is still very incomplete. Porté-Agel et al. [34] also highlighted that the effects of topography and its interaction with wind turbines, particularly those subject to ABL, have been the subject of relatively little research at the time of writing.

Some research has examined the effect of complex terrain such as a hill on a wind turbine. In 2013, Tian et al. have studied a row of five wind turbines located on a hill [185]. In 2017 Lange et al. investigated the effect of a 12 m high peninsula [186] (the Bolund peninsula [187]), and found that mean wind, wind shear and turbulence level are sensitive to the terrain details. They measured that small modifications of the edge of the scale model could result in a 50% reduction in annual energy production. In 2017, Shamsoddin and Porté-Agel [69] reproduced the Tian et al. experiment [185] using LES. However, this study does not take into account the atmospheric boundary layer. In 2017, Machefaux et al. [188] studied the Risø campus test site and Alaiz hill using different atmospheric stabilities. However, their model did not take the roughness effect into account. In 2021, Liu and Stevens considered the effect of a hill on a single wind turbine located downstream [189]. A non-neutral ABL was involved. They showed that an upstream hill can reduce power production by 35% in convective cases. Under a stable boundary layer, the power production increases by 24% due to a low-level jet, a fast moving ribbon of air in the low levels of the atmosphere.

While convincing, both Shamsoddin, Porté-Agel and Liu, Stevens studies are based on theoretical, Gaussian-like hill and do not take into account realistic topography. Indeed, structured grids, widely used in atmospheric flow simulations, have difficulties following complex geometries. Immersed boundary methods exist [190] but also have difficulties in discretizing the boundary layer. More realistic studies, such as Askervein hill [70], Perdigão mountains [191], WINSENT test site [192] can only be accurately performed using unstructured meshes. Elgendi et al. [172] produced a recent review of the literature on the impact of complex terrain on wind turbines. They conclude that topography, forest canopies, mountains and valleys have a vast impact on wind turbines and that further studies are needed.

2.2.6 Atmospheric flows solvers

Various micro-scale solvers exist in the literature with different assumptions and levels of reliability. As this work aims to model with accuracy the impact of atmospheric flows on wind turbines, only high-fidelity codes, i.e. LES codes, are reviewed here. These solvers have different approaches to micro- meso-scale coupling, but also different hypothesis and numerical schemes that can influence the accuracy of the results.

- **WRF:** The Weather Research and Forcasting (WRF) model [133] is developed by the National Center for Atmospheric Research (NCAR) in Boulder, Colorado, USA.While WRF is initially a RANS solver used for meso-scale study, the Advanced Research WRF (ARW) allows for a non-hydrostatic LES approach The turbulence subgrid scheme is the Constant Smagorinsky model [57] ($C_S = 0.25$ as default value). The spatial and temporal numerical schemes are respectively a 6^{th} order advection and a 3^{rd} order Runge-Kutta split-explicit. The code is based on a two-level domain decomposition for distributed and shared-memory parallel computation. Only structured grids can be used.

- **SOWFA:** The Simulator for On/Offshore Wind Farm Applications (SOWFA) [168] is developed by the National Renewable Energy Laboratory (NREL) as part of the open-source OpenFOAM solver. It is a finite volume, compressible and multiphase flows solver. Various turbulence model are included, such as the constant Smagorinsky, the dynamic Smagorinsky and the LASD. The spatial and temporal numerical schemes are respectively a 2^{nd} order advection and a 2^{nd} order Runge-Kutta. Wind turbine are represented using the actuator line method and a FAST controller is enable. Precursor method is used to generate turbulent inflow. Only structured grids can be used.

- **Meso-NH:** The non-hydrostatic meso-scale atmospheric model (Meso-NH) [135] has been jointly developed by the Laboratoire d'Aérologie and by the Centre National de Recherches Meteorologiques, Meteo-France. It is a finite volume, non-hydrostatic flow solver. The subgrid-scale modelling is performed using the Redelsperger and Sommeria [193, 194] model which has been implemented by Cuxart et al. [195]. This model is TKE like. The spatial and temporal numerical schemes are respectively a fourth order centered and a fourth order Runge-Kunta. As mentioned before, the grid nesting technique can be used. Only structured grids can be used.

- **SP-WIND:** SP-wind is a pseudo-spectral LES code developed at KU Leuven [196, 197]. It uses a fourth-order finite difference scheme for spatial integration and a fourth-order Runge-Kutta scheme for time integration. The subgrid-scale modelling is performed through the standard Smagorinsky model. As using pseudo-spectral methods, only simple geometries can be dealt with.

- **PALM:** The Parallelized Large Eddy Simulation Model (PALM) has been developed at the Institute of Meteorology and Climatology at Leibniz Universität Hannover [140]. The code is optimized for use on massively parallel computer architectures, using a two-level domain decomposition.The spatial and temporal numerical schemes are respectively a 5^{th} order advection and a 3^{rd} order Runge-Kutta. The turbulence model is the TKE Model. An alternative dynamic model, following Heinz [198] and [199] is available. Wind turbine modelling is performed using the actuator disk method. The turbulence recycling method is available for turbulence injection. Only structured grids can be used.

- **Winc3D:** Wind Incompressible 3-Dimensional (Winc3D) is a part of the incompact3d solver. It has been developed at the Imperial College of London [200] and at NREL. It is an open-source, finite-difference, incompressible, low-mach number solver. The turbulence model is the constant Smagorinsky. The spatial and temporal numerical schemes are, respectively, a 6^{th} order advection and a 3^{rd} order Runge-Kutta. For the atmospheric part, rough wall law is available. However, it lacks thermal stratification effects. Wind turbine modelling is performed using the actuator line method. A controller based on the work of Jonkman et al. [201] is available. Only structured grids can be used.

- **DALES:** The Dutch Atmospheric Large-Eddy Simulation (DALES) is an open-source code developed conjointly by Delft University, the Royal Netherlands Meteorological Institute (KNMI), Wageningen University and the Max Planck Institute for Meteorology [202]. The spatial and temporal numerical schemes are, respectively, a 5^{th} order advection and a 3^{rd} order Runge-Kutta. The turbulence model is the constant Smagorinsky. Only structured grids can be used.

- **TOSCA:** The Toolbox fOr Stratified Convective Atmospheres (TOSCA) is an open-source finite-volume LES solver developed at the University of British Columbia, Okanagan Campus, CA [203]. The subgrid-scale turbulence modelling is performed using the dynamic-Smagorinsky model. Both spatial and temporal numerical schemes are 2^{nd} order. Only structured grids can be used.

In all of these codes, only structured grids can be used. This highlights what was stated in Section 1.4. There is no solver in the atmospheric flows community that can perform LES, handle massively parallel computations, use high-order numerical schemes, and manage unstructured grids. That is why a new solver that has not yet been used for atmospheric flow simulations, but which meets these demands, will be employed: the YALES2 library [74].

2.3 Conclusion

As wind turbines rotor size increases, meso-scale phenomena impact their dynamic, performance and wake. These phenomena include the Coriolis force, thermal stratification, and geostrophic-balance. They are predominant in the behaviour of the atmospheric boundary layer. However, the YALES2 library is not a meso-scale solver. Regional wind dynamics cannot be modelled unlike the WRF or the meso-NH solver. However, by taking into account necessary meso-scale phenomena, the atmospheric boundary layer can be properly reproduced and its impact on a wind turbine can be studied. YALES2 is not the only LES solver that performs such simulations. With the increase in computational power, more and more micro-scale solvers can now take into account larger scales. Several atmospheric flow solvers exist in the literature. However, none handle unstructured grids, and in that regard, the YALES2 solver is a novelty. This feature opens up new possibilities, such as taking into account a complex terrain in atmospheric boundary layer simulations. With that tool, more realistic studies of wind turbines may be performed.

Chapter 3

Numerical methods and wind turbine modelling

Chapter 3 describes the methodology, outlines the theoretical background of fluid dynamics used in this work, and lays out the tools used for the Large-Eddy Simulation of wind turbines. The first section covers the numerical modelling of turbulent flows. Then numerical methods for simulating turbulent flows are presented with a focus on the Large-Eddy Simulation approach. The YALES2 CFD platform is presented in the second section. The incompressible constant density solver is described in detail. The third section deals with the modelling of horizontal axis wind turbines. Both actuator disk and actuator line methods are used and thus presented.

Contents

3.1 Numerical modelling for turbulent flows . . . 76
- 3.1.1 Navier-Stokes equations . . . 76
- 3.1.2 Turbulent flows . . . 76
- 3.1.3 Modelling approach . . . 78
- 3.1.4 LES equations . . . 80
- 3.1.5 Subgrid-scale modelling . . . 81
- 3.1.6 Meshing . . . 82

3.2 YALES2 platform . . . 84
- 3.2.1 Incompressible constant density solver . . . 85
- 3.2.2 Spatial discretisation . . . 86
- 3.2.3 Temporal discretisation . . . 87
- 3.2.4 Double-domain decomposition and parallelism . . . 88
- 3.2.5 Dynamic mesh adaptation . . . 89

3.3 Horizontal axis wind turbine modelling . . . 91
- 3.3.1 Actuator Disk Method . . . 91
- 3.3.2 Actuator Line Method . . . 93
- 3.3.3 Force mollification . . . 94

3.4 Conclusion . . . 95

3.1 Numerical modelling for turbulent flows

Computational Fluid Dynamics (CFD) is the study of the movement of a fluid, or their effects, through the numerical solution of the equations that characterises it. For a Newtonian flow, where the viscous stress and the strain rate are related by a constant viscosity tensor, the governing equations are the Navier-Stokes equations. For an adiabatic and inviscid flow, it corresponds to Euler's equations. CFD is applied to a wide range of research and engineering topics, such as aerodynamics, weather forecast, combustion, heat transfer, biological engineering, aerospace, etc. Through CFD simulations, data such as velocity, pressure, and concentration can be measured at any given point. In sectors where experiments are costly or unfeasible, due to harsh conditions or scaling problems, it provides a fantastic alternative.

3.1.1 Navier-Stokes equations

The Navier-Stokes set of equations can be rigorously derived from statistical mechanics on control volumes and from the mass and momentum conservation equations [204–206]. For incompressible flows, it can be written with two equations.

- The continuity equation

$$\frac{\partial u_i}{\partial x_i} = 0 \tag{3.1}$$

- The momentum-conservation equation

$$\frac{\partial u_j}{\partial t} + \frac{\partial u_i u_j}{\partial x_i} = \nu \frac{\partial^2 u_j}{\partial x_i \partial x_i} - \frac{1}{\rho}\frac{\partial P}{\partial x_j} + f_j \tag{3.2}$$

Where u is the fluid velocity, ν the kinematic viscosity, ρ the fluid density, P the pressure and f_j external forces such as gravity.

Due to the non-linearity of the convection term $u_i u_j$ no analytical form can be calculated. Using a spatial and a temporal discretization, the problem is transformed from a continuous one, for which no analytical solution exists, to a discontinuous one with local solutions. Details are given in Section 3.2.2 and 3.2.3.

3.1.2 Turbulent flows

The concept of turbulence flows has emerged in 1883 when O. Reynolds [207] identified two different states in fluid motion: laminar and turbulent. Laminar flows are a state in which each layers of the fluid are moving smoothly with little or no mixing. Molecular viscosities dissipate all perturbations forbidding the formation of eddies or swirls. This state is found when the fluid velocity is low and viscous forces are predominant. Conversely, turbulence refers to the state

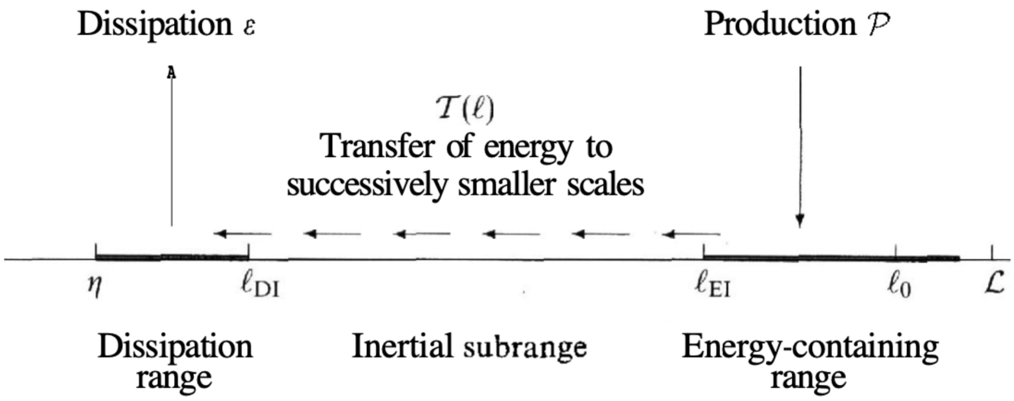

Figure 3.1: A schematic diagram of the energy cascade at very high Reynolds number. From Pope [204].

of flow of a fluid, liquid, or gas, in which velocity behaviour is chaotic. Often, as a result of a higher fluid velocity, molecular viscosities can no longer dissipate all perturbations. This state is found when the fluid velocity is high and inertial forces are predominant. Turbulent flows are characterised by a highly disordered appearance and thus a behaviour that is difficult to predict. Although opposed, laminar and turbulent flows are governed by the same conservation equations, Eq. 3.1 and Eq. 3.2. The Navier-Stokes equations through their non-linearity behaviour can "describe" laminar flow, turbulent flow, and the transition between the two states. To predetermine the flow state, a dimensionless number introduced by Reynolds is used. It measures the ratio between inertial forces and viscous forces:

$$Re = \frac{\mathcal{U}\mathcal{L}}{\nu} , \tag{3.3}$$

where $\mathcal{U}$ refers to the characteristic velocity scale of the flow, $\mathcal{L}$ to a characteristic length of the configuration, and ν represents the kinematic viscosity of the fluid. When the Reynolds number is low, the viscous forces are dominant and the flows tend to be laminar. Conversely, when the Reynolds number is high, inertial forces are predominant and flows tend to be turbulent. The Reynolds number also provides information on the scale of the turbulence and thus the energy cascade.

Turbulent flow consists of a multitude of turbulent structures of different sizes. Each scale can be associated to an energetic level. Largest structures, which determines the global behaviour of the flow, are the most energetic. They transfer energy through motion to smaller scales, and so on. This transfer stops when viscous forces become predominant and dissipate the remaining energy. The process is referred to as the "energy cascade". This notion was introduced by Richardson [208] and Kolmogorov [209]. The energy cascade phenomenon is represented in Fig. 3.1, where the spatial scale is divided into three ranges.

- **Energy-containing range:** Gathers the most energetic scales which correspond to the largest flow structures. It goes from the eddies largest size range lengthscale ℓ_0 to a length

l_{EI}. l_{EI} is the demarcation lengthscale between the anisotropic large eddies ($l > l_{EI}$) and the isotropic small eddies ($l < l_{EI}$). A common approximation is $l_{EI} \approx \frac{1}{6}\ell_0$. It should be noted that ℓ_0 is comparable to the flow scale $\mathcal{L}$.

- **Inertial subrange:** Inertial effects are dominant and viscous effects are still negligible. Energy is transferred from large anisotropic eddies to successively smaller scales. The rate of energy transfer $\mathcal{T}$ is constant and follows a $-5/3$ power law. This range goes from l_{EI} to l_{DI}. l_{DI} corresponds to the limit where viscous effects become predominant. A common approximation is $l_{DI} \approx 60\eta$ where η is the Kolmogorov scale.

- **Dissipation range:** Viscous effects are predominant. This range goes from l_{DI} to η, the Kolmogorov scale. η represents the lengthscale of the smallest turbulent structure in a flow. Their length and velocity are:

$$\eta = \left(\frac{\nu^3}{\varepsilon}\right)^{1/4} \quad \text{and} \quad u_\eta = (\nu\varepsilon)^{1/4}\,, \tag{3.4}$$

  where ε is the dissipation rate of the turbulent kinetic energy. At this scale, small turbulent structures, and consequently energy, are dissipated. Energy becomes heat as a result of the molecular viscosity of the fluid.

This theory relies on three main hypotheses. The first is Kolmogorov's hypothesis of local isotropy. At sufficiently high Reynolds numbers, the small-scale turbulent motions are statistically isotropic. The second is Kolmogorov's first similarity hypothesis. In every turbulent flow with a sufficiently high Reynolds number, the statistics of small-scale motions have a universal form that is uniquely determined by ν and ε. Third is the Kolmogorov's second similarity hypothesis. In every turbulent flow with a sufficiently high Reynolds number, the statistics of the motions have a universal form that is uniquely determined by ε independently of ν.

One element that should be mentioned is that the ratios of the smallest to largest scales are determined from the Kolmogorov theory as:

$$\frac{\eta}{\ell_0} \sim Re_t^{-3/4} \tag{3.5}$$

Leading that when the Reynolds number increases, the range from the smallest to the largest scales also increases. High Reynolds number flows are consequently more complicated to represent, since more scales are involved.

3.1.3 Modelling approach

To solve all scales of turbulence, hence having a complete resolution of the flow, the spatial discretization scale must be similar to the smallest turbulent structures, η. However, this is often unfeasible due to computational cost. There are three main approaches to the numerical resolution of a flow. Each of them is based on different assumptions and has specific advantages and disadvantages. A representation of these methods is shown in Fig. 3.2

- **DNS : Direct Numerical Simulation**
  The Direct Numerical Simulation method is an approach in which the Navier-Stokes equations are solved directly and all scales of turbulence are solved. As seen in Section 3.1.2 this implies a mesh size smaller than the dissipative scale. This method, which is extremely costly, can be used for small Reynolds number flows only. But for wind turbines study, where Reynolds number reaches 10^8, the ratio of the smallest to the largest scale is $\frac{\eta}{\ell_0} \sim 10^6$. Capturing the smallest scales, which dissipate the energy, while resolving the largest scales, which contain the energy, becomes unfeasible.

- **RANS : Reynolds-Averaged Navier-Stokes equation**
  The Reynolds-Averaged Navier-Stokes equation method solves the statistically averaged Navier-Stokes equations by applying the Reynolds decomposition. Hence, this formalism enables access to the static fields only as it computes the mean flow field while entirely modelling the fluctuating contribution of the flow. This is the least expensive approach as it does not require a refine mesh and is the most popular at the industrial level, even though it does not provide information on instantaneous fluctuations. For wind turbine simulations, this method is often used as it provides a fair cost-to-precision ratio. However, in order to tackle the challenges mentioned above, taking into account fluctuations is mandatory.

- **LES : Large Eddy Simulation**
  The Large Eddy Simulation approach is an intermediate cost-to-precision ratio approach. A filter size is defined, based on the mesh size, and transport equations are explicitly solved for eddies larger than this size. For smaller-size structures, a model is used. This approach makes perfect sense, as most of the energy is contained in the largest scales. The flow behaviour is captured. The effect of the smallest scales are modelled, significantly reducing the computational cost. This method is allowed since small structures are supposedly isotropic and have a more universal, and therefore predictable, behaviour [209]. A model can reflect the effect of molecular viscosity and dissipate the energy. As small structures have a universal behaviour, a unique model can be used for all high Reynolds number flows.

All simulations in this work are performed using the LES approach. The domain is too large to be solved using DNS, but requires instantaneous quantities and fluctuations which cannot be obtained using the RANS method.

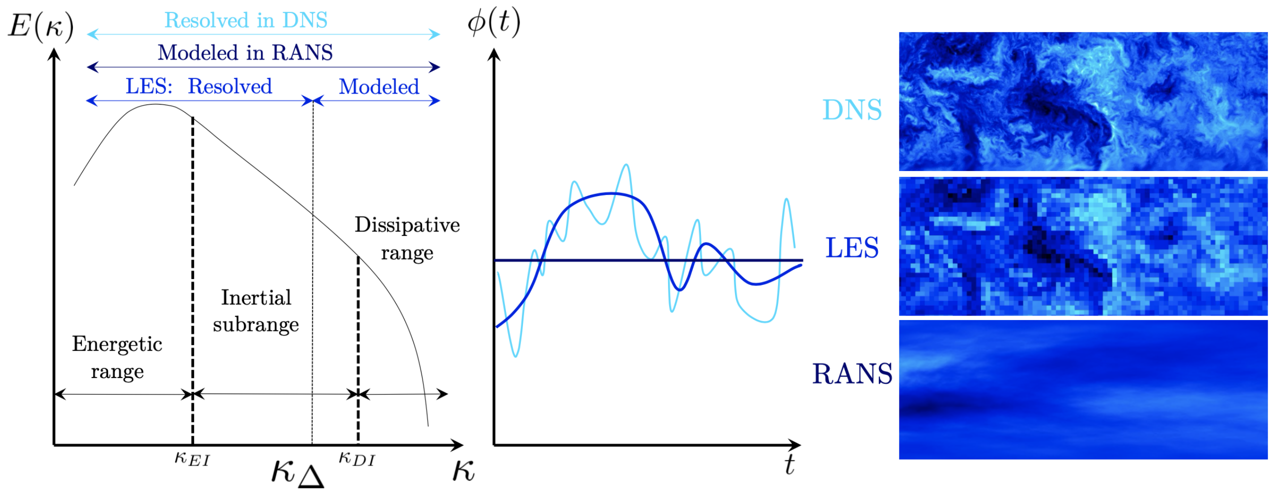

Figure 3.2: Representative overview of the different RANS, LES, DNS approach. From left to right: Spectra representing the Energy evolution as function of the wavenumber (proportional to the inverse of the length scales), temporal evolution of a local variable and slice of the velocity field representing the turbulent structures in an atmospheric flow. From [35].

3.1.4 LES equations

The LES formalism relies on modelling the small scales of the flow. The split between the resolved and modelled structures is performed using a spatial filtering operation applied to the Navier-Stokes equations. For a scalar $\phi(t, \mathbf{x})$ the low-pass spatial filtering process is defined by a spatial convolution product:

$$\tilde{\phi}(\mathbf{x}, t) = \int_{\mathbb{R}^3} \phi(\mathbf{y}, t) G_\Delta(\mathbf{y} - \mathbf{x}) \mathrm{d}\mathbf{y} \ , \tag{3.6}$$

where $\tilde{\phi}$ is the filtered scalar and G_Δ the filtering kernel related to the filter size Δ. The filter operator is normalized as:

$$\int_{\mathbb{R}^3} G_\Delta(\mathbf{x}) \mathrm{d}\mathbf{x} = 1 \ . \tag{3.7}$$

From this filter operator, the scalar ϕ may be decomposed into a part with a scale larger than Δ, noted $\tilde{\phi}$ and a second part with a scale lower than Δ, noted ϕ':

$$\phi(t, \mathbf{x}) = \tilde{\phi}(t, \mathbf{x}) + \phi'(t, \mathbf{x}) \ . \tag{3.8}$$

The filtering process noted $\tilde{\bullet}$ can be applied to Eq. 3.1 and Eq. 3.2. Using Einstein's notation these equations can be written:

- Filtered continuity equation

$$\frac{\partial \tilde{u}_i}{\partial x_i} = 0 \tag{3.9}$$

- Filtered momentum conservation equation

$$\frac{\partial \tilde{u}_j}{\partial t} + \frac{\partial \tilde{u}_i \tilde{u}_j}{\partial x_i} = \nu \frac{\partial^2 \tilde{u}_j}{\partial x_i \partial x_i} + \frac{1}{\rho} \frac{\partial}{\partial x_i} \underbrace{\tau_{ij}^R}_{(1)} - \frac{1}{\rho} \frac{\partial \tilde{P}}{\partial x_j} + \tilde{f}_j \tag{3.10}$$

Here (1) refers to the residual stress tensor, which represents the unresolved eddies. It is given by the following equation:

$$\tau_{ij}^R = -\rho(\overline{u_i u_j} - \overline{u}_i \overline{u}_j) \tag{3.11}$$

And can be rewritten following Germano formalism [210] in order to highlight three tensors:

$$\tau_{ij}^R = -\rho \left(\underbrace{\overline{\tilde{u}_i \tilde{u}_j} - \overline{\tilde{u}_i \tilde{u}_j}}_{\mathcal{L}_{ij}^{\circ}} + \underbrace{\overline{\tilde{u}_i u'_j} + \overline{u'_i \tilde{u}_j} - \overline{\overline{u_i} u'_j} - \overline{u'_i \overline{\overline{u_j}}}}_{\mathcal{C}_{ij}^{\circ}} + \underbrace{\overline{u'_i u'_j} - \overline{u'}_i \overline{u'}_j}_{\mathcal{R}_{ij}^{\circ}} \right). \tag{3.12}$$

$\mathcal{L}_{ij}^o$ is the Leonard stress which can be computed from the filtered values. $\mathcal{C}_{ij}^o$ is the cross stresses, reflecting the energy transfer from the largest scales to the smallest scales. Based on Kolmogorov lengthscales separations, if the LES filter cut-off range is within the inertial range, this term is negligible. $\mathcal{R}_{ij}^o$ is the sub-grid scale (SGS) Reynolds stress which stands for the energy dissipation by molecular viscosity. This tensor needs to be modelled to close the momentum conservation equation.

3.1.5 Subgrid-scale modelling

As there is no universal description of turbulence, various subgrid-scale turbulence models exist in the literature. However, most models are based on the Boussinesq hypothesis [211]. The assumption is based on an artificial eddy viscosity approach, where the kinetic energy dissipation at subgrid scales is analogous to molecular diffusion. The residual stress tensor can be written as:

$$\tau_{ij}^R = 2\rho\nu_{sgs}\tilde{\mathcal{S}}_{ij}, \tag{3.13}$$

Where ν_{sgs} is the sub-grid scale turbulent viscosity and $\mathcal{S}_{ij}$ the strain rate tensor noted:

$$\tilde{\mathcal{S}}_{ij} = \frac{1}{2} \left(\frac{\partial \tilde{u}_i}{\partial x_j} + \frac{\partial \tilde{u}_j}{\partial x_i} \right) \tag{3.14}$$

Finally, Eq. 3.10 can be re-written using the subgrid-scale turbulent viscosity and the strain rate tensor, leading to:

$$\frac{\partial \tilde{u}_j}{\partial t} + \frac{\partial \tilde{u}_i \tilde{u}_j}{\partial x_i} = \frac{\partial}{\partial x_i} \left[2\left(\nu + \nu_{sgs}\right) \tilde{\mathcal{S}}_{ij} \right] - \frac{1}{\rho} \frac{\partial \tilde{P}}{\partial x_j} + \tilde{f}_j \tag{3.15}$$

As stated above, the classical Smagorinsky SGS model [212] is based on the equilibrium between the kinetic energy production rate and the dissipation rate, at the LES filter size Δ. Turbulence at this scale can thus be considered as a purely dissipative phenomenon. The turbulent viscosity is expressed as:

$$\nu_{sgs} = C_s^2 \Delta^2 \tilde{\mathcal{S}} \tag{3.16}$$

Here, C_s is the Smagorinsky constant and $\overline{\mathcal{S}} = \sqrt{2\tilde{S}_{ij}\tilde{S}_{ij}}$. However, the Smagorinsky constant can vary according to the flow, ranging from $C_s = 0.1 - 0.4$. In addition, this model is related to the resolved velocity strain rate and is thus inadequate when modelling laminar flows or flows near wall regions.

A major improvement to this method is called the Dynamic Smagorinsky Model [105,106]. The Smagorinsky constant becomes the Smagorinsky parameter as it is locally determined by a dynamic procedure. The main idea is that the characteristics of the subgrid scales can be deduced from the smallest resolved scales. To do so, another filtering operation is performed with a filter size Δ' larger than Δ. The residual stress term based on the double-filtered velocity can be written:

$$\begin{aligned} \tau_{ij}^{R} &= 2C_s^2 \rho \Delta^2 \tilde{\mathcal{S}} \cdot \tilde{\mathcal{S}}_{ij} \\ \tau_{ij}^{R'} &= 2C_s^2 \rho \Delta'^2 \widehat{\tilde{\mathcal{S}}} \cdot \widehat{\tilde{\mathcal{S}}_{ij}} \end{aligned} \tag{3.17}$$

The resolved stress, $\mathcal{L}_{ij}$ between the two filtering sizes Δ' and Δ is called the Germano identity and can be expressed by taking the difference between the two previous residual stress tensors:

$$\mathcal{L}_{ij} = \tau_{ij}^{R'} - \tau_{ij}^{R} \tag{3.18}$$

From Eq. 3.18 the Smagorinsky parameter can be computed as:

$$(\widehat{\tilde{u}_i\tilde{u}_j} - \widehat{\tilde{u}}_i\widehat{\tilde{u}}_j)\tilde{\mathcal{S}}_{ij} = 2C_s^2 \left(\Delta^2 \widehat{\tilde{\mathcal{S}}\tilde{\mathcal{S}}_{ij}}\tilde{\mathcal{S}}_{ij} - \Delta'^2 \widehat{\tilde{\mathcal{S}}} \cdot \widehat{\tilde{\mathcal{S}}_{ij}}\tilde{\mathcal{S}}_{ij} \right) \tag{3.19}$$

The quantity in the right-hand side parentheses can locally be null or negative, sometimes leading to a negative Smagorinsky parameter C_s. This phenomenon implies a negative turbulent viscosity that corresponds to energy transfers from the small structures to the largest ones and is called backscatter [213]. For numerical stability reasons, the Smagorinsky parameter is kept positive.

3.1.6 Meshing

To solve the Navier-Stokes equations, the domain is partitioned into a set of geometrical elements which together form the mesh. In a domain of one dimension, the only way to divide the space is by intervals. In two or three dimensions, the mesh can have different geometries. It

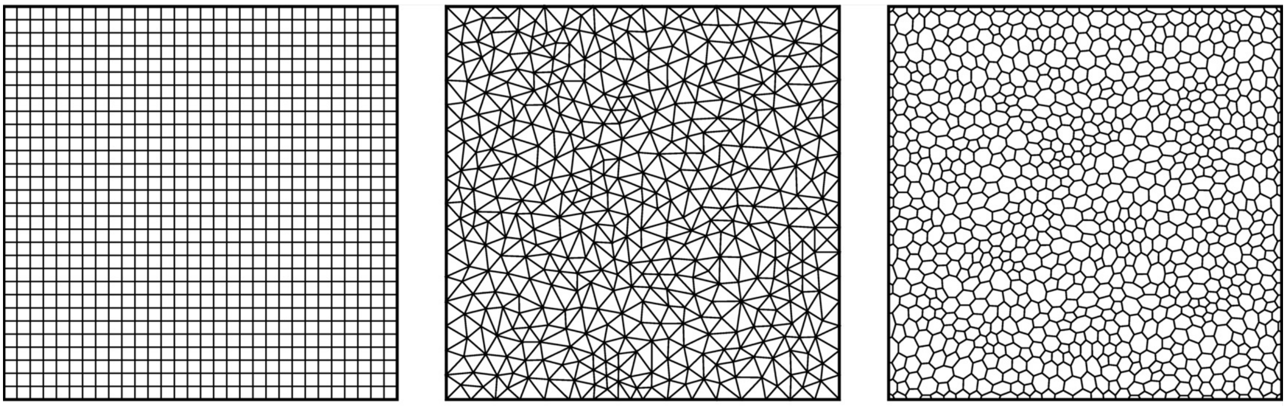

Figure 3.3: From left to right: Structured mesh, unstructured mesh based on triangles, unstructured mesh based on polygons. From [214].

can be either structured or unstructured. A representation of these meshes is given in Fig. 3.3.

- **The structured mesh:** Elements are quadrilateral in $2D$ and hexahedra in $3D$. All elements can be gathered in a positional table (i, j) for two-dimensional domains or (i, j, k) for three-dimensional domains. Lines can be curved, but the relative positioning of the elements in relation to each other does not change. Each element is linked to its neighbour that is in the $2D$ domain $(i \pm 1, j)$,$(i, j \pm 1)$. These meshes have the advantage to be regular and without sharp geometries. A coarse element does not impact the time-step of the whole simulation. The numerical schemes are more stable. However, a major limitation comes from the inability of these meshes to follow complex geometries.

- **The unstructured mesh:** Several geometries can be used in unstructured meshes. For two-dimensional domains, elements are usually triangles or quadrilaterals, whereas for three-dimensional domains, they can be tetrahedrons, hexahedrons, pyramids, prisms or polyhedrons. The connectivity is irregular, which means that it cannot be expressed as a two- or three-dimensional array in computer memory. Unlike structured meshes for which neighbourhood are implicit, this mesh calls for explicit storage of neighbourhood. The quality of such meshes is critical to minimize numerical errors and stabilise the numerical schemes. These meshes have the advantage of being suitable for complex geometries.

For simplicial meshes, i.e. triangular and tetrahedral, several criteria exist to ensure the quality of the mesh. In this work, the quality of the mesh is usually measured using the skewness. Its definition is based on the equilateral volume defined by the circumcircle. Let Δ be defined as the surface or volume of two- or three-dimensional meshes, respectively. The skewness becomes:

$$S = \frac{\Delta_{optimal} - \Delta}{\Delta_{optimal}} \tag{3.20}$$

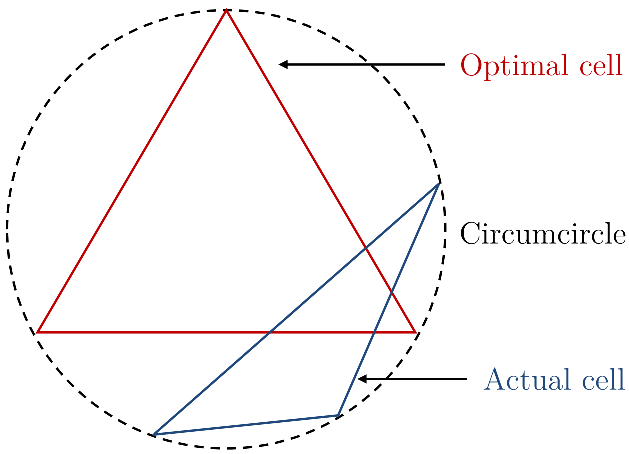

Figure 3.4: Illustration of the skewness computation based on the equilateral volume for a triangular mesh cell.

In two dimensions, the optimal and larger triangle surface is the equilateral triangle. In three dimensions, the optimal is the equilateral tetrahedral volume. As such, when the skewness tends towards 0, the actual cell is similar to the equilateral, and the mesh is of really good quality. On the other hand, when the skewness tends towards 1, the cell size is highly distorted, leading to more numerical errors and stability issues. A representation of the skewness measurement is given in Fig. 3.4.

As mentioned in Section 1.3.3, part of this work will be performed using unstructured meshes with the aim of modelling complex terrain. But for some simple cases, structured meshes have also been employed.

3.2 YALES2 platform

As mentioned in Section 1.3, all numerical modelling is performed using the YALES2 [74] platform. This library allows for having a multi-physics approach from the various solvers available in this library going from non-reactive turbulent flows [35, 215] to two-phase flows [216] and reactive variable density flows [217, 218]. However, the most used is an incompressible low-Mach number solver, called ICS. It relies on a fourth-order finite-volume central numerical scheme for spatial discretization and a fourth-order Runge-Kutta-like method for the time integration [219]. Moreover, YALES2 is specifically tailored to be used on massively parallel machines with billion-cell meshes. Scaling tests have been performed on the LUMI supercomputer to validate the use of large meshes. These tests can be found in **Appendix A**.

3.2.1 Incompressible constant density solver

The Navier-Stokes equation for incompressible flows (Eq. 3.1 and Eq. 3.2) can be rewritten in vectorial form as

$$\begin{aligned} &\nabla \cdot \mathbf{u} = 0 \ , \\ &\frac{\partial \mathbf{u}}{\partial t} + \nabla \cdot (\mathbf{u} \otimes \mathbf{u}) = -\frac{1}{\rho}\nabla P + \frac{1}{\rho}\nabla \cdot \boldsymbol{\tau} + \mathbf{f} \ . \end{aligned} \tag{3.21}$$

The solving of the Navier-Stokes equations for incompressible flows is based on the projection method proposed by Chorin [220] and modified by Kim and Moin [221]. Velocity is resolved at each time step (indices n, n+1, etc), while scalars, density and pressure are resolved at staggered time steps (indices n + 1/2, n + 3/2, etc). This projection method is based on the Helmholtz-Hodge decomposition, which states that a vector field can be decomposed into an irrotational part and a solenoidal part. For the velocity field, the decomposition is writen as:

$$\mathbf{u} = \mathbf{u}^i + \mathbf{u}^s \ . \tag{3.22}$$

The irrotational part derives from a scalar potential and can be written:

$$\boldsymbol{\nabla} \cdot \mathbf{u} = \boldsymbol{\nabla} \cdot \mathbf{u}^i = \boldsymbol{\nabla}^2 \phi \ . \tag{3.23}$$

From this decomposition, we can solve the momentum conservation equation in two steps.

- **Prediction step:** A first estimation $\mathbf{u}^*$ of the velocity at time $n+1$ is obtained by advancing the momentum without the pressure gradient term, which only contributes to the irrotational part of the velocity field:

$$\frac{\mathbf{u}^* - \mathbf{u}^n}{\Delta t} = -\boldsymbol{\nabla} \cdot (\mathbf{u}^* \mathbf{u}^n) + \frac{1}{\rho}\boldsymbol{\nabla} \cdot \boldsymbol{\tau}^n \ . \tag{3.24}$$

- **Correction step:** The velocity is then corrected by reintegrating the pressure gradient:

$$\frac{\mathbf{u}^{n+1} - \mathbf{u}^*}{\Delta t} = -\frac{1}{\rho}\boldsymbol{\nabla} P^{n+1/2} \ . \tag{3.25}$$

The calculation of $\mathbf{u}^{n+1}$ requires knowledge of $P^{n+1/2}$, which is determined by solving the Poisson equation for pressure, obtained by applying the divergence operator to Eq. 3.25, and reintegrating the zero divergence constraint for u^{n+1} :

$$\boldsymbol{\nabla}^2 P^{n+1/2} = \frac{\rho}{\Delta t}\boldsymbol{\nabla} \cdot \mathbf{u}^* \tag{3.26}$$

In YALES2 the implementation differs slightly from this method.

- **Prediction step:** The prediction step takes into account the pressure term at time $n-1/2$, which is generally quite close to $P^{n+1/2}$:

$$\frac{\mathbf{u}^{*}-\mathbf{u}^{n}}{\Delta t}=-\boldsymbol{\nabla}\cdot\left(\mathbf{u}^{*}\mathbf{u}^{n}\right)-\frac{1}{\rho}\boldsymbol{\nabla}P^{n-1/2}+\frac{1}{\rho}\boldsymbol{\nabla}\cdot\boldsymbol{\tau}^{n} \tag{3.27}$$

This term leads to a better estimation of $\mathbf{u}^{*}$.

- **Correction step:** Velocity correction step is therefore written with both $P^{n+1/2}$ and $P^{n-1/2}$ term.

$$\frac{\mathbf{u}^{n+1}-\mathbf{u}^{*}}{\Delta t}=-\frac{1}{\rho}\boldsymbol{\nabla}P^{n+1/2}+\frac{1}{\rho}\nabla P^{n-1/2} \tag{3.28}$$

The Poisson equation to calculate $P^{n+1/2}$ becomes:

$$\boldsymbol{\nabla}^{2}\left(P^{n+1/2}-P^{n-1/2}\right)=\frac{\rho}{\Delta t}\boldsymbol{\nabla}\cdot\mathbf{u}^{*} \tag{3.29}$$

Its resolution requires the use of a linear system solver. The need for iterative solvers and the number of iterations required to obtain a sufficiently accurate estimate of the solution can account for a very large proportion of the computing time required to simulate each time step. Depending on the algorithm used and the characteristics of the discrete Laplacian operator matrix the computational cost can vary a lot. In addition, interprocessor communications are required for each iteration of the linear solver, and these communications can account for a very large proportion of the total simulation time, up to 80% if no particular attention is paid to the implemented method [222]. Optimising the method for solving the Poisson equation is a key point for simulating incompressible flows [223]. Several algorithms are available in YALES2: The Preconditionned Conjugate Gradient (PCG) [224], the Deflated PCG (DPCG) [225], and also the BICGSTAB scheme [226].

3.2.2 Spatial discretisation

In YALES2, spatial discretisation is performed using the finite-volume method. The domain is divided into small volumes, and the governing equations are integrated in each volume. Volume integrals are converted to surface integrals through the divergence theorem and then evaluated as fluxes at the surfaces. The divergence of a differentiable vector field $\boldsymbol{F}$ integrated over a control volume can be written as:

$$\iiint_{\Omega}\nabla\cdot\boldsymbol{F}\mathrm{d}V=\oiint_{\partial\Omega}\boldsymbol{F}\cdot\boldsymbol{n}_{\partial\Omega}\mathrm{d}S \tag{3.30}$$

where Ω is the control volume, $\partial\Omega$ the closed surface defining the control volume boundary and $\boldsymbol{n}_{\partial\Omega}$ the unit normal to $\partial\Omega$ facing outwards from the control volume. Note that a similar

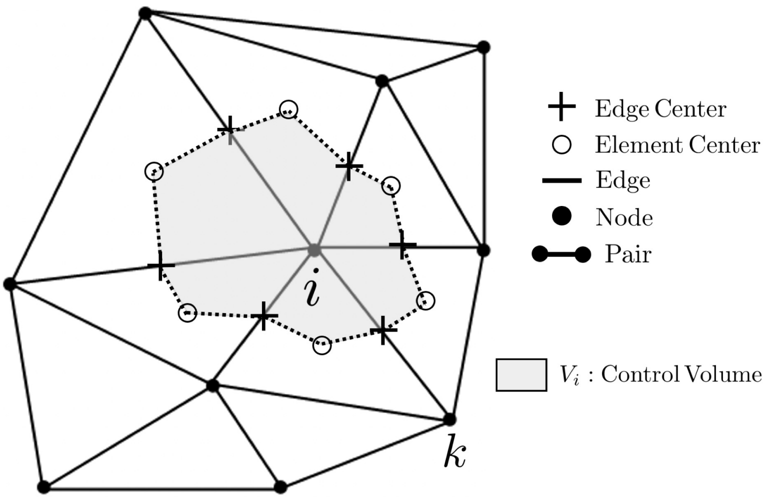

Figure 3.5: Grid notations for the YALES2 flow solver; Node-centered control volume. From [216].

equation (gradient theorem) allows us to transform the volume integral of a gradient into a surface integral. Instead of calculating the divergence of a field at the nodes of the mesh, we can evaluate the integral of the fluxes of this field at the edges of the control volume. So the finite volume method is intrinsically conservative. The flow leaving a control volume enters the adjacent control volume, ensuring the conservation of the volume integral of $\boldsymbol{F}$. Since flow simulations are based on the mass, momentum and energy conservation equations, the finite volume method is particularly suitable for solving this type of problem. The accuracy of a finite volume discretization is linked to several mathematical and algorithmic choices:

- Definition of the control volume and the normal to its boundary.
- Evaluation of the field at the edges of the control volume.
- Approximation of the surface integral.

In YALES2, the procedure for constructing 2D control volumes is illustrated in Fig. 3.5. The schemes are pair-based: the index i represents the node around which the control volume is defined, and k represents a neighbour of the node i, in the set of neighbours N_i.

3.2.3 Temporal discretisation

Mainly three temporal discretization methods exist: the explicit the implicit and the semi-implicit methods.

- **The explicit method:** For a function $F_{(x,t)}$, the explicit method calculates $\frac{\partial}{\partial t}F_{(x,t+\frac{\Delta t}{2})}$ as a function of $F_{(x,t)}$ but also of the terms $F_{(x-\Delta x,t)}$ and $F_{(x+\Delta x,t)}$. The aim is to evaluate the derivative on the right-hand side at t and centred at x. Although this method is faster

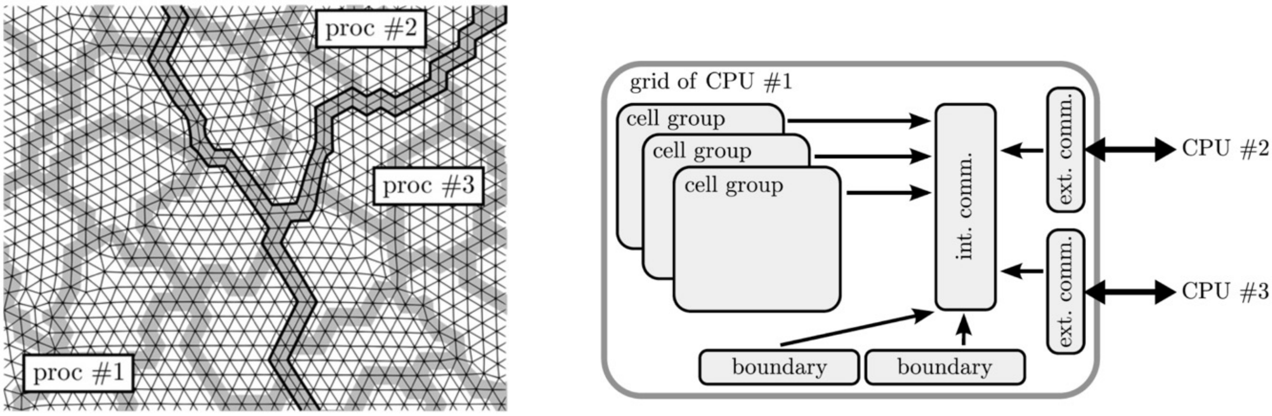

Figure 3.6: Representation of the Double-Domain Decomposition (DDD) (left). Black nodes are participating in the communications between processors. Highlighted nodes are participating in the communications inside and outside each processor. Scheme of the communications and structures used during the simulations (right). From [74].

due to a smaller system of equations, it becomes unstable if the time step is not small enough.

- **The implicit method:** The implicit method would be to calculate the same derivative, but as a function of $F_{(x,t+\Delta t)}$, $F_{(x-\Delta x,t+\Delta t)}$ and $F_{(x+\Delta x,t+\Delta t)}$. Unlike the first method, this involves evaluating the derivative on the left at t and centred at x. This method is stable and can be used with bigger time-step. Yet, it is usually much slower due to the computational cost of the large system of equations.

- **The semi-implicit method:** A final, semi-implicit method involves averaging the two evaluations to calculate $\frac{\partial}{\partial t}F$ centred in $(x, t + \frac{\Delta t}{2})$.

YALES2 has both explicit and implicit options available depending on the schemes. The schemes Runge-Kutta, Lax-Wendroff and TFV4A (an in house fourth order method) are fully explicit while Crank-Nicholson and Backward Differentiation Formula are implicit. In this work the TFV4A scheme is used [219]. The method is based on a mix of the fourth order Runge-Kutta (RK4) and the fourth order Lax-Wendroff like method named Two-step Taylor-Galerkin (TTG4A). The scheme is further detailed in **Appendix B**.

3.2.4 Double-domain decomposition and parallelism

To perform such computation, YALES2 splits its computational domain.

Each part of the domain is assigned to a processor. Communications between processors are taking care of the dependency between each sub-domain. These processors exchange information at the interface of each cell group using MPI (Message Passing Interface) instructions. The mesh decomposition must assure an optimal workload repartition between processors. For a structured grid, it can easily be done by generating sub-domains containing the same number of control volumes. However, for an unstructured grid, the decomposition is non-trivial. In YALES2, this operation is performed by the external libraries METIS [227] or SCOTCH [228].

In addition, YALES2 uses a Double-Domain decomposition (DDD). A first-level decomposition corresponds to external communications, managed by MPI communications. A second-level decomposition corresponds to internal communications, enabling exchanges between groups of cells (ELGRP) within the same processor. These communications are not affected by MPI instructions.

This DDD allows better memory management than Single-level Domain Decomposition in cache-aware type algorithms. The communication scheme between groups of elements, communicators, and boundaries is represented in Fig. 3.6. More informations on the structures can be found in [74], especially on the communications ELGRP-ELGRP, ELGRP-processor, and processor-processor. This DDD is also used to optimize the Poisson solver performances presented in Section 3.2.1.

3.2.5 Dynamic mesh adaptation

Dynamic mesh adaptation is a powerful tool for changing the mesh characteristics during a simulation. It can be used to optimise the number of cells by refining the mesh only in areas of interest whose position may change during the simulation. In this work, dynamic mesh adaptation is used in wind turbine wakes to properly capture vortices and a velocity deficit, which affects downstream wind turbines. Dynamic mesh adaptation was first used on Cartesian meshes [229], known as Adaptive Mesh Refinement (AMR). The idea was to use separate rectangular refinements to reduce truncation errors. On this type of mesh, refined region must be rectangles (2D) or rectangular parallelepiped (3D). It does not necessarily match area of interests, who can have different shapes. Moreover, nodes who only have one neighbour are seen at the interface between two regions with different cell size. Numerical special treatment must then be given [230]. Since then, a great deal of progress has been made, particularly when using unstructured meshes.

As computational power has increased, simulations are usually performed on massive meshes. Dynamic mesh adaptation must therefore be operational on multiple processors, which introduces additional complexity. Let's introduce a bounded domain $\Omega \subset \mathbb{R}^3$ and its mesh $\mathcal{T}$, a set of tetrahedra covering the space of the domain $\bar{\Omega}$. We obtain $\bar{\Omega} = \bigcup_{i=1}^{N_{elem}} \overline{\mathcal{T}_i}$. The boundaries of the mesh $\mathcal{S} \subset \mathbb{R}^3$ can be defined. It includes the boundaries of the domain Ω, but also the boundaries of each subdomain, characteristic of the YALES2 double-domain decomposition presented in Section 3.2.4. To perform mesh adaptation at these boundaries, a mesh adaptation algorithm is used [231]. It relies on the coupling between YALES2 and the external, sequential, remeshing library MMG [232], using the moving interface method. Each subdomain and associated sub-meshes $\mathcal{T}_k$ is paired with a processor, operating independently,

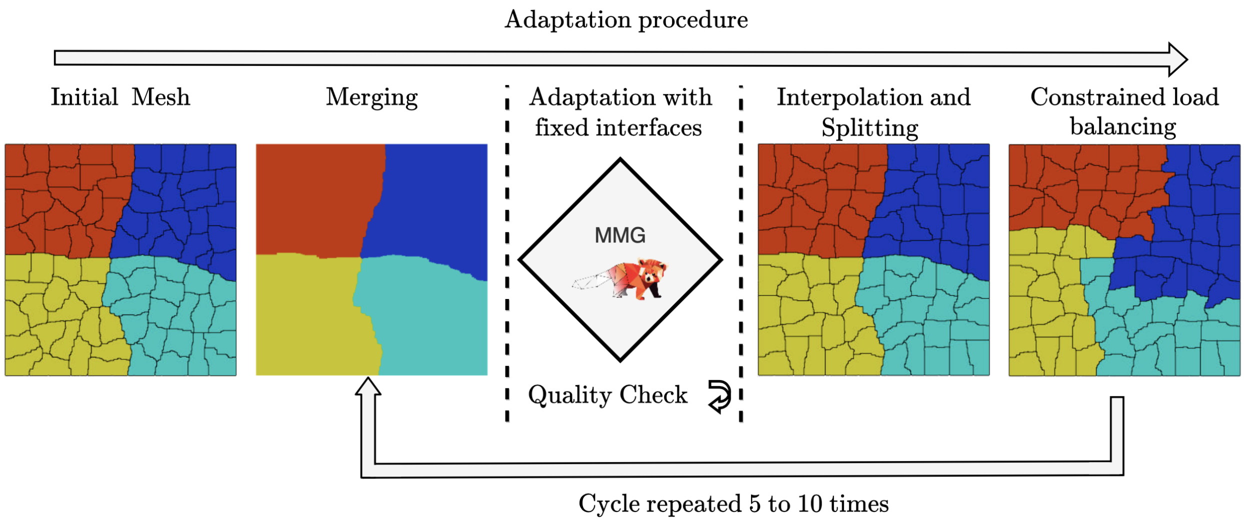

Figure 3.7: Schematic of the two-level moving interface parallel adaptation strategy. From [231].

where k denotes the processor's rank. A visual representation of the mesh adaptation algorithm is given in Fig. 3.7. Steps are the following:

1. All the element groups of each subdomain are merged.

2. This new contiguous block is transmitted to MMG whereupon it is refined in accordance with the user-defined mesh size. However, the initial boundaries $\mathcal{S}$ are preserved. At the end of the step, high-quality elements respecting the prescribed metric are found within each $\mathcal{T}_k$, but low-quality elements are still present in $\mathcal{S}$. This process does not require communications between processors.

3. The adapted subdomain $\mathcal{T}_k$ is split into a new set of subdomains $\mathcal{T}_k'$ following the YALES2 double domain decomposition. A load balancing algorithm is used to evenly distribute the grid on processors, while defining the new boundaries $\mathcal{S}'$, far from $\mathcal{S}$, where all the low-quality elements are located. The data and metrics of the previous grid $\mathcal{T}$ are interpolated on the new grid $\mathcal{T}'$.

4. The preceding steps are repeated until both the prescribed metric and a minimum element quality level, such as the skewness, criterion introduced in Section 3.1.6, are ensured.

The two-level domain decomposition method increases the efficiency of all the interpolation, load balancing, data transfer, connectivity reconstruction operations. For example, the load-balancing algorithm is applied to cell groups instead of cells. The same applies to transfer and reconstruction. The data interpolation is performed at each sub-step, but the two-level domain decomposition enables to quickly locate the nearest tetrahedron. Based on this algorithm, the grid can be adapted according to a desired metric, while guaranteeing a minimum level of quality. The desired metric can be based on the flow physics or user-dependent parameters.

This adaptation procedure can be performed on massively parallel computation, enabling its use for large wind turbine studies.

3.3 Horizontal axis wind turbine modelling

As mentioned in Section 1.2, this study will only focus on three blade horizontal axis wind turbines, as they are the most efficient and widely used. To take into account wind turbine effect on the flow, the whole rotor could be body fitted. Yet, this method is facing a multi-scale problem. For a body fitted geometry, the mesh resolution must be sufficient enough to capture the boundary layer on the blade, which is $O(\text{mm})$. But the order of magnitude of the blade profile is thousands greater, being $O(1\text{m})$. On a windfarm scale, $O(1\text{km})$ is reached. The spatial scales, velocity scale, associated Reynolds number, and time scale involved in wind farm simulations are summarized in Tab. 3.1.

	spatial scale [m]	velocity scale [m/s]	Re [−]	Time scale [s]
Boundary layer	10^{-3}	$0-100$	$\sim 10^3$	10^{-5}
blade profile	1	$0-100$	$\sim 10^6$	10^{-2}
rotor	10^2	10	$\sim 10^8$	10
wind farm	10^3	10	$\sim 10^9$	10^2

Table 3.1: order of magnitude of the scales involved in a wind farm simulation.

Because of this discrepancy in spatial scales, a body fitted geometry simulation of an entire wind farm is computationally expensive. Thus, different methodologies have been developed to render a wind turbine into a CFD framework. The two most widely used are the actuator disk method (ADM) and the actuator line methods (ALM). Fig. 3.8 represents these methods compared to a body fitted geometry. Both methods are related to a different cost-fidelity trade-off. For this reason, both ALM and ADM have been used in this work and thus detailed.

3.3.1 Actuator Disk Method

In the ADM framework, the geometry of the blades is not fully represented. The rotor effect is accounted for through a disk of equivalent forces, i.e. the actuator disk approach. The method considers the average effect of each blade on the swept disk area. Each blade is divided into radial elements that have an effect on the whole annular corresponding. The AD is discretized into a number of polar elements, as shown in Fig. 3.9. On each of the polar elements, forces are applied. Aerodynamic forces are governed by the local normal u_n and tangential velocities u_θ to the rotor plane. They are calculated using the blade element theory [50]. Therefore, in each time step and for each radial location r and azimuthal position θ the effect of each blade is modelled. The effect is weighted by the ratio between the surface element and the corresponding annular surface.

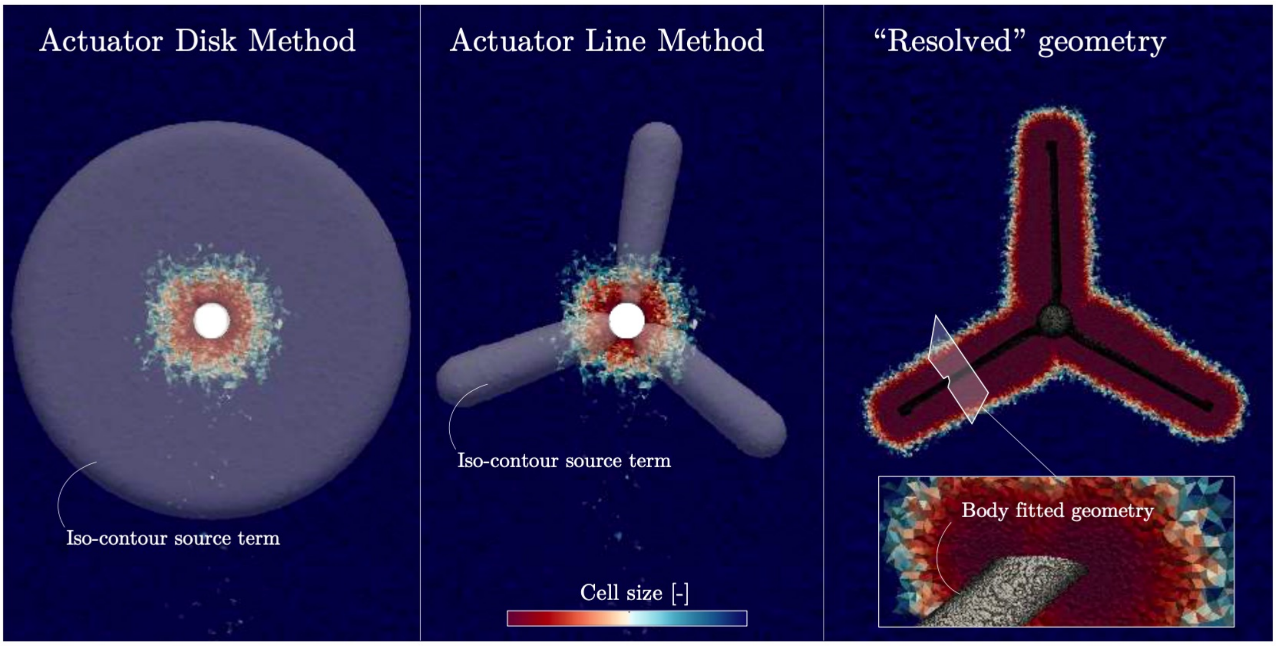

Figure 3.8: Example of the cell size requested around the rotor according to the Actuator Disk Method, Actuator Line Method or a "Resolved" geometry. From [35].

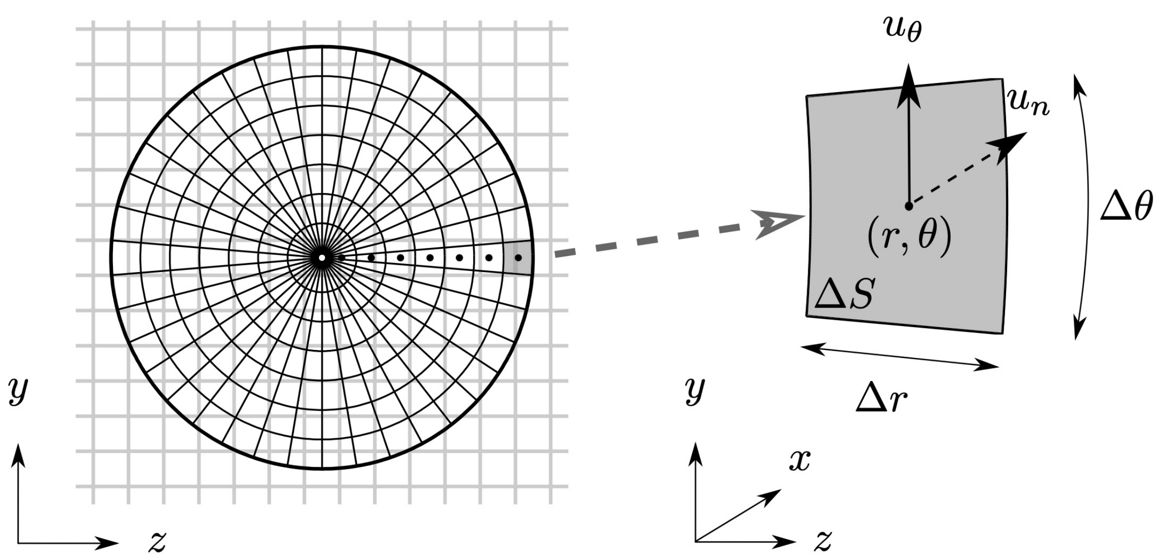

Figure 3.9: Disk discretization into polar cells on a Cartesian mesh. From [233].

The lift and drag aerodynamic forces on one blade section of length ω are thus computed as:

$$
\begin{aligned}
L &= \frac{1}{2}\rho V_{rel}^2 c(r)\omega C_L(\alpha) \ , \\
D &= \frac{1}{2}\rho V_{rel}^2 c(r)\omega C_D(\alpha) \ ,
\end{aligned}
\tag{3.31}
$$

where C_L and C_D are the lift and drag coefficients, α the local angle of attack, V_{rel} the local relative velocity, $c(r)$ the local chord length. The relative velocity is:

$$
V_{\text{rel}} = \sqrt{u_n^2 + (\Omega r - u_\theta)^2} \ , \tag{3.32}
$$

where Ω is the rotor speed. C_L and C_D are obtained from the local angle of attack α and the tabulated two-dimensional airfoil data. α is computed as the difference between the flow angle ϕ and the sum of the twist and pitch angles β and γ:

$$
\alpha = \phi - \beta - \gamma = \arctan\left(\frac{u_n}{\Omega r - u_\theta}\right) - \beta(r) - \gamma \tag{3.33}
$$

The lift and the drag aerodynamic forces can be expressed in the normal and tangential directions of the disk plane as shown in Fig. 3.10:

$$
F_N = L\cos\phi + D\sin\phi \quad \text{and} \quad F_\theta = L\sin\phi - D\cos\phi \tag{3.34}
$$

To obtain global loads on a polar surface ΔS, the lift and drag forces are multiplied by the number of blades N_b and by the corresponding weight between the surface element and the corresponding annular surface.

$$
\begin{aligned}
F_{N,AD} &= F_N N_b \frac{\Delta S}{2\pi r\omega} \\
F_{\theta,AD} &= F_\theta N_b \frac{\Delta S}{2\pi r\omega}
\end{aligned}
\tag{3.35}
$$

Forces are translated into bulk forces and mollified on the Eulerian grid. This methodology is detailed in Section 3.3.3.

3.3.2 Actuator Line Method

In the ALM framework, each blade of the wind turbine is represented. Compared to the ADM, this method is more accurate but also more expensive. Body forces are imposed along rotating lines that represent the aerodynamic loads of the wind turbine blades [234]. With ALM, blades are divided into elements that discretize the blade span and have a prescribed rotational motion. The methodology follows the one of the actuator disk, detailed in Section 3.3.1. The lift and drag forces are computed as in Eq. 3.31. As for the actuator disk model, the lift

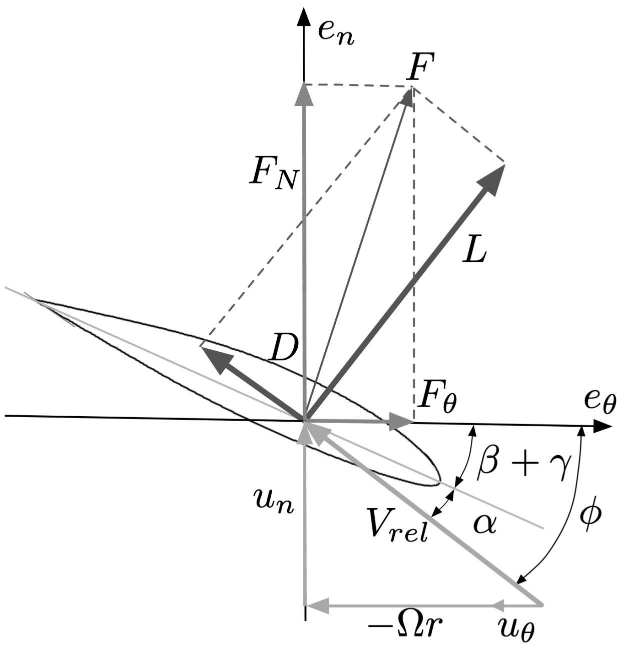

Figure 3.10: blade airfoil schematics. From [233].

and drag coefficients are determined from two-dimensional airfoil data and corrected for three-dimensional effects. The forces are then translated into bulk forces and mollified on the Eulerian grid. This methodology is detailed in Section 3.3.3.

To improve the accuracy of the model, corrections have been integrated. The first type of corrections emulates the rotational effects that limit the growth of the airfoil boundary layer. Several corrections formulas are present in the literature [235–238]. A second type is the tip loss correction [239–242], to take into account the turbulence generated at the tip of the blade. The correction is based on the aspect ratio of the blade and the proximity of the element to the root and tip. A third correction type considers the dynamic stall effect [243, 244]. These corrections are based on the temporal evolution of the angle of attack and the airfoil properties.

3.3.3 Force mollification

To transpose lift and drag forces on the Eulerian grid, a mollification process is used. The application is as follow. The local forces can be integrated over the element section i and can be expressed by:

$$\mathbf{F}_i = \int_\omega \mathbf{F}_{2D,i}\, \mathrm{d}\omega \; . \tag{3.36}$$

The force is now applied as source terms in the Navier-Stokes equations Eq. 3.2. To prevent singular momentum source value, forces are regularized on the Eulerian grid. It is performed using a mollifying function η [234, 245] defined as an isotropic Gaussian kernel:

$$\eta_\epsilon(d) = \frac{1}{\epsilon^3 \pi^{3/2}} \exp\left[-\left(\frac{d}{\epsilon}\right)^2\right] , \tag{3.37}$$

where d is the distance between a grid node and the element position and ϵ the mollifier width parameter. To ensure a conservative treatment of the forces on a numerical grid with a given cell size Δ, $\frac{\epsilon}{\Delta}$ has to be set such that:

$$\int_{\mathbb{R}^3} \eta_\epsilon(\mathbf{x})\mathbf{dx} = 1 . \tag{3.38}$$

A common value for the regularization parameter ϵ is $\epsilon/\Delta = 2$ [75, 246]. The force resulting from this convolution is given as:

$$\mathbf{F}_{\epsilon,i} = \mathbf{F} \times \eta_\epsilon . \tag{3.39}$$

Finally, the body force source term $\mathbf{f}$ at a position $\mathbf{x}$ in the momentum equation follows:

$$\mathbf{f}(\mathbf{x}) = -\frac{1}{\rho}\sum_{i=1}^{N} \mathbf{F}_i \eta_\epsilon\left(\|\mathbf{x} - \mathbf{x}_i\|\right) . \tag{3.40}$$

As wind turbines reach hundreds of meters, the blade deformation becomes non-negligible. As such, the notion of elastic/deformable actuator line is present in the literature [59, 247, 248]. For that reason, this topic has already been addressed in a previous work [35], where the actuator line was coupled with an aero-servo-elastic code. Using this coupling, the loads could be determined more accurately. However, it is beyond the scope of this work. In this thesis, only rigid wind turbine structures will be studied. which implies a strong hypothesis on the load computation. With this hypothesis, only non-prebended blades will be used.

3.4 Conclusion

This chapter reviews the physics and the principal methodologies used in this work. First, the context of turbulent flows and their modelling are introduced. Particular attention is paid to the Large-eddy simulation method. The subgrid-scale model used in this work is further developed. Second, the YALES2 library, the CFD solver used in this work, is detailed. The incompressible constant density solver is presented. Spatial and temporal discretization schemes are reviewed. The dynamic mesh adaptation methodology based on the MMG library is explained. Finally, the horizontal-axis wind turbine modelling is detailed, developing both the actuator disk and the actuator line methods. The mollification process is outlined. This framework is then used in the following chapters for atmospheric boundary layer simulations and wind turbine simulations.

Chapter 4

Development and application of the atmospheric solver

Chapter 4 describes the elaboration of the atmospheric solver, based on the YALES2 library. The several fundamental components of its development are detailed. It encompasses the Coriolis force, the Boussinesq buoyancy approximation and the wall modelling using the Monin-Obukhov Similarity Theory. The solver is then applied against numerical studies with varying stability configurations. The following sections present simulations of a neutral, convective and stable boundary layer. These studies enable the validation of the implementation of the Coriolis force, the Monin-Obukhov similarity theory, and the Boussinesq buoyancy approximation. The stable boundary layer is performed on both structured and unstructured grids, using different grid resolutions. This work has been the subject of a publication [78]. Conclusions are detailed in the last section.

Contents

4.1 Development of atmospheric models . . . 98

4.1.1 Coriolis force . . . 98

4.1.2 Boussinesq buoyancy approximation . . . 99

4.1.3 Wall model . . . 100

4.1.4 Wall law filtering . . . 101

4.2 Application to a Neutral Boundary Layer . . . 102

4.3 Application to a Convective Boundary Layer . . . 103

4.3.1 Numerical setup . . . 103

4.3.2 Results . . . 104

4.4 Application to a Stable Boundary Layer . . . 105

4.4.1 GABLS1 configuration . . . 107

4.4.2 Numerical set-up . . . 108

4.4.3 Results . . . 109

4.4.4 Conclusions of the GABLS1 study . . . 119

4.5 Conclusion . . . 120

4.1 Development of atmospheric models

The YALES2 library is used in this work. However, as mentioned in Section 1.4, this solver has not previously been employed for atmospheric flow simulations and does not encompass the requisite tools. Based on the literature review and what was already available in the solver, three development tasks have been identified:

1. Taking into account the Coriolis force, predominant at atmospheric flow scales.

2. Taking into account the density variations, induced by temperature fluctuations.

3. The use of a wall model as a wall-resolved LES is computationally unaffordable.

The initial objective is thus to develop up-to-date state-of-the-art tools to take these effects into account in the YALES2 platform.

4.1.1 Coriolis force

As mentioned in Section 2.1.3, the Coriolis force can be written:

$$\boldsymbol{F_c} = -2 \cdot m \cdot \omega \cdot \begin{pmatrix} sin(\phi) \cdot u_y \\ sin(\phi) \cdot u_x - cos(\phi) \cdot u_z \\ cos(\phi) \cdot u_y \end{pmatrix} \tag{4.1}$$

where m is the mass of the object, ω is the Earth angular velocity, ϕ the latitude and u_x, u_y, u_z the object velocity in the local coordinate system. Usually, simplifications are made, neglecting the z-component of the Coriolis force and the vertical velocity. However, in the code, no simplifications have been made.

In most benchmark cases, the geostrophic wind is given as a data. Therefore, the goal of the Coriolis force is to reproduce the geostrophic balance. As such, the geostrophic wind is deducted from the local velocity. The Coriolis force is written:

$$\boldsymbol{F_c} = -2 \cdot m \cdot \omega \cdot \begin{pmatrix} sin(\phi) \cdot (u_y - G_y) \\ sin(\phi) \cdot (u_x - G_x) - cos(\phi) \cdot (u_z - G_z) \\ cos(\phi) \cdot (u_y - G_y) \end{pmatrix} \tag{4.2}$$

where G_i is the Geostrophic wind. In doing so, the Coriolis force drives the flow to the geostrophic wind. At geostrophic height, where surface friction is negligible, the flow reaches geostrophic wind. Below, surface friction slows the flow, inducing the Ekman spiral.

In YALES2, the user specifies a geostrophic wind (which can be by components) so that the Coriolis force is computed as in Eq. 4.2. In addition, the user must specify the latitude.

Finally, the local frame orientation must be specified so that the Coriolis force is correctly computed. The Coriolis force is implemented in the incompressible constant density solver but also in an incompressible variable density solver which could also be used to perform non-neutral atmospheric boundary layers. However, its use is beyond the scope of this work. The Coriolis force is computed on each fluid node depending on the local velocity and applied through a source term.

4.1.2 Boussinesq buoyancy approximation

By using an incompressible solver we neglect density and effects such as sounds waves. However, to reproduce thermal stratification, a density-gravity effect, the buoyancy force must be added to the Navier-Stokes equation. For this purpose, most atmospheric flow codes use the Boussinesq approximation for buoyancy-driven flows [249]. Eq. 3.2 becomes:

$$\frac{\partial u_j}{\partial t} + \frac{\partial u_i u_j}{\partial x_i} = \nu \frac{\partial^2 u_j}{\partial x_i \partial x_i} - \frac{1}{\rho_0}\frac{\partial P}{\partial x_j} + \frac{\rho g}{\rho_0} \; . \tag{4.3}$$

where ρ_0 is the density of the flow. In the code, the temperature is taken into account by using a passive scalar. The transport equation for the temperature is:

$$\frac{\partial T}{\partial t} + \nabla \cdot (uT) = \nabla \cdot (D_T \nabla T) \tag{4.4}$$

where D_T is the scalar diffusion coefficient. This coefficient is related to the kinematic viscosity ν and the turbulent eddy viscosity ν_t as:

$$D_T = \frac{\nu}{Sc} + \frac{\nu_t}{Sc_t} \tag{4.5}$$

where Sc and Sc_t are the Schmidt and the turbulent Schmidt numbers, respectively. In the following work, the molecular Schmidt number is set to:

$$Sc = \frac{\nu_{air}}{D_{air}} \approx 0.8 \tag{4.6}$$

In contrast, the turbulent Schmidt number has no universal value. In the literature, the optimum values for Sc_t are widely distributed in the range of $0.2 - 1.3$ [250]. It appears that it depends on the flow characteristics. For atmospheric flows, the turbulent Schmidt number is usually set between $0.3 - 0.7$ [251]. As the turbulent Schmidt number depends on the flow characteristics, a dynamic model can be used. In several studies, the turbulent Schmidt number is expressed as a function of the Reynolds number [252–254]. To determine whether a dynamic model was required, different turbulent Schmidt numbers between $0.3 - 1$ have been tested in the configuration developed in Section 4.4. The influence was found to be negligible. Therefore, in the following, a constant turbulent Schmidt number $Sc_t = 0.5$ is used.

From the temperature, a density is computed through the ideal gas law:

$$\rho = \frac{P_{atm}}{RT} , \tag{4.7}$$

where R is the specific gas constant for dry air. Humidity effects are neglected.

4.1.3 Wall model

The wall modelling in this work is based on the Monin-Obukhov similarity theory. This theory relies on logarithmic velocity and temperature profiles, where correction terms ψ are introduced to adequately match the thermal configuration [255]. The velocity and temperature profiles can be expressed as Eq. 4.8

$$\begin{aligned} \bar{u}(z) &= \frac{u_*}{\kappa}\left[\ln\left(\frac{z}{z_0}\right) - \psi_m\left(\frac{z}{L}\right)\right] \\ \frac{\theta(z)-\theta_w}{\theta_*} &= \frac{1}{\kappa}\left[\ln\left(\frac{z}{z_0}\right) - \psi_h\left(\frac{z}{L}\right)\right] \end{aligned} \tag{4.8}$$

where $u_* = \sqrt{\tau_w/\rho}$ is the friction velocity. τ_w refers to the local shear stress on the wall. $\theta_* = -\overline{w'\theta'}/u_*$ where $\overline{w'\theta'}$ is the kinematic surface heat flux and θ_w is the wall temperature. κ the von Kármán constant, z the height, and z_0 the roughness length.

ψ_m and ψ_h are correction functions. L the Obukhov length that represents the height above the surface from where buoyancy first dominates shear computed as $L = -\frac{u_*^3\theta_0}{\kappa g \overline{w'\theta'}}$. g is the Earth's gravity. θ_0 is the reference potential temperature.

For neutral cases, the correction terms are zero, leading to a simple logarithmic velocity profile. For non-neutral configurations, correction functions ψ_m and ψ_h can be expressed as:

$$\psi_{m/h}(\zeta) = \int_{z_0/L}^{\zeta} \frac{1-\phi_{m/h}(\zeta)}{\zeta}\,\mathrm{d}z , \tag{4.9}$$

where $\zeta = z/L$. ϕ_m and ϕ_h are referred to as stability functions. They are empirically determined and can be expressed as:

$$\begin{aligned} \phi_m &= \begin{cases} (1-\gamma_m\zeta)^{-1/4}, & Q_w > 0 \\ 1+\beta_m\zeta, & Q_w < 0 \end{cases} , \\ \phi_h &= \begin{cases} (1-\gamma_h\zeta)^{-1/2}, & Q_w > 0 \\ 1+\beta_h\zeta, & Q_w < 0 \end{cases} . \end{aligned} \tag{4.10}$$

Correction functions can be integrated, giving for stable cases:

$$\begin{aligned} \psi_m(\zeta) &= 1 - \phi_m \ , \\ \psi_h(\zeta) &= 1 - \phi_h \ , \end{aligned} \tag{4.11}$$

and for unstable cases:

$$\begin{aligned} \psi_m(\zeta) &= 2\ln\left(\frac{1+\phi_m^{-1}}{2}\right) + \ln\left(\frac{1+\phi_m^{-2}}{2}\right) - 2\arctan\left(\phi_m^{-1}\right) + \frac{\pi}{2} \ , \\ \psi_h(\zeta) &= 2\ln\left(\frac{1+\phi_h^{-1}}{2}\right) \ . \end{aligned} \tag{4.12}$$

In the following studies, the parametrization prescribed in the GABLS1 setup, i.e. $\beta_m = 4.8$ and $\beta_h = 7.8$, will be used. The surface temperature is prescribed as the boundary condition, leading to a two-unknown problem, u_* and θ_*. To solve the system of equations, a double Newton-Raphson convergence method [256] is used in YALES2 for its quadratic convergence speed. The algorithm can be found in **Appendix C**.

4.1.4 Wall law filtering

As wall models are derived from averaged Navier-Stokes equations, quantities such as velocity and temperature must be spatially filtered [130]. For structured grids, averaging the quantities in the horizontal plane passing through the first nodes above the ground is straightforward. For unstructured grids, the first nodes plane does not exist. To overcome this problem, a "Gather-Scatter" filtering operator is applied to the latter, the first node velocity and temperature used to build the momentum and heat flux at the wall.

The "Gather-Scatter" operator first consists in averaging to the element the data located on the nodes (the gather step). Data on the elements are then distributed back to the attached nodes (the scatter step). As each node is connected to multiple elements, the data are averaged. As unstructured meshes are used, the averaging process can be weighted by the surface of the element if desired. By repeating this operation, the data is filtered, with a filtering size that depends on the number of operations. A two-dimensional scheme representing the gather-scatter filter is pictured in Fig. 4.1.

These new tools integrated into the YALES2 library must be tested and validated on cases from the literature. Going from the simplest to the complex configuration, a neutral boundary layer is first modelled to validate the Coriolis force implementation, as well as the Monin-Obukhov wall law for neutral configuration. Then an unstable case is reproduced to validate the Boussinesq buoyancy approximation and the wall law in convective configuration. Finally, the GABLS1 stable boundary layer is reproduced, encompassing all the developments.

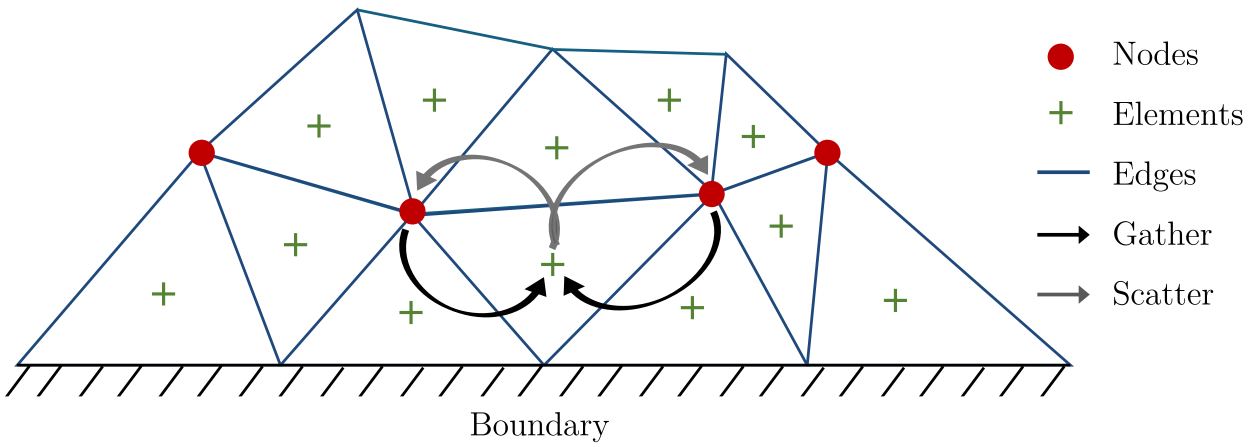

Figure 4.1: Two dimensional scheme of the Gather-Scatter filter operation on first nodes from the wall.

4.2 Application to a Neutral Boundary Layer

This work aims to validate the representation of a neutral boundary layer and by so the Coriolis force implementation. To do so, the case developed by Andren [257] is performed. Details of the configuration are given afterwards. Results are compared with three different studies. The first study [258] is based on the three-dimensional, compressible, nonhydrostatic, filtered Navier–Stokes equations ARPS code [259]. It is mainly used for mesoscale and small-scale atmospheric simulations. The second study [260] is based on the DHARMA hybrid RANS/LES code [261]. Time integration is performed using a second-order Runge-Kutta method, and the dynamic Smagorinsky method is used for subgrid-scale modelling. The last study [262] is based on the ProLB tool, based on the Lattice-Boltzmann method.

The simulation domain is a box of $1280 \times 1280 \times 1500$ m^3. Periodic conditions are used in the horizontal direction. A slip wall is placed at the top, while a rough wall of $z_0 = 0.1$ m is placed at the bottom. Monin-Obukhov for the neutral boundary layer is used for wall modelling. The Coriolis force, detailed in Section 4.1.1 drives the flow. The initial velocity profile is set as Eq. 4.13.

$$\begin{cases} u(z) = U_g\left(1 - \exp\left(-\frac{z}{H}\right)\cos\left(\frac{z}{H}\right)\right) \\ v(z) = U_g \exp\left(-\frac{z}{H}\right)\cos\left(\frac{z}{H}\right) \end{cases} \tag{4.13}$$

The convergence is running for 56h while statistics are gathered on 28h. The mesh size is set to $\Delta = 32$ m, identical to the proLB study.

The average velocity profile is shown in Fig. 4.2. The mean velocity is spatially averaged over horizontal planes and over time. The velocity profile shows a logarithmic behaviour. Balanced between the geostrophic wind and the surface friction. The results show a good

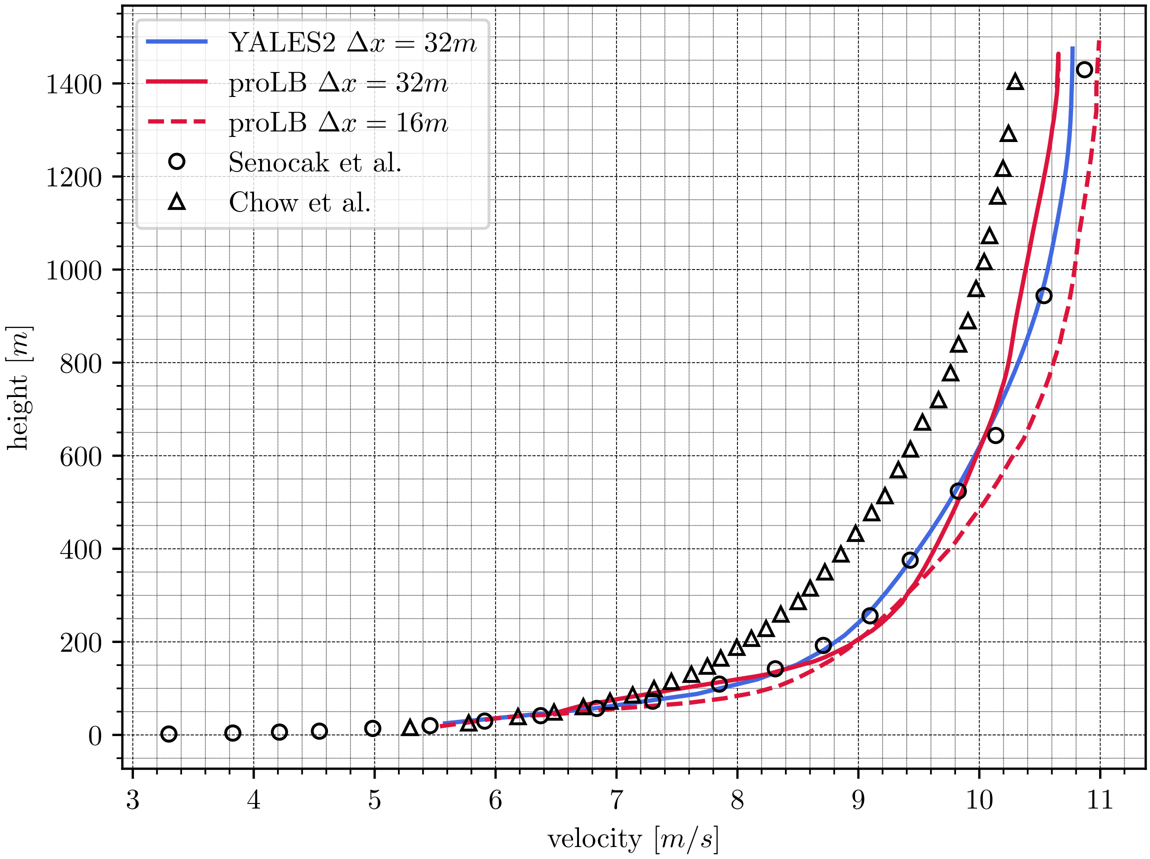

Figure 4.2: Average velocity profile of the Andren case gathered on 28h.

agreement with the three previous studies. It can be observed that even though the grid is coarse, the YALES2 solver with a dynamic Smagorinsky subgrid-scale model can well predict the flow structures. Although succinct, this study tends to validate the implementation of the Coriolis force for neutral cases. Additional configurations are required to assert it.

4.3 Application to a Convective Boundary Layer

Now that the Coriolis force implementation for neutral configuration is validated, validation of the wall model for non-neutral configurations can be performed. This methodology is tested through a case developed by Willis and Deardorff [263]. The results are compared with the experimental data obtained later by the same authors [263] and from Deardorff and Willis extensive results [264] as well as from Schmidt and Schumann numerical results [265].

4.3.1 Numerical setup

The case investigated corresponds to a Convective Boundary Layer uniformly heated from below and topped by a layer of uniformly stratified fluid (i.e. the inversion layer). The domain is a periodic box of size $L_x \times L_y \times L_z = 8000 \times 8000 \times 2400\,\mathrm{m}^3$ meshed with a structured grid of

$N_x \times N_y \times N_z = 256 \times 256 \times 128$ elements. The spatial resolution is thus $\Delta x = \Delta y = 31.25$ m and $\Delta z = 18.75$ m for all three directions. A scheme of the setup is pictured in Fig. 4.3. The initial height of the inversion layer is also used to specify the initial condition. The initial temperature profile corresponds to that of a mixed layer initially at $\theta_0 = 299.8\,\mathrm{K}$ topped by an inversion layer of uniform stability $\mathrm{d}\langle\theta\rangle/\mathrm{d}z = 0.0027\,\mathrm{K.m^{-1}}$. Both the temperature and velocity profiles are disturbed by a variable perturbation r randomly selected in $[-0.5; 0.5]$. The initial temperature profiles thus reads:

$$\theta(z) = \begin{cases} \theta_0 + 0.1r\left(1 - \frac{z}{z_m}\right)\theta_C^0 & \text{if } 0 < z \leq z_{z_m}, \\ \theta_0 + (z - z_m)\frac{\mathrm{d}\langle\theta\rangle}{\mathrm{d}z} & \text{if } z > z_m\ , \end{cases} \tag{4.14}$$

where $z_m = 1400\,\mathrm{m}$ is the initial height of the mixed layer and $\theta_C^0 = 0.041\,\mathrm{K}$. Similarly, the initial velocity profile is given by:

$$w(z) = \begin{cases} 0.1r\left(1 - \frac{z}{z_m}\right)w_C^0 & \text{if } 0 < z \leq z_m\ , \\ 0, & \text{if } z > z_m\ . \end{cases} \tag{4.15}$$

where $w_C^0 = 1.46\,\mathrm{m.s^{-1}}$.

The fluid properties are typical of those encountered on a sunny day in southern Germany i.e dry air of dynamic viscosity $\nu = 2.15 \times 10^{-5}\,\mathrm{m^2.s^{-1}}$ and thermal diffusivity $\alpha = 21.4 \times 10^{-6}\,\mathrm{m^2.s^{-1}}$.

In terms of boundary conditions, the ground is heated by a uniform kinematic heat flux, $q_w = 0.06\,\mathrm{K.m.s^{-1}}$, while the roughness height is $z_0 = 0.16\,\mathrm{m}$. Schmidt & Schumann introduced a radiation boundary condition at the top of the domain to avoid spurious reflections of gravity waves. In our case, a sponge layer where source terms smoothly bring the velocity and scalar profiles up to their theoretical value is implemented for this purpose. This sponge layer has a height of 750 m and is discretized by 40 points. Our final domain dimensions are then $L_x \times L_y \times L_z = 8000 \times 8000 \times 3150\,\mathrm{m^3}$ and the resolution remains the same as the one mentioned earlier. Finally, lateral boundary conditions are considered periodic.

4.3.2 Results

Fig. 4.4 and 4.5 represent the dimensionless horizontal and vertical velocity variance, respectively. The former is overall lower than the latter, except at the edges of the mixed layer. In fact, vertical velocity fluctuations are mostly due to buoyancy, whereas horizontal velocity fluctuations are mainly due to pressure fluctuations, which are lower overall but predominant at the edges of the mixed layer. Fig. 4.4 and 4.5 show that the velocity profiles match those of Schmidt and Schumann. However, Deardorff and Willis's experimental data predict higher horizontal velocity variances. Schmidt and Schumann [265] have suggested that horizontal

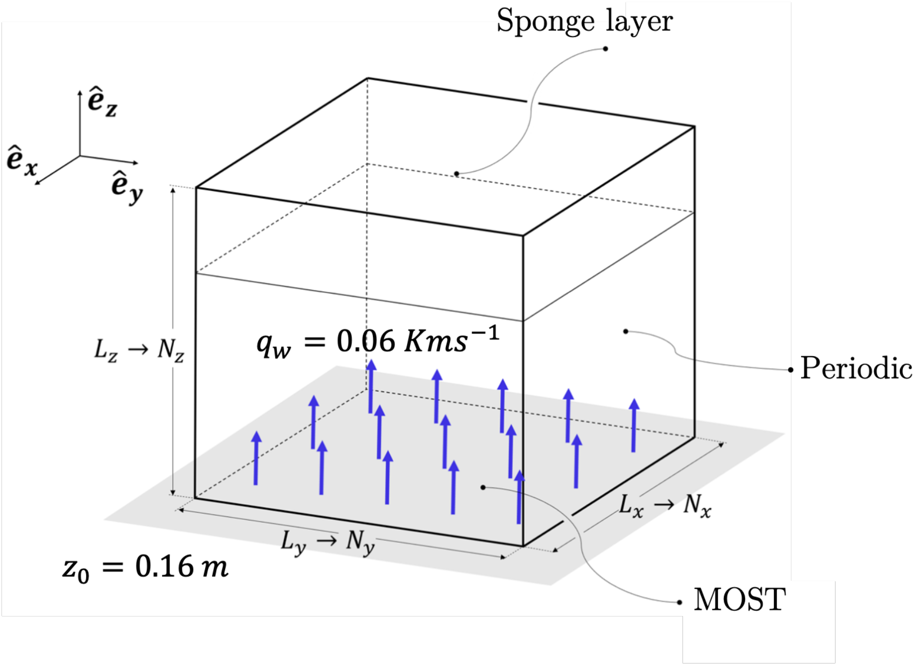

Figure 4.3: Scheme representing the Deardorff and Willis setup, adapted from [266].

variation of the surface heat flux and thus the experimental setup itself was the cause of those differences. Moreover, the older Willis and Deardorff measurements are much closer to all numerical results.

The dimensionless temperature and vertical heat flux variance are shown in Figures 4.6 and 4.7, respectively. The temperature variance is low overall, except at the edges of the mixed layer. In fact, temperature variances are produced by the product of heat flux and temperature gradient, which is large near the surface and at the inversion height. On the other hand, vertical turbulent heat flux decreases linearly with height up to the inversion layer. It implies a constant heating rate and thus the expected results. The obtained results match both Schmidt and Schumann's data and the experimental data.

The implementation of the Monin-Obukhov similarity theory in YALES2 was performed and validated with a comparison to both experimental and numerical data. Therefore, the convective boundary layer can now be used for real cases, such as wind turbine and wind farm simulations.

4.4 Application to a Stable Boundary Layer

To enhance comprehension of stable boundary layers by Large Eddy Simulation (LES), the Global Energy and Water Cycle Experiment (GEWEX) initiated the GEWEX Atmospheric Boundary Layer Study (GABLS). The objective was to enhance comprehension of stable bound-

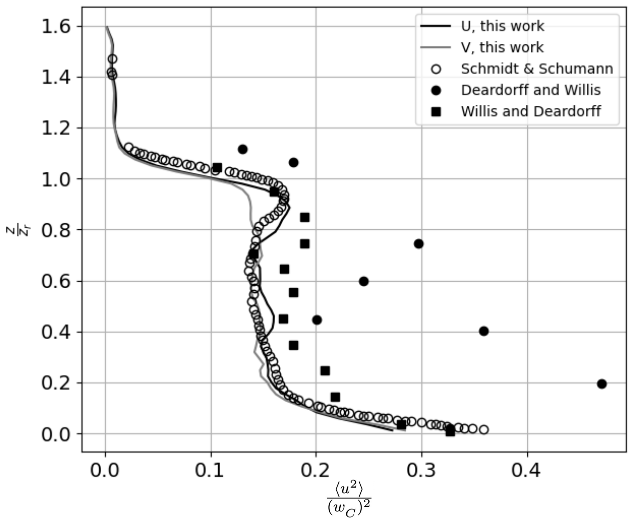

Figure 4.4: Dimensionless horizontal velocity variance function of dimensionless height.

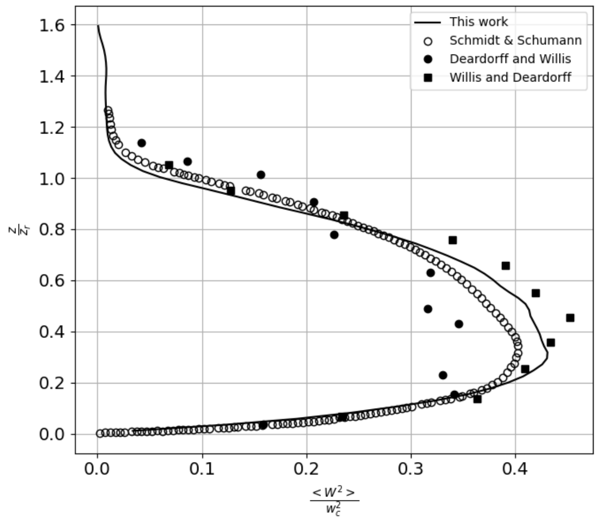

Figure 4.5: Dimensionless vertical velocity variance function of dimensionless height.

ary layer and improve its representation by LES models [61]. The focus of GABLS has been on SBLs over land and the representation of diurnal cycle. Three different GABLS intercomparisons have already been carried out, focusing on progressively more realistic cases. These benchmarks are considered important for improving the modelling of stable atmospheric layers [267]. In this work, we consider the GABLS1 benchmark targeting an idealized Arctic stable boundary layer case [104]. The GABLS1 setup consists of a periodic box with a uniform initial velocity profile, cooled by the bottom wall, where the surface temperature decreases over time.

Initially, a comparison of 11 LES codes was carried out [62]. A range of mesh resolution has been given in order to correctly capture the flow physics behaviour. The study has shown that the grid resolution employed has a high impact on the accuracy of the SBL modelling. Subsequent to the initial study, several LES have been conducted employing the GABLS1 configuration with the objective of replicating an SBL scenario. The benchmark results are used to validate the underlying framework, as well as to investigate the influence of finer grid [268,269], surface cooling rate [268,270,271] or subgrid-scale (SGS) [118,272,273] impact. Other studies have used the GABLS1 configuration to validate their RANS or pseudo-spectral methods [267,274]. Regardless of the approach employed, all of these studies accurately reproduce the physical behaviour of the stable boundary layer, but the use of finer grids does not prejudge the quality of the results. It is worth mentioning that all the aforementioned studies were conducted on structured grids. None have used unstructured grids since the cubic domain was not requesting it.

The simulation of wind flows in complex terrain is also a challenging topic due to the difficulty of creating a mesh that accurately reflects the topography [37]. More detail can be found in Chapter 6.2. To address the reluctance of the research community to employ such meshes, it is essential to validate their use in simple scenarios before progressing to more

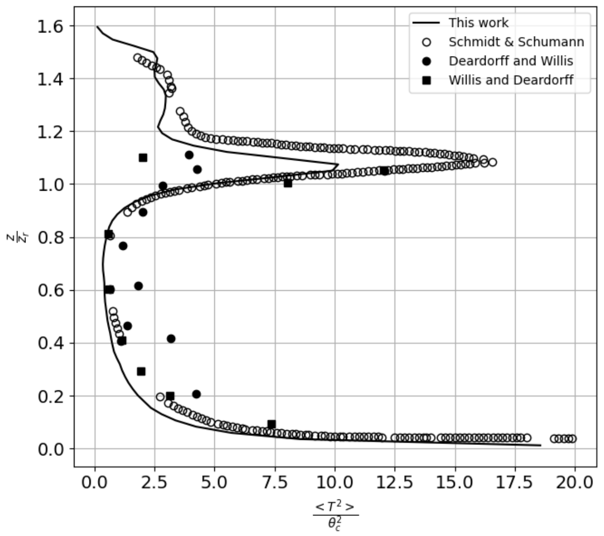

Figure 4.6: Dimensionless temperature variance function of dimensionless height.

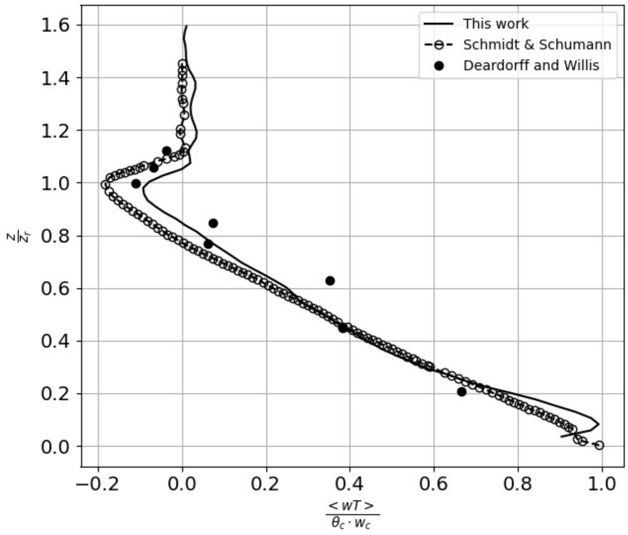

Figure 4.7: Dimensionless heat flux variance function of dimensionless height.

complex studies. Conclusions on the minimum and optimum mesh size [62] for robust LES are drawn using only a structured grid. Therefore, the aim of this study is to draw analogous conclusions for simulations using unstructured grids. To the author's knowledge, a Large Eddy Simulation of a stable boundary layer has never been performed on an unstructured grid, and this work aims to address this gap in the literature.

4.4.1 GABLS1 configuration

The GABLS1 intercomparison is based on an idealized Arctic stable boundary layer case [104]. A domain of $400 \times 400 \times 400\,\mathrm{m}^3$ with periodic walls in both the streamwise, x, and tangential, y, directions is employed. The bottom boundary condition is a rough wall with a $z_0 = 0.1\,\mathrm{m}$ roughness. The surface temperature is $T_w = 265\,\mathrm{K}$ with a cooling rate of $0.25\,\mathrm{K.h}^{-1}$. The top boundary condition is a slip wall. An imposed uniform geostrophic wind of $G_x = 8\,\mathrm{m.s}^{-1}$ in the east-west direction at latitude 73° north drives the stable boundary layer, corresponding to a Coriolis parameter of $f = 1.39 \times 10^{-4}\,\mathrm{s}^{-1}$. Gravity, reference potential temperature and density as well as the Von Karman constant are set to $g = 9.81\,\mathrm{m.s}^{-2}$, $\theta_0 = 263.5\,\mathrm{K}$, $\rho_0 = 1.3223\,\mathrm{kg.m}^{-3}$ and $\kappa = 0.4$, respectively. Figure 4.8 illustrates the configuration of the GABLS1 setup.

Initial velocity profile is set to geostrophic wind, i.e. a uniform $u_x = 8\,\mathrm{m.s}^{-1}$ velocity profile. The initial vertical temperature profile is uniform to 265 K in the first hundred meters and then increases by $0.01\,\mathrm{K.m}^{-1}$ to the top of the domain, reaching 268 K at the top. Random perturbations are introduced in the first fifty meters with an amplitude of 0.1 K as specified in [62].

To mitigate gravity-wave reflexion, a sponge layer (SL) is applied above three hundred meters. In order to smoothly relax the velocity and the temperature and thus avoid numerical

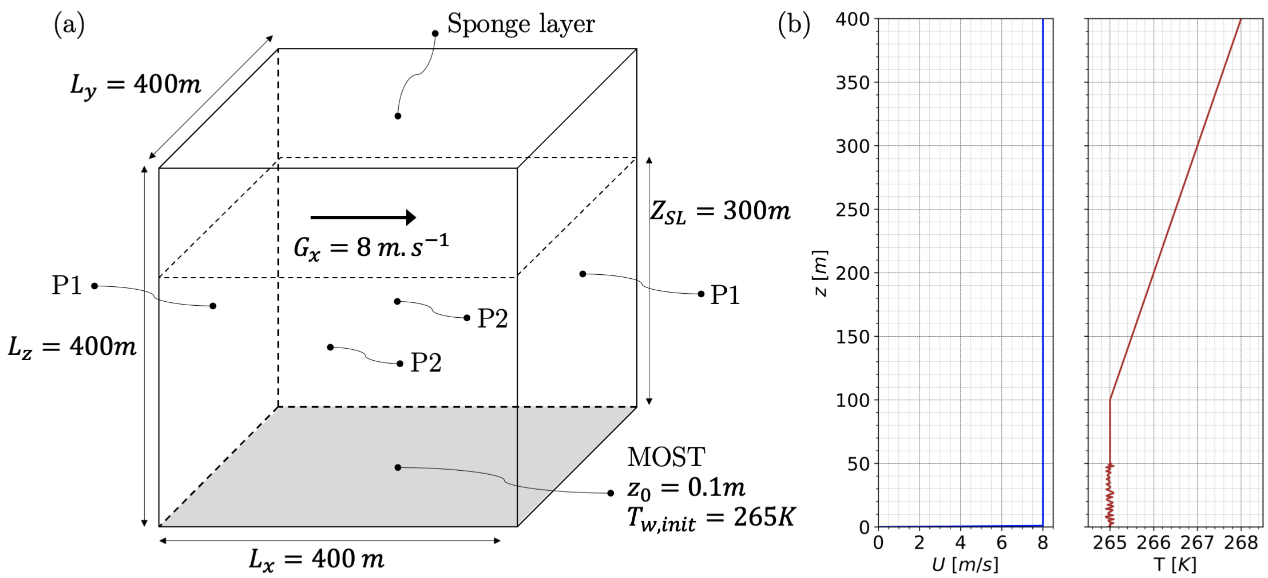

Figure 4.8: (a): GABLS1 setup configuration scheme. $P1$ and $P2$ for periodic walls in pairs. (b): initial velocity and temperature vertical profiles.

errors, the sponge layer follows:

$$SL_\phi = \gamma \times \sin^2\left(\frac{z - z_{SL}}{L_z - z_{SL}} \times \frac{\pi}{2}\right) \times (\phi_{target} - \phi)\,, \tag{4.16}$$

where ϕ represents the actual velocity or temperature. Here, ϕ_{target} is the target velocity or temperature, set to geostrophic wind or linear increasing temperature respectively. $\gamma = \frac{1}{5}$ is a time relaxation parameter and z is the height varying between the SL bottom height $z_{SL} = 300\,\text{m}$ and the domain top height $L_z = 400\,\text{m}$. The sponge layer is then smoothed over time and over space.

4.4.2 Numerical set-up

Structured (S) and unstructured (U) meshes with 4 different resolutions are used in this study. Tab. 4.1 gathers the mesh characteristics for these cases. The number of elements varies significantly between the structured and unstructured meshes of the same resolution, and similar number of nodes. Since the control volumes are defined at the mesh nodes in YALES2, the number of degrees of freedom remains approximately the same, and so the mesh type comparison is fair.

Subgrid scale modelling is performed using the dynamic Smagorinsky model [105, 106]. Although different models are sometimes used to better model anisotropic flows [118], Smagorinsky models are still the most commonly used in the literature and have been proven to perform reasonably well [204]. In addition, the dynamic Smagorinsky model has been shown to be more effective at sustaining deeper SBLs relative to the Smagorinsky model [62].

Mesh name	S1	U1	S2	U2	S3	U3	S4	U4
Δx [m]	12.5		6.25		3.125		2.0	
N_{elem} [$\times 10^3$]	32.8	148.2	262.1	1186	2097.2	9487.9	8000.0	35972.8
N_{node} [$\times 10^3$]	45.4	41.8	366.3	337.8	2919.7	2659.1	11255.5	10042.7
Δt [s]	0.2		0.1		0.05		0.032	

Table 4.1: Case set-up with Δx the mesh cell size, N_{elem} the number of mesh elements and Δt the time step.

Simulations are ran out for a total of 8 hours of physical time, representing a diurnal cycle. Statistics are collected on the last hour, that is, between the $7th$ and the $8th$ hour. Our results are compared with the eleven LES codes from the first GABLS1 intercomparison [62] but also with various studies that compared themselves with the first study [118, 121, 268, 270–273, 275].

The flow solver time step is here imposed to respect the Courant-Fredrichs-Lewy $CFL = |U|\Delta t/\Delta x$ condition. Due to the explicit integration of the Coriolis force, the time step is chosen following [276] so that $\Delta t = \frac{CFL \times \Delta x}{\|U\| + \sqrt{gH}}$ with H being the vertical depth of the fluid, i.e. the stable boundary layer height. The imposed time step is evaluated to ensure $CFL < 0.9$ with a convective velocity $\|U\| = 9\,\text{m.s}^{-1}$ and a boundary layer height $H = 200\,\text{m}$. All time steps used in this study are summarized in Table 4.1.

4.4.3 Results

Unstructured - Structured grids comparison

To validate the use of unstructured meshes for the simulation of atmospheric flows, the first step is to assess the mesh type impact by comparing results from both unstructured and structured grids. The mesh resolution is chosen as advised by [62] to be optimal for robust LES, i.e. $\Delta x = 3.125\,\text{m}$ for an isotropic grid. Grids are referred to as $S3$ and $U3$ for structured and unstructured grids, respectively, according to Tab. 4.1.

Time series of frictional velocity, wall heat flux, and Monin-Obukhov length are shown in Fig. 4.9. All of these variables fall within the dispersion envelope of the original GABLS1 study results [62]. As far as frictional velocity is concerned, the results are quite similar for both types of grids even if the results of the $S3$ grid are slightly lower. Particularly interesting, the $U3$ results fit its counterpart obtained with the state-of-the-art and commonly used tool PALM [275].

The same observation can be made for the Monin-Obukhov length, which is similar for both grids. After a strong decrease during the first hour, it quickly converges to $O(100)\,\text{m}$. Wall heat fluxes for the $S3$ and $U3$ cases exhibit similar physical behaviour and decrease with

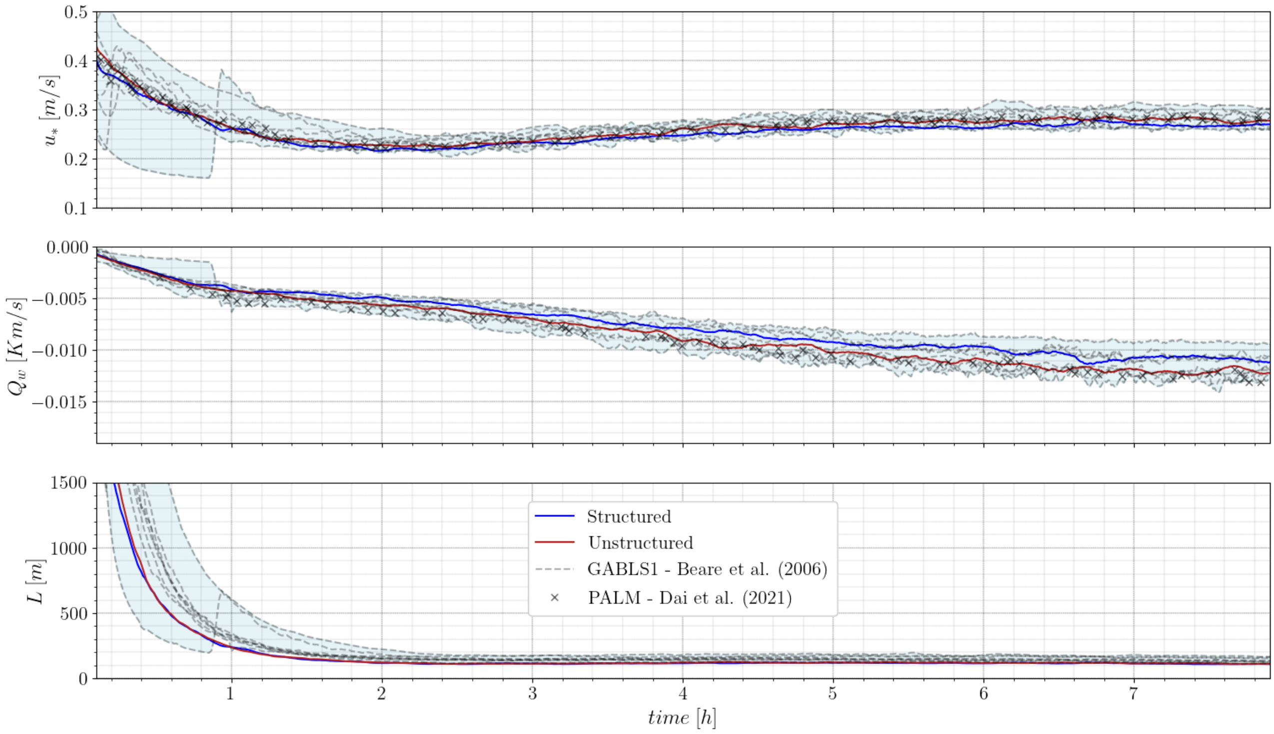

Figure 4.9: Frictional velocity, wall heat flux and Monin-Obukhov length with $S3$ and $U3$ grids, compared to original GABLS1 results dispersion [62] and PALM results [275].

time due to the cooling rate. However, a gap begins to develop after 1 h, reaching a maximum between the $7th$ and $8th$ hours where a 14% average wall heat flux difference is measured. This gap could be explained by a numerical effect of the mesh type.

Some time after the initialisation where the flow is laminar, a flow destabilization process occurs, leading to the development of the stable turbulent boundary layer. This development is directly impacted by the initial temperature field, which contains random values, which is different from one simulation to another. More information on these sources of errors are given into **Appendix D**. This destabilisation process could also explain the strong jump in some GABLS1 original results of Fig. 4.9. Consequently, the mesh type and resolution will have an impact on the flow development which cannot converge to the same results since the boundary conditions are unsteady.

Following the GABLS1 recommended post-processing procedure, the profiles are spatially averaged over horizontal planes and temporally averaged between the $7th$ and $8th$ hours. The streamwise velocity U, tangential velocity V and temperature T profiles are plotted in Fig. 4.10 and compared to the original GABLS1 results [62] as well as more recent studies [118, 268, 269, 272, 275]. The streamwise velocity is zero at the bottom of the domain and reaches the geostrophic wind at the top. The stable boundary layer develops with a velocity peak between 160 and 200 m. The tangential velocity, being zero in the geostrophic wind, starts to grow

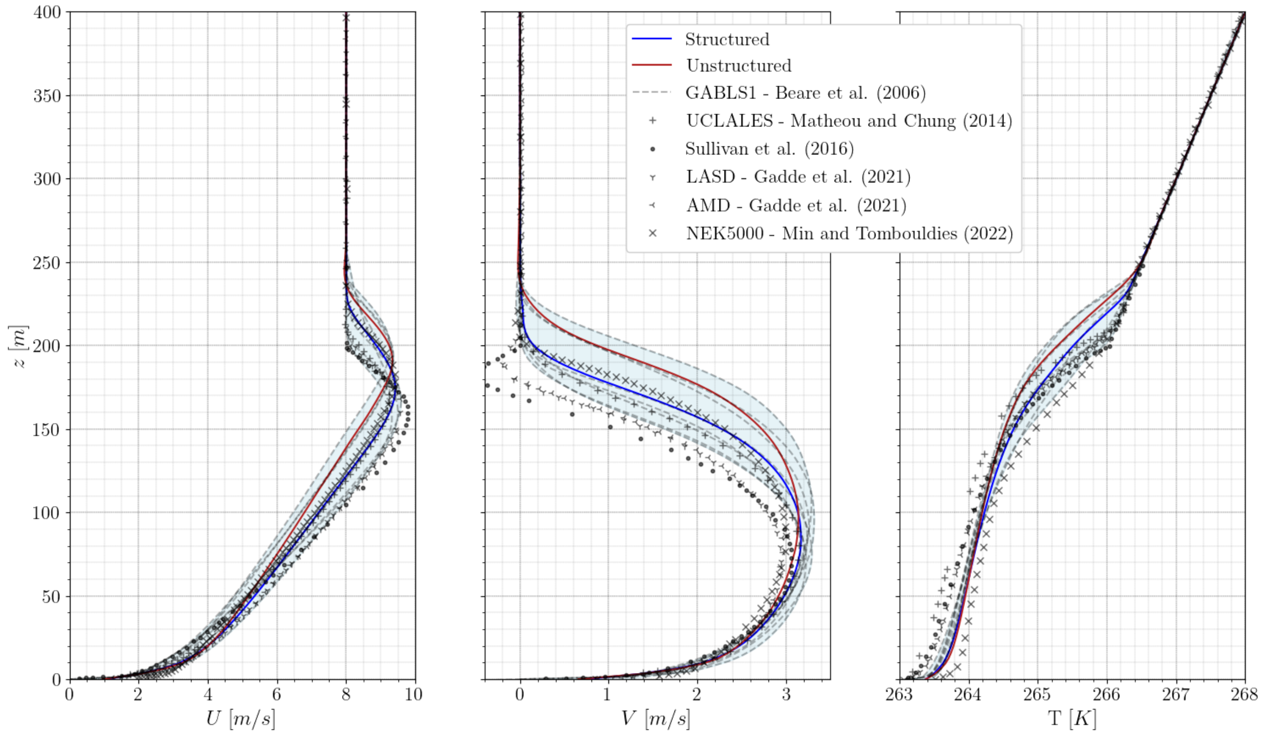

Figure 4.10: Streamwise and tangential velocities and temperature profile for meshes $S3$ and $U3$ with cell size $\Delta x = 3.125\,\mathrm{m}$. Blue shaded area stands for the original GABLS1 study results dispersion [62] and symbols for more recent studies [118, 268, 269, 272].

by descending into the domain due to the Coriolis effect. In the vicinity of the wall, where the friction effect is dominant, the tangential velocity is reduced to zero. The temperature profile shows a behaviour correlated with both velocity components, with an increase with height and a bend between 150 and 200 m. All three profiles show differences between $S3$ and $U3$ simulations but remain within the dispersion of the GABLS1 results. The $U3$ simulation has a streamwise velocity peak offset of 20 m compared to $S3$, also visible on the tangential velocity profile and on the temperature inflection point. More recent studies are also compared, most of which show a similar behaviour but also expand the original results dispersion. For example, Sullivan [268] exhibits an unexplained negative tangential velocity near the top of the boundary layer. This results spreading enlargement show the difficulty in having reference data, but assure some confidence in our results with both meshes.

Variances of streamwise $\overline{U'^2}$, tangential $\overline{V'^2}$ and vertical $\overline{W'^2}$ velocities are plotted in Fig. 4.11. All three velocity variances are zero in the geostrophic region due to the imposition of the sponge layer and increase as altitude decreases. In the vicinity of the wall the variances dampen through the wall model impact. For all three components, the $U3$ configuration always shows higher values than $S3$, regardless of the distance to the ground, showing a higher fluctuation level with the unstructured mesh.

The momentum fluxes $\langle\overline{U'W'}\rangle$, $\langle\overline{V'W'}\rangle$, and the heat flux $\langle\overline{W'T'}\rangle$ are plotted in Fig. 4.12.

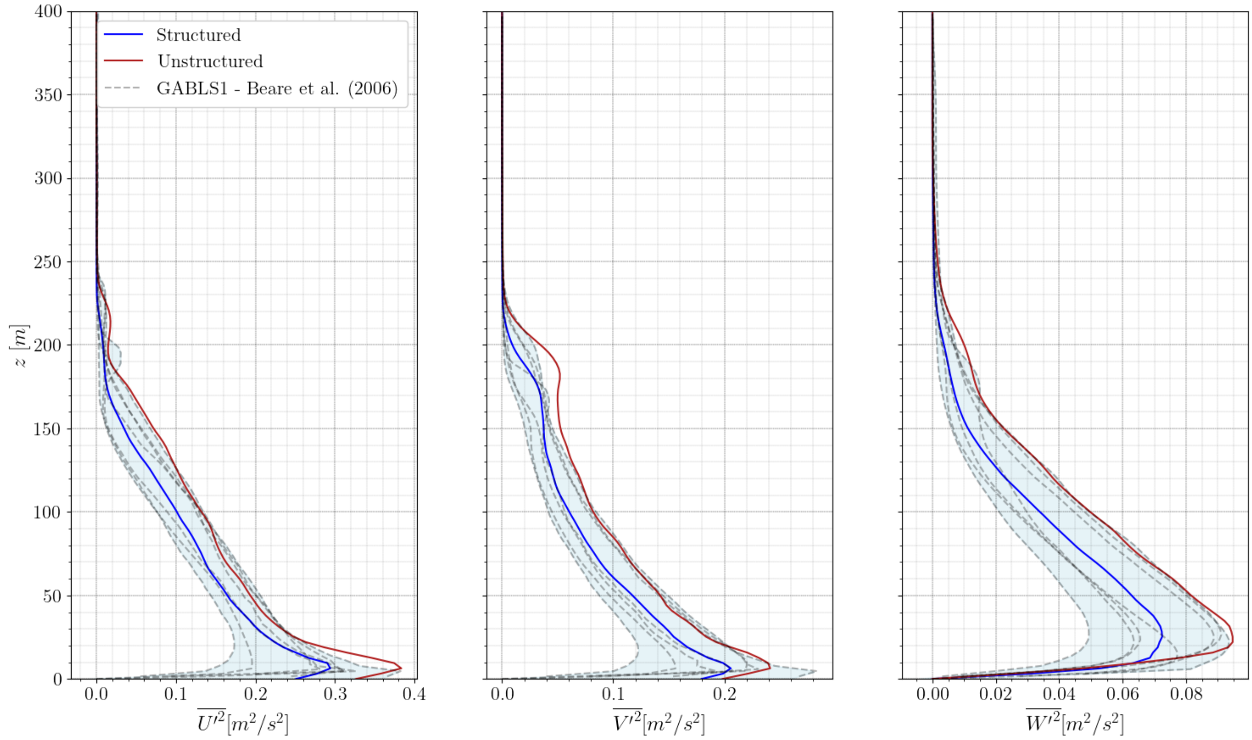

Figure 4.11: Streamwise, tangential and vertical velocity variances with $S3$ and $U3$ of cell size $\Delta x = 3.125\,\mathrm{m}$. Blue shading stands for the original GABLS1 study results dispersion [62].

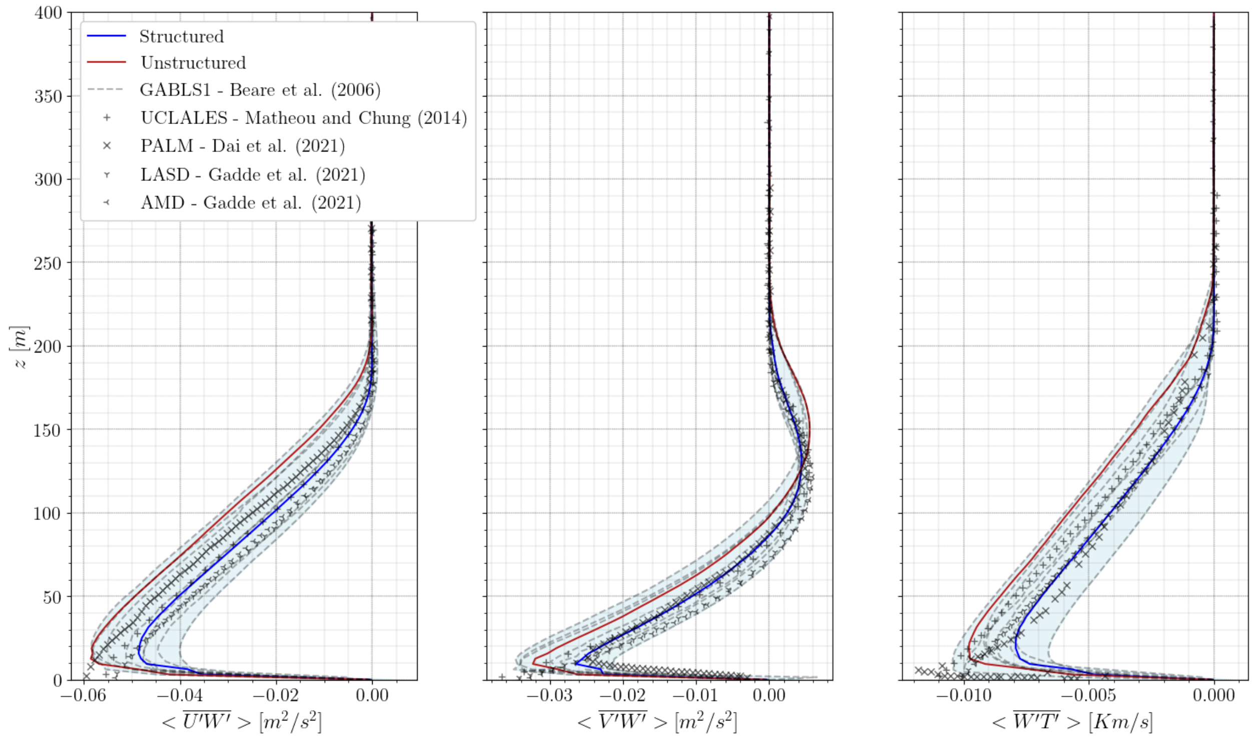

Figure 4.12: Momentum and heat fluxes for meshes $S3$ and $U3$ with cell size $\Delta x = 3.125\,\mathrm{m}$. Blue shading stands for the original GABLS1 study results dispersion [62] and symbols for more recent studies [118, 272, 275].

Similar global behaviour is observed for all fluxes. Nevertheless, a similar vertical offset for the $U3$ mesh compared to $S3$ is observed, here due to the higher level of fluctuations. These results are again well within the GABLS1 scatter and similar to recent studies.

In summary, both $S3$ and $U3$ simulations yield results similar to those of other studies, although differences are noticeable among them. Firstly, the $U3$ averaged temperature profile presents a lower temperature inflection. This gap is the source of the difference in the averaged velocity profiles. Secondly, a lower wall heat flux, but higher in norm, generates more turbulent kinetic energy and thus more velocity variances.

The gap in the heat flux profile might be the cause of the total wall heat flux time deviation. Indeed, a different momentum flux at the wall implies a different scalar flux, thus a different wall heat flux. Three causes have been identified for this phenomenon: the grid quality, the order of the numerical schemes, and the accuracy of the flux estimations. For grid quality, both grids have the same characteristic cell size, but not the same quality. As the $S3$ mesh is structured and possesses uniform hexahedron, its quality is good and homogeneous. In contrast, the $U3$ grid is unstructured and so each tetrahedron constituting the mesh can vary locally.

Grid quality can be evaluated via the skewness parameter, which measures the deviation between the existing cell and an optimal cell. Figure 4.13 shows the $U3$ grid skewness distribution. The $U3$ skewness is mainly arround 0.3, but reaches locally values of 0.96 with 0.5% of elements with a skewness higher than 0.8. Other unstructured meshes follow the same distribution. Spatial numerical schemes are known to commit interpolation and approximation errors while transporting the velocity and the temperature variables. Poor grid quality will increase these errors, leading to more numerical errors and therefore affecting the results.

Moreover, while YALES2 spatial numerical scheme are $4th$ order, this is only true on uniform and regular grid. Due to the cell size variations of the $U3$ mesh, this integration order drops, leading to a higher numerical error level, and thus may cause different flow behaviour. Finally estimating the flux at the wall is known to be quite an arduous task. For unstructured grids, the estimation becomes even more complex if the mesh is irregular, causing face-to-face flux irregularities related to the wall mesh. Because of these three sources of error, each grid-type simulation deviates from each other, ending on different wall fluxes and as a result different velocity and temperature fields.

However, it can be concluded that both structured and unstructured grid simulations correctly reproduce the SBL of the GABLS1 configuration. All quantities studied are within the data spread of previous studies. Minor differences between $S3$ and $U3$ have been highlighted particularly in the wall heat flux, and three sources of error have been highlighted: the grid quality, the order of the numerical schemes, and the accuracy of the flux estimation.

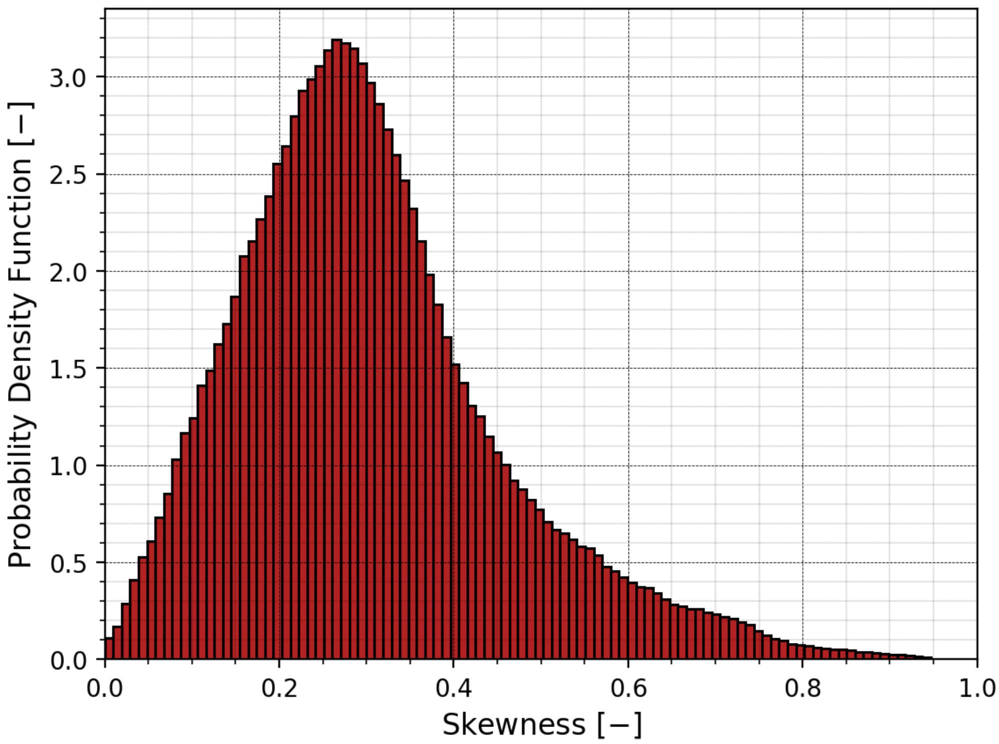

Figure 4.13: Probability density function (PDF) of the skewness distribution for $U3$ mesh.

Sensitivity to resolution

After assessing the impact of the use of unstructured meshes on a recommended mesh resolution, the impact of the grid resolution on the simulation results is now studied. Hence, a sensitivity to resolution study with a grid resolution varying from $\Delta x = 12.5\,\mathrm{m}$ to $\Delta x = 2\,\mathrm{m}$ is performed. Simulations are referred to as $S1$ to $S4$ and $U1$ to $U4$ for structured and unstructured grids, respectively. Each number corresponds to the resolution level according to Tab. 4.1.

Wall integrated quantities time series are shown in Fig. 4.14. All results behave similarly except for $U1$, which gives results that are irrelevant. Although the friction velocities for the structured grid simulations show slightly lower and more noisy values, the differences in the wall heat flux are more pronounced. Unstructured grid simulations show a greater heat flux with respect to the structured grids. This difference has an impact on the temperature, velocity, and flux profiles as seen in Section 4.4.3. However, finer meshes tend to converge to a similar value, although not perfectly matching, reducing the numerical diffusion and allowing for better gradient estimation. This behaviour supports the destabilization process influence caused by numerical error as the source of the gap between the two grid types. For the Monin-Obukhov length, which is a more global variable, all simulations are nearly identical.

Figs. 4.15 and 4.16 show instantaneous velocity and temperature planes, respectively.

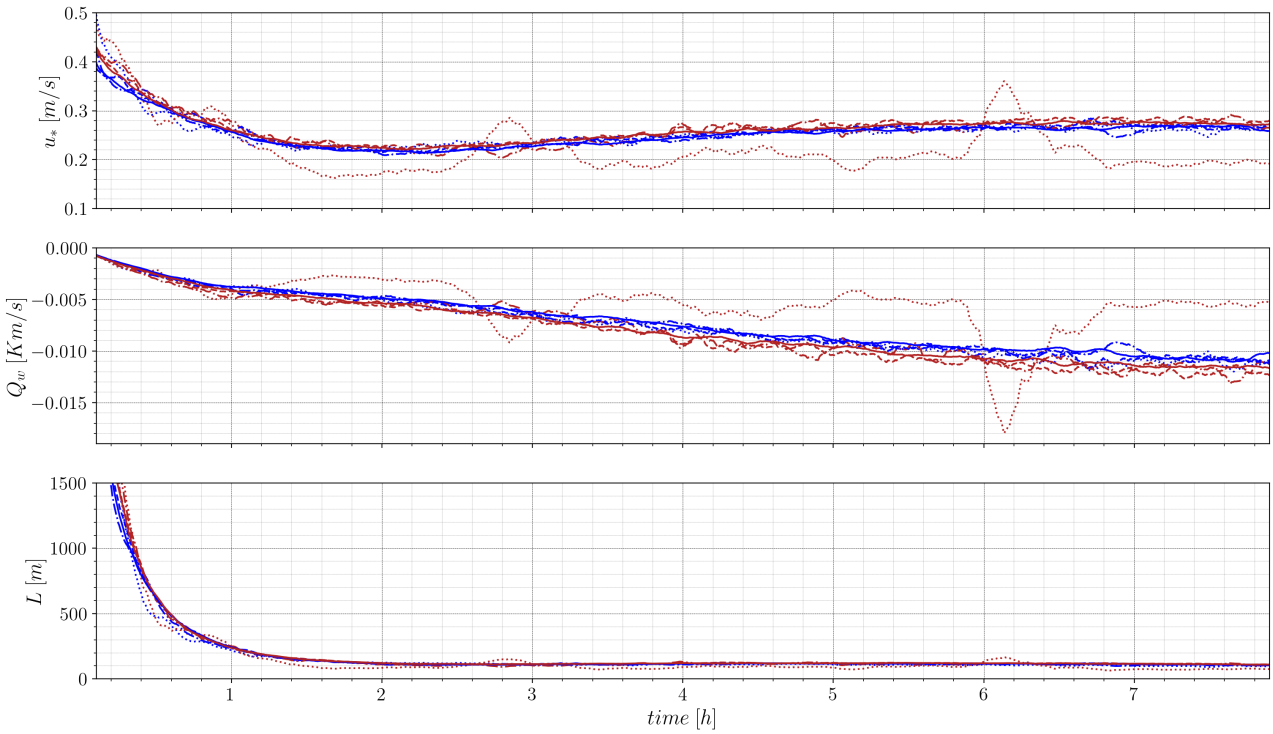

Figure 4.14: Frictional velocity, wall heat flux and Monin-Obukhov length time series. Blue and red lines stand for structured and unstructured grids, respectively. 4 resolutions are plotted: $\Delta x = 12.5$ m (·····), $\Delta x = 6.25$ m (-·-·), $\Delta x = 3.125$ m (- - -) and $\Delta x = 2$ m (——).

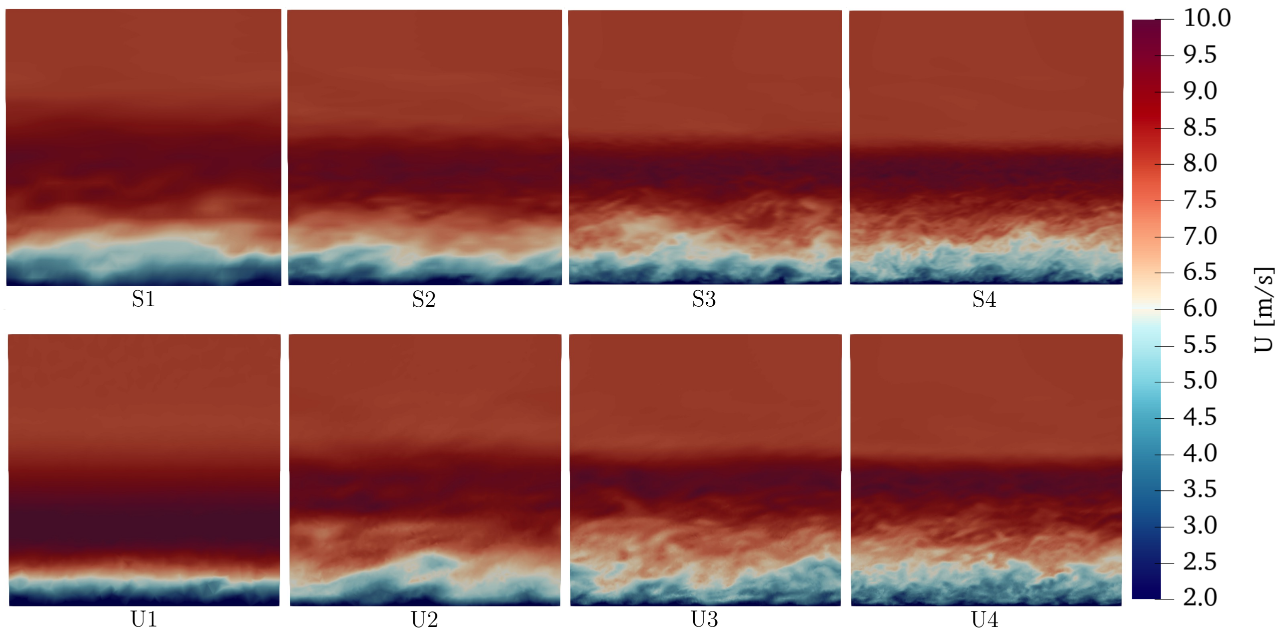

Figure 4.15: xz velocity planes at $y = 200$ m at $t = 8$h. Top: structured cases, bottom: unstructured cases. From left to right mesh resolution increases.

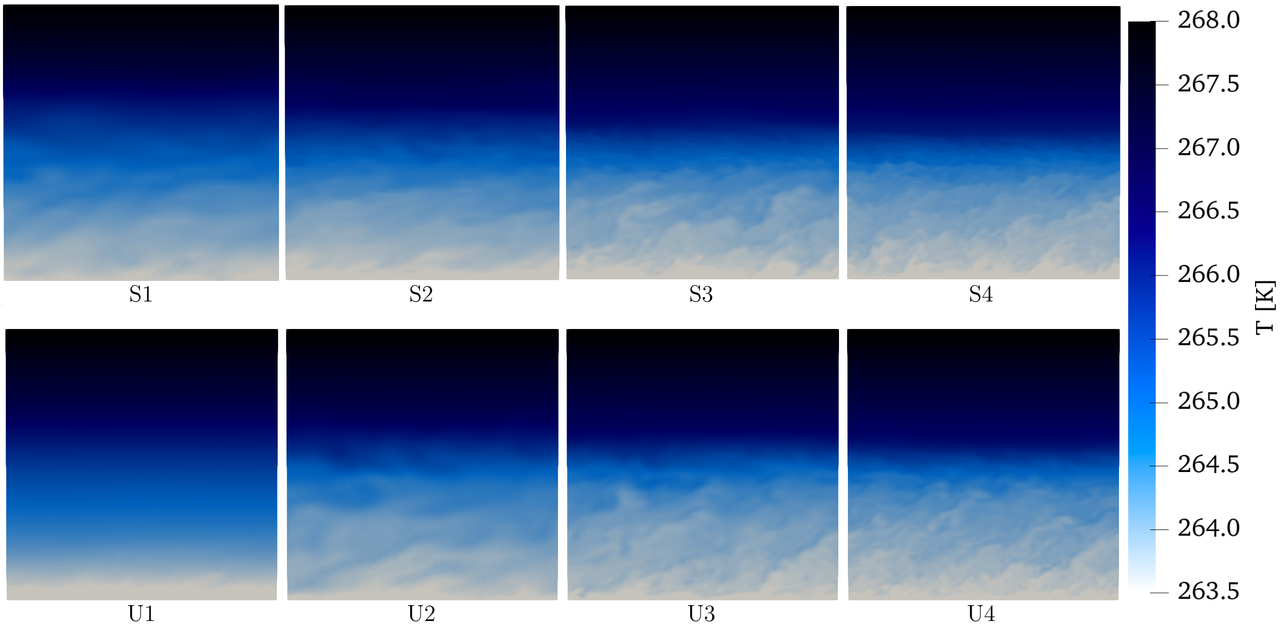

Figure 4.16: xz temperature planes at $y = 200\,\mathrm{m}$ at $t = 8\mathrm{h}$. Top: structured cases, bottom: unstructured cases. From left to right mesh resolution increases.

This qualitative display shows the impact of the mesh resolution on the flow. By refining, more vortices are captured. At a glance, there is a noticeable difference between the resolution levels, but not between the structured and unstructured cases.

Figure 4.17 presents the velocity and temperature profiles spatially averaged over horizontal planes and temporally averaged between the $7th$ and $8th$ hours. Again, except for $U1$, all other grids show similar behaviour. The trend highlighted in Section 4.4.3, where the unstructured grid has a temperature inflection above that of the structured case, is confirmed for all resolutions. The streamwise and tangential velocities return to the geostrophic wind at higher altitudes.

The momentum and heat flux profiles for all meshes are shown in Fig. 4.18. For all resolutions except the coarsest, the unstructured grids exhibit stronger fluxes. For the coarsest resolution, fluxes are near zero because the flow behaviour is far from expected with a boundary layer that no longer resembles a stable atmospheric layer. Fluxes are stronger with a finer mesh with both structured and unstructured grids. As expected, a finer grid is less dissipative and captures more turbulent kinetic energy. Again, the difference in wall heat fluxes leads to differences in momentum and heat flux profiles along the height. Stronger heat flux observed with the unstructured grid simulations leads to more fluctuations. Finally, all cases give satisfactory results except the structured and unstructured coarsest meshes, which will not be further considered into the analysis.

The boundary layer height was measured to assess the quality of the LES [62]. The

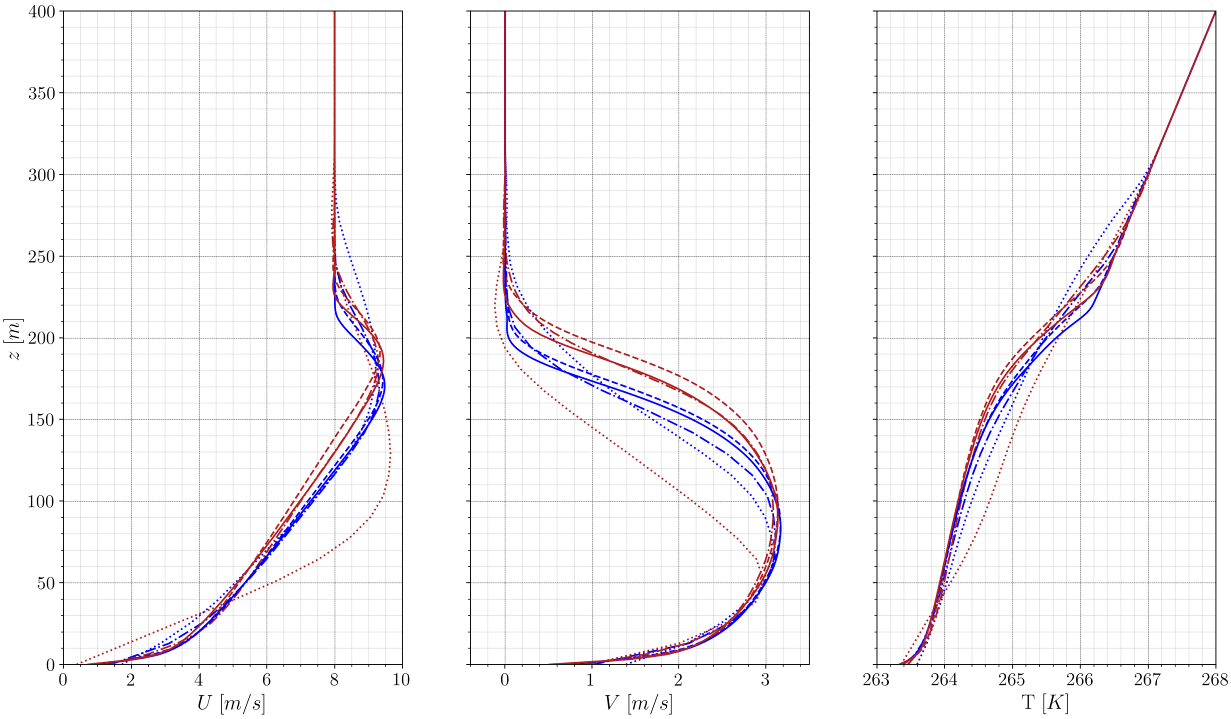

Figure 4.17: Averaged velocity and temperature profiles. Blue and red lines stand for structured and unstructured grids, respectively. 4 resolutions are plotted: $\Delta x = 12.5\,\mathrm{m}$ (·····), $\Delta x = 6.25\,\mathrm{m}$ (-·-·), $\Delta x = 3.125\,\mathrm{m}$ (- - -) and $\Delta x = 2\,\mathrm{m}$ (——).

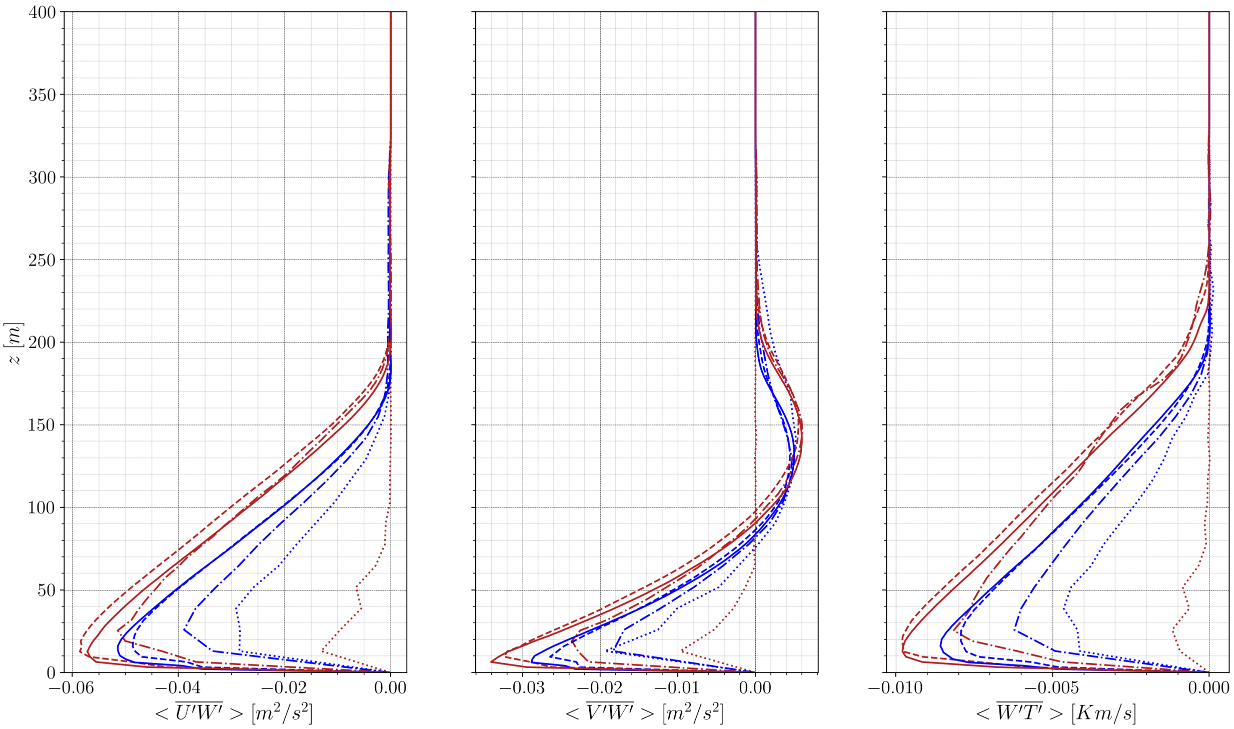

Figure 4.18: Average momentum and heat fluxes profile. Blue and red lines stand for structured and unstructured grids, respectively. 4 resolutions are plotted: $\Delta x = 12.5\,\mathrm{m}$ (·····), $\Delta x = 6.25\,\mathrm{m}$ (-·-·), $\Delta x = 3.125\,\mathrm{m}$ (- - -) and $\Delta x = 2\,\mathrm{m}$ (——).

Δx [m]	12.5	6.25	3.125	2
GABLS1 [62]	215	188	182	174
Cuxart et al. [277] - LES	-	-	177	-
Stoll and Porté-Agel [278]	-	-	173	-
Huang and Bou-Zeid [271]	-	-	-	158
Abkar and Moin [121]	168	165	169	-
Gadde et al. [118]	-	-	-	166 – 176
Min et al. [269]	-	-	160	-
Current work - Unstructured	149	180	186	179
Current work - Structured	149	163	162	161

Table 4.2: Boundary layer heights in various studies, depending on the grid resolution.

calculation of the boundary layer height is based on the turbulent stress [104]. Its disappearance means a transition to a non-turbulent layer, i.e. the top of the ABL. It is worth noting that the calculation of the boundary layer height is often based on the heat flux. However, it may be inaccurate if the heat flux is affected by gravity waves, which predominate at the top of the ABL. Following this definition, the SBL top height is defined as the one where the tangential turbulent stress is reduced to $\alpha = 5\%$ of its surface value. Linear extrapolation is then used to evaluate the boundary layer height:

$$h = \frac{z\big|_{\langle \overline{U'W'} \rangle = \alpha u_*^2}}{1-\alpha}. \tag{4.17}$$

Table 4.2 summarizes the boundary layer height from different studies with different codes and grid resolution. In both of our simulations as well as in other studies, the boundary layer heights tend to decrease with the grid resolution, converging towards $\sim 160 - 175$ m. This trend is due to more turbulent fluctuations being captured by a more refined mesh, as shown in Fig. 4.18. It should be noted that simulations based on unstructured grids provide a boundary layer that is 10% higher.

The original GABLS1 study [62] used their most refined mesh simulations, with a grid cell size of $\Delta x = 1$ m, as references. The average boundary layer height at this resolution is 157 m. Compared to this reference, all computations showing an ABL height difference of less than 20% are considered accurate. Following this criterion, both structured and unstructured grids present an accurate behaviour, i.e. from 3.8% to 2.5% deviation for the structured grid and from 18% to 14% deviation for the unstructured one. This is in line with the requirements advised by the original study: a minimum grid length of $\Delta x = 6.25$ m to obtain a stable boundary layer height accuracy of 20%.

Mesh type	Quantity	Δx [m] 12.5	6.25	3.125	2
Unstructured	$\langle U \rangle$	9.2	4.8	5.9	4.6
	$\langle T \rangle$	0.09	0.08	0.09	0.07
Structured	$\langle U \rangle$	5.3	2.9	2.7	1.9
	$\langle T \rangle$	0.09	0.06	0.05	0.03

Table 4.3: Relative L2 norm error in % of the horizontal average velocity and temperature profiles compared to the reference profiles from [62].

Quantifying the height of the boundary layer is essential but not sufficient. Although interesting, a similar boundary layer height does not reflect the global behaviour of the boundary layer or the amplitude of the over-speed region. To be more quantitative in this respect, another criterion has been used; the relative L2 norm error. The error is computed as:

$$\|x\|_2 = \sqrt{\sum_{k=1}^{n} |x_k|^2} \tag{4.18}$$

The simulation designed as a reference in [62] has been used as reference. The relative L2 norm error has been measured on horizontal average velocity and temperature profiles. The values are gathered in Tab 4.3. Excluding the coarsest meshes, the L2 norm error in streamwise velocity does not exceed 6%, while on temperature it remains below 0.1%. By refining the mesh, the L2 norm error decreases but is within an envelope, showing a grid convergence below $\Delta x = 6.25$ m. Overall, the results obtained are in very good agreement with the original study, demonstrating the validity of the methodology to correctly reproduce the stable atmospheric boundary layer dynamics.

4.4.4 Conclusions of the GABLS1 study

A high-order incompressible Navier-Stokes solver able to perform LES of a stable boundary layer on unstructured meshes was developed, which is not straightforward. It takes into account the Coriolis force, the Boussinesq approximation for buoyancy-driven flows, and the Monin-Obukhov similarity theory for wall modelling. This framework was validated against the GABLS1 setup. Time-averaged and variance of quantities such as velocity, temperature and fluxes were compared with structured and unstructured meshes of similar advised homogeneous cell size $\Delta x = 3.125$ m. Very good agreement was obtained with both meshes compared to the initial and more recent studies. Minor differences between the two setups were highlighted: the unstructured grid produces slightly more numerical diffusion of the temperature scalar than the structured grid.

Moreover, gradient estimation is also more difficult in the unstructured formalism, leading to a less accurate prediction of the flux. As a consequence, the destabilization of the stable boundary layer occurs differently, resulting in a slight gap between the results at the end of the simulation. The boundary layer height is 10% higher with the unstructured grid, with stronger velocity variances such as momentum and heat fluxes. However, these differences remain small compared to the range of results from other studies. It appears that sub-grid scale models [118], numerical methods [267,274], and grid resolutions [275] have more influence on the results than the use of an unstructured grid.

A sensitivity to grid resolution study was also performed. The boundary layer height was measured and showed that a grid length of $\Delta x = 6.25\,\mathrm{m}$ is sufficient to obtain a 20% accuracy. The relative L2 norm errors of streamwise velocity and temperature profiles to a reference high resolution study were also calculated for both structured and unstructured grids with less than 6% for both meshes. Thus, a $\Delta x = 6.25\,\mathrm{m}$ grid size for structured and unstructured meshes is sufficient to produce a simulation with reasonable accuracy, but a $\Delta x = 3.125\,\mathrm{m}$ grid size is ideal for a robust LES.

To conclude, properly reproducing a stable boundary layer using an unstructured grid has been performed for the first time to the author's knowledge. More geometrically complex cases will then be investigated where structured grids are unqualified like complex terrain simulations.

4.5 Conclusion

This chapter first reviews the development of the atmospheric solver on the YALES2 platform. Then it is applied to neutral, unstable, and stable boundary layer configurations. The atmospheric solver takes into account the Coriolis force, the Boussinesq approximation for buoyancy-driven flows, and the Monin-Obukhov similarity theory for wall modelling. The atmospheric solver successfully reproduces all three boundary layers. The results are validated against other studies and show good agreement. In addition, it has been shown that unstructured grids can be used to simulate stable boundary layers. Although it is not necessary to mesh a cubic domain, it may become valuable when studying complex terrains. Reproducing realistic topography relies on the use of unstructured grids, as structured grids cannot reflect complex geometries.

In this study, it was highlighted that a fine mesh is required to properly reproduce a stable boundary layer. This is due to the SBL reduced turbulence and height, which produces vorticies with smaller characteristic sizes. This limitation is especially true for unstructured meshes for which the numerical errors appear to be higher. In particular, it is harder to accurately estimate the fluxes at the wall. However, large-eddy simulation is already an expensive technique for studying wind turbines. Optimising the cost-fidelity trade-off becomes a notable issue. This objective is to be pursued in the next chapter.

Chapter 5

A new adaptive mesh refinement strategy for wind turbine application

Large-eddy simulation is an expensive technique for studying wind turbines. To accurately predict the flow behaviour most of the turbulence has to be resolved. To do so, the grid is refined. However, refinement comes at the expense of an increase in computational cost. A cost-fidelity trade-off is to be found. Its optimisation is of importance. In Section 5.2, a methodology is developed to decrease the simulation cost while maintaining the same physical precision. The tracking of the wind turbine wake is performed using a progress variable with a source term in the rotor region. Adaptive mesh refinement is used to refine the mesh within the wake to capture smaller vorticies and improve the accuracy of the simulation. The AMR strategy is compared to a reference case with uniform cell size in a coarsely defined wake region. The results of the study are detailed in Section 5.3.3. Finally, the conclusions and the remaining work are detailed in Section 5.4. This work has been presented at the 2022 *TORQUE conference and is the subject of a publication [76].*

Contents

5.1 Introduction **122**

5.2 Methodology **123**

5.3 Application to yawed wind turbine wakes **124**

5.3.1 Context 124

5.3.2 Framework 124

5.3.3 Results 127

5.4 Conclusion **132**

5.1 Introduction

LES are performed on grid fine enough to correctly capture the large scale of the flow. Yet, as the grid gets finer, the computational cost increases. A compromise between cost and accuracy must be found. To alleviate this limitation, the Adaptive Mesh refinement (AMR) technique is used. AMR allows for dynamical adaptation of the mesh resolution during computation. This technique features the following advantages compared to refined static meshes:

- The adaptive approach requires less a-priori knowledge of the solution.
- It requires significantly less meshing human efforts.
- It allows to save computational elements and thus reduce the computational cost.

AMR is widely used in CFD to simulate a broad range of physical phenomena where local refinement is required, such as in shock waves [279], flame front [217], bluff body wakes [280], two-phase flows [281]. To the authors' best knowledge, only scarce literature exists concerning AMR methods applied to wind turbine problems. Similarly to atmospheric flow simulation, studies use structured grids. Most of the literature includes strategies based on Cartesian grids in which the mesh is locally refined based on the global truncation error solution as in [282–284]. Kirby et al. [284] proposed a mesh composed of two parts where the adaptation is performed only on the Cartesian off-body mesh region while the region close to the bodies is fully unstructured. In contrast to these investigations, the strategy relies on the use of fully unstructured conformal tetrahedral LES grids to cope with both geometrical and unsteady effects, either due to the turbulent nature of the flow or the change of the wind turbine operating condition (i.e. turbulence, wind turbine movement, etc.). The use of unstructured meshes is also driven by their value when studying complex terrains. The strategy could be used at the latter stage to study wind turbines in a complex terrain.

In a previous work [285], the goal was to use AMR to generate Eulerian elements only where flow physics requires a finer mesh. In wind turbine simulations, it corresponds to wind turbine wakes. For that, a physical criterion was introduced to detect the area of interest and calculate the target cell size required to capture the flow physics. This work limitation was that the strategy did not work under turbulent inflows. Indeed, the criterion was based on the velocity gradient and thus activated in the wake and all turbulent regions of the computational domain. This led to a very expensive mesh. Here, this work is extended while focusing on the detection part. To detect wind turbines wakes, several methods are used in the literature [286–289]. It is typically used to track the position of the wake for turbines with yaw misalignment. These techniques are based on linear/angular impulse, velocity/momentum deficit and available power in the flow for run-time tracking of the wake centerline. These wind turbine wake detection methods are mainly limited by two factors: computational cost and accuracy in highly turbulent conditions. Thus, a new wake detection method is developed, satisfying both issues. Once the wake is adequately detected, the AMR strategy is applied within this envelope without impacting the other turbulent regions of the domain.

5.2 Methodology

The methodology developed is divided into three parts: detection to capture the wake, definition of the target mesh size, and adaptation frequency.

• **Detection:** To properly capture wind turbine wakes a strategy based on a progress variable ϕ is ued. A progress variable is a passive scalar with a source term transported on the Eulerian grid. Here, the source term is nonzero in the cylinder inscribed in the rotor region. The transport equation for a progress variable ϕ is

$$\frac{\partial \rho \phi}{\partial t} + \nabla \cdot (\rho \mathbf{u} \phi) = \nabla \cdot (\rho D_\phi \nabla \phi) + \dot{\omega}_\phi \,, \tag{5.1}$$

where ρ is the density, $\mathbf{u}$ the local velocity on the Eulerian grid, D_ϕ the diffusion coefficient of the variable and $\dot{\omega}_\phi$ its source term. A representation of the progress variable can be seen in fig. 5.1. This method captures the instantaneous wake. To have an average wake position, at every fluid iteration, the progress variable is overlayed with the previous one, leading to a 3D field called $\widehat{\phi}$. In other words, a threshold method is applied: $\phi > 0.1$ leads to $\widehat{\phi} = 1$. Since $\widehat{\phi}$ is never reset, the wake envelope only grows and converges to an area where the wind turbine wake is located. The $\widehat{\phi}$ quantity follows:

$$\widehat{\phi}(\mathbf{x}, t + dt) = \max\left(\widehat{\phi}(\mathbf{x}, t), \phi^\star(\mathbf{x})\right) \text{ with } \phi^\star(\mathbf{x}) = \begin{cases} 1, & \text{if } \phi(\mathbf{x}) > 0.1 \\ 0, & \text{if } \phi(\mathbf{x}) \leq 0.1 \end{cases} \tag{5.2}$$

Figure 5.1 shows that the instantaneous ϕ plane is highly turbulent and exhibits pockets while $\widehat{\phi}$ covers a larger area containing any wake position. Given that turbine spacing in wind farms usually falls within the range of 3 to 10 rotor diameters [34], the authors chose to stop the wake analysis, and thus $\widehat{\phi}$, at $6D$ downstream of the wind turbine. Likewise, the $\phi = 0.1$ value seems arbitrary and questionable, but testing different values has shown no significant influence on the wake envelope.

• **Mesh size:** To properly capture the flow physics, the cell size should depend on it. Since this work has already been performed [285] and for simplicity purposes, the cell size is imposed as a user-dependent target value. A future task will be to assemble both works.

• **Frequency:** AMR is occurring iteratively. The adaptation is triggered when the current mesh is too far from the objective mesh. To this end, a metric error is measured on each control volume as the local ratio between actual and target cell sizes. When this ratio exceeds

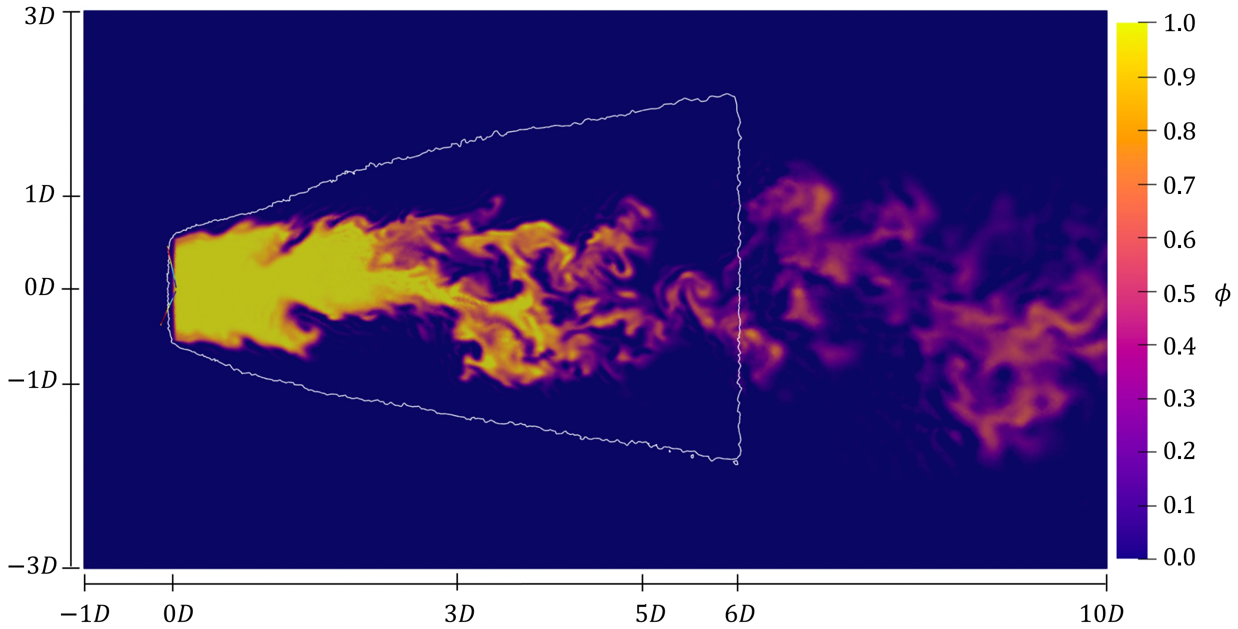

Figure 5.1: Mid-place passive scalar ϕ field highlighting the wind turbine and $\widehat{\phi} = 1$ iso-contour (in white) representing the mesh refinement envelope

a specified threshold value, 50%, on a sufficiently large number of elements, 0.2%, the AMR is triggered. In other words the AMR is triggered when 0.2% elements will have an error superior to 50%.

5.3 Application to yawed wind turbine wakes

5.3.1 Context

To validate this approach, two configurations are investigated. One is a single wind turbine case with dynamic yaw misalignment. The second case is based on the first one, with the addition of a downstream aligned wind turbine. For both configurations, two methodologies are compared. The reference case is computed on a mesh with a large refined area over the turbine position and the supposed wake position. The second case is based on the AMR strategy introduced in this work, where the mesh is progressively optimized during the simulation.

5.3.2 Framework

Wind turbine modelling

In this work, the modeled wind turbine is the academic DTU10MW [290]. This turbine follows the technological evolution of offshore wind turbines, for which the rotor reaches diameter values of $100 - 200$ m. In the following, all quantities are scaled by the wind turbine diameter $D = 178.3$ m. The blades use multiple airfoils along the span with variable chord and twist [290].

The deformation of the blades is not taken into account in this study, which implies a strong hypothesis on the loads computation. With this hypothesis, the choice was to use the non-prebended blades with the designed cone angle of 2.5°. The rotation speed is imposed for the upstream wind turbine to obtain the design tip speed ratio $\lambda_{opt} = 7.5$, giving a Reynolds number of approximately $Re_{tip} \approx 6 \times 10^6$ at the blade tip. The DTU10MW controller developed in [290] is applied to the downstream wind turbine to obtain consistent results. The rotor blades are modeled with the Actuator Line Method 3.3.2. The lift C_L and drag C_D coefficients are obtained from the tabulated airfoil properties [290]. Each blade is discretized using 50 sections, i.e 50 points per actuator lines.

Turbulence injection

As developed in Section 2.2.4, turbulence injection is a key parameter for high-fidelity wind turbine simulations. Different turbulent inlet boundary conditions for LES exist. Here, the precursor method was chosen. A single pre-processing computation is needed for every case in every configuration and thus reduces the global computational cost. The precursor computation is a half-channel flow of height H with periodic inlet and outlet boundary and a wall model at the bottom. It is driven using a constant pressure gradient forcing Eq. 5.3, where u_τ is the wall friction velocity.

$$\left(\frac{dP}{dx}\right)_f = \frac{u_\tau^2}{H} \tag{5.3}$$

It simulates a velocity profile similar to that in Eq. 5.4 where the roughness length is here taken as $z_0 = 0.02\,\text{m}$ and $\kappa = 0.41$. u_τ is determined so that u_{ref} is near $10\,\text{m/s}$ at hub height ($z_{ref} = 119\,\text{m}$).

$$u(z) = \frac{u_\tau}{\kappa} \log\left(\frac{z + z_0}{z_0}\right) \tag{5.4}$$

2D cross-flow planes are then injected into the wind turbine computation as inlet velocity, accounting for turbulence and vertical logarithmic law velocity profile. Velocity profile and Turbulent Intensity (TI) are shown in Fig. 5.2. The velocity profile shows good agreement between the theoretical and actual velocity profiles observed in the precursor computation. At hub height, the mean velocity, which will be called u_{ref} is $10.5\,\text{m/s}$. The streamwise turbulent intensity is near 10% at hub height. The transverse turbulent intensity has a similar appearance with a lower value. At the bottom, the vertical turbulent intensity is minimum because of the boundary but near 5% at hub height.

Configuration

The methodology is applied to two configurations involving the DTU10MW [290] wind turbine. Configuration (A) investigates a single turbine with a time-varying yaw misalignment defined in Eq. 5.5. In configuration (B) a second wind turbine is added downstream the first turbine

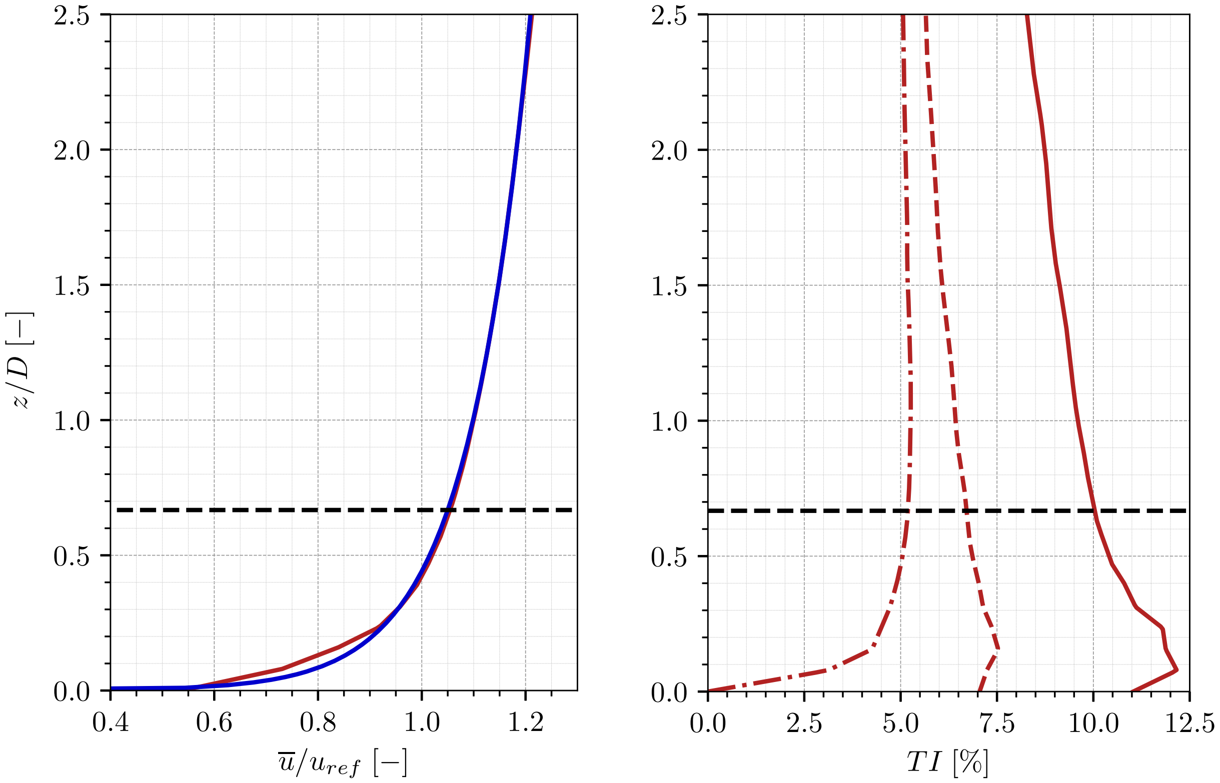

Figure 5.2: Velocity profiles and precursor turbulence intensity, zoomed in rotor region. Left : (—) for the precursor simulation, (—) for the theoretical velocity profile. Right : (—) for $\mathrm{TI_X}$, (- - -) for $\mathrm{TI_Y}$ and (-·-·) for $\mathrm{TI_Z}$. (- - -) for the rotor hub position.

operating with a dynamic yaw misalignment.

$$\gamma = 15 \sin\left(\frac{\pi}{60} \times t\right) \tag{5.5}$$

The AMR methodology is compared to a reference case (refine REF) with uniform cell size in the wake region for both configurations. Figure 5.3 presents the mesh for both AMR and REF cases. Wind turbines are indicated as T for the configuration (A) and as $T1$ and $T2$ respectively for the upstream and the downstream wind turbine for the configuration (B). The domain is a $14D \times 10D \times 10D$ box for case (A) and $18D \times 10D \times 10D$ for case (B), with a $6D$ distance between both turbines. Such dimensions allow to properly study the wake and to prevent confinement effect due to the boundary proximity [75, 291, 292]. For both configurations, two regions are refined: the wind turbine wake and the rotor region. The wind turbine wake region is refined to capture the flow physics adequately. As said in section 5.2, for simplicity purposes, a user-dependent target cell size is imposed, which will be constant in the wind turbine wake region. The rotor region is refined to mollify the Gaussian kernel properly. As mentioned in section 5.3.2, the Gaussian kernel width depends on the mesh, and thus, more

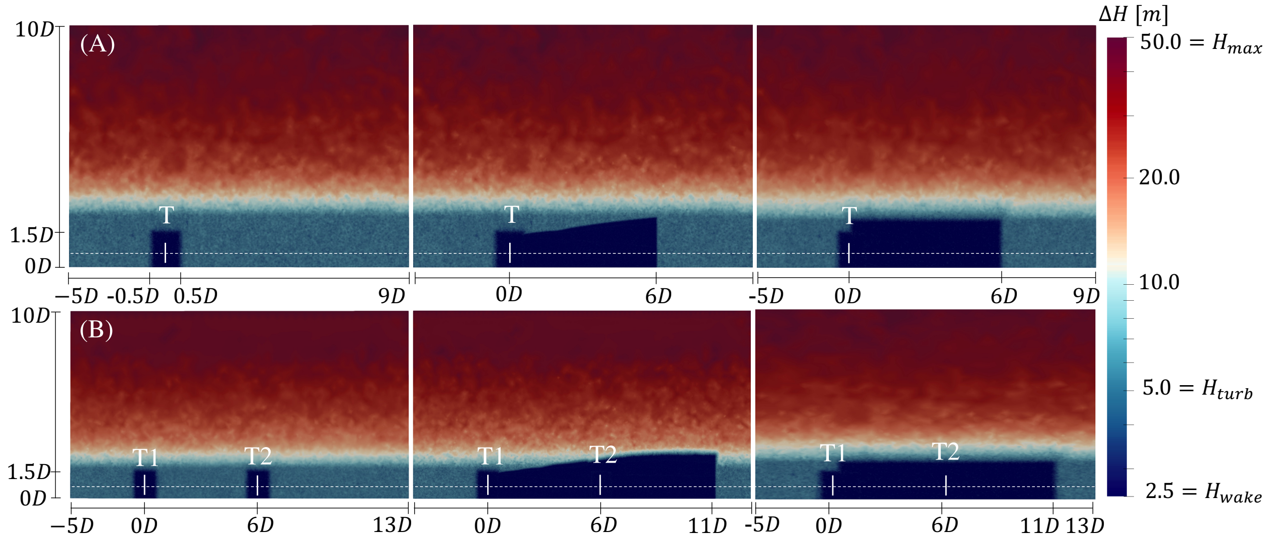

Figure 5.3: Mid-plane visualisation of the meshes with configuration (A) at the top and configuration (B) at the bottom. From left to right : initial AMR mesh, final AMR mesh, REF mesh.

refined mesh results in a smaller kernel size.

A third case, named coarse REF, is computed to measure the sensitivity of the results to mesh resolution. Its cell size is twice the one of the refine REF in every three directions. It is, therefore, a mesh with eight times fewer elements.

5.3.3 Results

Flow dynamics analysis

For configuration (A), the mesh goes from 76.8 to 134 million tetrahedrons, while the REF mesh contains 160 million elements. For configuration (B), the mesh goes from 83 to 290 million elements, while the REF mesh has 500 million tetrahedrons.

In the rotor region the cell size is $\Delta h_{rotor} = 2.5\,\mathrm{m}$ leading to 72 points per blade discretization. The cell size is the same for the wake region. The background cell size at hub height is twice bigger: $2\Delta h_{rotor}$. This cell size is the minimum required, according to the Shannon sampling theorem, to capture the precursor inflow velocity and turbulence properly. In the vertical direction, the mesh size increases linearly, up to $20\Delta h_{rotor}$. As mentioned in section 5.3.2, coarse REF mesh size is twice as larger as the finer REF. Therefore, the cell size in the refined region is $2\Delta h_{rotor}$ while the background cell size at hub height is $4\Delta h_{rotor}$.

Each case in each configuration is performed in two parts. The first is the convergence part, where the flow reaches a "steady" state; during this part, the inlet turbulence and the generated wind turbine wakes are slowly transported in the domain. Once convergence is

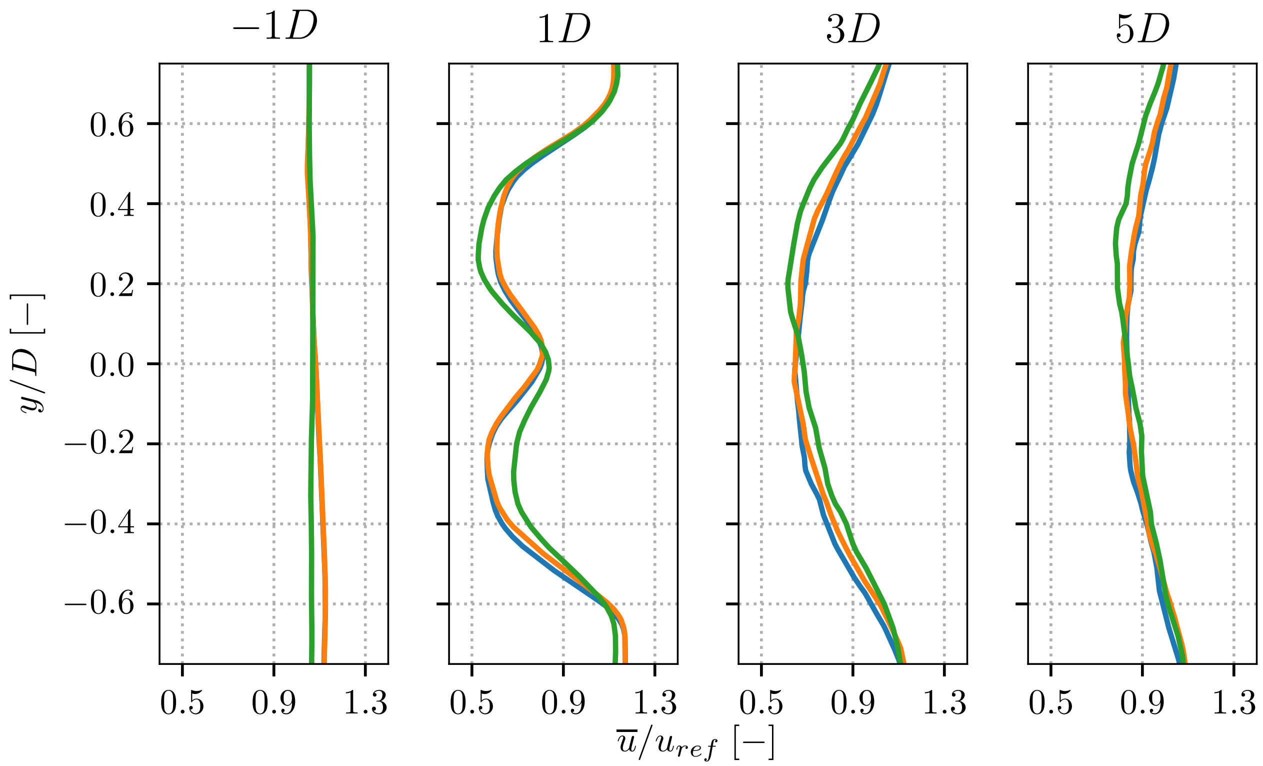

Figure 5.4: Mean streamwise velocity at hub height at various stream position in transversal (y) direction for (A) configuration. (—) for the AMR, (—) for the refine REF and (—) for the coarse REF.

achieved, the second part consists in accumulating statistics over the flow quantities. For the AMR case, the first part also allows to obtain a converged wake envelope and, consequently, to refine the mesh in the wake area. During the statistic accumulation time, the adaptation process isn't triggered anymore. At every iteration, the wind turbine wake is within the wake envelope. Therefore, statistical accumulations are made on a constant mesh.

Fig. 5.4 and Fig. 5.5 present the behaviour of the time-averaged streamwise velocity in transversal direction at various streamwise positions for both (A) and (B) configurations, respectively. The three cases (AMR, refine REF and coarse REF) mean velocity profiles present a good agreement: only minor discrepancies can be observed in the downstream region. The mean streamwise velocity profiles indicate that the wake velocity deficit recovers at a similar position in the three cases. The relative L2 norm error on horizontal mean velocity profiles quantifies the discrepancies to the refine REF case set as the reference case. Results are shown in Tab. 5.1. For the (A) configuration, the AMR case has an error smaller than 1%, while the coarse REF case has around 18%. For the (B) configuration, the AMR case has an error of around 2.4%, while the coarse REF case has around 10%.

The L2 norm error reaches 1.4% for the AMR case and 19% for the coarse REF case on mean vertical streamwise velocity profiles. Since vertical and transverse direction velocities

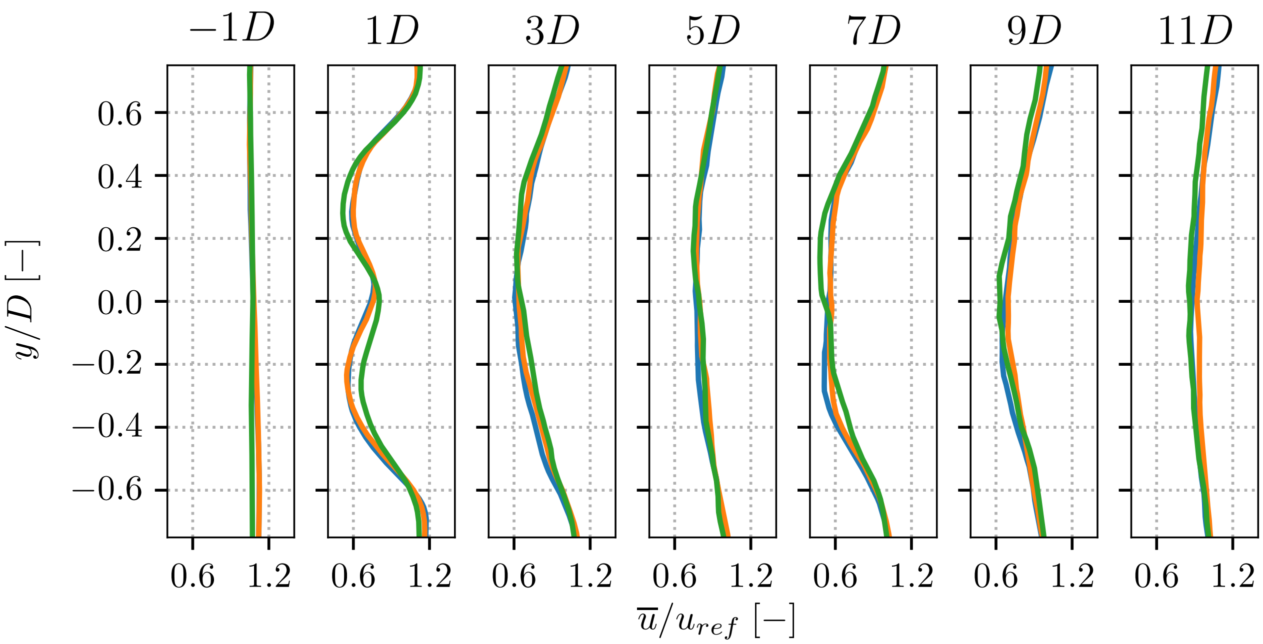

Figure 5.5: Mean streamwise velocity at hub height at various stream position in the transverse (y) direction for (B) configuration. (—) for the AMR, (—) for the refine REF and (—) for the coarse REF.

show similar results, profiles are not shown here for the sake of brevity. These results prove that the AMR strategy leads to quasi-identical time-averaged velocity.

Another measured quantity is the Turbulent Kinetic Energy (TKE), calculated as:

$$TKE = \frac{1}{2}\left(\overline{u'^2} + \overline{v'^2} + \overline{w'^2}\right) , \tag{5.6}$$

where u', v' and w' are the fluctuations of the three velocity components. The TKE can have many sources, such as fluid shear, friction, and buoyancy. The turbulent kinetic energy is then transferred down the turbulence energy cascade and dissipated by viscous forces at the Kolmogorov scale. Therefore, the mesh size should influence the TKE.

Figures 5.6 and 5.7 present the behaviour of the TKE in the transverse direction for the configurations (A) and (B), respectively. The AMR and refined case TKE profiles exhibit similar trends in both configurations. However, the coarse REF case TKE is significantly weaker. The results are shown in Tab. 5.1. The AMR case shows an error around 5.5% while the coarse REF case reaches 60% for the configuration (A). For the configuration (B), a similar behaviour is observed. The AMR detection strategy demonstrates its reliability with these low differences in TKE, which can be complex to predict.

The similar results between the AMR and refined REF cases showed that they both have the same precision. On the other hand, the coarse REF case shows moderate deviations in the

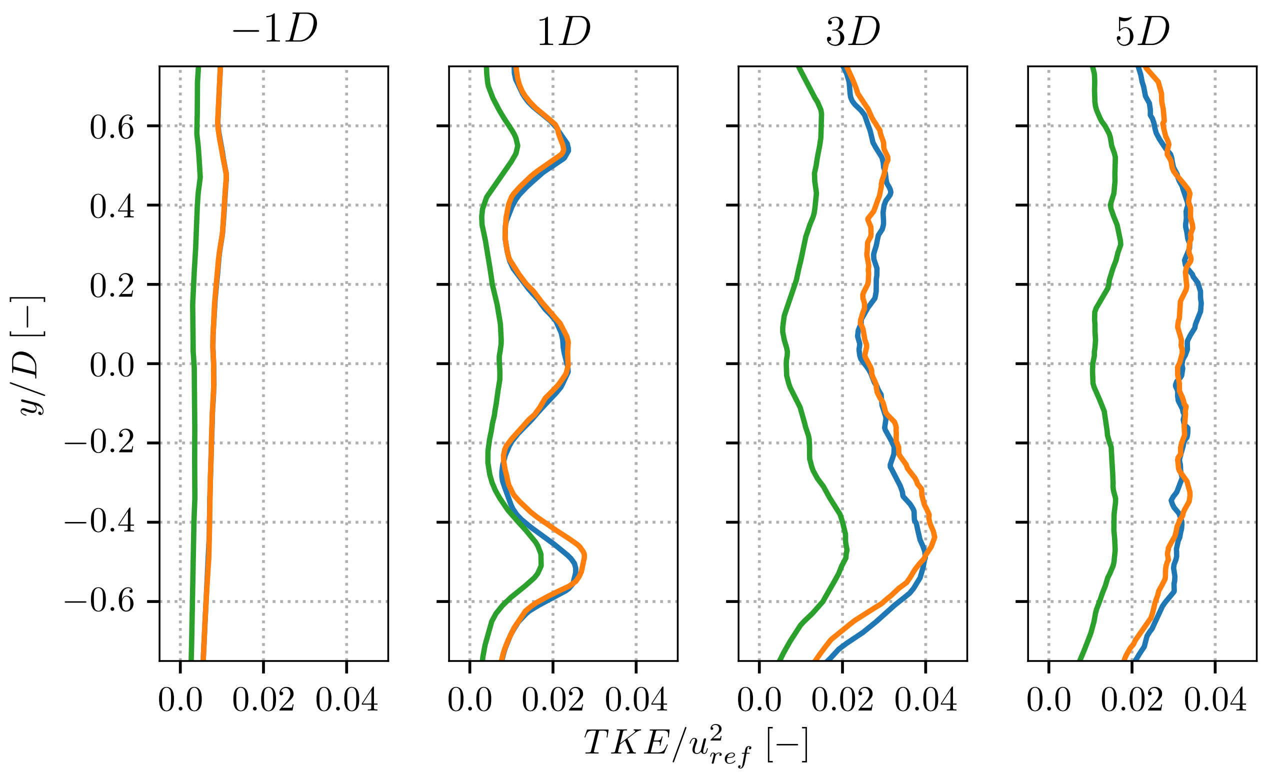

Figure 5.6: TKE at hub height at various stream position in the transverse (y) direction for (A) configuration. (—) for the AMR, (—) for the refine REF and (—) for the coarse REF.

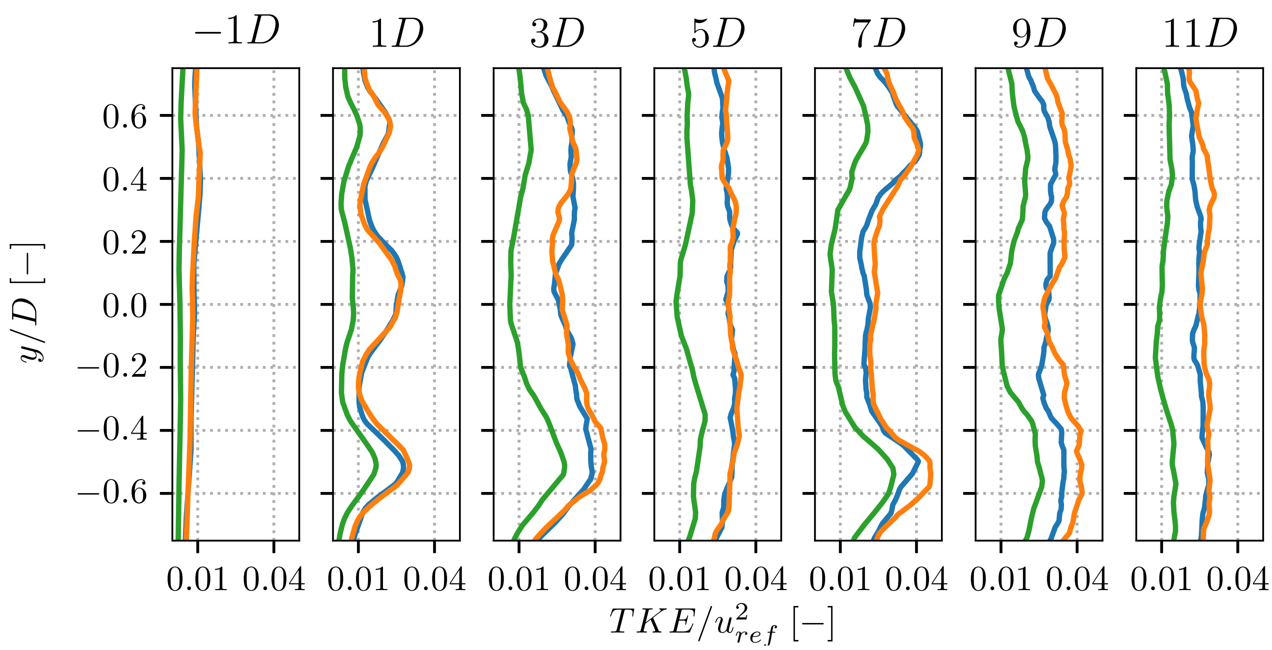

Figure 5.7: TKE at hub height at various stream position in the transverse (y) direction for (B) configuration. (—) for the AMR, (—) for the refine REF and (—) for the coarse REF.

Config	cases	$\overline{u}_y$ [%]	TKE [%]	ΔC_P [%]	ΔC_T [%]
(A)	AMR	1	5.5	0.8	0.18
	coarse REF	18	60	4.2	1.37
(B)	AMR	2.4	11.3	0.77	0.23
	coarse REF	10	72	3.7	1.57

Table 5.1: relative L2 norm error recapitulation table for mean velocity, TKE, power and thrust coefficient of both AMR and coarse REF cases, compared to the refine REF, in both (A) and (B) configuration.

mean velocity and strong discrepancies on the TKE. Therefore, results are strongly sensitive to the mesh resolution and sufficient refinement is needed for the physical precision.

The power coefficient, C_P, and the thrust coefficient C_T, defined as Eq. 5.7, are also compared. Results are shown in Tab. 5.1. For the configuration (A), coefficients difference between the AMR case and the refine REF case respectively are $\Delta C_P = 0.8\%$ and $\Delta C_T = 0.18\%$. The refine REF case and the coarse REF case, respectively, are $\Delta C_P = 4.2\%$ and $\Delta C_T = 1.37\%$. The configuration (B) shows similar results. Thus, the AMR and the refine REF cases have similar results, while the coarse REF tends to be less precise.

$$C_P = \frac{P}{\frac{1}{2}\rho A U_{h,\infty}^3} \quad \text{and} \quad C_T = \frac{T}{\frac{1}{2}\rho A U_{h,\infty}^2 R} \tag{5.7}$$

Computational cost comparison

Mesh adaptation is applied to reduce the mesh size and thus the computational cost. The computational cost comparison is performed for both the convergence and the statistic accumulation. The computational performances are summarized in Tab. 5.2.

For the configuration (A), refine REF case costs 24.2 khCPU, while the AMR case costs 16.3 khCPU, leading to a 30% gain. Both the convergence part and the statistic accumulation part gain are similar. In the AMR case, a similar cost is found between convergence and statistic accumulation parts because the adaptation process represents only 6.9% of the computation time. This emphasizes that the mesh contains fewer elements at the beginning of the simulation before reaching its final state. For the configuration (B), the refine REF case costs 174 khCPU and the AMR case 83 khCPU, representing a 50% gain. The gain is here bigger due to the higher difference in the number of elements for the REF case: the mesh contains 42% fewer elements, while this gap was 16% on the (A) configuration. It must also be noted that the REF simulation had to be performed on more processors because of this difference in mesh size.

Config	cases	C/S	#elem [$\times 10^6$]	#proc	timestep [ms]	adapt time [%]	khCPU
(A)	REF	CONV	160	1024	32.2	-	12.1
		STAT	160	1024	32.5	-	12.1
	AMR	CONV	77-135	1024	46.2	6.9	8
		STAT	135	1024	45.0	0.0	8.3
(B)	REF	CONV	500	2048	40.8	-	80
		STAT	500	2048	41.0	-	94
	AMR	CONV	83-290	1024	34.5	4.1	45
		STAT	290	1024	45.8	0.0	38

Table 5.2: computational performances recapitulation table of both refine REF and AMR cases in both (A) and (B) configuration. Each (A) configuration simulation represent 720 s physical time while each (B) configuration simulation represent 1440 s physical time.

The computational cost difference is mainly due to two factors for both configurations: the mesh size and the timestep. The timestep is not imposed but computed via the CFL stability condition. A high skewness cell associated with a small cell size and a high local velocity leads to a smaller timestep. Both cases have a similar level of skewness, with a 0.8 maximum, but without the guarantee that these cells are in the same region, with similar cell size and local velocity. Therefore, a similar timestep for both configurations is not guaranteed. This difference is unfortunate because it prevents us from having a straightforward comparison between mesh size and computational cost. Nevertheless, the timestep difference cannot explain the computational cost difference on its own. The configuration (A) shows that for a 30% timestep difference, there is a 33% computational cost difference. The configuration (B) shows that for a 1.8% timestep difference, there is a 52% computational cost difference, which is therefore mainly due to a 42% mesh size difference. Thereby, AMR does decrease the computational cost and the mesh size. It also allows for a less user-dependent mesh which may imply better quality.

5.4 Conclusion

It has been shown that adaptive mesh refinement could minimize computational cost and, therefore, be useful in wind turbine computation for the same physical precision. The detection methodology is based on a progress variable transported in the wake with a source term in the rotor region. It allows to adequately capture the wind turbine wake within which the mesh is refined. Results have shown that the AMR case exhibits a similar physical precision for both single and two-turbines configurations as the REF case. Moreover, the AMR case showed a 30% computational cost reduction in configuration (A) and 50% in configuration (B). Therefore, this methodology coupled with adaptive mesh refinement has two advantages:

- Proper capture of the wind turbine wake and an accurate wake envelope definition.
- Cost reduction for the same physical precision.

And can be used in wind turbine simulations.

Chapter 6

Realistic wind turbine studies

In Chapter 4, the modelling of atmospheric boundary layers under the three thermal configurations has been validated. In Chapter 5, a new adaptive mesh refinement strategy has been developed for wind turbine simulation, enabling the optimisation of the computational cost for such simulation. This chapter assembles both previous work to enable the study of wind turbines in realistic environments. First, Section 6.1 covers the study of a wind turbine under realistic atmospheric conditions. Based on the experimental and numerical benchmark named SWiFT, both neutral and stable configurations are studied. Finally, as an opening, Section 6.2 deals with the topic of complex terrain. The tools and methodology used to generate complex terrains are presented.

Contents

6.1 Atmospheric boundary layer impact on wind turbines 136

6.1.1 Presentation of the SWiFT benchmark 136

6.1.2 Methodology 138

6.1.3 Numerical setup 139

6.1.4 Neutral benchmark 140

6.1.5 Stable benchmark 149

6.1.6 Conclusion of the SWiFT benchmark 158

6.2 Complex terrain impact on wind turbines wake 160

6.2.1 Mesh generation 160

6.2.2 Application setup 162

6.2.3 Results 163

6.2.4 Conclusion 164

6.1 Atmospheric boundary layer impact on wind turbines

The tools requisite to perform non-neutral atmospheric boundary layer simulations have been developed and validated in Chapter 4. The impact of such atmospheric flows on a wind turbine can now be studied. This work is based on a well-known realistic benchmark called SWiFT (Scaled Wind Farm Technology) [293].

6.1.1 Presentation of the SWiFT benchmark

SWiFT is a facility funded by the United States Department of Energy, operated by Sandia National Laboratories and the National Renewable Energy Laboratory (NREL), and is hosted at the Texas Tech University National Wind Institute Research Center in Lubbock, Texas. In the region of the Great Plains, the site is assumed to be exempt from complex terrain-induced flow patterns. In the absence of weather phenomena, the atmospheric conditions at the SWiFT site approximate canonical diurnal cycles: the characteristics of wakes can be measured without the influence of complex terrain and weather [293].

To enhance comprehension of atmospheric boundary layer impact on wind turbine, NREL has organised an international exercise of code intercomparison based on this facility, i.e. the SWiFT benchmark. The benchmark is part of the International Energy Agency (IEA) Wind Task 31, which aims to develop an international wind farm flow modelling and evaluation framework. Different institutions took part in this benchmark, using different modelling approaches such as steady-state analytical models, DWM-type models, RANS and LES. This benchmark aimed to assess the capability of the different codes to reproduce the wake of a single wind turbine in an atmospheric inflow.

The turbine is a three-blade horizontal-axis wind turbine. The rotor diameter is $D =$ 27 m with a hub height of $z_h = 32.1$ m. To collect experimental data, a meteorological mast measures inflow conditions, sensors collected the wind turbine response, and a LiDAR (Light Detection And Ranging) instrument mounted on the nacelle measures the wind turbine wake at different locations downstream. A scheme of the experimental facility is shown in Fig. 6.1. The meteorological tower is located approximately 2.5D upstream of the turbine. The objective is to measure the flow coming onto the wind turbine, but also to categorise the flow in terms of stability. In that regard, several instruments are used at different heights:

- Sonic anemometers at 10 m, 18 m, 32 m, 45 m, and 58 m above the ground.
- Cup anemometers at 18 m, 31.5 m, and 45 m above the ground.
- Wind vane at 29.5 m above the ground.
- Two barometric pressure sensors at 2.5 m and 30 m above the ground.
- Three relative humidity sensors at 2.5 m, 30 m, and 56.5 m above the ground.
- Three air temperature sensors at 2.5 m, 30 m, and 56.5 m above the ground.

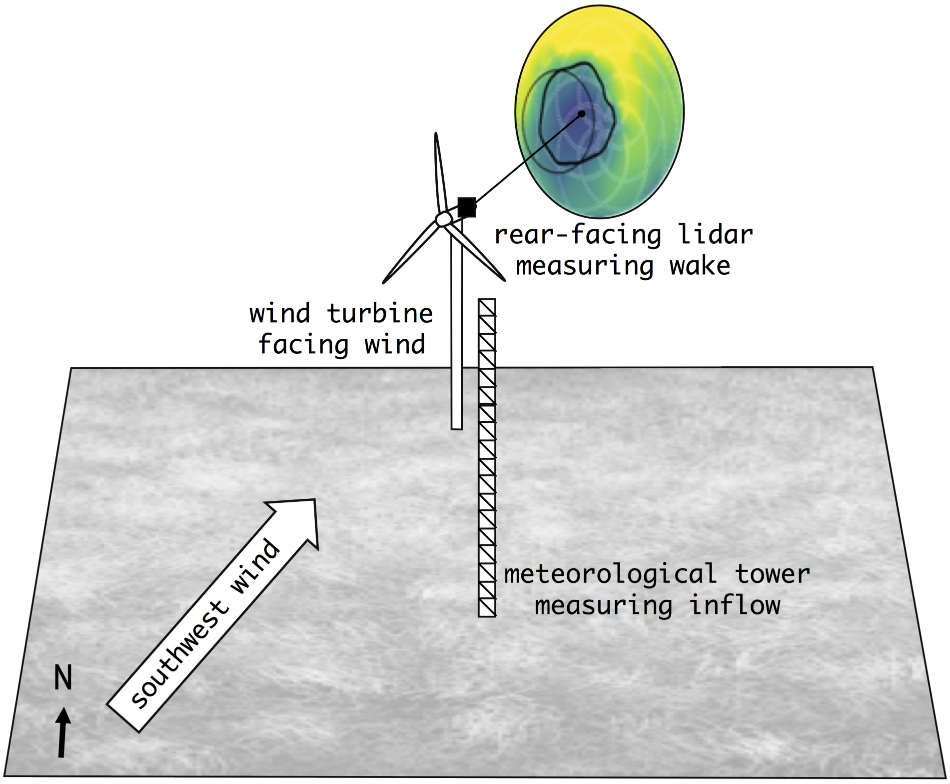

Figure 6.1: Schematic of the SWiFT facility used for this benchmark. From https://wakebench-swift.readthedocs.io.

Several quantities are diagnosed from these measurements. These quantities are computed over periods of $10-$ minute. Measurements occur over days. Individual $10-$ minute periods with similar atmospheric inflow were then combined to obtain average quantities. Based on the flow physics, three configurations were identified: a neutral stratification, an unstable stratification and a stable stratification. Six $10-$ minute periods with similar data were combined for each of these configurations, leading to three distinct benchmarks.

Wind turbine measurements are collected with the following sensors:

- Wind speed and direction sensor at the back of the nacelle.
- Yaw heading sensor.
- Generator power and torque sensors.
- Blade-pitch sensor.
- Loads measurements: Four strain gauges at the blade root, which give the flap and edge moments in the blade coordinate system

Finally, wake measurements are performed using the SpinnerLidar from the Technical University of Denmark (DTU), which characteristics are:

- Line-of-sight velocity (v_{los}) is measured in curved surfaces that span a large extent in y

and z but a small extent in x. In this benchmark, these curved surfaces are assumed to be $y - z$ planes at a fixed x distance downstream of the rotor.
- One plane of v_{los} is retrieved approximately every 2 s.
- Focal length was kept constant throughout the 10−minute measuring span. This provides high-frequency data from which to quantify the dynamic behaviour of the wake.
- Focal length cycled through several x values, typically between 1D and 5D. The temporal frequency is lower, but the wake evolution can be quantified as it propagates downstream.

6.1.2 Methodology

Each of the three SWiFT benchmarks is decomposed into three steps.

- **The inflow turbulence.** To assess the capacity of the different codes to reproduce the wake of a single wind turbine, it is necessary to reproduce the inflow conditions as accurately as possible. In this work, the inflow is generated using the precursor database method, developed in Section 2.2.4. However, unlike in Chapter 5 where the flow was driven by a constant pressure gradient forcing, in this work the flow is driven by the geostrophic wind. The atmospheric conditions obtained from the measurements are provided for each of the benchmarks. Data are gathered in Tab. 6.1. However, only several parameters have been measured and it is up to the participants to choose their parameters to reproduce as accurately as possible the inflow conditions.

- **The wind turbine response.** Four wind turbines variables are experimentally measured: thrust coefficient, power, torque, and rotational speed. The thrust coefficient is expressed as:
$$C_T = \frac{T}{\frac{1}{2}\,\rho\,A\,U_{h,\infty}^2}\ , \tag{6.1}$$
where T is the total thrust of the turbine, ρ the air density, A the swept rotor area and $U_{h,\infty}$ the streamwise velocity at hub height at a far distance from the wind turbine. In this work, the wind turbine is modelled using the actuator line method. The wind turbine rotational speed is imposed and set to the average measurement output.

- **The wind turbine wake.** The velocity deficit in the wake is computed using the same streamwise velocity at hub height $U_{h,\infty}$ as a reference velocity following:
$$\Delta U = \frac{U - U_{h,\infty}}{U_{h,\infty}} \tag{6.2}$$
The results are plotted as a function of the spanwise (y) variable. The velocity deficit is measured at four downstream positions: 2D, 3D, 4D, and 5D.

From these three neutral, unstable, and stable benchmarks, only two will be carried out in this study, the neutral and the stable benchmark. As stated before, the stable boundary

Variable	Notation	Unit	Neutral	Unstable	Stable
Horizontal inflow velocity	$\overline{U}_{h,\infty}$	[m/s]	8.7	6.7	4.8
Turbulence intensity	TI	[%]	10.7	12.6	3.4
Friction velocity	u_*	[m/s]	0.45	0.33	0.08
Stability parameter at $z = 10$m	$\zeta = z/L_{MO}$	[-]	0.004	-0.089	1.151
Kinematic vertical heat flux	$\overline{w'\theta'}$	[K.m/s]	-0.002	0.023	-0.005
Roughness length range	z_0	[mm]	$5 - 50$	$5 - 50$	$5 - 50$

Table 6.1: Atmospheric variables obtained from measurements. Data are averaged based on the three identified configurations.

layer is the most troublesome to model using LES due to its reduced turbulence and smaller vorticies characteristic sizes. As a result, this work will focus on neutral and stable benchmarks to ensure that this contribution is as relevant as possible. The results will be compared with the experimental measurements and the LES results of the original study [124] as well as the results of a subsequent LES study using the Meso-NH code [294].

6.1.3 Numerical setup

In the SWiFT benchmark, most of the parameters are left to the participant. The only specifications are those in Tab. 6.1. Therefore, the methods and parameters used vary greatly depending on the participants [124]. Some participants directly prescribed the inflow corresponding to the data, while others tried to generate a more realistic inflow based on the Mann model or the precursor database method. A study even used the nesting technique [294]. However, since only few data are fixed, the simulation parameters vary greatly within the participants that tried to replicate a realistic inflow. Each participant tries to generate the inflow that best matches the atmospheric conditions obtained from the measurements.

To remain consistent, most of the parameters used in the neutral and stable benchmarks are similar. In both studies, the subgrid-scale model used is the dynamic Smagorinsky model [105, 106]. The density is imposed at $\rho = 1.06$ kg/m^3. Gravity is set to $g = 9.81$ m/s^2. The Van Kármán constant is set to $\kappa = 0.4$. The location of the site is 33.61°N, 102.05°W. The bottom boundary condition is a wall with a roughness of $z_0 = 0.014$ m. The wall is modelled using the Monin-Obukhov Similarity Theory. Five steps of wall law filtering is applied using the Gather-Scatter filter developed in Section 4.1.4. The upper boundary condition is a slip-wall. The two lateral boundaries are periodic. For precursor simulations, the two streamwise boundaries are also periodic. Conversely, for wind turbine simulations, these boundaries are set to be the inlet and outlet. Precursor simulations run until the flow is established, which varies depending on the conditions. Wind turbine simulations are run for 4200 s. The first 600 s, equivalent to one $10-$minute periods and corresponding to approximately 10 flow through the domain, allows for the establishment of the flow. The remaining 3600 s, equivalent to the six $10-$minute periods, serves to gather statistics on the flow and the wind turbine response,

The wind turbine used at the SWiFT facility is a modified Vestas V27 with a rotor diameter of $D = 27$ m and a hub height of $z_h = 32.1$ m. The hub radius is 0.5 m. The wind turbine is modified as after an optimisation phase, the pitch angle is modified by $-0.75°$. The rotation speed is set to be constant, depending on the benchmark. For the neutral benchmark, the rotation speed is set to $\Omega = 4.56$ rad/s, while for the stable benchmark, the rotation speed is set to $\Omega = 2.79$ rad/s. Wind turbine modelling is performed using the actuator line method. All data are gathered on Tab. 6.2.

Simulation parameters		Turbine parameters	
Parameter	Value	Parameter	Value
Density	$\rho = 1.06$ kg/m^3	Rotor diameter	$D = 27$ m
Gravity	$g = 9.81$ m/s^2	Hub height	$z_h = 32.1$ m
Van Kármán constant	$\kappa = 0.4$	Hub radius	$r_h = 0.5$ m
Latitude	33.61°N	Pitch angle	$\gamma = -0.75°$
Wall roughness	$z_0 = 0.014$ m	Rotation speed	$\Omega = 4.56 - 2.79$ rad/s

Table 6.2: Global simulation and wind turbine parameters for both the neutral and the stable benchmarks.

6.1.4 Neutral benchmark

Inflow turbulence

The precursor corresponds to a neutral boundary layer in a periodic box. The size of the domain has been fixed to $L_x \times L_y \times L_z = 3200 \times 3200 \times 1000$ m^3, and is meshed with a structured grid of $N_x \times N_y \times N_z = 200 \times 200 \times 100$ elements. The spatial resolution of the Cartesian mesh is thus $\Delta x = \Delta y = 16$ m and $\Delta z = 10$ m for all three directions. The geostrophic wind is set to $U_G = 11.35$ m/s and $V_G = -3.91$ m/s, similar to the study performed using the Meso-NH code [294]. The geostrophic wind is chosen so that the velocity, TKE and wind direction are as close as possible to the measurements. Data are gathered in Tab. 6.3. A qualitative display of the precursor simulation is shown in Fig. 6.2. The initial velocity profile is set to be logarithmic with a random perturbation r, with an amplitude of 0.1 m/s, which speeds up the establishment of the flow. It follows:

$$u(z) = \frac{u_*}{\kappa} \times \log(\frac{z + z_0}{z_0}) \times (1 + r) \; . \tag{6.3}$$

The precursor simulation is performed in two parts. The first is the establishment part, where the flow reaches a statistically converged state. Once established, the second part consists

Parameters	Precursor simulation	Wind turbine simulation
Domain size	$3200 \times 3200 \times 1000$ m^3	$459 \times 270 \times 270$ m^3
#elem	4×10^6	46.3×10^6
#node	5.6×10^6	13.1×10^6
Δ $[m]$	$16 \times 16 \times 10$	$0.625 - 3.5$
Geostrophic wind	$(11.35, -3.91)$	

Table 6.3: Neutral benchmark simulation parameters for both the precursor and the wind turbine domain.

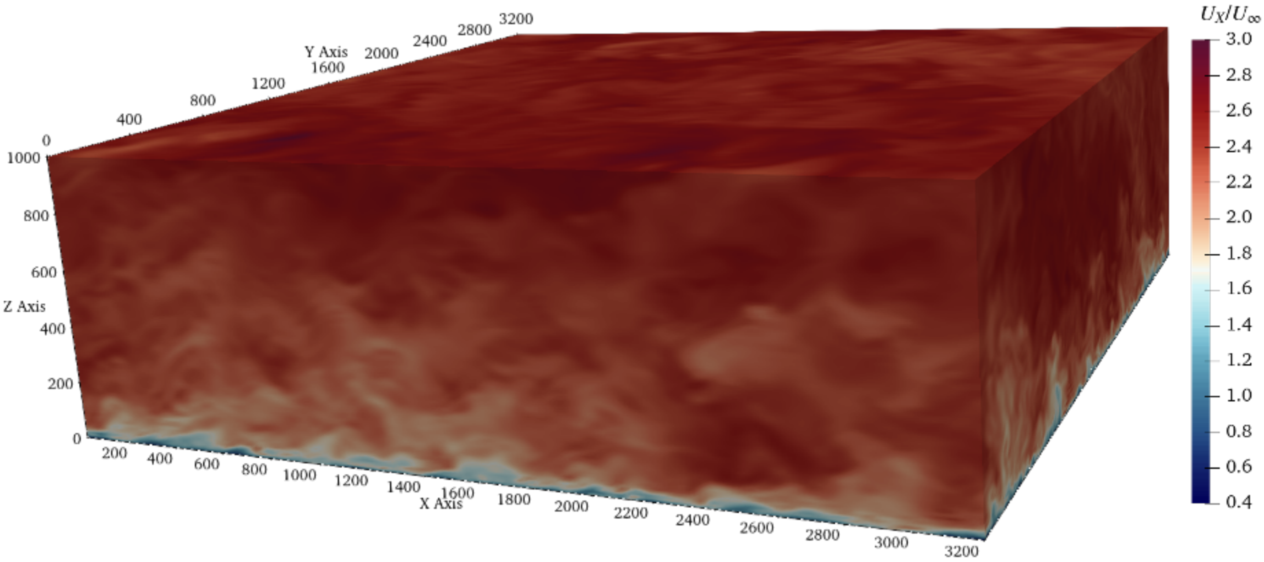

Figure 6.2: Precursor simulation for the neutral benchmark.

of accumulating statistics on the flow quantities. During this first part, a velocity controller is added [203]. Its purpose is to guarantee the prescribed velocity at hub height. For that, the proportional-integral velocity controller acts in the whole domain to drive the flow towards the required velocity. In addition to having the exact recommended streamwise velocity at hub height, the velocity controller can force the tangential velocity at the hub height to be zero. This feature is particularly useful for the wind turbine simulation, as it ensures a streamwise flow and thus guarantees that the wind turbine is not yawed.

The establishment of the precursor simulation flow is measured based on the convergence of the shear stress at the wall. The shear stress is averaged at the boundary and is expressed as a function of the adimentional time: $t^+ = t/t_0$ where $t_0 = H/u_*$, H being the precursor height and u_* the friction velocity. The temporal evolution of the shear stress is shown in Fig. 6.3. At the beginning of the simulation, the shear stress tends to fluctuate. This reflects the accelerations and decelerations of the flow near the wall. After some time ($t^+ = 35$), the shear

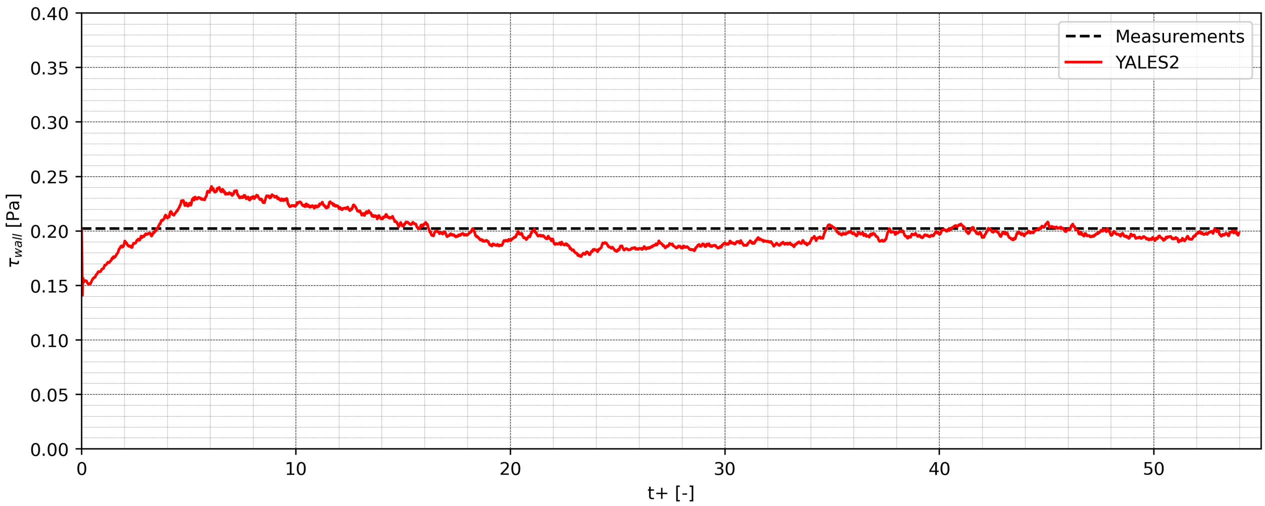

Figure 6.3: Shear stress temporal evolution of the neutral benchmark precursor simulation.

stress stabilises, which means that the flow established itself. The shear stress obtained in the precursor simulation is in agreement with the one measured experimentally. As the frictional velocity is proportional to the shear stress, this result shows that the frictional velocities are also in a good agreement, around $u_* = 0.45$ m/s.

Once the flow reaches a statistically converged state, statistics of the flow quantities can be gathered. A qualitative view of the precursor simulation is shown in Fig. 6.4. The instantaneous velocity field shows the turbulent flow. Large structures are present, consistent with a neutral atmospheric layer. The time-averaged velocity field shows the neutral boundary layer velocity, exhibiting a logarithmic velocity profile, increasing with height. Finally, the RMS velocity field shows the fluctuation in the flow. Higher fluctuations are present near the wall because of the roughness of the wall. This result supports the notion that most of the turbulence production comes from the wall.

Following the SWiFT post-processing procedure, the profiles are spatially averaged over horizontal planes and temporally averaged. The streamwise velocity $\overline{U_x}$, turbulent kinetic energy and relative wind direction profiles are plotted in Fig. 6.5 and compared to the measurements, the LES results from the original study [124], and the LES results from the Meso-NH study [294]. As mentioned in the original study, the TKE is computed as:

$$\text{TKE} = 0.5 \times (U^2_{RMS,x} + U^2_{RMS,y} + U^2_{RMS,z}) \ , \tag{6.4}$$

while the relative wind direction (WD) is computed as the angle between the tangential and the streamwise velocity, relatively to the angle measured between 10 m and 45 m, i.e. the height at which experimental data are measured.

The streamwise velocity profile exhibits a logarithmic velocity profile, expected for a

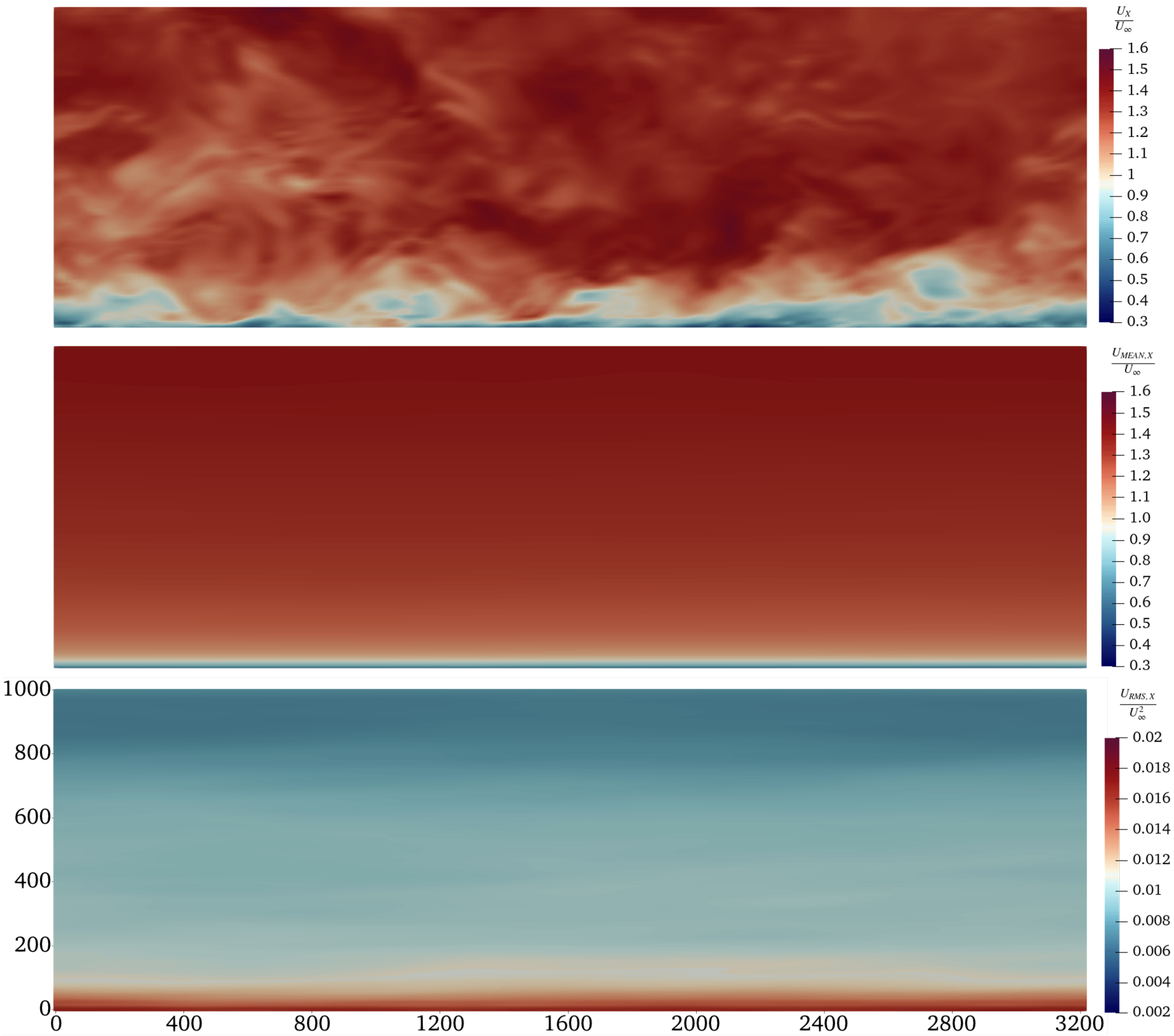

Figure 6.4: Normal planes normal to the tangential direction. From top to bottom, Streamiwse instantaneous, time-averaged and RMS velocity.

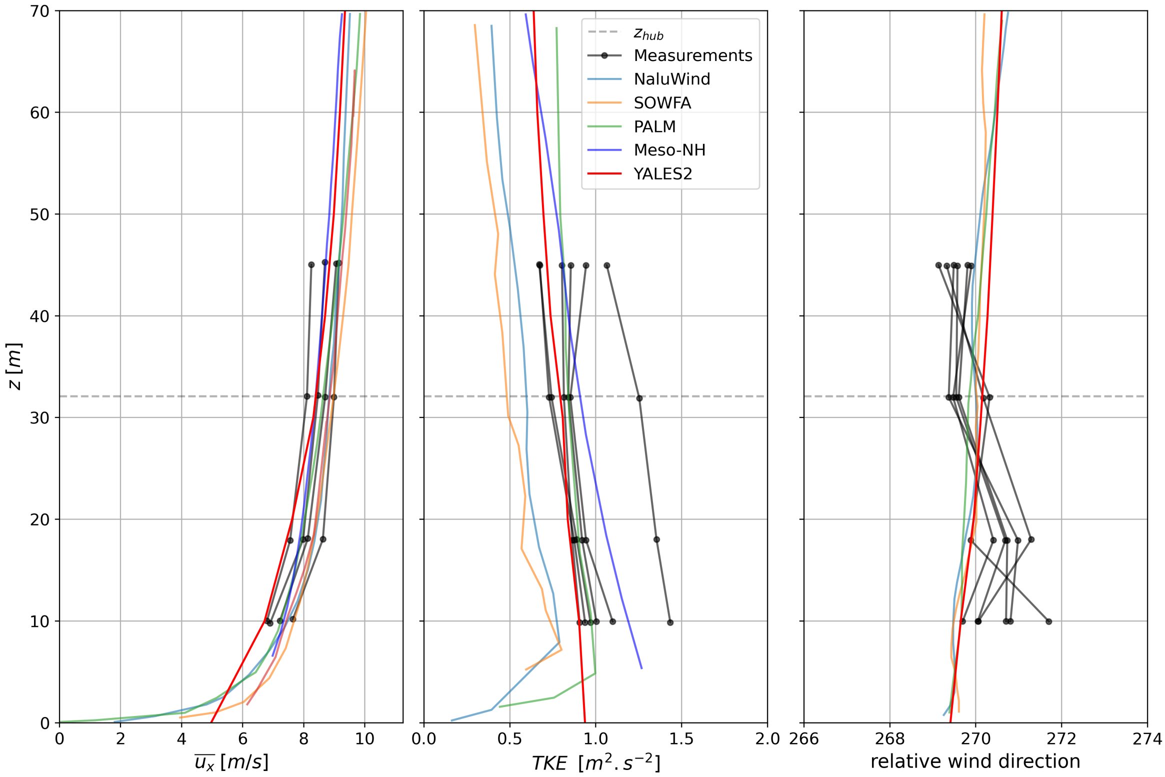

Figure 6.5: Precursor from the neutral benchmark. From left to right, average streamwise velocity, turbulent kinetic energy, and relative wind direction.

neutral boundary layer. YALES2 results are in agreement with the measurements and the LES studies. The obtained average streamwise velocity at hub height is $U_h = 8.7$ m/s, equivalent to the experimental study. Although the overall shape of the YALES profile is similar to other studies, we can notice minor differences, mainly in the lower 20 m. The streamwise velocity does not exhibit a curve as steep as the others. This main difference may be due to the grid resolution. In this study, the vertical grid resolution is set to $\Delta z = 10$ m, while for other participants studies it is set to $\Delta z = 5$ m.

The turbulent kinetic energy is almost constant and slowly decreases with height. The experimental data show a wide range of values: at hub height, the TKE vary from TKE $=$ 0.75 m^2/s^2 to TKE $=$ 1.25 m^2/s^2. YALES2 TKE at hub height is nearly identical to the measurements, i.e. $TI = 10.7\%$. In light of this result, it appears that the difference in grid resolution does not affect the turbulent kinetic energy. Near the wall, YALES2 predicts a constant TKE while other studies predict a reduction, tending toward zero. This result can probably be explained depending on the subgrid-scale model used, as their behaviour near walls highly vary.

The relative wind direction shows the veer in the flow. Due to the Coriolis force and frictional velocity, the flow rotates with height. YALES2 results are similar to other LES studies, exhibiting a slight wind direction increase with height. Conversely, the experimental

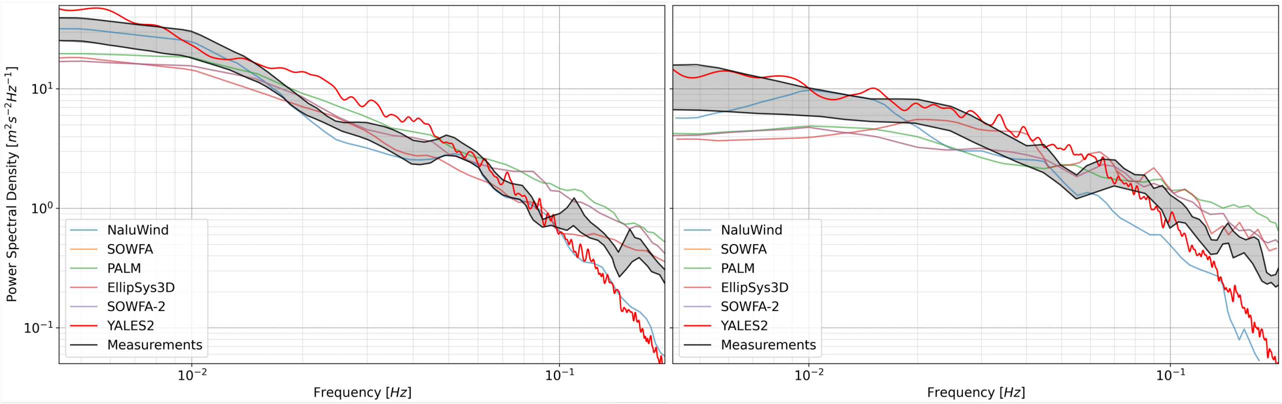

Figure 6.6: Turbulence spectra of the streamwise and tangential velocity component of the neutral benchmark precursor.

results do not show any rotation. However, the magnitude of these direction changes is small.

Finally, to obtain a quantitative characterisation of the flow structure, Fig. 6.6 shows the power spectral density for the streamwise and tangential velocities. The turbulence spectra are based on Taylor's hypothesis or the frozen-turbulence approximation, which evaluates spatial correlations using temporal correlations. Four probes are located in the horizontal plane at hub height to collect the data. Then each spectra are smoothed using a Gaussian filter with a standard deviation of $\sigma = 10\ \mathrm{m^2\,s^{-2}\,Hz^{-1}}$. Finally, the four spectra are averaged, rendering a smooth curve. The turbulence spectra show the distribution of turbulent kinetic energy among the different sizes of eddies.

YALES2 results exhibit a similar behaviour than the measurements and the other LES studies. The largest flow structures, corresponding to the low frequency, are well represented. Minor differences can be noted at higher frequencies. YALES2 exhibits spectra that decrease faster than most others. This discrepancy is probably due to the mesh size, as a finer mesh captures smaller structures. However, this minor difference does not affect the flow behaviour as both the streamwise velocity and turbulent kinetic energy profile are in agreement with the experimental and the LES results. It should be noted that Taylor's hypothesis is valid only if the velocity fluctuations are small compared to the mean streamwise velocity. Thus, in this simulation, it appears to be valid.

Now that the inflow has been properly generated using the precursor database method, the wind turbine simulation can be carried out. Although minor differences are noted between this study and others, it has also been noted that it does not affect the global behaviour of the flow in terms of average velocity and turbulent kinetic energy profile.

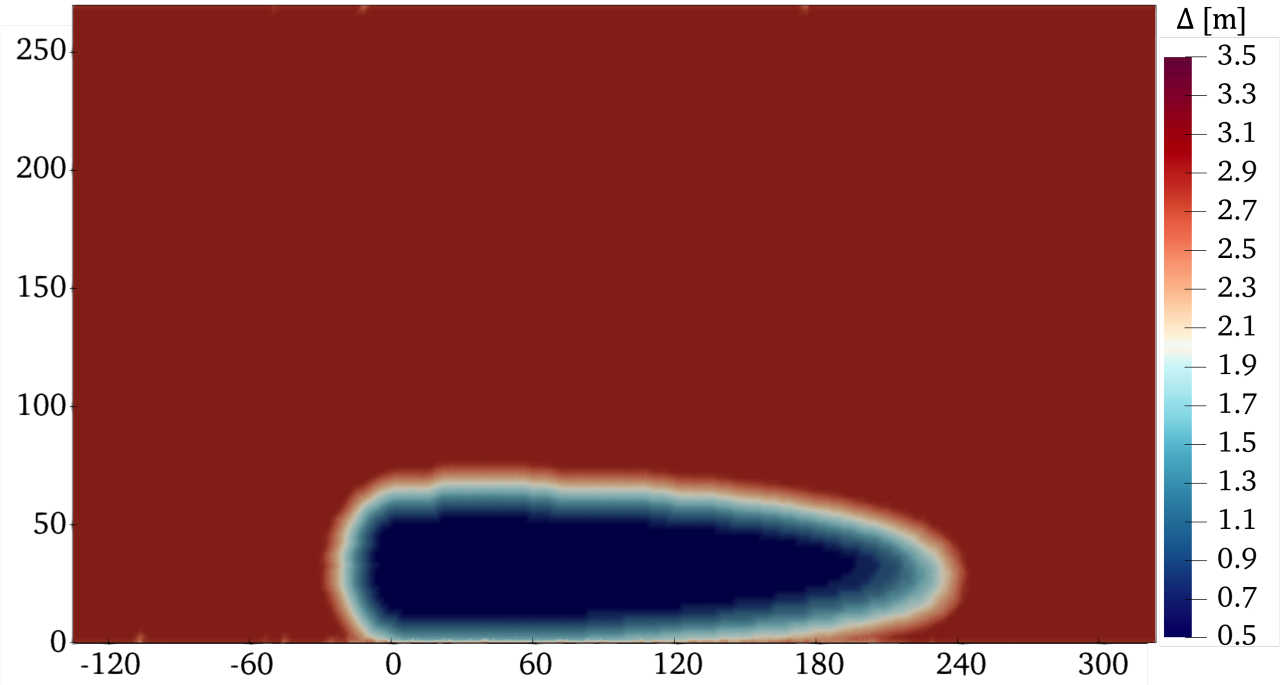

Figure 6.7: Mid-plane visualisation of the mesh.

Mesh generation

The AMR strategy developed in Chapter 5 is applied in this study. The objective is to refine the mesh within the wake region to capture smaller vorticies and improve the accuracy of the simulation. For that, the methodology is based on the tracking of the wind turbine wake using a progress variable with a source term in the rotor region. The AMR strategy is applied within the envelope defined by this progress variable, without impacting the rest of the domain.

The size of the domain has been fixed to $L_x \times L_y \times L_z = 459 \times 270 \times 270$ m^3, equivalent to 27D $\times$ 10D $\times$ 10D m^3. The final grid has a mesh size of $\Delta = 3.5$ m in the far region and reaches a mesh size of $\Delta = 0.625$ m in the rotor and the wake region. Data are gathered in Tab. 6.3, and a visualisation of the mesh is shown in Fig. 6.7.

Although the wind turbine wake expands far downstream, the adaptation area has been limited to 8D downstream. The growth rate of the metric is restricted to obtain a good quality mesh. The skewness is mainly around 0.4, with almost all cells having a skewness below 0.6. However, it reaches locally values of 0.98.

Wind turbine response

The second step of the SWiFT benchmark is to study the response of the wind turbine. The simulation is performed in two parts. The first is to establish the flow. The simulation runs for 600 s, allowing the flow to reach a statistically converged state. During this part, the

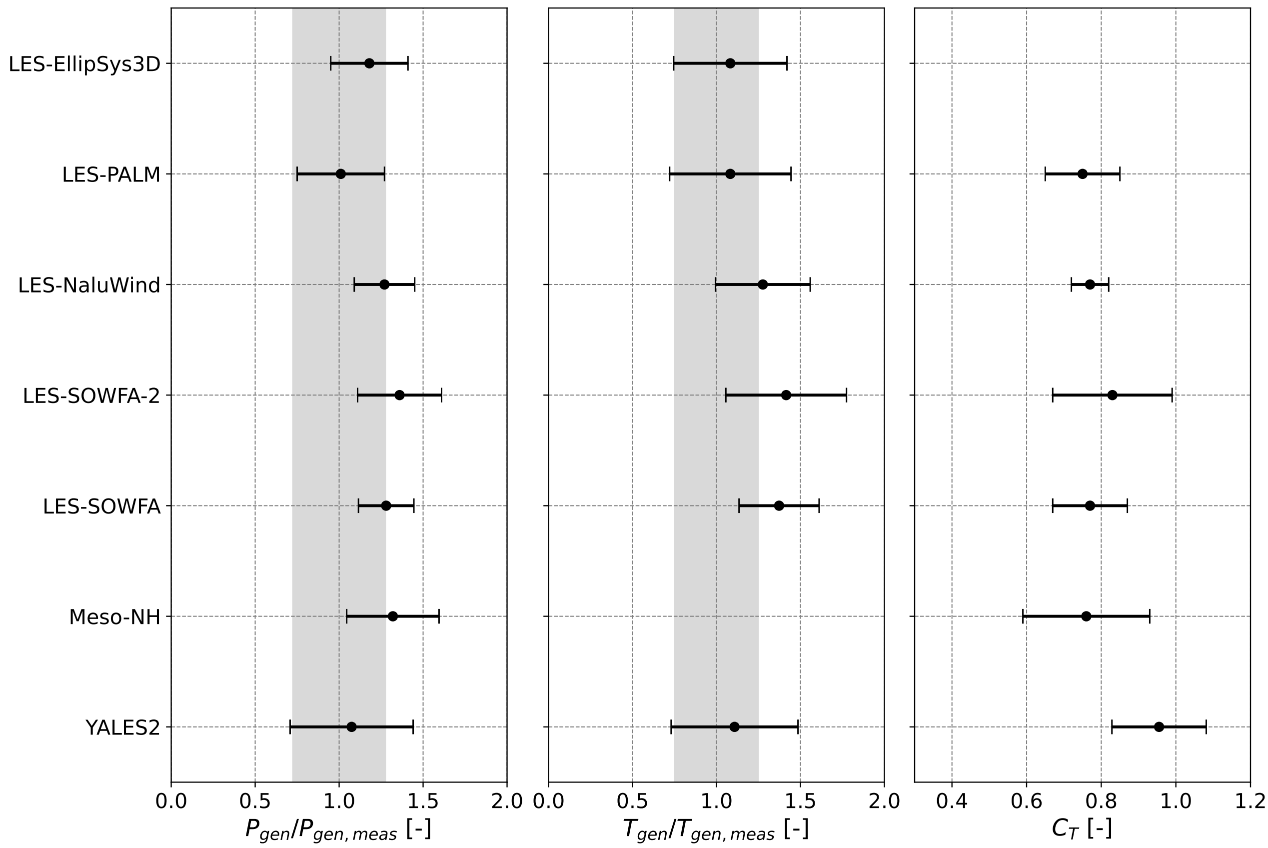

Figure 6.8: Mean and standard deviation for time series of wind turbine response quantities for the neutral benchmark. From left to right: power output, torque, and thrust coefficient.

inlet turbulence is slowly transported in the domain. Second, the statistics are collected over 3600 s, equivalent to the six $10-$minute periods of data accumulation of the experimental measurements. During this time, three wind turbines variables are measured and compared: the power output, torque, and thrust coefficient. These data are shown in Fig. 6.8. The rotational speed being fixed in this study, its comparison is irrelevant.

Experimental measurements are represented by the gray shade, centred around 1 as it serves as an adimentionalisation parameter. The error bars highlight the standard deviation for each study. Again, the results are compared to the LES results of the original study and the Meso-NH study. The power output is adimentionalised by the average power output experimentally measured, evaluated as: $P_{gen,meas} = 79.1$ kW. The average wind turbine power output in YALES2 is, like in most studies, in the range of the experimental measurements. However, all studies tend to overestimate it. This result comes from a torque overestimation that is not explained in the original publication. Although noticeable, YALES2 tends to less overestimate the power output than most other studies. In addition, the power output is expected to be of secondary importance for the wake velocity deficit, as the thrust is the main factor.

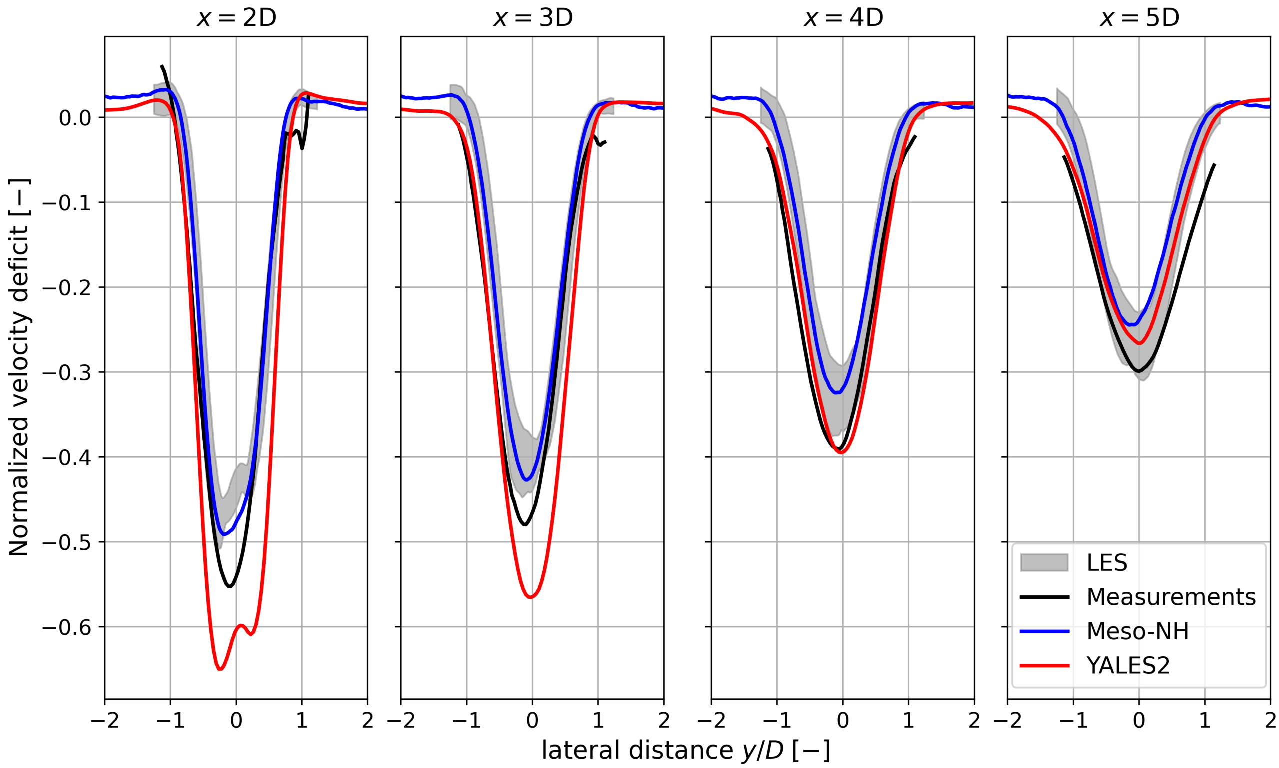

Figure 6.9: Neutral benchmark: mean velocity deficit in the wake at hub height. From left to right: 2D, 3D, 4D, and 5D.

The torque output is adimentionalised by the average torque measured experimentally, evaluated as: $T_{gen,meas} = 622.3$ N.m. As the rotation speed is fixed, the power and torque output follows the same behaviour. Again, LES studies, including YALES2, overestimate torque output, although this study has one of the lowest overestimations. Finally, the thrust coefficient C_T is measured as detailed in Section 6.1.2. Unfortunately, it could not be measured experimentally. YALES2 gives a larger thrust than other LES codes.

Velocity deficit

Finally, the third step of the SWiFT benchmark is to study the velocity deficit in the wind turbine wake. Fig. 6.9 shows the time-averaged velocity deficit profiles at four downstream positions in the wake. The velocity deficit is measured horizontally, following the tangential direction, at hub height. For the sake of clarity, the five LES studies from the original publication are merged, resulting in the gray shade. YALES2 results are compared against this LES ensemble average, the Meso-NH results, and the measurements.

At x = 2D, the maximum velocity deficit is higher in YALES2. The wake width is also slightly wider. This result is consistent with the thrust coefficient being larger than others. YALES2 results then show a faster wake dissipation than others, predicting a correct velocity deficit x = 4D downstream. The increased dissipation rate is probably related to the inflow

TKE in YALES2, with a higher TKE value than most LES codes (Fig. 6.5). To explain the velocity deficit discrepancy at $x = 2 - 3$D, the first parameter to mention is the size of the domain. The wind turbine simulation domain is significantly reduced compared to the precursor domain. This choice has been made to limit the mesh size while maintaining a fine enough spatial resolution, but this strategy can have an impact on flow behaviour, with a containment effect. In addition, a velocity controller is used in the inflow simulation to guarantee the average velocity at hub height. However, this controller cannot be used in the wind turbine simulation as it would have an effect on the wake. Therefore, the wind turbine inflow may differ from the inflow simulation.

Although the velocity deficit near the wind turbine is not in close agreement with the experimental results, the global behaviour of the wake is captured. From $x = 4$D upward, the velocity deficit is in close agreement with the measurements. Overall, the wake behaviour is consistent with the turbine response.

6.1.5 Stable benchmark

Inflow turbulence

Similar to the neutral benchmark inflow turbulence, the stable benchmark is performed in two steps. First, the inflow turbulence is generated using the precursor database method, then the wind turbine simulation is performed. The precursor corresponds to a stable boundary layer in a periodic box, similar to the one in Section 4.4. The size of the domain has been fixed to $L_x \times L_y \times L_z = 300 \times 300 \times 300$ m^3, and is meshed with a structured grid of $N_x \times N_y \times N_z = 50 \times 50 \times 50$ elements. The spatial resolution is thus $\Delta = 6$ m for all three directions. The wall heat flux is set to $q_w = -0.005$ K.m/s, similar to the kinematic vertical heat flux experimentally measured. Although it is mentioned in Section 2.2.2 that the MOST wall law is more reliable when prescribing the surface temperature instead of the surface heat flux as a boundary condition, the temperature at the ground is not measured experimentally.

To obtain a result as close to the experiment as possible, the most suitable geostrophic wind was found at $U_G = 6.84$ m/s and $V_G = -2.79$ m/s, slightly lower than the Meso-NH study [294]. The flow field is initialised with a constant-velocity profile equal to the geostrophic wind. A constant temperature profile is set up to an arbitrary defined ABL height, set at $z = 200$m, capped by an inversion region 5K/50m. The geostrophic wind and ABL height are chosen so that the velocity, TKE, and wind direction are as close to the measurements as possible. Data are gathered in Tab. 6.4.

Again, the establishment of the precursor simulation flow is measured based on the convergence of the shear stress at the wall. The temporal evolution of the shear stress is shown in Fig. 6.10. At the beginning of the simulation, the shear stress is very high, due to the initial velocity conditions being set to the geostrophic wind. The velocity near the wall is much

Parameters	Precursor simulation	Wind turbine simulation
Domain size	$300 \times 300 \times 300$ m^3	$540 \times 300 \times 300$ m^3
#elem	125×10^3	24.9×10^6
#node	174×10^3	35×10^6
Δ $[m]$	$6 \times 6 \times 6$	$1.25 \times 1.25 \times 1.25$
Geostrophic wind	$(6.84, -2.79)$	
Heat flux	$q_w = -0.005$ K.m/s	

Table 6.4: Stable benchmark simulation parameters for both the precursor and the wind turbine domain.

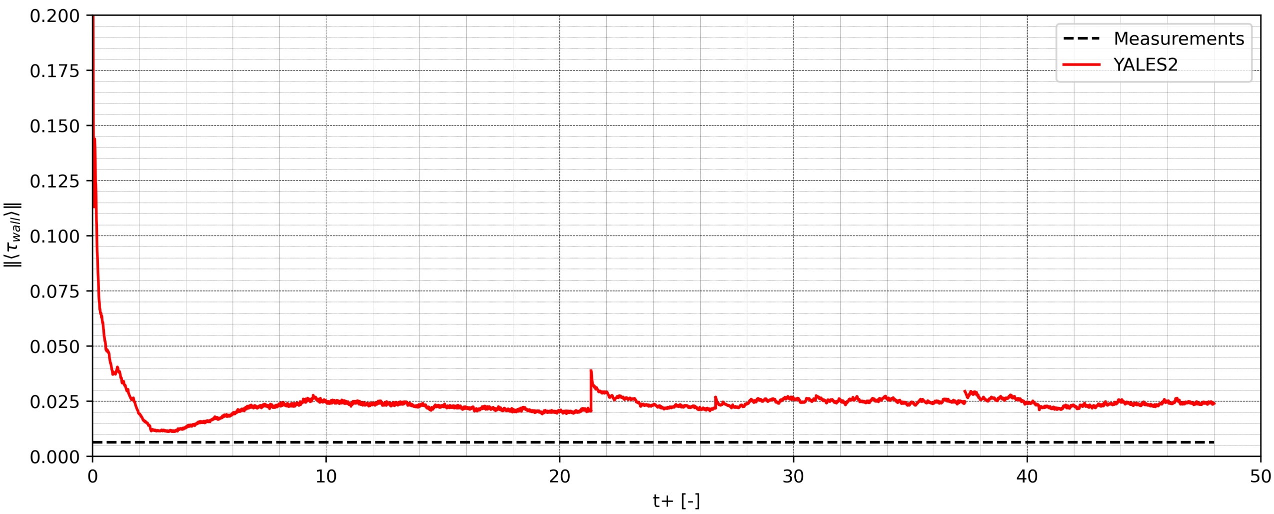

Figure 6.10: Shear stress temporal evolution of the stable benchmark precursor simulation.

higher than the one expected. After some time ($t^+ = 8$), the shear stress stabilises reaching its convergence value. The peak seen at $t^+ = 21$ is a consequence of the management of the run. It corresponds to the time the computation has been restarted, due to time limitation on supercomputers. Unfortunately, the statistics have also been restarted, leading to this peak. However, it has no impact on the flow behaviour. Finally, we can see that the wall shear stress, while converged, is greater than the experimental. The frictional velocity reaches a value of $u_* = 0.16$ m/s. Experimentally, it was measured at $u_* = 0.08$ m/s.

In this simulation, the velocity controller could not be used. It appears that while working correctly for neutral configurations, the velocity controller in this form is lacking for stable configurations. The velocity controller is unable to reach the prescribed value at hub height. As a consequence, as the source term of the velocity controller is integrated over the entire domain, the velocity in the higher region of the domain is drastically reduced. Thus, it has been decided not to use the velocity controller in this simulation. A qualitative view of the precursor simulation is shown in Fig. 6.11. The instantaneous velocity field shows the turbulent

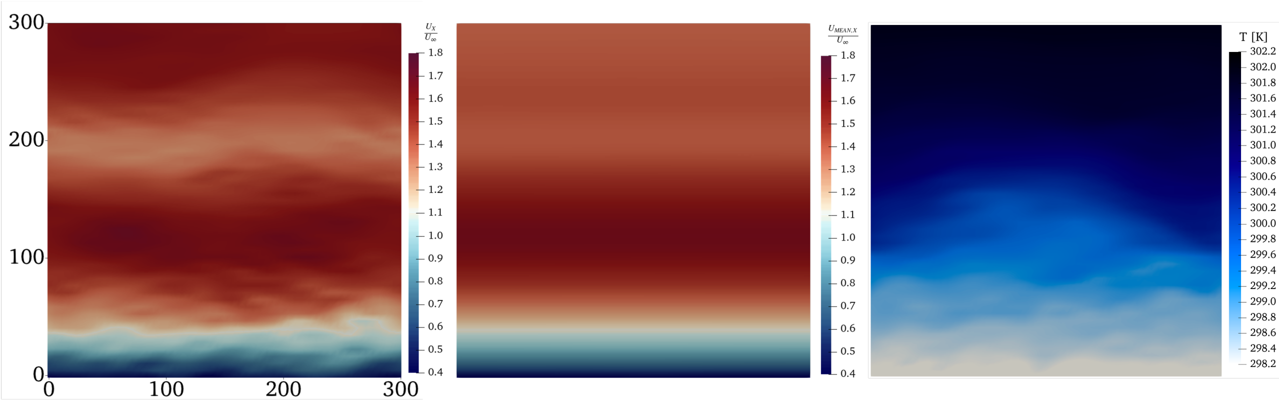

Figure 6.11: Normal planes to the tangential direction. From left to right, instantaneous velocity, average velocity, and temperature fields.

flow. Compared to the neutral velocity field, it is clear that the structures are significantly smaller. The time-averaged velocity field shows the stable boundary layer velocity, exhibiting an over-speed region at a height of around $z = 100$ m. This behaviour is similar to that of the GABLS1 study, performed in Section 4.4. This result is expected, as the boundary layer is capped by an inversion region at $z = 200$m height. Finally, the temperature field shows the cooling caused by the surface heat flux.

For a quantitative display, Fig. 6.12 shows the streamwise velocity profile, the turbulent kinetic energy profile, and the relative wind direction. Compared to the neutral benchmark, only a few participants have contributed to the stable benchmark using LES. One is based on the SOWFA code in the initial study [124], the other is a more recent study based on the Meso-NH code [294]. In the following discussions, they will be referred to as SOWFA and Meso-NH. The streamwise velocity profile exhibits a logarithmic velocity profile. The over-speed region cannot be seen as this region is at a higher height than the experimental measurements. The obtained average streamwise velocity at hub height is $U_h = 4.8$ m/s, equivalent to the experimental study. Although the overall shape of the profile is similar, one can notice minor differences, mainly in the lower 20 m. The streamwise velocity appears to be higher than the experimental and that of SOWFA. This velocity over-prediction is correlated with the higher frictional velocity.

The turbulent kinetic energy is almost constant and slowly decreases with height. However, TKE is found to be much higher than both the experimental and LES studies. At hub height, the TKE is doubled. Again, this result is correlated with the frictional velocity. A higher frictional velocity near the wall leads to higher turbulence generation and thus to higher TKE. Finally, the relative wind direction shows large discrepancies between the results. The SOWFA study shows a pronounced veer that was not seen in the field measurements. In this work, the wind direction is found to be between the experimental and the SOWFA study. Part of the difference was explained in the original study, which stated that, potentially, the stable

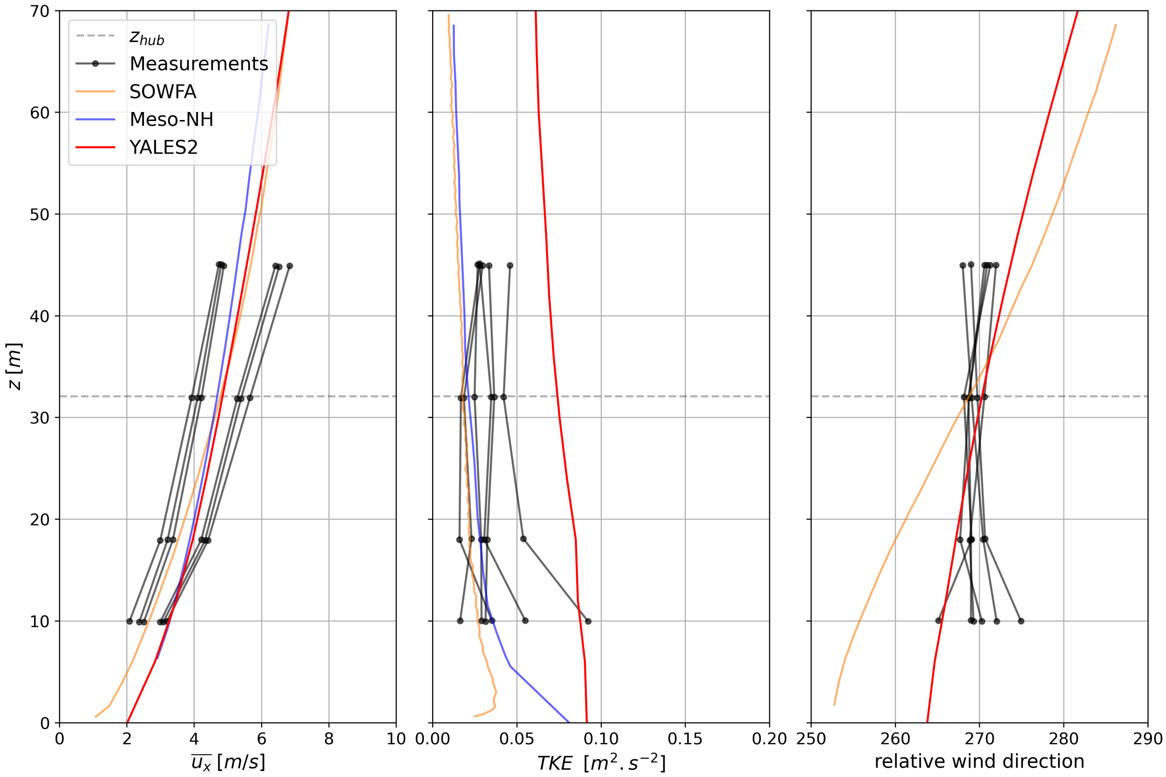

Figure 6.12: Precursor from the stable benchmark. From left to right, average streamwise velocity, turbulent kinetic energy, and relative wind direction.

benchmark was defined based on measurements of a baroclinic atmosphere. In these conditions, horizontal temperature gradients can result in geostrophic wind shear and veer, which can reduce the amount of wind veer down in the surface layer.

To understand the discrepancies on the obtained TKE, further investigation is performed. First, like for the neutral precursor, the turbulence spectra are computed. Both streamwise and tangential velocity components are shown in Fig. 6.13. The same approach as for the neutral study was used. The streamwise velocity spectra exhibit the correct behaviour, which is a power spectral density decreasing as the frequency increases. However, for tangential velocity spectra, a decrease in the power spectral density is displayed between $f = 10^{-3}$ Hz and $f = 10^{-2}$ Hz. Although unexpected, this behaviour can be caused by several factors. First, the probes are located at hub height and thus are close to the wall. This proximity can have an impact, with some frequencies being less represented. Second, the statistics accumulation time might not be enough, with the sampling missing some frequencies. Unfortunately, because no other studies have provided their turbulence spectra, comparisons cannot be established.

As the turbulent kinetic energy and the frictional velocity are too high compared to other studies, the stability parameter is evaluated. In the experimental study, it has been measured at $\zeta = 1.151$. Although for the SOWFA study the parameter is not indicated, the Meso-NH study showed $\zeta = 0.4$. The authors explained that they could not reach the stability of the

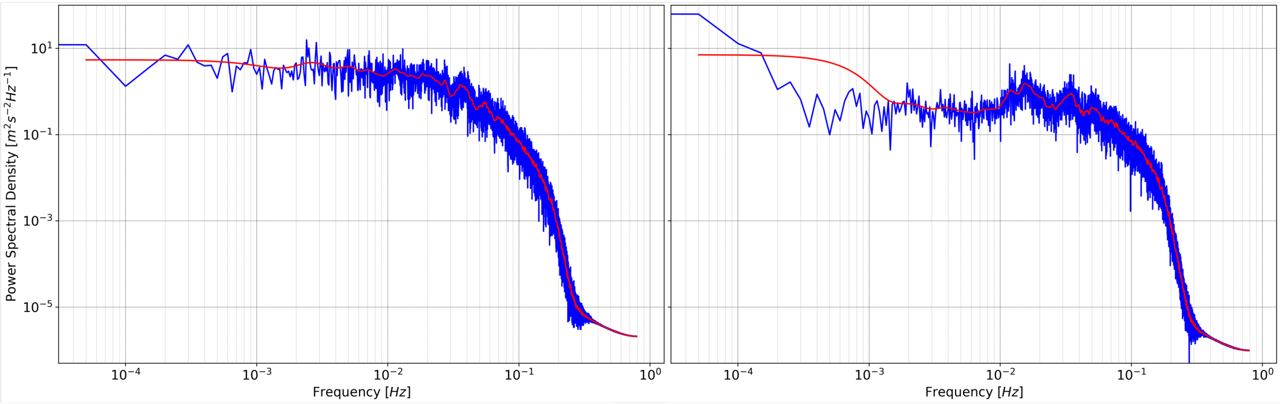

Figure 6.13: Turbulence spectra of the streamwise (left) and tangential (right) velocity component of the stable benchmark precursor. (—) for the turbulence spectra, (—) for the Gaussian filtered turbulence spectra.

experimental measurements. In this study, the stability parameter is measured as:

$$\zeta = \frac{z}{L} = \frac{z\,\kappa\,g\,\overline{w'\theta'}}{u_*^3\,\theta_0}\,, \tag{6.5}$$

where:

- $z = 10$ m is the height at which the stability parameter is computed,
- $u_* = 0.16$ m/s is the frictional velocity,
- $\overline{w'\theta'} = -0.002$ K.m/s is the kinematic vertical heat flux at 10 m.

In this study, the stability parameter is obtained $\zeta = 0.07$, being much smaller than expected. This result explains the gap found in the turbulent kinetic energy. This discrepancy is mainly due to two factors. First, the frictional velocity almost doubles that of the experimental study, which greatly affects the stability parameter. Second, the lower kinematic vertical heat flux. In fact, the wall heat flux in this study has been set to $q_w = -0.005$ K.m/s, based on the experimental measurements "near-surface". However, the experimental measurements are not made on the ground, but at 10 m height. At this height, the kinematic vertical heat flux has been reduced by 60%. If the stability parameter is to be achieved, the wall heat flux must be increased.

Increasing the stability parameter

To increase the stability parameter, it is required to increase the wall heat flux. However, a more stable boundary layer will have smaller vorticies. In order to resolve most of the turbulent kinetic energy, the mesh needs to be refined. The size of the domain remains constant, fixed to $L_x \times L_y \times L_z = 300 \times 300 \times 300$ m^3. However, the domain is meshed with a structured grid of $N_x \times N_y \times N_z = 150 \times 150 \times 150$ elements. The spatial resolution is thus $\Delta = 2$ m for all three directions. The wall heat flux is doubled, set to $q_w = -0.01$ K.m/s. The geostrophic wind as

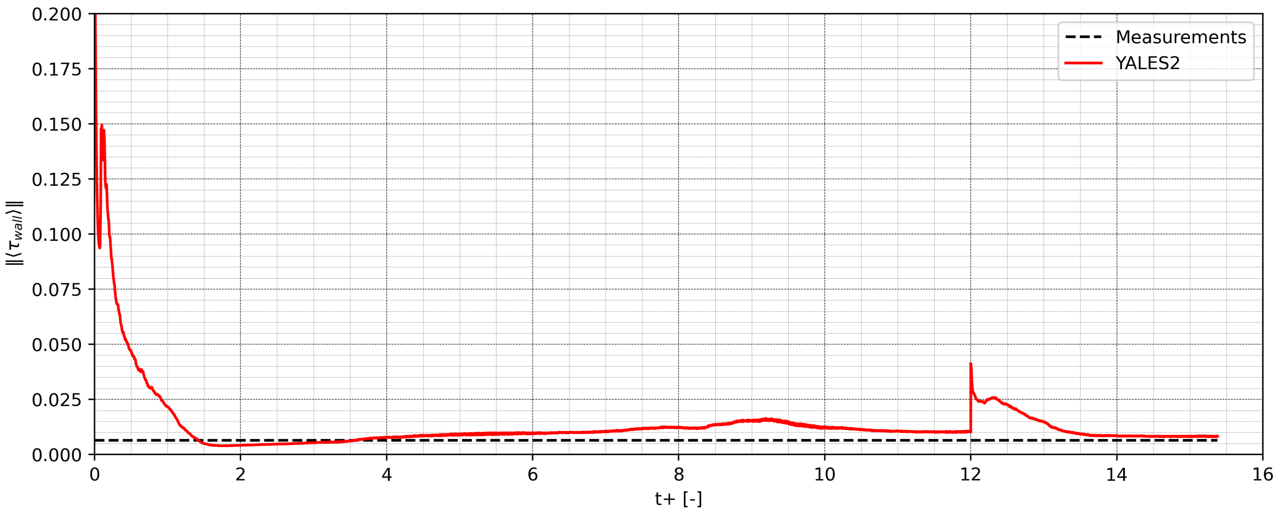

Figure 6.14: Shear stress temporal evolution of the increased heat flux stable benchmark precursor simulation.

well as the flow field initialisation is kept constant. Data are gathered in Tab. 6.5.

Parameters	Precursor simulation
Domain size	$300 \times 300 \times 300$ m^3
#elem	3.4×10^6
#node	4.7×10^6
Δ [m]	$2 \times 2 \times 2$
Geostrophic wind	$(6.84, -2.79)$
Heat flux	$q_w = -0.01$ K.m/s

Table 6.5: Stable benchmark simulation parameters for the increased wall heat flux and resolution simulation.

The temporal evolution of the shear stress is shown in Fig. 6.14. Again, the peak seen at $t^+ = 12$ is due to a reset of the statistics. The frictional velocity establishes around $u_* = 0.1$ m/s, closer to the experimental measurement of $u_* = 0.08$ m/s. The kinematic vertical heat flux is measured at $\overline{w'\theta'} = 0.0035$ K.m/s, resulting in a stability parameter of $\zeta = 0.39$. Although the stability parameter is still not at the experiment level, it reaches the value of the Meso-NH study.

A qualitative view of the precursor simulation is shown in Fig. 6.15. Increasing the stability parameter affects the flow behaviour, lowering the height of the boundary layer, and increasing the velocity in the over-speed region. In addition, as the wall heat flux decreases (increases in norm), the temperature is lower in the overall domain.

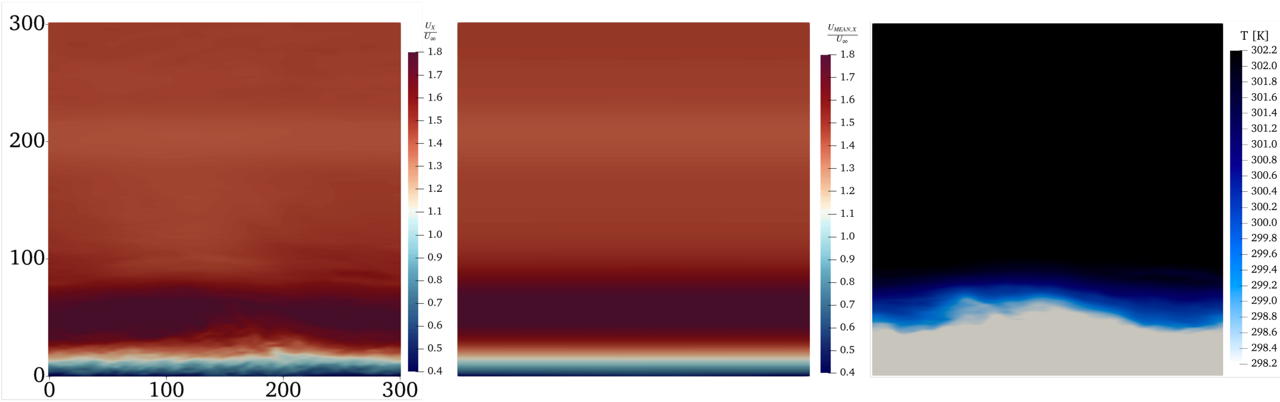

Figure 6.15: Normal planes to the tangential direction. From left to right, instantaneous velocity, average velocity, and temperature fields.

Fig. 6.16 shows the streamwise velocity profile, the turbulent kinetic energy profile, and the relative wind direction. The streamwise velocity at hub height is much higher than expected, reaching a value of $\overline{U_x} = 7.8$ m/s. Furthermore, while the turbulent kinetic energy at the lower 20 meters is adequate with both experimental measurements and LES studies, it increases greatly with height, reaching a value of TKE $= 0.1$ m^2/s^2, greater than the turbulent kinetic energy of the previous stable configuration. Lastly, the relative wind direction has increased, exhibiting a veer similar to that of the SOWFA study. It appears that, although the stability parameter is closer to the one measured experimentally, the flow behaviour in terms of averaged velocity and turbulent kinetic energy is further afield.

Based on this result, a few parameters have been modified to try to more accurately reproduce the behaviour of the flow measured experimentally. By modifying the wall roughness, reducing the geostrophic wind, no convincing results were found. As many parameters are left free to the participants, a parameter study is needed to find the correct set. However, since LES is a computationally expensive technique, doing so requires large computational resources and a lot of time. Based on these findings, it was decided to study the wind turbine response using the first inflow turbulence with the lower heat flux. Although the stability parameter is higher, the flow behaviour is closer to the measurements.

Wind turbine response

The size of the domain has been fixed to $L_x \times L_y \times L_z = 540 \times 300 \times 300$ m^3, equivalent to 20D $\times$ 11D $\times$ 11D. Conversely to the neutral boundary layer where a coarse grid can suffice to capture most vorticies, a stable boundary layer requires a fine grid. Thus, it was decided to use a grid with a constant cell size of $\Delta = 1.25$ m. Data are gathered in Tab. 6.4. Again, the simulation is performed in two parts. After 600 s for the establishment of the flow, 3600 s are used to collect statistics. It equivokes with the six $10-$minute periods of data accumulation of the experimental measurements. The power output, torque, and thrust coefficient are shown in Fig. 6.17 from left to right, respectively.

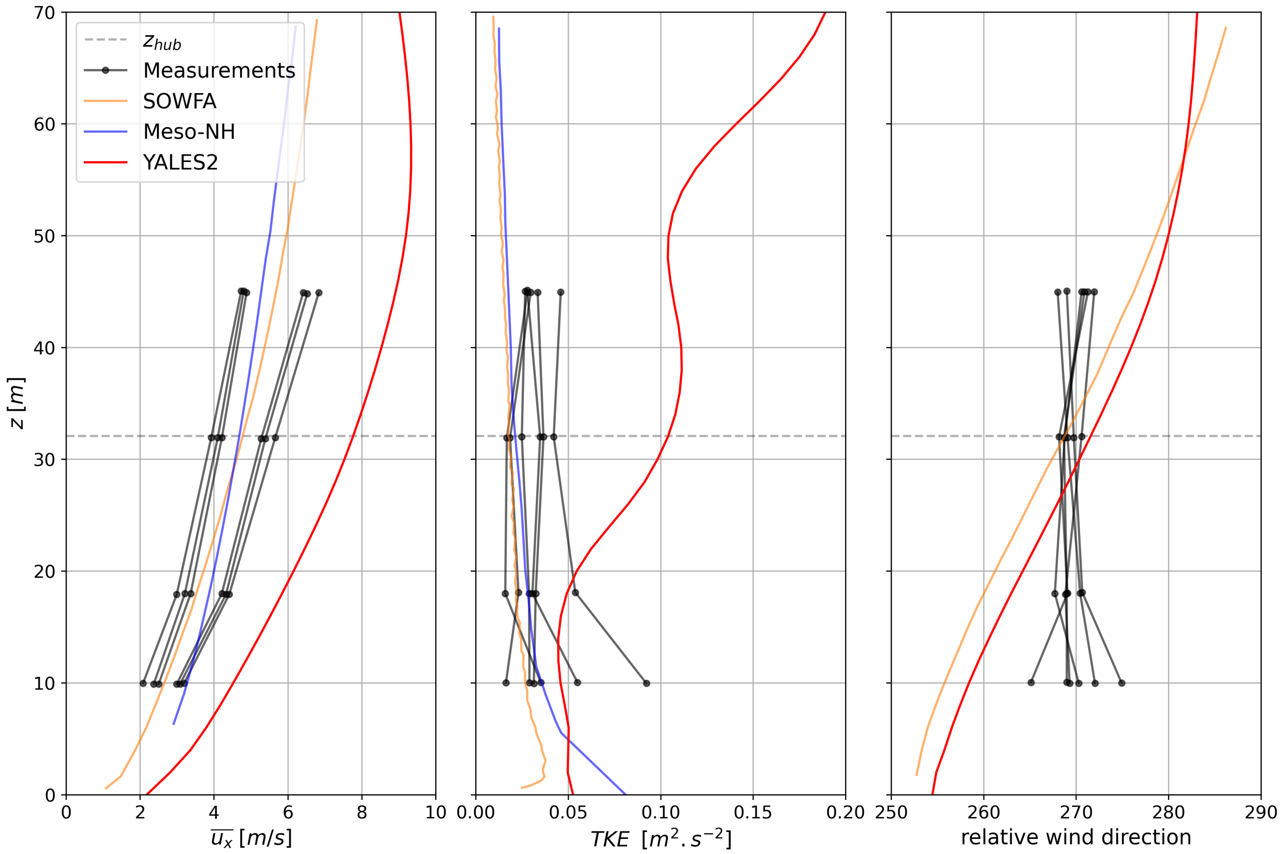

Figure 6.16: Precursor from the increased heat flux stable benchmark. From left to right, average streamwise velocity, turbulent kinetic energy, and relative wind direction.

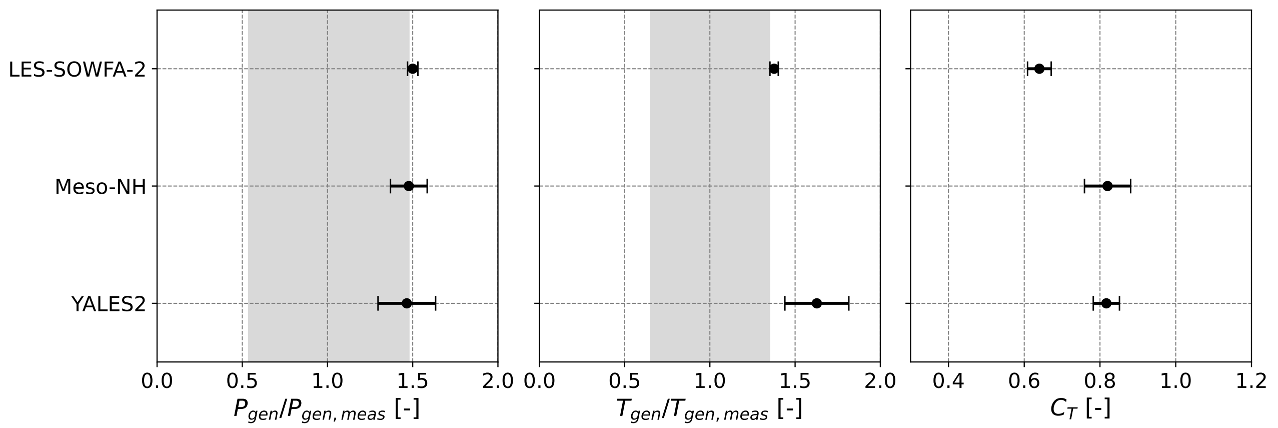

Figure 6.17: Mean and standard deviation for time series of wind turbine response quantities for the stable benchmark.

Experimental measurements are represented by the gray shade, centred around 1 as it serves as an adimentionalisation parameter. The error bars highlight the standard deviation for each study. The results are compared to the SOWFA and Meso-NH studies. The power output is adimentionalised by the average power output experimentally measured, evaluated as: $P_{gen,meas} = 13.2$ kW. The average wind turbine power output in YALES2 is in close agreement with both other LES studies. Again, LES studies tend to overestimate the power output compared to measurements.

The torque output is adimentionalised by the average torque measured experimentally, evaluated as: $T_{gen,meas} = 169.3$ N.m. As the rotation speed is fixed, the power and torque output should follow the same behaviour. However, in this study the torque is overestimated. This might be caused by the inflow that is not strictly streamwise. As the velocity controller could not be used in this study, it was near impossible to guarantee a fully streamwise flow provoking the rotor to be in a yawed configuration with $\gamma = 6°$.

Finally, the thrust coefficient C_T is measured as detailed in Section 6.1.2. The thrust coefficient is equivalent to Meso-NH. The SOWFA study predicts a lower thrust. Unfortunately, it could not be measured experimentally.

Velocity deficit

Finally, Fig. 6.18 shows the time-averaged velocity deficit profiles at four downstream positions in the wake. The velocity deficit is measured horizontally, following the tangential direction, at hub height. YALES2 results are compared against the SOWFA, Meso-NH, and experimental measurements.

At $x = 2$D YALES2 results are in agreement with other LES studies. YALES2 velocity deficit is slightly more pronounced. All three studies exhibit a similar pattern with an over-speed region in the middle of the profile. This behaviour is not measured experimentally and can be due to the lack of nacelle in the simulation. In a further downstream position it appears that the YALES2 wind turbine wake recovers faster than SOWFA, Meso-NH, and the measurements. This result was expected as the inflow turbulence has a much more pronounced TKE and a lower stability parameter. The greater the turbulence, the faster the wake recovery. However, it can still be noted that even though the stability parameter could not be reached, the wake recovery is still slower than the neutral case.

In addition, it can be noted that the LES study velocity deficit profiles do not exhibit a Gaussian profile. Due to the large amount of veer upwind of the turbine, the profiles are skewed. Indeed, the veer does not dissipate the wake, but it skews it more and more as it travels downstream. However, the measurements do not exhibit similar behaviour. This behaviour was already highlighted in the inflow turbulence generation with an experimental relative wind direction near constant with height. LES have reproduced a barotropic SBL while

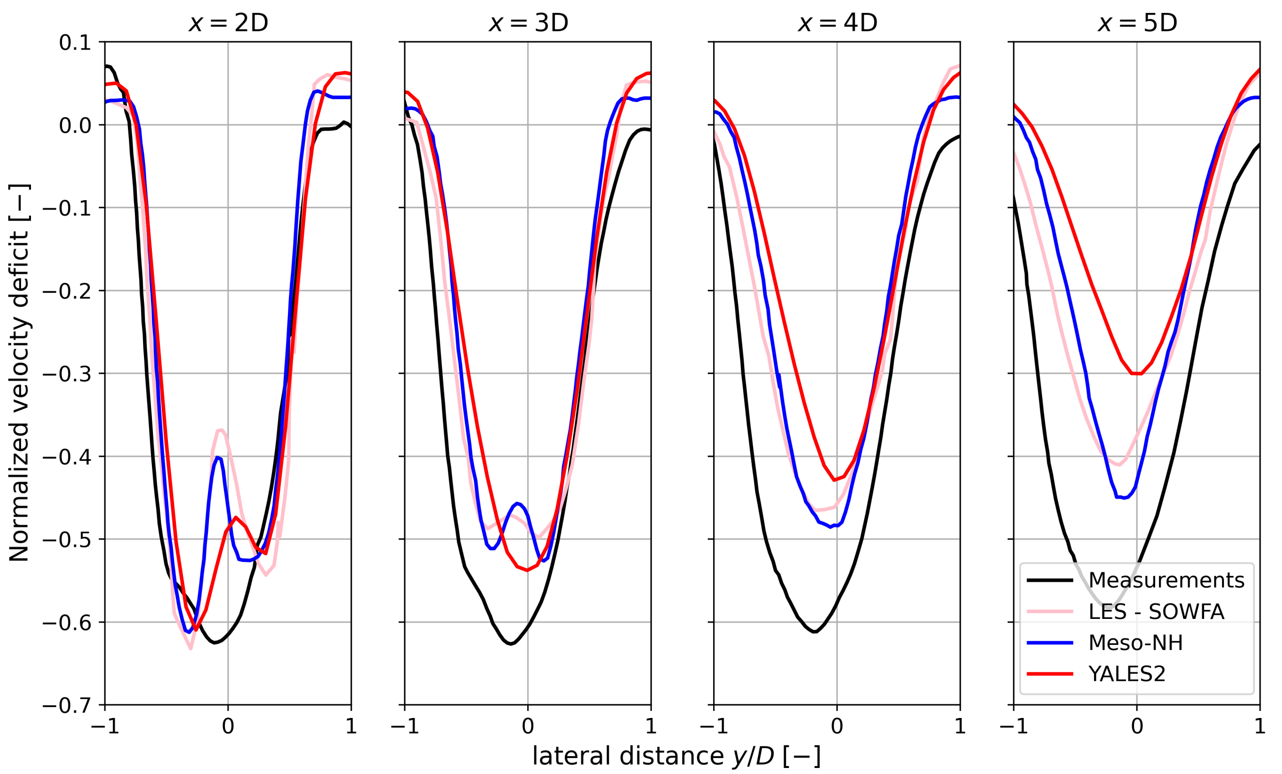

Figure 6.18: Stable benchmark: mean velocity deficit in the wake at hub height. From left to right: 2D, 3D, 4D, and 5D.

the measurements correspond to a baroclinic atmosphere.

6.1.6 Conclusion of the SWiFT benchmark

The SWiFT benchmark has been reproduced using the YALES2 library and the atmospheric solver developed and validated in Chapter 4. The benchmark is divided into two parts, one dealing with a neutral boundary layer and the other with a stable boundary layer. Both cases are decomposed into three steps, which are the generation of the inflow turbulence, the analysis of the rotor response, and the study of the wind turbine wake. In both neutral and stable benchmark, the inflow turbulence is produced using the precursor database method. The wind turbine is a modified Vestas V27 modelled using the actuator line method.

The neutral benchmark inflow turbulence has shown results that are in agreement with the experimental measurements and other LES studies. Although the grid used is coarser than other LES studies, the frictional velocity, the time-averaged velocity, the turbulent kinetic energy, and the relative wind direction profiles exhibit the expected behaviour. The power and torque output are within the standard deviation of the measurements. The thrust coefficient is above other LES studies, but no measurements are available for comparison. The velocity deficit in the wind turbine wake is over-predicted in the near-rotor region. However, beyond 4D downstream, the wake is accurately predicted.

The reproduction of the stable benchmark inflow turbulence is found to be troublesome. Finding the correct set of parameters in terms of geostrophic wind, wall heat flux, and wall roughness is complex. The inflow that best matches the SWiFT parameters correctly reproduces the average velocity. However, the frictional velocity as well as the turbulent kinetic energy are over-predicted. The stability parameter is not reached, even when the wall heat flux is increased. Using this imperfect inflow, the rotor response is studied. The power output and thrust coefficient are well within the range of other studies. The velocity deficits in the wind turbine wake are as expected. Near the wind turbine, the wake is well predicted. However, the wake recovers faster as there is more TKE and less stability in the inflow turbulence. Additionally, the velocity deficit profiles of the LES studies are skewed due to the veer present in the simulation. Conversely, the experimental study which probably measures a baroclinic atmosphere does not exhibit such behaviour.

The purpose of the SWiFT benchmark is to assess the ability of different codes to reproduce the wake of a single wind turbine in an atmospheric inflow. To be able to compare the wind turbine wake, the inflow turbulence of the different studies must match. In that regard, it has been decided to provide the average quantities obtained from the measurements. Based on these data, it is up to the participant to properly reproduce the inflow. However, it appears that, in both neutral and stable benchmarks, the inflow turbulence characteristics are a determining factor in the simulated results. Unfortunately, the parameters given are mainly a consequence of the simulation. The horizontal inflow velocity and the turbulence intensity are a consequence of the flow behaviour, governed by the geostrophic wind, the wall roughness, and the surface heat flux. Thus, it is up to the participants to find the correct set of parameters. However, LES is an expensive technique for studying wind turbines. Performing parametric studies is not feasible at a reasonable computational cost.

To enhance the comprehension of atmospheric boundary layer impact on wind turbine, it would be beneficial to first assess the capacity of the codes to properly reproduce inflow turbulence. For that, the global characteristics of the flow, such as the geostrophic wind, are required. As such, participants would be able to improve their models due to the use of an identical set of parameters. It would be more profitable than performing parametric studies to find the set of parameters that worked best. Especially, it appears that the flow behaviour is partially code-dependent, with different results obtained from different codes using identical sets of parameters. Setting the global parameters could allow for a code-to-code comparison. Although it represents a tremendous amount of work, in the end, it would only be beneficial to assess the ability of different codes to reproduce wind turbine wakes in an atmospheric inflow.

Finally, the SWiFT benchmark is located in the Great Plains region, which means that the site is exempt from the impact of complex terrain. However, the atmospheric solver has been developed in the YALES2 solver because the library can handle complex terrain simulation using unstructured grids. The next part is thus an opening towards the simulation of complex terrain impact on wind turbines, which, after this work, can be carried out using YALES2.

6.2 Complex terrain impact on wind turbines wake

As onshore wind is considered to remain the most cost-efficient form of power generation in Europe [295], it is important to take into account the complexity of the terrain and its interaction with the wakes of wind turbines. However, there are several challenges. The first is the representation of a complex boundary based on topography onto the mesh. Structured meshes, widely used in atmospheric flow simulations, have difficulties following complex geometries. Simple topology might be meshed using a C-shape method [69] but complex terrain, such as the Askervein hill [70], makes it impossible. Alternatives such as Immersed Boundary methods exist, but also have difficulties in well discretizing the boundary layer. The use of an unstructured grid, able to faithfully represent complex geometries, is then very appealing.

However, the complexity of developing high-order flow solvers for unstructured meshes has limited their use in real atmospheric studies. Nevertheless, the YALES2 solver has been chosen for this specific reason. Unstructured meshes can be handled while using high-order numerical schemes. This work is an opening on this subject. An original methodology for ABL flow in complex topography is being designed. Based on a simple scenario, the complex terrain generation and meshing technique are detailed. More complex studies may be considered in the future but are beyond the scope of this work.

6.2.1 Mesh generation

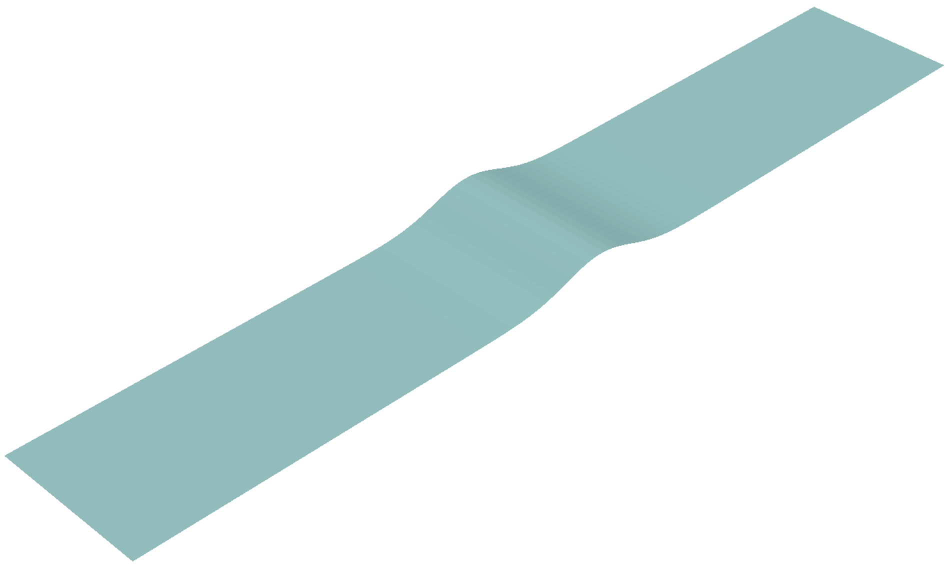

Figure 6.19: Ground topology representation.

An original 3D unstructured mesh generation from a given external surface has been designed in YALES2 [296] and applied into this work. The user-defined parameters required for this methodology are: an unstructured triangulated surface file using STL format, the desired cell size on the surface, coordinates of the 3D domain, and one interior domain point.

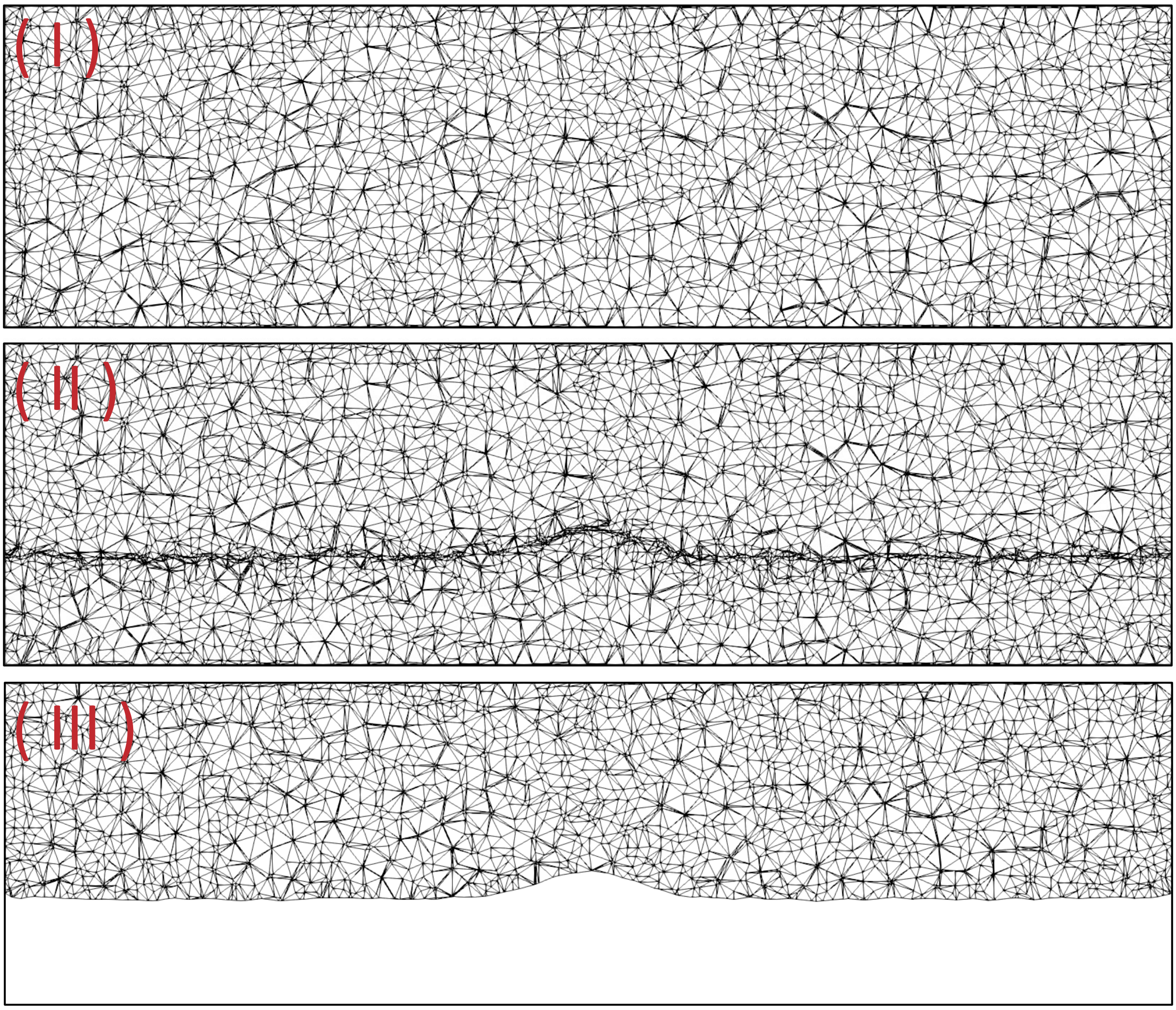

Figure 6.20: 2D slices of the 3D mesh at different steps of mesh generation with complex surface.

This algorithm is illustrated by reproducing a wind tunnel experiment [185], with the 2D Gaussian hill shape topography displayed on Fig. 6.19, proceeds as follows:

1. First, an initial 3D domain coarse mesh is generated thanks to the input coordinates. This mesh is fully unstructured and composed of tetrahedral elements, illustrated by step (I) of Fig. 6.20.

2. The surface STL file is then read, followed by an isotropic surface adaptation step to correctly discretize it. Lagrangian particles are created at the triangle barycenter and at the nodes of the surface. These particles are relocated on the domain grid to find out which cell they belong to. Then, the approximate distance of each node of the volume mesh to the surface is computed.

3. Cells in the vicinity of the surface are then refined by defining a specific metric field. The latter is smaller at the surface location and respects a maximum cell-size gradient condition thanks to an iterative process preserving mesh quality. At this stage, the interior and the exterior of the final flow domain are not distinguishable; moreover, the cells close to the surface do not coincide with it.

4. To obtain a body-fitted mesh, the surface has to be materialized in the 3D unstructured mesh. For this purpose, an implicit representation of the surface is created thanks to a signed distance function generated such that the surface is the zero iso-contour of this level set. All edges, faces and cells that are crossed by the level set function are tessellated in order to transform the implicit surface into an explicitly meshed surface, as shown by step (II) of Fig. 6.20.

5. After the Eulerian mesh cut, the outer domain cells, i.e. below the surface, are flagged thanks to the input interior point coordinate. As illustrated by step (III) of Fig. 6.20, these cells are then removed from the volume mesh and the new surface boundary is created. Finally, to recover a better mesh quality at the surface, a parallel volume and surface adaptation is performed.

The algorithm has also been applied with success on more complex topography than the one studied here. Its major advantage remains on the fully automatic procedure with almost no user action.

6.2.2 Application setup

This work is based on a wind tunnel experiment study of an ABL flow through a wind farm sited on topography [69, 185]. Rotors are modelled using the classical Actuator Disk Method. Turbulence injection is performed using the precursor database method [297]. The subgrid-scale model used is the dynamic Smagorinsky model [105, 106]. The automatic mesh adaptation method [76] is applied, in order to improve the 3D mesh by refining locally based on flow physics. The wind turbine wake is detected during the convergence process and the mesh is consequently adapted in these regions.

We consider a wind tunnel of $12 \times 2 \times 2.3\,\mathrm{m}^3$, in the streamwise, spanwise, and vertical orientations, respectively. The ground follows a two-dimensional hill shape illustrated on Fig. 6.19, described by:

$$Z_S(x) = h \times \exp\left(-0.5\left(\frac{x}{\sigma}\right)^2\right), \tag{6.6}$$

where $h = 285\,\mathrm{mm}$ is the hill height, $L = 570\,\mathrm{mm}$ the hill half-length and $\sigma = L/1.1774$ the standard deviation. The bottom boundary condition is a rough wall with a ratio of roughness to boundary layer height $z_0/h_{BL} = 5.6 \times 10^{-5}$. Five wind turbines, referred to as $T1$ to $T5$, are located on the hill, in the vertical mid-plane with a $3D$ distance between each other, as shown

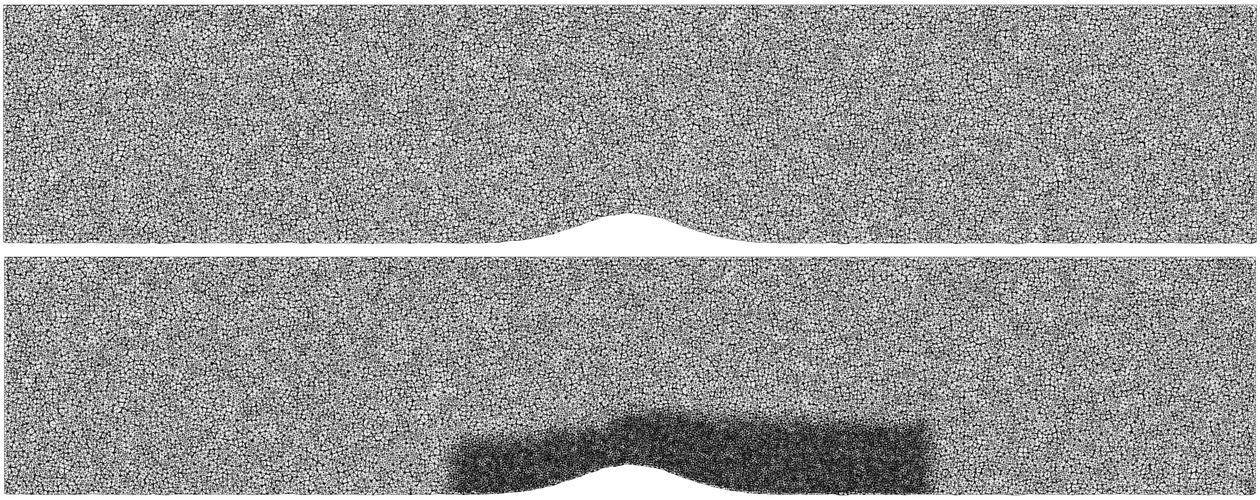

Figure 6.21: Representation of "baseline" (top) and "fine grid" (bottom) meshes.

in Fig. 6.22. Rotor diameter is $D = 0.254\,\text{m}$ and hub height is $Z_h = 0.225\,\text{m}$ above the ground. The thrust coefficients measured experimentally [185] given in Tab. 6.6 are directly imposed in the ADM. Statistics are accumulated over 40 s of physical time, that is, $\tau = 47D/u_{x,\infty} = 13$ domain flow-through times.

	T1	T2	T3	T4	T5
C_T	0.14	0.132	0.287	0.129	0.091

Table 6.6: Thrust coefficient C_T of the five turbines

Two studies are carried out. The first one is performed using a homogeneous unstructured grid with a mesh size equivalent to the one used in [69], i.e. $\Delta = 0.047\,\text{m}$, listed as the "baseline" study. The second is carried out using the automatic mesh adaptation process. The mesh size in the wind turbine wakes is set at $\Delta = 0.0225\,\text{m}$, which corresponds to approximately $\Delta/D = 10$ cells per rotor diameter. The mesh is then twice finer is the wake area, allowing to better capture the flow dynamics. This study will be referred to as the "fine grid". Figure 6.21 displays both "baseline" and "fine grid" meshes.

6.2.3 Results

Figure 6.22 displays the vertical midplane instantaneous streamwise velocity field. The global flow behaviour represents an ABL which follows a logarithmic law. An overspeed zone is located over the hill, while a low speed region is found behind it. Wind turbines are therefore not in the same velocity range, explaining the different thrust coefficients used from one wind turbine to another by the ADM.

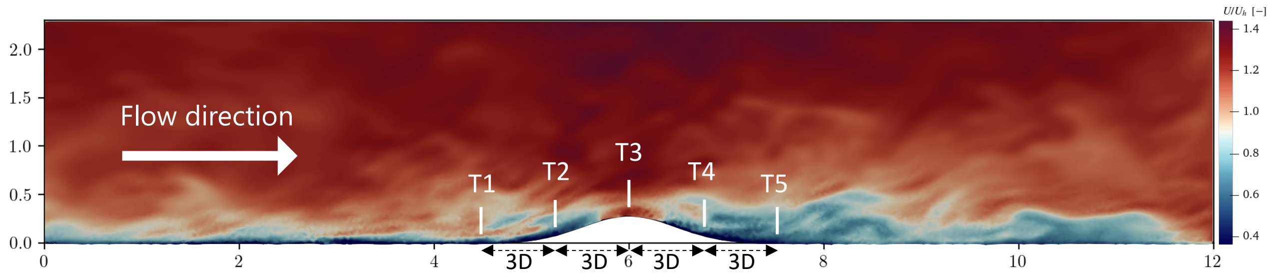

Figure 6.22: Instantaneous streamwise velocity field in the vertical midplane.

Dimensionless vertical profiles of the time-averaged streamwise velocity at each wind turbine location are shown in Fig. 6.23. The results are compared with previous experimental [185] and numerical [69] profiles. The relative L2 norm error is computed for each mean streamwise velocity profiles with the experimental study [185] as a reference. The results are gathered in Tab. 6.7. For the "baseline" case, the error varies from 4.2% to 8%. The previous LES study showed similar gaps, varying from 2.2% to 7.3%.

	T1	T2	T3	T4	T5
ε_{L2}	8.0%	7.2%	4.2%	7.1%	5.1%

Table 6.7: Relative L2 norm error, ε_{L2}, to the experimental data for the five average velocity profiles.

6.2.4 Conclusion

A methodology has been developed to take into account the complex terrain in LES. It is based on a high-order flow solver and an original 3D unstructured mesh generator from an external surface, embedded. In addition, the automatic grid adaptation strategy based on flow dynamics has been employed to refine the wake area. The full methodology has been compared to a small-scale experimental campaign and previous LES study, by performing LES on both a homogeneous and a refined grids. Time-averaged streamwise velocity profiles at wind turbine positions show good agreement. The overall methodology has been verified and is ready to be applied to more complex topography.

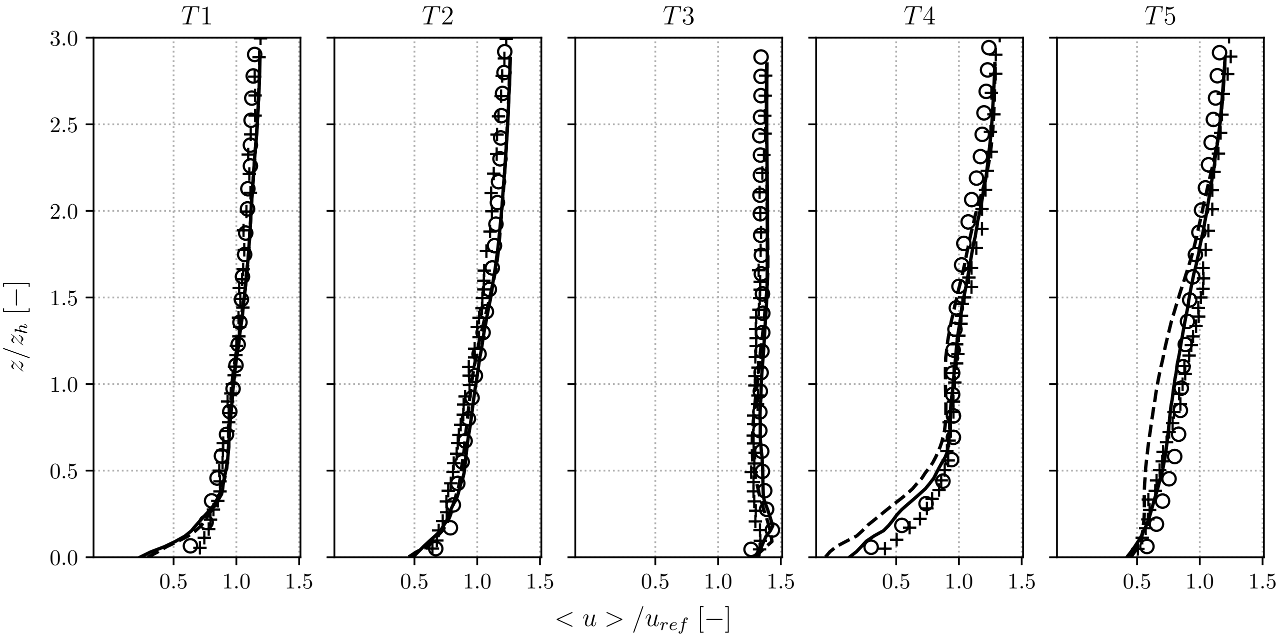

Figure 6.23: Time-averaged streamwise velocity profiles at wind turbine positions. (+) for the experiment results [185], (∘) for the LES results [69], (——) for the "baseline" results, (- - -) for the "fine grid" results.

Chapter 7

Conclusion and perspectives

In the final chapter, general conclusions of this thesis are drawn and perspectives for future investigations are discussed in the field of atmospheric boundary layer and complex terrain impact on wind turbines.

Contents

7.1 Conclusion 168

7.1.1 General background 168

7.1.2 Development and validation of the atmospheric solver 168

7.1.3 The adaptive mesh refinement strategy 170

7.1.4 Application to realistic wind turbine studies 171

7.2 Perspectives 172

7.2.1 Optimisations and improvements of the atmospheric solver 173

7.2.2 Improving the realistic inflow turbulence 173

7.2.3 Enhance the adaptive mesh refinement strategy 174

7.2.4 Long term perspectives 175

7.1 Conclusion

7.1.1 General background

In the introduction to this dissertation, the alarming toll of global warming has been taken. The key role of wind energy in the energy transition has been stressed. Continued innovation is still needed for wind energy to achieve its full potential with affordable and reliable machines. Increasing the size of wind turbines is one path to achieve the wind-sourced electrical production targets. Yet, it involves new challenges regarding the new scales and physics involved. Specifically, wind turbines are no longer solely impacted by the micro-scale, but also by the meso-scale. This gives rise to the first wind turbine grand challenges, improving the understanding of atmospheric and wind power plant flow physics.

This work aims to tackle several challenges, notably the accurate simulation of atmospheric boundary layers, their impact on wind turbines, and the effect of complex terrains on such flows. To address these issues, this work uses a solver that can perform large-eddy simulations, handle massively parallel computations, manage unstructured grids, and use high-order numerical schemes. To the author's knowledge, there was no solver in the atmospheric flow community that met these criteria. Therefore, a new solver has been developed based on the YALES2 library.

This library had already been used multiple times for wind turbine simulations. However, it had never been used for atmospheric flow simulations. The first steps of this work was therefore to develop an atmospheric solver that can reproduce atmospheric flows in a wind turbine simulation framework. For that, it was necessary to develop a number of fundamental components. This encompasses the Coriolis force, predominant in the flow behaviour; the Boussinesq buoyancy approximation, to take into account density variation induced by temperature fluctuations; and the Monin-Obukhov Similarity Theory, a wall model to accurately deal with the flow at the wall.

This newly developed atmospheric flow solver had to be validated before it could be used for realistic wind turbine studies. On the road, an adaptive mesh refinement strategy has been developed to optimise the computational costs. Through this final chapter, a summary of the most significant contributions identified in this work is provided, and potential improvements and perspectives are discussed.

7.1.2 Development and validation of the atmospheric solver

Development

The first step in this thesis has been to develop an atmospheric solver in the YALES2 library. By looking at the literature, three fundamental components were identified as key parameters.

The first is the Coriolis force. Atmospheric flows are largely impacted by geostrophic balance, in which the Coriolis force is a primary factor. Accurately representing an atmospheric boundary layer involves taking into account the Coriolis force. For its implementation, the Coriolis force is not implemented straightforwardly. Instead, a source term in the velocity field acts to drive the flow towards the geostrophic wind. At altitude, the velocity reaches the geostrophic wind, whereas, lower, the wall friction slows the flow. It enables the representation of the geostrophic balance.

The second is the Boussinesq buoyancy approximation. Thermal effects greatly impact the flow behaviour and must therefore be taken into account. However, atmospheric simulations do not require a fully compressible solver as temperature variations are limited. In the literature, numerous codes use the Boussinesq approximation to take into account thermal effects. In the flow, a passive scalar that accounts for the temperature is transported. The density is computed from the temperature on the basis of the ideal gas law. From this scalar density, a source term in the velocity field is imposed, allowing for density effects. However, with this approximation, only vertical temperature gradients are taken into account.

The third is a wall model. A wall-resolved LES for atmospheric flows is computationally unaffordable. Therefore, a wall model must be used to correctly take into account the effect of the wall on the flow. In the literature, the Monin-Obukhov similarity theory is widely used. This wall model has thus been implemented in YALES2. This theory relies on logarithmic velocity and temperature profiles with correction terms to adequately match the thermal configuration. A particular focus was given to two points. First, it was mentioned in the literature that the MOST wall law for stable stratification is more reliable when prescribing the surface temperature instead of the surface heat flux as a boundary condition. However, as seen in the studies performed in this work, some benchmarks prescribe the wall temperature, while others prescribe the wall heat flux. Thus, both methods have been implemented into the YALES2 library. Second, since wall models are derived from averaged Navier-Stokes equations, quantities such as velocity and temperature must be spatially filtered. Although filtering quantities at the first node horizontal plane is straightforward for structured grids, it turns out to be much more complicated for unstructured grids. To overcome this difficulty, a "Gather-Scatter" filtering operator has been adopted.

Validation

The newly developed atmospheric solver has been validated against several atmospheric scenarios with various thermal configurations. First, the neutral configuration isolates the use of the Coriolis force, with the MOST wall law being simplified in its neutral configuration. Although the study is brief with only one configuration being studied, the results are promising as they match other numerical results.

In a second stage, an unstable configuration has been studied. It uses the Coriolis force, the Boussinesq approximation and the wall law in its non-neutral form. Yet, this configuration has been performed numerous times in the literature. The CBL is known to be easier to reproduce than an SBL due to its increased turbulence and vorticies characteristic sizes. The CBL results were conclusive, as they match both experimental measurements and numerical results.

Finally, a stable configuration has been studied, the GABLS1 benchmark. The GABLS1 benchmark has been widely performed in the literature. It serves as a reference case for simulating an SBL. The results of this benchmark are in good agreement with other LES studies. Various resolutions have been used to provide a minimum cell size, required to perform an accurate stable boundary layer simulation. However, two sources of debate have been highlighted in the design of the benchmark. The first is the definition of the initial condition, and the second is the accumulation of numerical errors. Both could lead to unexpected errors, and it would be better to limit their impact.

The stable study was also carried out on an unstructured grid. The main objective of this work was to enable the use of unstructured meshes for the LES of SBLs as, to the author's knowledge, it has never been performed. The idea behind this is that unstructured grids may not be required to mesh a cubic domain such as GABLS1, but it may become valuable when studying complex terrains. Reproducing realistic topography relies on the use of unstructured grids, as structured grids cannot reflect complex geometries.

7.1.3 The adaptive mesh refinement strategy

In the previous chapter, it has been highlighted that a fine mesh is required to properly reproduce a stable boundary layer. This is due to the SBL reduced turbulence and height, which produces vorticies with smaller characteristic sizes. However, the LES is already an expensive technique for studying wind turbines. Optimising the cost-fidelity trade-off becomes a notable issue. The aim was to develop a strategy to reduce the computational cost of wind turbine simulations while ensuring physical precision in the regions of interest. Although one strategy could be to use a fine mesh throughout the entire domain, it is computationally unaffordable. Therefore, the first step is to detect the regions of interest.

In wind turbine simulation, when using the actuator line method, the regions of interest are the rotor region and the wind turbine wake. The rotor region must be finely discretised to accurately reproduce the effect of the wind turbine on the flow. The wake region must be finely discretised so that turbulence in this region is accurately transported. The wake of a wind turbine being the inflow of another in wind farms, it becomes an important region to study. The wind turbine region is easy to predetermine as it is established by the user. However, the wake is a turbulent region with meandering and a fluctuating position. This is particularly true for a yawed turbine. To track the wake, the methodology developed in this thesis is based on a progress variable with a source term in the rotor region. The scalar is then transported on the Eulerian grid, defining the wake envelope.

The second step of the strategy is to define the cell size inside the regions of interest. In this work, the cell size is constant and set by the user. Finally, the third and last step of the strategy is to define the frequency at which the adaptation will occur. For that, a metric error is measured on each control volume as the local ratio between actual and target cell sizes. When this ratio exceeds a specified threshold value on a sufficiently large number of elements, the AMR is triggered.

The AMR strategy was compared to a reference case with uniform cell size in a coarsely defined wake region. The results are conclusive with a reduction in mesh size and computational cost while maintaining the same physical precision. This methodology is therefore validated and can be used in future wind turbine studies.

7.1.4 Application to realistic wind turbine studies

Previous chapters have enabled to tackle realistic wind turbine simulation studies. The first study has been dedicated to the atmospheric boundary layer impact on a single wind turbine. For that, different atmospheric stabilities have been reproduced and their impact on a wind turbine has been quantified. This work is based on a SWiFT benchmark. The second is the study of a complex terrain impact on wind turbines wake. More than a comprehensive study, this section is an opening, reviewing the mesh generation methodology.

Atmospheric boundary layer impact on wind turbines

The SWiFT benchmark is part of the IEA Wind Task 31, and aims to enhance comprehension of atmospheric boundary layer impact on wind turbine. Based on experimental measurements, the benchmark is divided into three configurations: neutral, unstable, and stable thermal stratification. In this work, only two configurations have been carried out, the neutral configuration and the stable configuration.

The neutral benchmark inflow turbulence was correctly reproduced. Average quantities such as frictional velocity, streamwise velocity, turbulent kinetic energy, and relative wind direction are in agreement with the measurements and other LES studies. Wind turbine responses are also in the results range, apart from the thrust coefficient which is over-estimated. This is reflected in the wake, where the velocity deficit near the wind turbine is over-estimated. However, beyond some distance, it again matches the experimental results.

The stable benchmark inflow turbulence has been found to be difficult to reproduce. Matching all the parameters in terms of velocity, turbulent kinetic energy, frictional velocity, and stability parameter at the same time was not possible. Increasing the stability parameter only resulted in increasing the velocity and TKE at hub height. Therefore, a compromise between stability, velocity, and TKE has been selected. The rotor outputs fall within the range of data. The velocity deficit is, as expected, recovering faster than in other studies as the stability parameter could not be reached.

Finally, the conclusions of the SWiFT benchmark are that although it can be improved, the atmospheric solver is capable of handling realistic wind turbine simulation studies. However, it was pointed out that to assess the ability of different codes to reproduce the wake of a wind turbine in an atmospheric inflow, it would be preferable to impose the global characteristics of the flow such as the geostrophic wind. As such, participants would be able to improve their models due to the use of an identical set of parameters. It would be more profitable than performing parametric studies to find the set of parameters that worked best.

Complex terrain impact on wind turbines

The atmospheric solver has been developed and successfully validated in various thermal stability scenarios. Unstructured grids have been shown to correctly reproduce ABLs. However, the main goal of using a solver capable of handling unstructured grids using high-order numerical schemes was to be able to perform complex terrain simulation. For that, a simple scenario has been used, with five wind turbines located on a 2D Gaussian hill shape topography.

The first stage of this methodology is the generation of the ground. For that, the "pyvista" python module is used. Once the boundary is generated, this work relies on an original 3D unstructured mesh generation from a given external surface. Isotropic surface adaptation is used to discretise the boundary. Cells in the vicinity of the surface are then refined. Finally, a Eulerian mesh cut is performed, deleting the cells below the new boundary.

With the new meshed domain, a complex terrain study can be performed. This study is based on a wind tunnel experiment. The AMR methodology is used to refine the mesh in the wind turbine wake region. This work uses the precursor database method for the inflow turbulence generation and the actuator disk method for the wind turbine modelling. Finally, the wind tunnel experiments could be reproduced. Although this study is not based on a realistic experimental benchmark, it opens the door to further studies and further work.

7.2 Perspectives

From a broad perspective, this thesis has contributed to the field of atmospheric flow impact on wind turbines, relying on numerical simulation tools. Some perspectives emerge as a direct continuation of the work reported in this dissertation. Others are more general and longer-term. They are presented below.

7.2.1 Optimisations and improvements of the atmospheric solver

The most straightforward perspective following this work is to improve the atmospheric solver. Although able to reproduce atmospheric boundary layers, improvements in terms of physics and numerics can still be made. The first improvement would be to implement a subgrid-scale model that can accurately handle stratified atmospheric flows. The SGS model used in this thesis is the dynamic Smagorinsky model. This model is widely used because it is universal, has no tuning parameter; and local, the Smagorinsky constant adapts to weakly/strongly turbulent regions by locally reducing/increasing dissipation. However, this model is based on the assumption of small-scale isotropy. Although valid in neutral configurations, stable configurations have anisotropic behaviour on small scales. Based on the literature review performed in Chapter 2, the anisotropic minimum dissipation model appears to be the one that is the most suitable. Even though it has tuning coefficients, the model relies on three-dimensional variation of the SGS coefficients allowing to deal with anisotropic turbulence.

An addition to the atmospheric solver would be the use of a low-Mach number variable density solver. Today, the only thermal effects that are taken into account are density-based and thus only vertical. However, in realistic wind turbine scenarios, horizontal temperature gradients can also occur, particularly in a wind turbine wake, a highly turbulent region. Developing a full incompressible variable density solver is probably not worth the time, as these effects are probably minor. However, in YALES2, such a solver already exists, and the atmospheric solver has been designed to be compatible with it. Therefore, further studies can be performed to try to quantify the impact of non-gravity-induced density effects.

Finally, given the computational cost of wind turbine LES studies, improving the code performance is always valuable. Quantifying the computational cost of the different parts of the code, it appears that most of the computational time is spent in the linear solver. While the wall law with filtering operations takes less than 3% of the computational time, the linear solver to solve the Poisson equation takes up to 60%. Although the linear solver is expected to be time-consuming, improvements can be made. In particular, in atmospheric flow simulations, the Coriolis force and the Boussinesq approximation are source terms imposed on the velocity field. The pressure correction step thus takes longer. Adding these terms directly into the momentum equations could reduce the pressure correction step time and thus improve the overall performance.

7.2.2 Improving the realistic inflow turbulence

In Chapter 6 it has been highlighted that inflow turbulence is a major parameter for realistic wind turbine simulations. In this thesis, the inflow turbulence is based on the precursor database method. However, there is room for improvement. First, in the SWiFT neutral study, a velocity controller has been used. It ensures that the flow reaches the prescribed velocity at hub height. However, the velocity controller could not be used in the wind turbine simulation domain as it would impact the wind turbine wake. An improvement would be to enable its use in the wind turbine simulation domain and not only on the precursor.

Another issue that has been highlighted is that the velocity controller does not act as expected in the stable study. In the SWiFT stable study, it appeared that the flow could not reach the prescribed velocity at hub height. Unfortunately, as the controller acts on the whole domain, the source term was continuously reducing the global velocity. By the end of the simulation, the velocity at geostrophic height had decreased drastically. For this particular reason, the velocity controller was not used. Consequently, this has prevented the flow to be solely streamwise. An addition to the velocity controller would be to be able to use it in all thermal conditions.

The stable SWiFT benchmark was performed using a constant cooling rate at the bottom. Gradually, the heat flux led to a decline in flow temperature. Although this cooling did not seem to greatly impact the flow, it remains that the overall energy continues to reduce. For longer simulations, this might cause disturbances. A solution would be to implement throughout a modified temperature a wall temperature gradient forcing. It would compensate the temperature decrease in the periodic streamwise direction.

7.2.3 Enhance the adaptive mesh refinement strategy

The adaptive mesh refinement strategy proposed in Chapter 5 is based on three stages. The first stage is the detection of the area to refine, the second is the target cell size definition in this area and finally, the third is the frequency at which adaptation occurs. The first stage is performed using a progress variable with a source term in the rotor region. The third stage is performed based on a metric error evaluation and a threshold value. However, for the moment, the second stage is based on a user-dependent target value. This results in a constant cell size in the area of interest. Although functioning, this strategy could benefit from a local target cell size computed on the basis of flow physics. Several criteria exist in the literature. The cell Reynolds number, based on the local vorticity and cell size, could be used. The kinetic energy budget could also be a satisfying option.

The adaptive mesh refinement strategy could be expanded. In other YALES2 wind turbine studies, wake tracking was performed using an Accurate Conservative Level Set function. These methods are known for their strictly conservative behaviour with low diffusion errors. For this particular reason, using this method instead of the progress variable could be advantageous. However, before drawing any definitive conclusions, a comparison study should be performed. In particular, it seems that both methods undergo the same issue. When simulating a large domain, such as a wind farm or a row of wind turbines, the progress variable and the level-set function expend heights as moving forward in the field. They follow the internal boundary layer of the wind farm. The detection area is thus enlarged, leading to large and unnecessary refined areas. To offset this phenomenon, using different progress variable or level set functions for each wind turbine and limiting the expansion of each variable could operate.

7.2.4 Long term perspectives

Finally, the objectives of this thesis have been met. An atmospheric solver has been developed and validated against several studies with various thermal configurations. An adaptive mesh refinement strategy to reduce the computational cost has been developed. Applications to realistic wind turbine studies have been performed. However, these studies only used a limited number of wind turbines. Based on this work, simulations of full-scale wind farms can now be performed. As such, the interaction between wind turbines in atmospheric flows could be studied. This would make a real contribution, as most wind turbines are grouped into farms for operational reasons.

Moving from the wind turbine scale to the wind farm scale raises the question of the coupling with a meso-scale solver. In the literature review in Chapter 2, it has emerged that for large-scale studies, meso-scale modelling offers insights into atmospheric dynamics at regional scales. These models bridge the gap between global climate models and micro-scale simulations, providing essential boundary conditions for wind farm flows. Therefore, the coupling of YALES2 with a meso-scale solver such as WRF would only be beneficial for large-scale realistic studies.

Finally, during this work, validation is often mentioned. As a new atmospheric solver was developed, each piece had to be validated. For that, comparisons with other studies have been made. Usually, to compare two different profiles, the relative L2 norm error was measured. However, this measurement is hardly sufficient. In has been demonstrated in the literature the potential of applying uncertainty quantification methods to address validation with field measurements and to develop a more realistic approach. This could be a future objective to complete the validation carried out in this work.

Appendices

A YALES2 Scaling on LUMI supercomputer

YALES2 is a software designed for supercomputer massively parallel computation. To measure its performance and validate its use on large meshes, scaling tests on the LUMI supercomputer are performed. The test is based on a Taylor-Green vortex simulation with a Reynolds number at $Re = 2500$. Statistics are gathered over 10 iterations. Strong and weak scaling have been performed. Fig. 1 presents the strong scaling speed-up and element per core evolution. Fig. 2 presents the weak scaling speed-up.

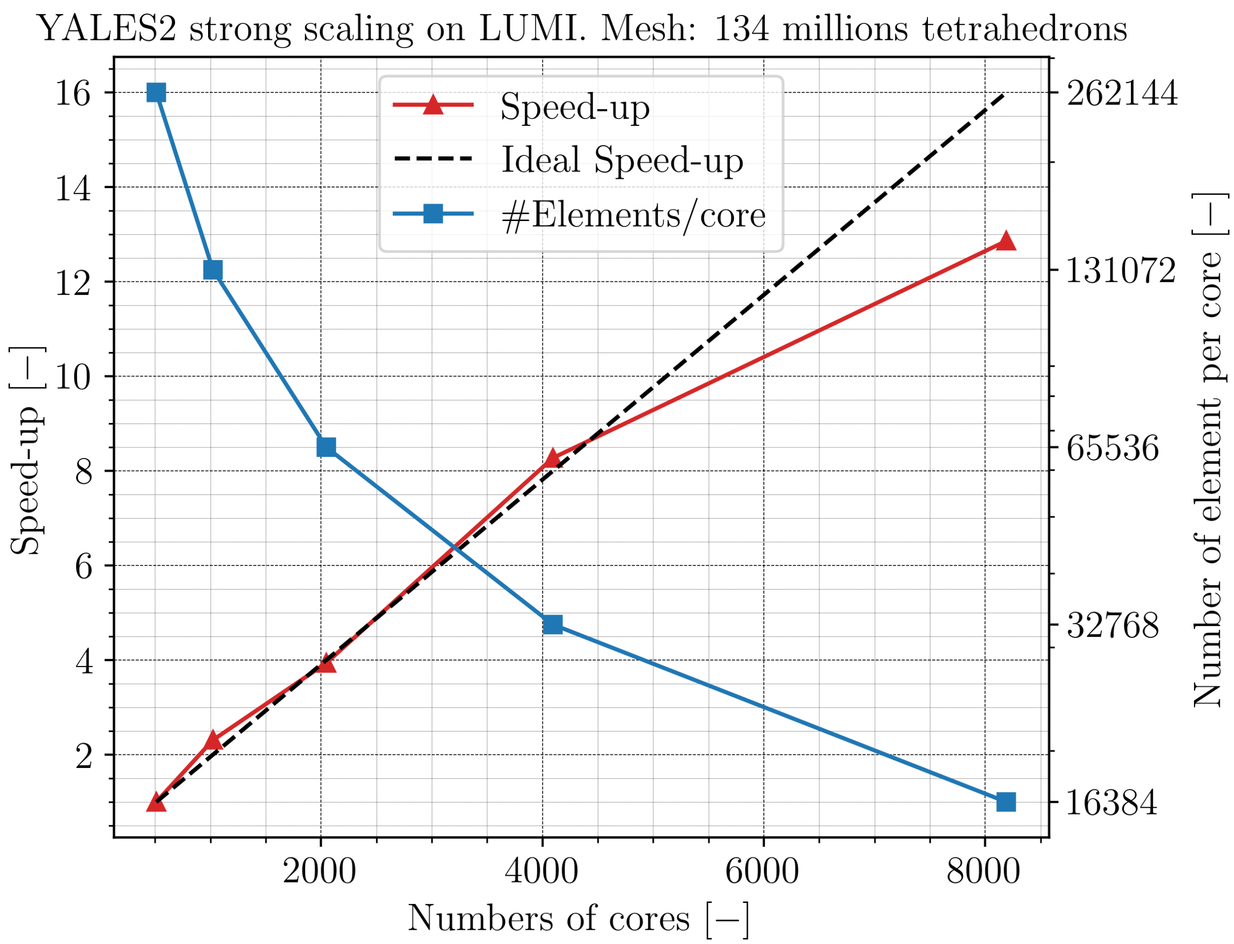

Figure 1: Strong scaling on LUMI. Mesh: 134 million tetrahedrons.

In the strong scaling test, as the problem is identical but the number of cores increase, the number of elements per cores decrease. Conversely, for the weak scaling test, as the problem

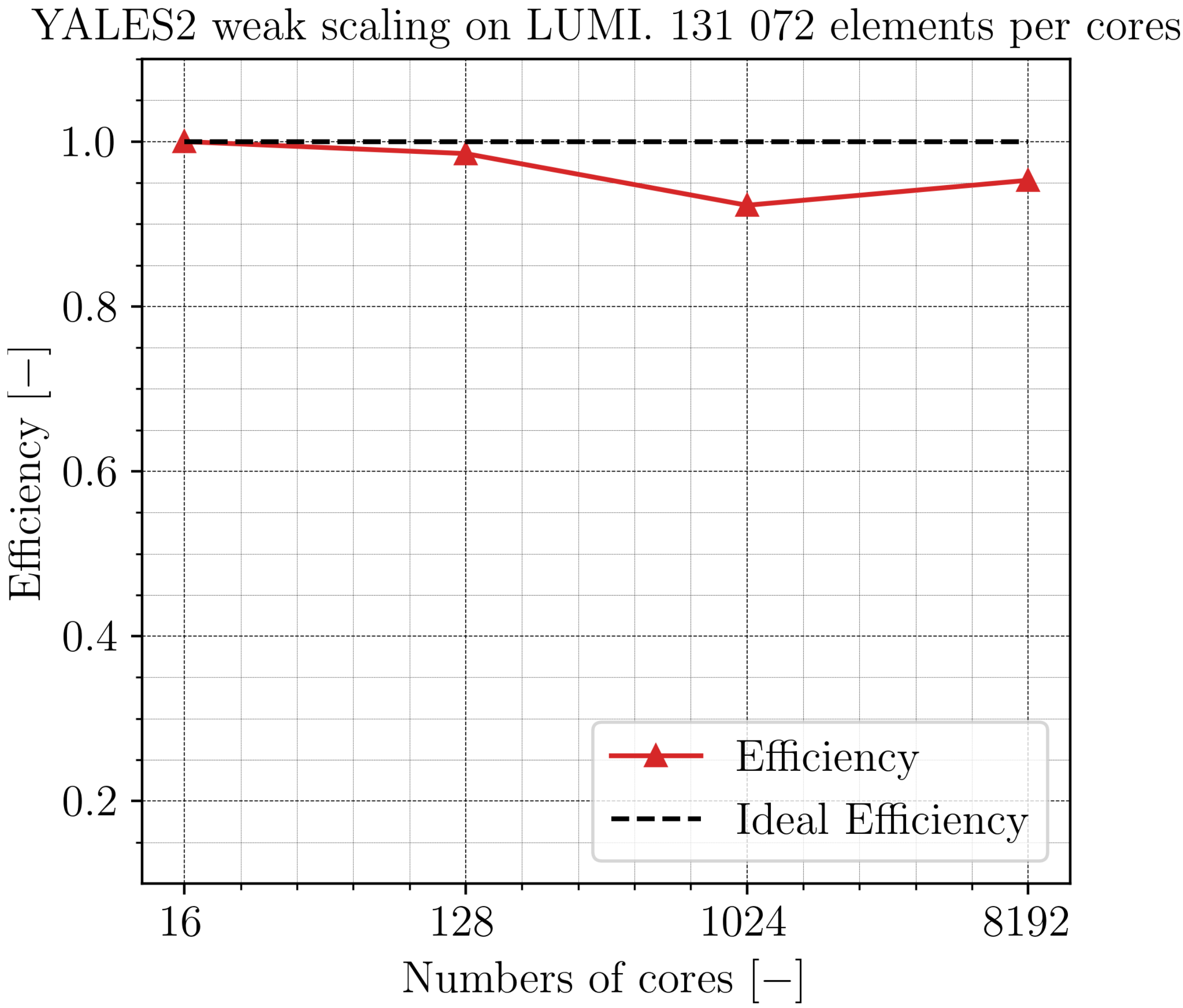

Figure 2: Weak scaling on LUMI. 131 072 elements per cores.

size increase, the number of elements per core is constant. The weak scaling shows us that YALES2 behaves correctly when using multiple number of cores. Between 16 and 8192 cores, the efficiency as only decrease by 5%. The strong scaling shows us that below 4096 cores, the scaling is almost perfect compared to the theoretical curve. Beyond that point, efficiency is reduced. But as weak scaling as shown, the issue is not to use multiple cores, but to use very high number of cores per elements (number of elements per core below 32000). As YALES2 is designed to be scalable between 50k and 500k elements/cores, the scaling test performed on LUMI is consistent.

B TFV4A temporal discretization scheme

For a given quantity ζ the transport equation follows:

$$\frac{\partial \zeta}{\partial t} + \mathbf{u} \cdot \nabla \zeta = 0 \tag{1}$$

where the flow velocity u is assumed constant. For a discretized convection term C_i at node i, a simple one-step discretized transport equation would be:

$$\zeta_i^{n+1} = \zeta_i^n - \Delta t \mathcal{C}_i \left(\zeta_i^n, \mathbf{u}_i\right) \tag{2}$$

In the RK4 method, the advancement is decomposed into four steps, following:

$$\begin{cases} \zeta_i^{(1)} = \zeta_i^n - \frac{\Delta t}{4} \mathcal{C}_i \left(\zeta_i^n, \mathbf{u}_i\right) \\ \zeta_i^{(2)} = \zeta_i^n - \frac{\Delta t}{3} \mathcal{C}_i \left(\zeta_i^{(1)}, \mathbf{u}_i\right) \\ \zeta_i^{(3)} = \zeta_i^n - \frac{\Delta t}{2} \mathcal{C}_i \left(\zeta_i^{(2)}, \mathbf{u}_i\right) \\ \zeta_i^{n+1} = \zeta_i^n - \Delta t \mathcal{C}_i \left(\zeta_i^{(3)}, \mathbf{u}_i\right) \end{cases} \tag{3}$$

For the TFV4A scheme, the Eq. 3 can be rewritten as a two-step method by recursion as:

$$\begin{cases} \zeta_i^{(2)} = \zeta_i^n - \frac{\Delta t}{3} \mathcal{C}_i \left(\zeta_i^n, \mathbf{u}_i\right) + \frac{\Delta t^2}{12} \mathcal{C}_i^2 \left(\zeta_i^n, \mathbf{u}_i\right) \\ \zeta_i^{n+1} = \zeta_i^n - \Delta t \mathcal{C}_i \left(\zeta_i^n, \mathbf{u}_i\right) + \frac{\Delta t^2}{2} \mathcal{C}_i^2 \left(\zeta_i^{(2)}, \mathbf{u}_i\right) \end{cases} \tag{4}$$

Where $\mathcal{C}^2 = \mathcal{C} \circ \mathcal{C} = \mathbf{u} \cdot \boldsymbol{\nabla}(\mathbf{u} \cdot \nabla \zeta)$ is the twice-applied convection operator.

The TTG4A can be written as:

$$\begin{cases} \zeta_i^{(2)} = \zeta_i^n - \frac{\Delta t}{3} \mathcal{C}_i \left(\zeta_i^n, \mathbf{u}_i\right) + \frac{\Delta t^2}{12} \mathcal{D}_i \left(\zeta_i^n, \mathbf{u}_i\right) \\ \zeta_i^{n+1} = \zeta_i^n - \Delta t \mathcal{C}_i \left(\zeta_i^n, \mathbf{u}_i\right) + \frac{\Delta t^2}{2} \mathcal{D}_i \left(\zeta_i^{(2)}, \mathbf{u}_i\right) \end{cases} \tag{5}$$

where the twice-composed convection operator $\mathcal{C}^2$ in RK4 is replaced by a compact diffusion operator $\mathcal{D}$. A linear combination between RK4 and TTG4A yields:

$$\begin{cases} \zeta_i^{(2)} = \zeta_i^n - \alpha \frac{\Delta t}{3} \mathcal{C}_i \left(\zeta_i^n, \mathbf{u}_i\right) + (1-\alpha) \frac{\Delta t^2}{12} \mathcal{C}_i^2 \left(\zeta_i^n, \mathbf{u}_i\right) + \alpha \frac{\Delta t^2}{12} \mathcal{D}_i \left(\zeta_i^n, \mathbf{u}_i\right) \\ \zeta_i^{n+1} = \zeta_i^n - \alpha \Delta t \mathcal{C}_i \left(\zeta_i^n, \mathbf{u}_i\right) + (1-\alpha) \frac{\Delta t^2}{2} \mathcal{C}_i^2 \left(\zeta_i^{(2)}, \mathbf{u}_i\right) + \alpha \frac{\Delta t^2}{2} \mathcal{D}_i \left(\zeta_i^{(2)}, \mathbf{u}_i\right) \end{cases} \tag{6}$$

where α is an adjustable parameter, to set the impact of the diffusive terms. If $\alpha = 1$, the method relies on the TTG4A, while for $\alpha = 0$, the method relies on the RK4 scheme.

C Newton-Raphson algorithm

When surface temperature is prescribed, a two-unknown problem, u_* and θ_*, has to be resolved. For that we use a double Newton-Raphson convergence method for its quadratic convergence speed.

We define:

$$\mathbf{X} = \begin{bmatrix} u_* \\ \theta_* \end{bmatrix} \quad \text{and} \quad F(\mathbf{X}) = \begin{bmatrix} f_1(u_*, \theta_*) \\ f_2(u_*, \theta_*) \end{bmatrix} \tag{7}$$

where f_1 and f_2 can be expressed as:

$$\begin{aligned} f_1(u_*, \theta_*) &= u_* - \frac{u\kappa}{\ln\left(\frac{z}{z_0}\right) - \psi_m\left(\frac{z-z_0}{L}\right)} \\ f_2(u_*, \theta_*) &= \theta_* - \frac{\Delta T u_* \kappa}{\ln\left(\frac{z}{z_0}\right) - \psi_m\left(\frac{z-z_0}{L}\right)} \end{aligned} \tag{8}$$

The system is resolved when $F(\mathbf{X}) = 0$. But $F(\mathbf{X})$ can be expressed as:

$$F(\mathbf{X}^n) = F(\mathbf{X}^{n-1}) + \frac{\partial \mathbf{F}}{\partial \mathbf{X}} \left(\mathbf{X}^n - \mathbf{X}^{n-1}\right) \tag{9}$$

$$0 = F(\mathbf{X}^{n-1}) + \frac{\partial \mathbf{F}}{\partial \mathbf{X}} \left(\mathbf{X}^n - \mathbf{X}^{n-1}\right) \tag{10}$$

$$\mathbf{X}^n = \mathbf{X}^{n-1} - \left(\frac{\partial \mathbf{F}}{\partial \mathbf{X}}\right)^{-1} F(\mathbf{X}^{n-1}) \tag{11}$$

Following Newton-Raphson's algorithm, Eq. 11 can be iterated until $\Delta\mathbf{X} = \mathbf{X}^n - \mathbf{X}^{n-1} \leq \epsilon$ where $\epsilon \to 0$. However, in order to gain of accuracy and robustness, Eq. 11 is rather rewritten to obtain a linear system:

$$\frac{\partial \mathbf{F}}{\partial \mathbf{X}} \Delta\mathbf{X} = -F(\mathbf{X}^{n-1}) \tag{12}$$

The linear system can therefore be resolved using a Gauss elimination method and the vector $\mathbf{X}$ is updated as:

$$\mathbf{X}^n = \mathbf{X}^{n-1} + \Delta\mathbf{X} \tag{13}$$

Although the Newton-Raphson algorithm is used for its quadratic convergence speed, this method does not ensure convergence. In some cases, if the first derivative is not well behaved in the neighbourhood of a particular root, the method fails to converge. To overcome this, the number of iterations is limited and the solution is bounded to an interval known to contain the root. If convergence fails, u_* is taken to be equal to the initial solution, i.e. a neutral configuration.

D GABLS1 source of errors

Two sources of debate can be highlighted in the design of the GABLS1 benchmark [62]: initial condition definition and numerical errors accumulation.

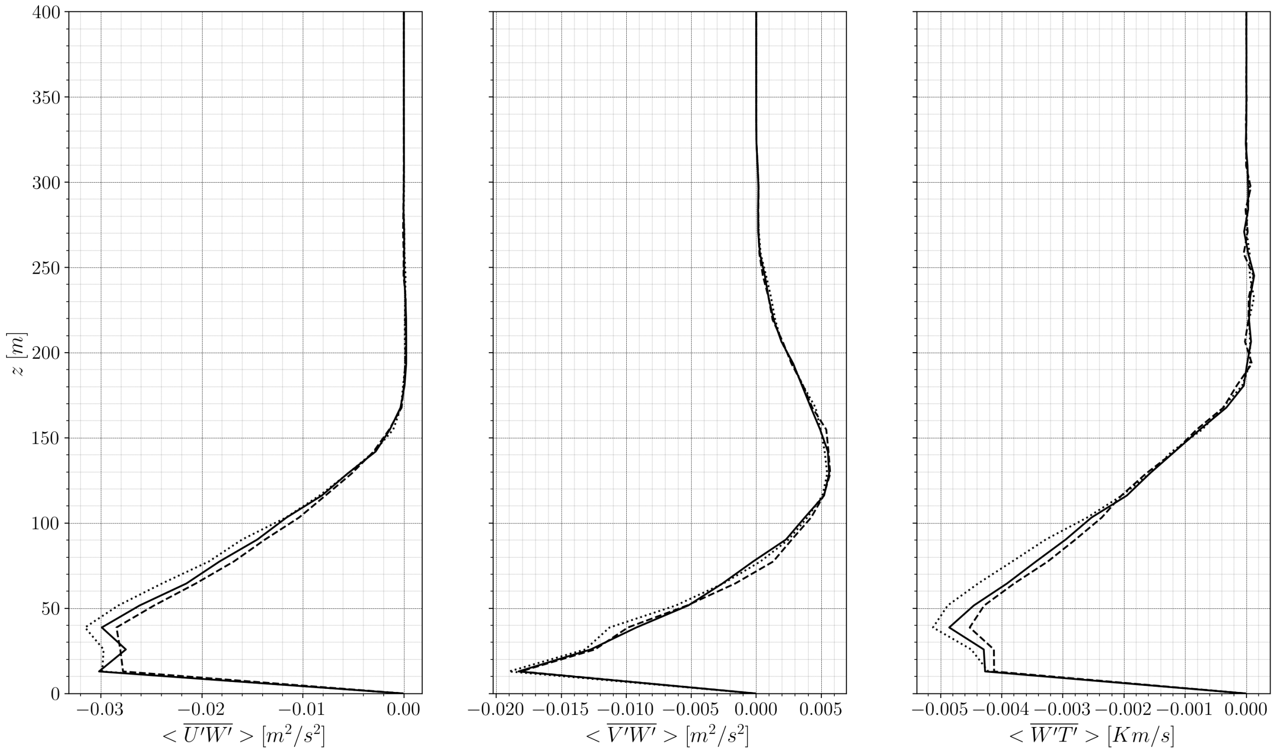

Figure 3: Horizontally averaged momentum and heat fluxes vertical profile s on S3 mesh. Results with seed 1 and 1 CPU core (—), seed 2 and 1 CPU Core (- - -) and seed 1 and 4 CPU cores(·····).

Initial condition definition

The initial condition vertical temperature profile of the GABLS1 benchmark is spatially uniform, set to $T = 265\,\mathrm{K}$ from the ground up to $z = 100\,\mathrm{m}$ and then increases by $1\,\mathrm{K}/100\,\mathrm{m}$. To help the flow destabilization process, a random potential temperature perturbation of $0.1\,\mathrm{K}$ amplitude is superposed to the profile between $z = 0\,\mathrm{m}$ and $z = 50\,\mathrm{m}$. The definition of this random perturbation is left to the user's discretion, which is questionable. Commonly, users add a randomly generated noise on each control volume which is spatially uncorrelated. This can clearly have an impact on the flow evolution and will depends on the mesh resolution and grid partitioning.

To quantify its impact on the flow behaviour, two identical simulations based on the $\Delta x = 12.5\,\mathrm{m}$ structured grid are performed with the only difference being the random number seeds. Fig. 3 shows the momentum and heat fluxes profiles spatially averaged over horizontal planes and temporally averaged between the $7th$ and the $8th$ hour, so long after initialization. Results present a clear dependency on the random seed, with noticeable differences, showing a different flow evolution between the initialisation and the $8th$ hour. Similar gaps are observed for average velocity, temperature and velocity variance and these results are reproducible for different grid resolutions and numerical schemes, but not shown here for the sake of clarity.

This effect means that a small change in the initial profile affect the behaviour of the flow ans so the collected statistics. It can distort the comparison between codes since the random number generation will necessarily be different. Moreover, this random number is only determined by an amplitude and a mean, analogous to a white noise without spatial coherence. As different grid resolution were used in all GABLS1 studies, different fluctuation frequency were added. Since the flow behaviour is sensitive to this initial profile, part of the differences obtained when comparing two resolutions can be explained by this phenomenon. Similarly, it could also explain differences between structured and unstructured grids. Adding constraints on the random number, such as giving the fluctuation frequency or giving some spatial correlation, would help in having similar initial condition, whatever the mesh type and resolution. The perturbation would then be analogous to pink noise instead of white noise. The results would still depend on the random number seed but at least would minimize differences when comparing different resolutions.

Numerical errors accumulation

Theoretically, a deterministic behaviour of the simulation is expected, since the resolution of the Navier-Stokes equations is fully deterministic. Simulations are reproducible and all states can be derived from the input data. However, numerical errors can lead to non-deterministic flows, i.e. different results can be obtained with identical input data. The sources of numerical errors are various: node reordering, machine precision, operation orders, etc. In this respect, the grid partitioning and so the number of CPU cores used in a LES can cause variations in the results. It has been demonstrated that the propagation of numerical errors is linear for laminar flows but exponential for turbulent flows [298]. This difference between laminar and turbulent flows is due to the true chaotic nature of turbulence.

To illustrate this effect, two identical simulations were performed on the $\Delta x = 12.5\,\mathrm{m}$ structured grid with different number of CPU cores: one simulation with 1 CPU, the other with 4 CPUs and by keening the same random generator seed). Fig. 3 shows the momentum and heat fluxes profiles for both cases. Momentum and heat fluxes profiles show discrepancies depending on the number of CPUs used. Similar gaps are observed for other quantities and is reproducible with other grid resolutions and numerical schemes but are not shown fot the sake of brevety. As the errors accumulate quickly, working with higher machine precision will not suppress the error propagation but only delay it. Since error propagation is exponential, the flow paths will always diverge [298]. To circumvent this effect, several simulations with different random number generations could be performed and averaged to give more statistical accuracy.

E Determining the Geostrophic wind from frictional velocity.

In experimental cases, the geostrophic wind is usually not measured as measurement are focused on wind turbine heights. Geostrophic wind can be deduced from the geostrophic drag law, also known as the resistance law. The classical resistance law for the steady-state atmospheric planetary boundary layer is:

$$\begin{aligned} \frac{k}{C_g}\, cos(\alpha) &= ln(C_g\, R_O) - A \\ \frac{k}{C_g}\, sin(\alpha) &= \pm B \end{aligned} \tag{14}$$

Where:

- C_g is the geostrophic drag coefficient, $C_g = \frac{u_*}{\boldsymbol{G}}$,
- α is the cross-isobaric angle (the angle between near-surface and geostrophic wind),
- k is the Von Kármán constant,
- R_O is the surface Rossby number, $R_O = \frac{\boldsymbol{G}}{z_0\, f}$,
- z_0 is the surface roughness,
- f is the Coriolis parameter,
- A, B are dimensionless coefficients,
- The sign on the right-hand side of the second equation is plus in northern and minus in southern hemispheres.

Various parametrization of the constant A and B have been introduced in the years. Initially, it was set to $A = 1.8$ and $B = 4.5$. But these values are only usable for NBL as the "constant" have been found to be functions of stability parameters. The up-to-date formulation [88] is a general formulation of the resistance law even for non-neutral stratifications:

$$A = \ln \frac{u_*}{f z_*} - \sqrt{\frac{k u_*}{f z_*}} \int_0^{\hat{h}} \hat{\tau}_x d\widehat{z}\ , \qquad B = -\sqrt{\frac{k u_*}{f z_*}} \int_0^{\hat{h}} \hat{\tau}_y d\widehat{z}. \tag{15}$$

Where the integrals are expressed as functions of the dimensionless height:

$$\hat{h} = \frac{h_* - z_*}{\sqrt{k u_* z_* / f}} \tag{16}$$

And where h_* is the PBL height-scale: $h_* \sim \sqrt{K_*/f}$ and z_* is the height of the near-surface layer: $z_* = l_T/k$. K_* is the eddy viscosity scale $K_* = u_* l_T$ and l_T is proportional to the turbulent length scales, which highly depends on the ABL type:

$$l_{\mathrm{T}} \sim \begin{cases} L_f = u_*/f & \text{for TN PBL} \\ L_N = u_*/N & \text{for CN PBL} \\ L = -u_*^3/F_{\mathrm{bs}} & \text{for NS PBL} \end{cases} \tag{17}$$

h_* and z_* are determined using:

$$\begin{aligned} \left(\frac{u_*}{f z_*}\right)^2 &= \frac{1}{C_{*\mathrm{TN}}} + \frac{\mu_N^2}{C_{*\mathrm{CN}}} + \frac{\mu^2}{C_{*\mathrm{NS}}} \\ \left(\frac{u_*}{f h_*}\right)^2 &= \frac{1}{C_{\mathrm{TN}}} + \frac{\mu_N}{C_{\mathrm{CN}}} + \frac{\mu}{C_{\mathrm{NS}}} \end{aligned} \tag{18}$$

Where:

$$\mu = \frac{-F_{bs}}{f\,u_*^2}\,, \qquad \mu_N = \frac{N}{f} \tag{19}$$

Where F_{bs} is the buoyancy flux at the surface and N the Brunt-Väisälä frequency.

The constants above have been calibrated as:

- For **TN PBL:** $C_{*TN} = 0.10$, $C_{TN} = 0.53$.
- For **CN PBL:** $C_{*CN} = 6.4$, $C_{CN} = 5.9$.
- For **NS PBL:** $C_{*NS} = 0.076$, $C_{NS} = 0.97$.

List of Figures

1.1 World primary energy consumption by source, from [2]. 18
1.2 Projected annual global carbon emissions. From [7]. 20
1.3 Projected global temperatures. From [7]. 21
1.4 Average oil liquids net-energy production from 1950 to 2050, compared to the gross energy. From [15]. 23
1.5 Levelized cost of energy per megawatt-hour evolution, from [21]. 25
1.6 Onshore wind cumulative installed capacity projection, from [23]. 26
1.7 Offshore wind cumulative installed capacity projection, modified from [23]. 26
1.8 Evolution of the planetary boundaries between 2009 and 2023, based on [25–27]. . . . 28
1.9 Aerodynamic efficiencies comparison for several types of wind turbines. Adapted from [30]. 29
1.10 Main components of a 3 blades horizontal axis wind turbine. 30
1.11 Left: pitch, yaw and tilt angle. Right: twist angle. Modified from [32]. 31
1.12 Evolution of wind turbine diameter and capacity growth, modified from [36]. 32
1.13 Representation of various physical phenomena involved in wind energy. 34
1.14 Outline of the different chapters, their links and the organisation of this work. 43

2.1 Physical quantities variation with the altitude in the Atmosphere. From left to right: Temperature, pressure, speed of sound, density. 47
2.2 Three-dimensional representation of the atmospheric circulation. From [79] 48
2.3 Planetary boundary layer representation. Adapted from [80] and [81]. 49
2.4 Temperature (- - -) and potential temperature (—) vertical profiles for neutral, unstable and stable configurations, illustrating the buoyancy effect on a air parcel (blue circle) that is moving upwards. F_b represents the buoyancy force. Inspired from [82]. . . 50
2.5 Planetary boundary layer representation. Adapted from [80]. 51
2.6 Coordinate system at latitude ϕ with x-axis north, y-axis west, and z-axis upward (i.e. radially outward from centre of sphere). 52
2.7 Geostrophic balance representation in the free atmosphere and in the ABL. 54
2.8 Velocity field. From top to bottom: Precursor method, Mann algorithm method, synthetic method: Homogeneous isotropic turbulence (HIT) and a constant velocity . . 64
2.9 TKE field. From top to bottom: Precursor method, Mann algorithm method, synthetic method: Homogeneous isotropic turbulence (HIT) and a constant velocity profile with no fluctuations. 65
2.10 Schematic of the Precursor database method. 68
2.11 Model-chain for wind farm flow modelling. "QoI" stands for quantities of interest and "Apps." for application. Shading represents the accuracy. From [39]. 69

3.1 A schematic diagram of the energy cascade at very high Reynolds number. From Pope [204]. . . . 77
3.2 Representative overview of the different RANS, LES, DNS approach. From left to right: Spectra representing the Energy evolution as function of the wavenumber (proportional to the inverse of the length scales), temporal evolution of a local variable and slice of the velocity field representing the turbulent structures in an atmospheric flow. From [35]. 80
3.3 From left to right: Structured mesh, unstructured mesh based on triangles, unstructured mesh based on polygons. From [214]. . . . 83
3.4 Illustration of the skewness computation based on the equilateral volume for a triangular mesh cell. . . . 84
3.5 Grid notations for the YALES2 flow solver; Node-centered control volume. From [216]. 87
3.6 Representation of the Double-Domain Decomposition (DDD) (left). Black nodes are participating in the communications between processors. Highlighted nodes are participating in the communications inside and outside each processor. Scheme of the communications and structures used during the simulations (right). From [74]. 88
3.7 Schematic of the two-level moving interface parallel adaptation strategy. From [231]. . 90
3.8 Example of the cell size requested around the rotor according to the Actuator Disk Method, Actuator Line Method or a "Resolved" geometry. From [35]. . . . 92
3.9 Disk discretization into polar cells on a Cartesian mesh. From [233]. . . . 92
3.10 blade airfoil schematics. From [233]. . . . 94

4.1 Two dimensional scheme of the Gather-Scatter filter operation on first nodes from the wall. . . . 102
4.2 Average velocity profile of the Andren case gathered on 28h. . . . 103
4.3 Scheme representing the Deardorff and Willis setup, adapted from [266]. . . . 105
4.4 Dimensionless horizontal velocity variance function of dimensionless height. . . . 106
4.5 Dimensionless vertical velocity variance function of dimensionless height. . . . 106
4.6 Dimensionless temperature variance function of dimensionless height. . . . 107
4.7 Dimensionless heat flux variance function of dimensionless height. . . . 107
4.8 (a): GABLS1 setup configuration scheme. $P1$ and $P2$ for periodic walls in pairs. (b): initial velocity and temperature vertical profiles. . . . 108
4.9 Frictional velocity, wall heat flux and Monin-Obukhov length with $S3$ and $U3$ grids, compared to original GABLS1 results dispersion [62] and PALM results [275]. . . . 110
4.10 Streamwise and tangential velocities and temperature profile for meshes $S3$ and $U3$ with cell size $\Delta x = 3.125\,\mathrm{m}$. Blue shaded area stands for the original GABLS1 study results dispersion [62] and symbols for more recent studies [118, 268, 269, 272]. . . . 111
4.11 Streamwise, tangential and vertical velocity variances with $S3$ and $U3$ of cell size $\Delta x = 3.125\,\mathrm{m}$. Blue shading stands for the original GABLS1 study results dispersion [62]. 112
4.12 Momentum and heat fluxes for meshes $S3$ and $U3$ with cell size $\Delta x = 3.125\,\mathrm{m}$. Blue shading stands for the original GABLS1 study results dispersion [62] and symbols for more recent studies [118, 272, 275]. . . . 112
4.13 Probability density function (PDF) of the skewness distribution for $U3$ mesh. . . . 114

4.14 Frictional velocity, wall heat flux and Monin-Obukhov length time series. Blue and red lines stand for structured and unstructured grids, respectively. 4 resolutions are plotted: $\Delta x = 12.5\,\mathrm{m}$ (·····), $\Delta x = 6.25\,\mathrm{m}$ (-·-·), $\Delta x = 3.125\,\mathrm{m}$ (- - -) and $\Delta x = 2\,\mathrm{m}$ (—). 115
4.15 xz velocity planes at $y = 200\,\mathrm{m}$ at $t = 8\mathrm{h}$. Top: structured cases, bottom: unstructured cases. From left to right mesh resolution increases. 115
4.16 xz temperature planes at $y = 200\,\mathrm{m}$ at $t = 8\mathrm{h}$. Top: structured cases, bottom: unstructured cases. From left to right mesh resolution increases. 116
4.17 Averaged velocity and temperature profiles. Blue and red lines stand for structured and unstructured grids, respectively. 4 resolutions are plotted: $\Delta x = 12.5\,\mathrm{m}$ (·····), $\Delta x = 6.25\,\mathrm{m}$ (-·-·), $\Delta x = 3.125\,\mathrm{m}$ (- - -) and $\Delta x = 2\,\mathrm{m}$ (—). 117
4.18 Average momentum and heat fluxes profile. Blue and red lines stand for structured and unstructured grids, respectively. 4 resolutions are plotted: $\Delta x = 12.5\,\mathrm{m}$ (·····), $\Delta x = 6.25\,\mathrm{m}$ (-·-·), $\Delta x = 3.125\,\mathrm{m}$ (- - -) and $\Delta x = 2\,\mathrm{m}$ (—). 117

5.1 Mid-place passive scalar ϕ field highlighting the wind turbine and $\widehat{\phi} = 1$ iso-contour (in white) representing the mesh refinement envelope 124
5.2 Velocity profiles and precursor turbulence intensity, zoomed in rotor region. Left : (—) for the precursor simulation, (—) for the theoretical velocity profile. Right : (—) for $\mathrm{TI_X}$, (- - -) for $\mathrm{TI_Y}$ and (-·-·) for $\mathrm{TI_Z}$. (- - -) for the rotor hub position. 126
5.3 Mid-plane visualisation of the meshes with configuration (A) at the top and configuration (B) at the bottom. From left to right : initial AMR mesh, final AMR mesh, REF mesh. 127
5.4 Mean streamwise velocity at hub height at various stream position in transversal (y) direction for (A) configuration. (—) for the AMR, (—) for the refine REF and (—) for the coarse REF. 128
5.5 Mean streamwise velocity at hub height at various stream position in the transverse (y) direction for (B) configuration. (—) for the AMR, (—) for the refine REF and (—) for the coarse REF. 129
5.6 TKE at hub height at various stream position in the transverse (y) direction for (A) configuration. (—) for the AMR, (—) for the refine REF and (—) for the coarse REF. 130
5.7 TKE at hub height at various stream position in the transverse (y) direction for (B) configuration. (—) for the AMR, (—) for the refine REF and (—) for the coarse REF. 130

6.1 Schematic of the SWiFT facility used for this benchmark. From https://wakebench-swift.readthedocs.io. 137
6.2 Precursor simulation for the neutral benchmark. 141
6.3 Shear stress temporal evolution of the neutral benchmark precursor simulation. 142
6.4 Normal planes normal to the tangential direction. From top to bottom, Streamiwse instantaneous, time-averaged and RMS velocity. 143
6.5 Precursor from the neutral benchmark. From left to right, average streamwise velocity, turbulent kinetic energy, and relative wind direction. 144

6.6 Turbulence spectra of the streamwise and tangential velocity component of the neutral benchmark precursor. . . . 145
6.7 Mid-plane visualisation of the mesh. . . . 146
6.8 Mean and standard deviation for time series of wind turbine response quantities for the neutral benchmark. From left to right: power output, torque, and thrust coefficient. 147
6.9 Neutral benchmark: mean velocity deficit in the wake at hub height. From left to right: 2D, 3D, 4D, and 5D. . . . 148
6.10 Shear stress temporal evolution of the stable benchmark precursor simulation. . . . 150
6.11 Normal planes to the tangential direction. From left to right, instantaneous velocity, average velocity, and temperature fields. . . . 151
6.12 Precursor from the stable benchmark. From left to right, average streamwise velocity, turbulent kinetic energy, and relative wind direction. . . . 152
6.13 Turbulence spectra of the streamwise (left) and tangential (right) velocity component of the stable benchmark precursor. (—) for the turbulence spectra, (—) for the Gaussian filtered turbulence spectra. . . . 153
6.14 Shear stress temporal evolution of the increased heat flux stable benchmark precursor simulation. . . . 154
6.15 Normal planes to the tangential direction. From left to right, instantaneous velocity, average velocity, and temperature fields. . . . 155
6.16 Precursor from the increased heat flux stable benchmark. From left to right, average streamwise velocity, turbulent kinetic energy, and relative wind direction. . . . 156
6.17 Mean and standard deviation for time series of wind turbine response quantities for the stable benchmark. . . . 156
6.18 Stable benchmark: mean velocity deficit in the wake at hub height. From left to right: 2D, 3D, 4D, and 5D. . . . 158
6.19 Ground topology representation. . . . 160
6.20 2D slices of the 3D mesh at different steps of mesh generation with complex surface. . 161
6.21 Representation of "baseline" (top) and "fine grid" (bottom) meshes. . . . 163
6.22 Instantaneous streamwise velocity field in the vertical midplane. . . . 164
6.23 Time-averaged streamwise velocity profiles at wind turbine positions. (+) for the experiment results [185], (∘) for the LES results [69], (—) for the "baseline" results, (- - -) for the "fine grid" results. . . . 165

1 Strong scaling on LUMI. Mesh: 134 million tetrahedrons. . . . 177
2 Weak scaling on LUMI. 131 072 elements per cores. . . . 178
3 Horizontally averaged momentum and heat fluxes vertical profile s on S3 mesh. Results with seed 1 and 1 CPU core (—), seed 2 and 1 CPU Core (- - -) and seed 1 and 4 CPU cores(·····). . . . 181

List of Tables

1.1 CO_2eq emissions by type of power plant. Most data are from [14]. 22
1.2 Wind energy production in 2022, From [3]. 24

2.1 Summary of the advantages and disadvantages for the main SGS models in atmospheric flows for wind turbine application. 60

3.1 order of magnitude of the scales involved in a wind farm simulation. 91

4.1 Case set-up with Δx the mesh cell size, N_{elem} the number of mesh elements and Δt the time step. 109
4.2 Boundary layer heights in various studies, depending on the grid resolution. 118
4.3 Relative L2 norm error in % of the horizontal average velocity and temperature profiles compared to the reference profiles from [62]. 119

5.1 relative L2 norm error recapitulation table for mean velocity, TKE, power and thrust coefficient of both AMR and coarse REF cases, compared to the refine REF, in both (A) and (B) configuration. 131
5.2 computational performances recapitulation table of both refine REF and AMR cases in both (A) and (B) configuration. Each (A) configuration simulation represent 720 s physical time while each (B) configuration simulation represent 1440 s physical time. . 132

6.1 Atmospheric variables obtained from measurements. Data are averaged based on the three identified configurations. 139
6.2 Global simulation and wind turbine parameters for both the neutral and the stable benchmarks. 140
6.3 Neutral benchmark simulation parameters for both the precursor and the wind turbine domain. 141
6.4 Stable benchmark simulation parameters for both the precursor and the wind turbine domain. 150
6.5 Stable benchmark simulation parameters for the increased wall heat flux and resolution simulation. 154
6.6 Thrust coefficient C_T of the five turbines 163
6.7 Relative L2 norm error, ε_{L2}, to the experimental data for the five average velocity profiles. 164

Bibliography

[1] H. Ritchie, P. Rosado, Fossil fuels, Our World in DataHttps://ourworldindata.org/fossil-fuels (2017).

[2] Energy Institute - Statistical Review of World Energy (2024); Smil (2017) – with major processing by Our World in Data. "Primary energy from biofuels". Energy Institute, "Statistical Review of World Energy"; Smil, "Energy Transitions: Global and National Perspectives". (2024).

[3] IEA, World Energy Statistics and Balances, IEA, Paris https://www.iea.org/data-and-statistics/data-product/world-energy-statistics-and-balances, Licence: Terms of Use for Non-CC Material (2024).

[4] J. Lelieveld, K. Klingmüller, A. Pozzer, R. Burnett, A. Haines, V. Ramanathan, Effects of fossil fuel and total anthropogenic emission removal on public health and climate, Proceedings of the National Academy of Sciences 116 (15) (2019) 7192–7197.

[5] Air quality in Europe — 2018 report, European Environment Agency (EEA). (2018).

[6] United Nations (2021). Climate Change 'Biggest Threat Modern Humans Have Ever Faced', World-Renowned Naturalist Tells Security Council, Calls for Greater Global Cooperation. United Nations Security Council. https://press.un.org/en/2021/sc14445.doc.htm (2021).

[7] IPCC,WGI SPM, 2021 (2021).

[8] IPCC 5th Assessment Synthesis Report. table SPM.1. (2014).

[9] IPCC 5th Assessment Synthesis Report. 2.3.1. (2014).

[10] V. Masson-Delmotte, P. Zhai, H.-O. Pörtner, D. Roberts, J. Skea, P. R. Shukla, et al., Global Warming of 1.5 C: IPCC special report on impacts of global warming of 1.5 C above pre-industrial levels in context of strengthening response to climate change, sustainable development, and efforts to eradicate poverty, Cambridge University Press, 2022.

[11] Https://unfccc.int/fr/a-propos-des-ndcs/l-accord-de-paris (2024).

[12] Z. Hausfather, G. P. Peters, Emissions–the 'business as usual'story is misleading (2020).

[13] C. R. Schwalm, S. Glendon, P. B. Duffy, Rcp8. 5 tracks cumulative co2 emissions, Proceedings of the National Academy of Sciences 117 (33) (2020) 19656–19657.

[14] S. Schlömer, T. Bruckner, L. Fulton, E. Hertwich, A. McKinnon, D. Perczyk, J. Roy, R. Schaeffer, R. Sims, R. W. Pete Smith, Annex III: Technology-specific cost and performance parameters. In: Climate Change 2014: Mitigation of Climate Change. Contribution of Working Group III to the Fifth Assessment Report of the Intergovernmental Panel on Climate Change, Cambridge University Press, 2014.

[15] L. Delannoy, P.-Y. Longaretti, D. J. Murphy, E. Prados, Peak oil and the low-carbon energy transition: A net-energy perspective, Applied Energy 304 (2021) 117843.

[16] K. Pahud, G. De Temmerman, Overview of the eroi, a tool to measure energy availability through the energy transition, 8th International Youth Conference on Energy (2022) 1–14.

[17] D. J. Murphy, M. Raugei, M. Carbajales-Dale, B. Rubio Estrada, Energy return on investment of major energy carriers: Review and harmonization, Sustainability 14 (12) (2022) 7098.

[18] C. J. Cleveland, Net energy from the extraction of oil and gas in the united states, Energy 30 (5) (2005) 769–782.

[19] INSEE - Provenances du pétrole brut importé en France (2024). SDES, enquête auprès des raffineurs (2024).

[20] Belgium's oil imports offset by Norway and US (2024), The Brussels Times with Belga (2024).

[21] G. Bilicic, S. Scroggins, Lazard's levelized cost of energy analysis, Tech. rep., Lazard (2023).

[22] R. Wiser, Z. Yang, M. Hand, O. Hohmeyer, D. Infield, P. H. Jensen, V. Nikolaev, M. O'Malley, G. Sinden, A. Zervos, Wind Energy. In IPCC Special Report on Renewable Energy Sources and Climate Change Mitigation, Cambridge University Press, Cambridge, United Kingdom and New York, NY, USA., 2011.

[23] IRENA, Future of wind: Deployment, investment, technology, grid integration and socio-economic aspects, Future of wind: Deployment, investment, technology, grid integration and socio-economic aspects (2019).

[24] Intergovernmental Panel on Climate Change (IPCC), Summary for Policymakers, Cambridge University Press, 2023.

[25] J. Rockström, W. Steffen, K. Noone, Å. Persson, F. S. Chapin III, E. Lambin, T. M. Lenton, M. Scheffer, C. Folke, H. J. Schellnhuber, et al., Planetary boundaries: exploring the safe operating space for humanity, Ecology and society 14 (2) (2009).

[26] W. Steffen, K. Richardson, J. Rockström, S. E. Cornell, I. Fetzer, E. M. Bennett, R. Biggs,

S. R. Carpenter, W. De Vries, C. A. De Wit, et al., Planetary boundaries: Guiding human development on a changing planet, science 347 (6223) (2015) 1259855.

[27] K. Richardson, W. Steffen, W. Lucht, J. Bendtsen, S. E. Cornell, J. F. Donges, M. Drüke, I. Fetzer, G. Bala, W. Von Bloh, et al., Earth beyond six of nine planetary boundaries, Science advances 9 (37) (2023) eadh2458.

[28] L. Millon, C. Colin, F. Brescia, C. Kerbiriou, Wind turbines impact bat activity, leading to high losses of habitat use in a biodiversity hotspot, Ecological Engineering 112 (2018) 51–54.

[29] Y. Teff-Seker, O. Berger-Tal, Y. Lehnardt, N. Teschner, Noise pollution from wind turbines and its effects on wildlife: A cross-national analysis of current policies and planning regulations, Renewable and Sustainable Energy Reviews 168 (2022) 112801.

[30] O. C. Castillo, V. R. Andrade, J. J. R. Rivas, R. O. González, Comparison of power coefficients in wind turbines considering the tip speed ratio and blade pitch angle, Energies 16 (6) (2023) 2774.

[31] A. Betz, Wind-energie und ihre ausnutzung durch windmühlen, Vol. 2, Vandenhoeck & Ruprecht, 1926.

[32] P. J. Schubel, R. J. Crossley, Wind turbine blade design review, Wind engineering 36 (4) (2012) 365–388.

[33] S. Rehman, M. M. Alam, L. M. Alhems, M. M. Rafique, Horizontal axis wind turbine blade design methodologies for efficiency enhancement—a review, Energies 11 (3) (2018) 506.

[34] F. Porté-Agel, M. Bastankhah, S. Shamsoddin, Wind-turbine and wind-farm flows: a review, Boundary-Layer Meteorology 174 (1) (2020) 1–59.

[35] F. Houtin-Mongrolle, Investigations of yawed offshore wind turbine interactions through aero-servo-elastic large eddy simulations, Ph.D. thesis, Normandie Université (2022).

[36] M. Coquelet, Numerical investigation of wind turbine control schemes for load alleviation and wake effects mitigation, Ph.D. thesis, UCL-Université Catholique de Louvain (2022).

[37] P. Veers, K. Dykes, E. Lantz, S. Barth, C. L. Bottasso, O. Carlson, A. Clifton, J. Green, P. Green, H. Holttinen, et al., Grand challenges in the science of wind energy, Science 366 (6464) (2019) eaau2027.

[38] D. J. Stensrud, Importance of low-level jets to climate: A review, Journal of Climate (1996) 1698–1711.

[39] J. Sanz Rodrigo, R. A. Chávez Arroyo, P. Moriarty, M. Churchfield, B. Kosović, P.-E. Réthoré, K. S. Hansen, A. Hahmann, J. D. Mirocha, D. Rife, Mesoscale to microscale

wind farm flow modeling and evaluation, Wiley Interdisciplinary Reviews: Energy and Environment 6 (2) (2017) e214.

[40] D. S. Cousins, Y. Suzuki, R. E. Murray, J. R. Samaniuk, A. P. Stebner, Recycling glass fiber thermoplastic composites from wind turbine blades, Journal of cleaner production 209 (2019) 1252–1263.

[41] J. G. Schepers, K. Boorsma, N. Sørensen, G. Sieros, H. Rahimi, H. Heisselmann, E. Jost, T. Lutz, T. Maeder, A. Gonzalez, et al., Final results from the eu project avatar: Aerodynamic modelling of 10 mw wind turbines, Journal of Physics: Conference Series 1037 (2018) 022013.

[42] D. Micallef, A. Rezaeiha, Floating offshore wind turbine aerodynamics: Trends and future challenges, Renewable and Sustainable Energy Reviews 152 (2021) 111696.

[43] B. Kroposki, B. Johnson, Y. Zhang, V. Gevorgian, P. Denholm, B.-M. Hodge, B. Hannegan, Achieving a 100% renewable grid: Operating electric power systems with extremely high levels of variable renewable energy, IEEE Power and energy magazine 15 (2) (2017) 61–73.

[44] T. Ackermann, T. Prevost, V. Vittal, A. J. Roscoe, J. Matevosyan, N. Miller, Paving the way: A future without inertia is closer than you think, IEEE Power and Energy Magazine 15 (6) (2017) 61–69.

[45] P. M. Gebraad, F. W. Teeuwisse, J. Van Wingerden, P. A. Fleming, S. D. Ruben, J. R. Marden, L. Y. Pao, Wind plant power optimization through yaw control using a parametric model for wake effects—a cfd simulation study, Wind Energy 19 (1) (2016) 95–114.

[46] A. Duckworth, R. Barthelmie, Investigation and validation of wind turbine wake models, Wind Engineering 32 (5) (2008) 459–475.

[47] F. Carbajo Fuertes, C. D. Markfort, F. Porté-Agel, Wind turbine wake characterization with nacelle-mounted wind lidars for analytical wake model validation, Remote sensing 10 (5) (2018) 668.

[48] B. D. Hirth, J. L. Schroeder, W. S. Gunter, J. G. Guynes, Coupling doppler radar-derived wind maps with operational turbine data to document wind farm complex flows, Wind Energy 18 (3) (2015) 529–540.

[49] M. Bastankhah, F. Porté-Agel, Wind tunnel study of the wind turbine interaction with a boundary-layer flow: Upwind region, turbine performance, and wake region, Physics of Fluids 29 (6) (2017).

[50] J. N. Sørensen, General momentum theory for horizontal axis wind turbines, Vol. 4, Springer, 2016.

[51] R. Lanzafame, , M. Messina, Fluid dynamics wind turbine design: Critical analysis, optimization and application of bem theory, Renewable energy 32 (14) (2007) 2291–2305.

[52] M. Bastankhah, F. Porté-Agel, A new analytical model for wind-turbine wakes, Renewable energy 70 (2014) 116–123.

[53] M. Abkar, F. Porté-Agel, The effect of free-atmosphere stratification on boundary-layer flow and power output from very large wind farms, Energies 6 (5) (2013) 2338–2361.

[54] M. Abkar, F. Porté-Agel, A new wind-farm parameterization for large-scale atmospheric models, Journal of Renewable and Sustainable Energy 7 (1) (2015).

[55] D. Mehta, A. Van Zuijlen, B. Koren, J. Holierhoek, H. Bijl, Large eddy simulation of wind farm aerodynamics: A review, Journal of Wind Engineering and Industrial Aerodynamics 133 (2014) 1–17.

[56] R. J. Stevens, L. A. Martínez-Tossas, C. Meneveau, Comparison of wind farm large eddy simulations using actuator disk and actuator line models with wind tunnel experiments, Renewable energy 116 (2018) 470–478.

[57] J. Smagorinsky, General circulation experiments with the primitive equations: I. the basic experiment, Monthly weather review 91 (3) (1963) 99–164.

[58] R. Stoll, J. A. Gibbs, S. T. Salesky, W. Anderson, M. Calaf, Large-eddy simulation of the atmospheric boundary layer, Boundary-Layer Meteorology 177 (2020) 541–581.

[59] M. J. Churchfield, S. Lee, J. Michalakes, P. J. Moriarty, A numerical study of the effects of atmospheric and wake turbulence on wind turbine dynamics, Journal of turbulence 13 (2012) N14.

[60] M. Abkar, F. Porté-Agel, Influence of atmospheric stability on wind-turbine wakes: A large-eddy simulation study, Physics of fluids 27 (3) (2015).

[61] A. Holtslag, G. Svensson, S. Basu, B. Beare, F. Bosveld, J. Cuxart, Overview of the gewex atmospheric boundary layer study (gabls), ECMWF GABLS workshop on Diurnal cycles and the stable boundary layer 7-10 November 2011 (2012).

[62] R. J. Beare, M. K. Macvean, A. A. Holtslag, J. Cuxart, I. Esau, J.-C. Golaz, M. A. Jimenez, M. Khairoutdinov, B. Kosovic, D. Lewellen, et al., An intercomparison of large-eddy simulations of the stable boundary layer, Boundary-Layer Meteorology 118 (2006) 247–272.

[63] F. Porté-Agel, Y.-T. Wu, H. Lu, R. J. Conzemius, Large-eddy simulation of atmospheric boundary layer flow through wind turbines and wind farms, Journal of Wind Engineering and Industrial Aerodynamics 99 (4) (2011) 154–168.

[64] M. Dörenkämper, B. Witha, G. Steinfeld, D. Heinemann, M. Kühn, The impact of stable

atmospheric boundary layers on wind-turbine wakes within offshore wind farms, Journal of Wind Engineering and Industrial Aerodynamics 144 (2015) 146–153.

[65] D. Allaerts, J. Meyers, Gravity waves and wind-farm efficiency in neutral and stable conditions, Boundary-layer meteorology 166 (2) (2018) 269–299.

[66] L. Ramírez, D. Fraile, G. Brindley, Offshore wind in europe: Key trends and statistics 2020, Tech. rep., Wind Europe (2020).

[67] P. H. Alfredsson, A. Segalini, Introduction wind farms in complex terrains: an introduction (2017).

[68] E. S. Politis, J. Prospathopoulos, D. Cabezon, K. S. Hansen, P. Chaviaropoulos, R. J. Barthelmie, Modeling wake effects in large wind farms in complex terrain: the problem, the methods and the issues, Wind Energy 15 (1) (2012) 161–182.

[69] S. Shamsoddin, F. Porté-Agel, Large-eddy simulation of atmospheric boundary-layer flow through a wind farm sited on topography, Boundary-layer meteorology 163 (2017) 1–17.

[70] P. Taylor, H. Teunissen, The askervein hill project: overview and background data, Boundary-layer meteorology 39 (1987) 15–39.

[71] A. Bechmann, N. N. Sørensen, J. Berg, J. Mann, P.-E. Réthoré, The bolund experiment, part ii: blind comparison of microscale flow models, Boundary-layer meteorology 141 (2011) 245–271.

[72] H. Fernando, J. Mann, J. Palma, J. K. Lundquist, R. J. Barthelmie, M. Belo-Pereira, W. Brown, F. Chow, T. Gerz, C. Hocut, et al., The perdigão: peering into microscale details of mountain winds, Bulletin of the American Meteorological Society 100 (5) (2019) 799–819.

[73] P. Santos, J. Mann, N. Vasiljević, E. Cantero, J. Sanz Rodrigo, F. Borbón, D. Martínez-Villagrasa, B. Martí, J. Cuxart, The alaiz experiment: untangling multi-scale stratified flows over complex terrain, Wind Energy Science 5 (4) (2020) 1793–1810.

[74] V. Moureau, P. Domingo, L. Vervisch, Design of a massively parallel cfd code for complex geometries, Comptes Rendus Mécanique 339 (2-3) (2011) 141–148.

[75] P. Bénard, A. Viré, V. Moureau, G. Lartigue, L. Beaudet, P. Deglaire, L. Bricteux, Large-eddy simulation of wind turbines wakes including geometrical effects, Computers & Fluids 173 (2018) 133–139.

[76] U. Vigny, P. Benard, P. T. Hedje, F. Houtin-Mongrolle, L. Bricteux, S. Zeoli, A new wake detection methodology to capture wind turbine wakes using adaptive mesh refinement and large eddy simulation, Journal of Physics: Conference Series 2265 (2022) 022005.

[77] E. Muller, S. Gremmo, F. Houtin-Mongrolle, B. Duboc, P. Bénard, Field-data-based val-

idation of an aero-servo-elastic solver for high-fidelity large-eddy simulations of industrial wind turbines, Wind Energy Science 9 (1) (2024) 25–48.

[78] U. Vigny, L. Voivenel, M. Safdari Shadloo, P. Bénard, S. Zeoli, Enabling the use of unstructured meshes for the large eddy simulation of stable atmospheric boundary layers, Available at SSRN 4995353 (2024).

[79] V. Bjerknes, atmospheric circulation, Britannica, The Editors of Encyclopaedia, 7 Mar. 2019.

[80] R. B. Stull, An introduction to boundary layer meteorology, Vol. 13, Springer Science & Business Media, 1988.

[81] H. Polinder, F. F. Van der Pijl, G.-J. De Vilder, P. J. Tavner, Comparison of direct-drive and geared generator concepts for wind turbines, IEEE Transactions on energy conversion 21 (3) (2006) 725–733.

[82] D. Allaerts, Large-eddy simulation of wind farms in conventionally neutral and stable atmospheric boundary layers, Ph.D. thesis, kuleuven (2016).

[83] J. C. Wyngaard, Turbulence in the Atmosphere, Cambridge University Press, 2010.

[84] G. Csanady, Equilibrium theory of the planetary boundary layer with an inversion lid, Boundary-Layer Meteorology 6 (1) (1974) 63–79.

[85] S. Zilitinkevich, I. Esau, On integral measures of the neutral barotropic planetary boundary layer, Boundary-layer meteorology 104 (2002) 371–379.

[86] G. Hess, The neutral, barotropic planetary boundary layer, capped by a low-level inversion, Boundary-layer meteorology 110 (3) (2004) 319–355.

[87] D. Allaerts, J. Meyers, Boundary-layer development and gravity waves in conventionally neutral wind farms, Journal of Fluid Mechanics 814 (2017) 95–130.

[88] E. Kadantsev, E. Mortikov, S. Zilitinkevich, The resistance law for stably stratified atmospheric planetary boundary layers, Quarterly Journal of the Royal Meteorological Society 147 (737) (2021) 2233–2243.

[89] H. Lettau, A re-examination of the "leipzig wind profile" considering some relations between wind and turbulence in the frictional layer, Tellus 2 (2) (1950) 125–129.

[90] Z. Shu, Q. Li, Y. He, P. Chan, Observational study of veering wind by doppler wind profiler and surface weather station, Journal of Wind Engineering and Industrial Aerodynamics 178 (2018) 18–25.

[91] Z. Shu, Q. Li, Y. He, P. W. Chan, Investigation of marine wind veer characteristics using wind lidar measurements, Atmosphere 11 (11) (2020) 1178.

[92] H. Lu, F. Porté-Agel, Large-eddy simulation of a very large wind farm in a stable atmospheric boundary layer, Physics of Fluids 23 (6) (2011).

[93] H.-C. Tsai, T. Colonius, Coriolis effect on dynamic stall in a vertical axis wind turbine, AIAA Journal 54 (1) (2016) 216–226.

[94] S. B. Roy, Simulating impacts of wind farms on local hydrometeorology, Journal of Wind Engineering and Industrial Aerodynamics 99 (4) (2011) 491–498.

[95] S. K. Siedersleben, J. K. Lundquist, A. Platis, J. Bange, K. Bärfuss, A. Lampert, B. Cañadillas, T. Neumann, S. Emeis, Micrometeorological impacts of offshore wind farms as seen in observations and simulations, Environmental Research Letters 13 (12) (2018) 124012.

[96] L. Mishnaevsky Jr, A. Tempelis, N. Kuthe, P. Mahajan, Recent developments in the protection of wind turbine blades against leading edge erosion: Materials solutions and predictive modelling, Renewable Energy (2023) 118966.

[97] A. I. of Aeronautics, Astronautics, AIAA guide for the verification and validation of computational fluid dynamics simulations, American Institute of aeronautics and astronautics., 1998.

[98] J. Berg, N. Troldborg, N. N. Sørensen, E. Patton, P. P. Sullivan, Large-eddy simulation of turbine wake in complex terrain, in: Journal of Physics: Conference Series, Vol. 854, IOP Publishing, 2017, p. 012003.

[99] H. H. Shin, J. Dudhia, Evaluation of pbl parameterizations in wrf at subkilometer grid spacings: Turbulence statistics in the dry convective boundary layer, Monthly Weather Review 144 (3) (2016) 1161–1177.

[100] A. C. Fitch, J. B. Olson, J. K. Lundquist, Parameterization of wind farms in climate models, Journal of Climate 26 (17) (2013) 6439–6458.

[101] P. A. Jiménez, J. Navarro, A. M. Palomares, J. Dudhia, Mesoscale modeling of offshore wind turbine wakes at the wind farm resolving scale: a composite-based analysis with the weather research and forecasting model over horns rev, Wind Energy 18 (3) (2015) 559–566.

[102] Y.-T. Wu, F. Porté-Agel, Large-eddy simulation of wind-turbine wakes: evaluation of turbine parametrisations, Boundary-layer meteorology 138 (3) (2011) 345–366.

[103] P. Mason, S. Derbyshire, Large-eddy simulation of the stably-stratified atmospheric boundary layer, Boundary-layer meteorology 53 (1990) 117–162.

[104] B. Kosović, J. A. Curry, A large eddy simulation study of a quasi-steady, stably stratified atmospheric boundary layer, Journal of the atmospheric sciences 57 (8) (2000) 1052–1068.

[105] M. Germano, U. Piomelli, P. Moin, W. H. Cabot, A dynamic subgrid-scale eddy viscosity model, Physics of Fluids A: Fluid Dynamics 3 (7) (1991) 1760–1765.

[106] D. K. Lilly, A proposed modification of the germano subgrid-scale closure method, Physics of Fluids A: Fluid Dynamics 4 (3) (1992) 633–635.

[107] J. W. Deardorff, A three-dimensional numerical investigation of the idealized planetary boundary layer, Geophysical and Astrophysical Fluid Dynamics 1 (3-4) (1970) 377–410.

[108] J. W. Deardorff, Stratocumulus-capped mixed layers derived from a three-dimensional model, Boundary-layer meteorology 18 (1980) 495–527.

[109] B. Stevens, C.-H. Moeng, P. P. Sullivan, Entrainment and subgrid lengthscales in large-eddy simulations of atmospheric boundary-layer flows, in: IUTAM symposium on developments in geophysical turbulence, Springer, 2000, pp. 253–269.

[110] S. S. Zilitinkevich, T. Elperin, N. Kleeorin, I. Rogachevskii, Energy-and flux-budget (efb) turbulence closure model for stably stratified flows. part i: Steady-state, homogeneous regimes, Boundary-Layer Meteorology 125 (2) (2007) 167–191.

[111] S. Zilitinkevich, T. Elperin, N. Kleeorin, I. Rogachevskii, I. Esau, A hierarchy of energy- and flux-budget (efb) turbulence closure models for stably-stratified geophysical flows, Boundary-layer meteorology 146 (3) (2013) 341–373.

[112] F. Nicoud, F. Ducros, Subgrid-scale stress modelling based on the square of the velocity gradient tensor, Flow, turbulence and Combustion 62 (3) (1999) 183–200.

[113] M. Ghobrial, T. Stallard, D. Schultz, P. Ouro, Evaluation of six subgrid-scale models for les of wind farms in stable and conventionally-neutral atmospheric stratification (2024).

[114] F. Nicoud, H. B. Toda, O. Cabrit, S. Bose, J. Lee, Using singular values to build a subgrid-scale model for large eddy simulations, Physics of fluids 23 (8) (2011) 085106.

[115] M. Rieth, F. Proch, O. Stein, M. Pettit, A. Kempf, Comparison of the sigma and smagorinsky les models for grid generated turbulence and a channel flow, Computers & Fluids 99 (2014) 172–181.

[116] C. Meneveau, J. Katz, Scale-invariance and turbulence models for large-eddy simulation, Annual Review of Fluid Mechanics 32 (1) (2000) 1–32.

[117] E. Bou-Zeid, C. Meneveau, M. Parlange, A scale-dependent lagrangian dynamic model for large eddy simulation of complex turbulent flows, Physics of fluids 17 (2) (2005).

[118] S. N. Gadde, A. Stieren, R. J. Stevens, Large-eddy simulations of stratified atmospheric boundary layers: Comparison of different subgrid models, Boundary-Layer Meteorology 178 (3) (2021) 363–382.

[119] R. Verstappen, When does eddy viscosity damp subfilter scales sufficiently?, Journal of Scientific Computing 49 (1) (2011) 94–110.

[120] W. Rozema, H. J. Bae, P. Moin, R. Verstappen, Minimum-dissipation models for large-eddy simulation, Physics of Fluids 27 (8) (2015).

[121] M. Abkar, P. Moin, Large-eddy simulation of thermally stratified atmospheric boundary-layer flow using a minimum dissipation model, Boundary-layer meteorology 165 (2017) 405–419.

[122] P. J. Mason, Large-eddy simulation: A critical review of the technique, Quarterly Journal of the Royal Meteorological Society 120 (515) (1994) 1–26.

[123] H. Sarlak, C. Meneveau, J. N. Sørensen, Role of subgrid-scale modeling in large eddy simulation of wind turbine wake interactions, Renewable Energy 77 (2015) 386–399.

[124] P. Doubrawa, E. W. Quon, L. A. Martinez-Tossas, K. Shaler, M. Debnath, N. Hamilton, T. G. Herges, D. Maniaci, C. L. Kelley, A. S. Hsieh, et al., Multimodel validation of single wakes in neutral and stratified atmospheric conditions, Wind Energy 23 (11) (2020) 2027–2055.

[125] L. Prandtl, 7. bericht über untersuchungen zur ausgebildeten turbulenz, ZAMM-Journal of Applied Mathematics and Mechanics/Zeitschrift für Angewandte Mathematik und Mechanik 5 (2) (1925) 136–139.

[126] A. S. Monin, A. M. Obukhov, Basic laws of turbulent mixing in the surface layer of the atmosphere, Contrib. Geophys. Inst. Acad. Sci. USSR 151 (163) (1954) e187.

[127] L. Landau, E. Lifshitz, Fluid mechanics. pergamon press, oxford, Section 92, problem 2 (1959).

[128] R. Stoll, F. Porté-Agel, Effect of roughness on surface boundary conditions for large-eddy simulation, Boundary-Layer Meteorology 118 (1) (2006) 169–187.

[129] S. Basu, A. Lacser, A cautionary note on the use of monin–obukhov similarity theory in very high-resolution large-eddy simulations, Boundary-Layer Meteorology 163 (2) (2017) 351–355.

[130] J. Larsson, S. Kawai, J. Bodart, I. Bermejo-Moreno, Large eddy simulation with modeled wall-stress: recent progress and future directions, Mechanical Engineering Reviews 3 (1) (2016) 15–00418.

[131] S. Basu, A. A. Holtslag, B. J. Van De Wiel, A. F. Moene, G.-J. Steeneveld, An inconvenient "truth" about using sensible heat flux as a surface boundary condition in models under stably stratified regimes, Acta Geophysica 56 (2008) 88–99.

[132] J. C. Wyngaard, Toward numerical modeling in the "terra incognita", Journal of the

atmospheric sciences 61 (14) (2004) 1816–1826.

[133] W. C. Skamarock, J. B. Klemp, J. Dudhia, D. O. Gill, Z. Liu, J. Berner, W. Wang, J. G. Powers, M. G. Duda, D. M. Barker, et al., A description of the advanced research wrf model version 4, National Center for Atmospheric Research: Boulder, CO, USA 145 (2019) 145.

[134] M. A. Prósper, C. Otero-Casal, F. C. Fernández, G. Miguez-Macho, Wind power forecasting for a real onshore wind farm on complex terrain using wrf high resolution simulations, Renewable energy 135 (2019) 674–686.

[135] C. Lac, J.-P. Chaboureau, V. Masson, J.-P. Pinty, P. Tulet, J. Escobar, M. Leriche, C. Barthe, B. Aouizerats, C. Augros, et al., Overview of the meso-nh model version 5.4 and its applications, Geoscientific Model Development 11 (5) (2018) 1929–1969.

[136] J. Stein, E. Richard, J.-P. Lafore, J. Pinty, N. Asencio, S. Cosma, High-resolution non-hydrostatic simulations of flash-flood episodes with grid-nesting and ice-phase parameterization, Meteorology and Atmospheric Physics 72 (2000) 203–221.

[137] A. A. Wyszogrodzki, S. Miao, F. Chen, Evaluation of the coupling between mesoscale-wrf and les-eulag models for simulating fine-scale urban dispersion, Atmospheric research 118 (2012) 324–345.

[138] P. Piroozmand, G. Mussetti, J. Allegrini, M. H. Mohammadi, E. Akrami, J. Carmeliet, Coupled cfd framework with mesoscale urban climate model: Application to microscale urban flows with weak synoptic forcing, Journal of Wind Engineering and Industrial Aerodynamics 197 (2020) 104059.

[139] J. Vogel, A. Afshari, G. Chockalingam, S. Stadler, Evaluation of a novel wrf/palm-4u coupling scheme incorporating a roughness-corrected surface layer representation, Urban Climate 46 (2022) 101311.

[140] B. Maronga, S. Banzhaf, C. Burmeister, T. Esch, R. Forkel, D. Fröhlich, V. Fuka, K. F. Gehrke, J. Geletič, S. Giersch, et al., Overview of the palm model system 6.0, Geoscientific Model Development 13 (3) (2020) 1335–1372.

[141] R. Vasaturo, I. Kalkman, B. Blocken, P. Van Wesemael, Large eddy simulation of the neutral atmospheric boundary layer: performance evaluation of three inflow methods for terrains with different roughness, Journal of Wind Engineering and Industrial Aerodynamics 173 (2018) 241–261.

[142] M. S. Thordal, J. C. Bennetsen, S. Capra, H. H. H. Koss, Engineering approach for a cfd inflow condition using the precursor database method, Journal of Wind Engineering and Industrial Aerodynamics 203 (2020) 104210.

[143] W. De Paepe, S. Pindado, S. Bram, F. Contino, Simplified elements for wind-tunnel

measurements with type-iii-terrain atmospheric boundary layer, Measurement 91 (2016) 590–600.

[144] P. Phuc, T. Nozu, H. Kikuchi, K. Hibi, Y. Tamura, A numerical study on wind pressure on a building with a setback using large eddy simulation, in: 6th International Symposium on Computational Wind Engineering, Hamburg, Vol. 107, 2014, p. 105407.

[145] S. Capra, S. Cammelli, D. Roeder, J. Knir, Numerically simulated wind loading on a high-rise structure and its correlation with experimental wind tunnel testing, in: The 7th International Symposium on Computational Wind Engineering, 2018, pp. 18–22.

[146] A. Smirnov, S. Shi, I. Celik, Random flow generation technique for large eddy simulations and particle-dynamics modeling, J. Fluids Eng. 123 (2) (2001) 359–371.

[147] R. H. Kraichnan, Diffusion by a random velocity field, The physics of fluids 13 (1) (1970) 22–31.

[148] S. Huang, Q. Li, J. Wu, A general inflow turbulence generator for large eddy simulation, Journal of Wind Engineering and Industrial Aerodynamics 98 (10-11) (2010) 600–617.

[149] H. G. Castro, R. R. Paz, V. E. Sonzogni, Generation of turbulent inlet velocity conditions for large eddy simulations, Mecánica Computacional 30 (29) (2011) 2275–2288.

[150] H. Aboshosha, A. Elshaer, G. T. Bitsuamlak, A. El Damatty, Consistent inflow turbulence generator for les evaluation of wind-induced responses for tall buildings, Journal of Wind Engineering and Industrial Aerodynamics 142 (2015) 198–216.

[151] X. Wu, Inflow turbulence generation methods, Annual Review of Fluid Mechanics 49 (2017) 23–49.

[152] L. Di Mare, M. Klein, W. Jones, J. Janicka, Synthetic turbulence inflow conditions for large-eddy simulation, Physics of Fluids 18 (2) (2006) 025107.

[153] M. Klein, A. Sadiki, J. Janicka, A digital filter based generation of inflow data for spatially developing direct numerical or large eddy simulations, Journal of computational Physics 186 (2) (2003) 652–665.

[154] I. Veloudis, Z. Yang, J. McGuirk, G. Page, A. Spencer, Novel implementation and assessment of a digital filter based approach for the generation of les inlet conditions, Flow, Turbulence and Combustion 79 (1) (2007) 1–24.

[155] Z.-T. Xie, I. P. Castro, Efficient generation of inflow conditions for large eddy simulation of street-scale flows, Flow, turbulence and combustion 81 (3) (2008) 449–470.

[156] Y. Kim, I. P. Castro, Z.-T. Xie, Divergence-free turbulence inflow conditions for large-eddy simulations with incompressible flow solvers, Computers & Fluids 84 (2013) 56–68.

[157] T. Okaze, A. Mochida, Cholesky decomposition–based generation of artificial inflow turbulence including scalar fluctuation, Computers & Fluids 159 (2017) 23–32.

[158] E. Sergent, Vers une methodologie de couplage entre la simulation des grandes echelles et les modeles statistiques, Ph.D. thesis, Ecully, Ecole centrale de Lyon (2002).

[159] F. Mathey, D. Cokljat, J. P. Bertoglio, E. Sergent, Assessment of the vortex method for large eddy simulation inlet conditions, Progress in Computational Fluid Dynamics, An International Journal 6 (1-3) (2006) 58–67.

[160] N. Jarrin, S. Benhamadouche, D. Laurence, R. Prosser, A synthetic-eddy-method for generating inflow conditions for large-eddy simulations, International Journal of Heat and Fluid Flow 27 (4) (2006) 585–593.

[161] R. Poletto, T. Craft, A. Revell, A new divergence free synthetic eddy method for the reproduction of inlet flow conditions for les, Flow, turbulence and combustion 91 (3) (2013) 519–539.

[162] J. Mann, The spatial structure of neutral atmospheric surface-layer turbulence, Journal of fluid mechanics 273 (1994) 141–168.

[163] J. Mann, Wind field simulation, Probabilistic engineering mechanics 13 (4) (1998) 269–282.

[164] Y. M. Chung, H. J. Sung, Comparative study of inflow conditions for spatially evolving simulation, AIAA journal 35 (2) (1997) 269–274.

[165] N. Nikitin, Spatial periodicity of spatially evolving turbulent flow caused by inflow boundary condition, Physics of Fluids 19 (9) (2007) 091703.

[166] X. Wu, P. Moin, J.-P. Hickey, Boundary layer bypass transition, Physics of Fluids 26 (9) (2014) 091104.

[167] X. Wu, P. Moin, J. M. Wallace, J. Skarda, A. Lozano-Durán, J.-P. Hickey, Transitional–turbulent spots and turbulent–turbulent spots in boundary layers, Proceedings of the National Academy of Sciences 114 (27) (2017) E5292–E5299.

[168] M. J. Churchfield, L. Sang, P. J. Moriarty, Adding complex terrain and stable atmospheric condition capability to the openfoam-based flow solver of the simulator for on/offshore wind farm applications (sowfa), Tech. rep., National Renewable Energy Lab.(NREL), Golden, CO (United States) (2013).

[169] S. Lee, S. K. Lele, P. Moin, Simulation of spatially evolving turbulence and the applicability of taylor's hypothesis in compressible flow, Physics of Fluids A: Fluid Dynamics 4 (7) (1992) 1521–1530.

[170] T. S. Lund, X. Wu, K. D. Squires, Generation of turbulent inflow data for spatially-

developing boundary layer simulations, Journal of computational physics 140 (2) (1998) 233–258.

[171] F. Porté-Agel, H. Lu, Y.-T. Wu, Interaction between large wind farms and the atmospheric boundary layer, Procedia Iutam 10 (2014) 307–318.

[172] M. Elgendi, M. AlMallahi, A. Abdelkhalig, M. Y. Selim, A review of wind turbines in complex terrain, International Journal of Thermofluids 17 (2023) 100289.

[173] S. Ivanell, R. Mikkelsen, J. Sørensen, D. Henningson, Acd modelling of wake interaction in the horns rev wind farm, in: Extended Abstracts for Euromech Colloquium, Vol. 508, 2009, pp. 1–10.

[174] Y.-T. Wu, F. Porté-Agel, Modeling turbine wakes and power losses within a wind farm using les: An application to the horns rev offshore wind farm, Renewable Energy 75 (2015) 945–955.

[175] R. J. Stevens, C. Meneveau, Flow structure and turbulence in wind farms, Annual review of fluid mechanics 49 (1) (2017) 311–339.

[176] H. Abedi, S. Sarkar, H. Johansson, Numerical modelling of neutral atmospheric boundary layer flow through heterogeneous forest canopies in complex terrain (a case study of a swedish wind farm), Renewable Energy 180 (2021) 806–828.

[177] C. M. et al., Large eddy simulation study of fully developed wind-turbine array boundary layers, Physics of fluids (2010).

[178] C. VerHulst, C. Meneveau, Large eddy simulation study of the kinetic energy entrainment by energetic turbulent flow structures in large wind farms, Physics of Fluids 26 (2) (2014).

[179] L. Lanzilao, J. Meyers, A parametric large-eddy simulation study of wind-farm blockage and gravity waves in conventionally neutral boundary layers, Journal of Fluid Mechanics 979 (2024) A54.

[180] J. P. Goit, J. Meyers, Effect of ekman layer on windfarm roughness and displacement height, in: Direct and Large-Eddy Simulation IX, Springer, 2015, pp. 423–434.

[181] W. Zhang, C. D. Markfort, F. Porté-Agel, Wind-turbine wakes in a convective boundary layer: A wind-tunnel study, Boundary-layer meteorology 146 (2013) 161–179.

[182] H. Lu, F. Porté-Agel, On the impact of wind farms on a convective atmospheric boundary layer, Boundary-Layer Meteorology 157 (2015) 81–96.

[183] J. M. Strickland, S. N. Gadde, R. J. Stevens, Wind farm blockage in a stable atmospheric boundary layer, Renewable Energy 197 (2022) 50–58.

[184] M. Abkar, F. Porté-Agel, Mean and turbulent kinetic energy budgets inside and above

very large wind farms under conventionally-neutral condition, Renewable Energy 70 (2014) 142–152.

[185] W. Tian, A. Ozbay, W. Yuan, P. Sarakar, H. Hu, W. Yuan, An experimental study on the performances of wind turbines over complex terrain, in: 51st AIAA aerospace sciences meeting including the new horizons forum and aerospace exposition, 2013, pp. 7–10.

[186] J. Lange, J. Mann, J. Berg, D. Parvu, R. Kilpatrick, A. Costache, J. Chowdhury, K. Siddiqui, H. Hangan, For wind turbines in complex terrain, the devil is in the detail, Environmental Research Letters 12 (9) (2017) 094020.

[187] J. Berg, J. Mann, A. Bechmann, M. Courtney, H. E. Jørgensen, The bolund experiment, part i: flow over a steep, three-dimensional hill, Boundary-layer meteorology 141 (2011) 219–243.

[188] E. Machefaux, G. C. Larsen, T. Koblitz, N. Troldborg, M. C. Kelly, A. Chougule, K. S. Hansen, J. S. Rodrigo, An experimental and numerical study of the atmospheric stability impact on wind turbine wakes, Wind Energy 19 (10) (2016) 1785–1805.

[189] L. Liu, R. J. Stevens, Effects of atmospheric stability on the performance of a wind turbine located behind a three-dimensional hill, Renewable Energy 175 (2021) 926–935.

[190] G. Iaccarino, R. Verzicco, Immersed boundary technique for turbulent flow simulations, Appl. Mech. Rev. 56 (3) (2003) 331–347.

[191] R. Barthelmie, S. Pryor, N. Wildmann, R. Menke, Wind turbine wake characterization in complex terrain via integrated doppler lidar data from the perdigão experiment, Journal of Physics: Conference Series 1037 (2018) 052022.

[192] A. El Bahlouli, A. Rautenberg, M. Schön, K. zum Berge, J. Bange, H. Knaus, Comparison of cfd simulation to uas measurements for wind flows in complex terrain: Application to the winsent test site, Energies 12 (10) (2019) 1992.

[193] J. Redelsperger, G. Sommeria, Methode de representation de la turbulence associee aux precipitations dans un modele tri-dimensionnel de convection nuageuse, Boundary-Layer Meteorology 24 (2) (1982) 231–252.

[194] J.-L. Redelsperger, G. Sommeria, Three-dimensional simulation of a convective storm: Sensitivity studies on subgrid parameterization and spatial resolution, Journal of the atmospheric sciences 43 (22) (1986) 2619–2635.

[195] J. Cuxart, P. Bougeault, J.-L. Redelsperger, A turbulence scheme allowing for mesoscale and large-eddy simulations, Quarterly Journal of the Royal Meteorological Society 126 (562) (2000) 1–30.

[196] J. Meyers, P. Sagaut, Evaluation of smagorinsky variants in large-eddy simulations of

wall-resolved plane channel flows, Physics of Fluids 19 (9) (2007).

[197] J. Meyers, C. Meneveau, Large eddy simulations of large wind-turbine arrays in the atmospheric boundary layer, in: 48th AIAA aerospace sciences meeting including the new horizons forum and aerospace exposition, 2010, p. 827.

[198] S. Heinz, Realizability of dynamic subgrid-scale stress models via stochastic analysis, Monte Carlo Methods and Applications (2008).

[199] R. Mokhtarpoor, S. Heinz, Dynamic large eddy simulation: Stability via realizability, Physics of Fluids 29 (10) (2017) 105104.

[200] G. Deskos, S. Laizet, R. Palacios, Winc3d: A novel framework for turbulence-resolving simulations of wind farm wake interactions, Wind Energy 23 (3) (2020) 779–794.

[201] J. Jonkman, S. Butterfield, W. Musial, G. Scott, Definition of a 5-mw reference wind turbine for offshore system development, Tech. rep., National Renewable Energy Lab.(NREL), Golden, CO (United States) (2009).

[202] T. Heus, C. Van Heerwaarden, H. J. Jonker, A. Pier Siebesma, S. Axelsen, K. Van Den Dries, O. Geoffroy, A. Moene, D. Pino, S. De Roode, et al., Formulation of the dutch atmospheric large-eddy simulation (dales) and overview of its applications, Geoscientific Model Development 3 (2) (2010) 415–444.

[203] S. Stipa, A. Ajay, D. Allaerts, J. Brinkerhoff, Tosca–an open-source finite-volume les environment for wind farm flows, Wind Energy Science Discussions 2023 (2023) 1–41.

[204] S. B. Pope, Turbulent flows, Measurement Science and Technology 12 (11) (2001) 2020–2021.

[205] J. O. Hirschfelder, C. F. Curtiss, R. B. Bird, The molecular theory of gases and liquids, John Wiley & Sons, 1964.

[206] R. B. Bird, E. N. L. WES, Transport phenomena. 2nd edision ed (1924).

[207] O. Reynolds, Xxix. an experimental investigation of the circumstances which determine whether the motion of water shall be direct or sinuous, and of the law of resistance in parallel channels, Philosophical Transactions of the Royal society of London 174 (1883) 935–982.

[208] L. F. Richardson, The supply of energy from and to atmospheric eddies, Proceedings of the Royal Society of London. Series A, Containing Papers of a Mathematical and Physical Character 97 (686) (1920) 354–373.

[209] A. N. Kolmogorov, The local structure of turbulence in incompressible viscous fluid for very large reynolds numbers, Proceedings of the Royal Society of London. Series A: Mathematical and Physical Sciences 434 (1890) (1991) 9–13.

[210] M. Germano, A proposal for a redefinition of the turbulent stresses in the filtered navier-stokes equations, Physics of Fluids 29 (7) (1986) 2323–2324.

[211] J. Boussinesq, Théorie de l'écoulement tourbillonnant et tumultueux des liquides dans les lits rectilignes à grande section..., Vol. 1, Gauthier-Villars, 1897.

[212] P. Benard, Analyse et amélioration d'une chambre de combustion centimétrique par simulations aux grandes échelles, Ph.D. thesis, Rouen, INSA (2015).

[213] D. Carati, S. Ghosal, P. Moin, On the representation of backscatter in dynamic localization models, Physics of Fluids 7 (3) (1995) 606–616.

[214] F. Evrard, F. Denner, B. van Wachem, Estimation of curvature from volume fractions using parabolic reconstruction on two-dimensional unstructured meshes, Journal of Computational Physics 351 (2017) 271–294.

[215] N. Legrand, G. Lartigue, V. Moureau, A multi-grid framework for the extraction of large-scale vortices in large-eddy simulation, Journal of Computational Physics 349 (2017) 528–560.

[216] R. Janodet, C. Guillamón, V. Moureau, R. Mercier, G. Lartigue, P. Bénard, T. Ménard, A. Berlemont, A massively parallel accurate conservative level set algorithm for simulating turbulent atomization on adaptive unstructured grids, Journal of Computational Physics 458 (2022) 111075.

[217] P. Bénard, G. Lartigue, V. Moureau, R. Mercier, Large-eddy simulation of the lean-premixed preccinsta burner with wall heat loss, Proceedings of the Combustion Institute 37 (4) (2019) 5233–5243.

[218] P. Domingo-Alvarez, P. Benard, V. Moureau, G. Lartigue, F. Grisch, Impact of spray droplet distribution on the performances of a kerosene lean/premixed injector, Flow, Turbulence and Combustion 104 (2020) 421–450.

[219] M. Kraushaar, Application of the compressible and low-mach number approaches to large-eddy simulation of turbulent flows in aero-engines, Theses, Institut National Polytechnique de Toulouse - INPT (Dec. 2011).
URL https://tel.archives-ouvertes.fr/tel-00711480

[220] A. J. Chorin, Numerical solution of the navier-stokes equations, Mathematics of computation 22 (104) (1968) 745–762.

[221] J. Kim, P. Moin, Application of a fractional-step method to incompressible navier-stokes equations, Journal of computational physics 59 (2) (1985) 308–323.

[222] M. Malandain, N. Maheu, V. Moureau, Optimization of the deflated conjugate gradient algorithm for the solving of elliptic equations on massively parallel machines, Journal of

Computational Physics 238 (2013) 32–47.

[223] M. Malandain, Massively parallel simulation of low-mach number turbulent flows, HAL 2013 (2013).

[224] E. F. Kaasschieter, Preconditioned conjugate gradients for solving singular systems, Journal of Computational and Applied mathematics 24 (1-2) (1988) 265–275.

[225] R. A. Nicolaides, Deflation of conjugate gradients with applications to boundary value problems, SIAM Journal on Numerical Analysis 24 (2) (1987) 355–365.

[226] H. A. Van der Vorst, Bi-cgstab: A fast and smoothly converging variant of bi-cg for the solution of nonsymmetric linear systems, SIAM Journal on scientific and Statistical Computing 13 (2) (1992) 631–644.

[227] G. Karypis, Metis: Unstructured graph partitioning and sparse matrix ordering system, Technical report (1997).

[228] C. Chevalier, F. Pellegrini, Pt-scotch: A tool for efficient parallel graph ordering, Parallel computing 34 (6-8) (2008) 318–331.

[229] W. C. Skamarock, J. B. Klemp, Adaptive grid refinement for two-dimensional and three-dimensional nonhydrostatic atmospheric flow, Monthly Weather Review 121 (3) (1993) 788–804.

[230] S. Popinet, An accurate adaptive solver for surface-tension-driven interfacial flows, Journal of Computational Physics 228 (16) (2009) 5838–5866.

[231] G. Balarac, F. Basile, P. Bénard, F. Bordeu, J.-B. Chapelier, L. Cirrottola, G. Caumon, C. Dapogny, P. Frey, A. Froehly, et al., Tetrahedral remeshing in the context of large-scale numerical simulation and high performance computing, MathematicS In Action 11 (1) (2022) 129–164.

[232] C. Dapogny, C. Dobrzynski, P. Frey, Three-dimensional adaptive domain remeshing, implicit domain meshing, and applications to free and moving boundary problems, Journal of computational physics 262 (2014) 358–378.

[233] M. Moens, Large eddy simulation of wind farm flows: improved actuator disk model and investigations of wake phenomena, Ph.D. thesis, UCL-Université Catholique de Louvain (2018).

[234] J. N. Sorensen, W. Z. Shen, Numerical modeling of wind turbine wakes, J. Fluids Eng. 124 (2) (2002) 393–399.

[235] H. Snel, R. Houwink, J. Bosschers, Sectional prediction of lift coefficients on rotating wind turbine blades in stall, Tech. rep., ECN Renewable Energy, Petten (Netherlands) (1994).

[236] P. Chaviaropoulos, M. O. Hansen, Investigating three-dimensional and rotational effects on wind turbine blades by means of a quasi-3d navier-stokes solver, J. Fluids Eng. 122 (2) (2000) 330–336.

[237] C. Lindenburg, Modelling of rotational augmentation based on engineering considerations and measurements, Tech. rep., ECN Renewable Energy, Petten (Netherlands) (2004).

[238] Z. Du, M. Selig, A 3-d stall-delay model for horizontal axis wind turbine performance prediction, in: 1998 ASME Wind Energy Symposium, 1998, p. 21.

[239] H. Glauert, Airplane propellers, Aerodynamic theory (1935).

[240] W. Z. Shen, R. Mikkelsen, J. N. Sørensen, C. Bak, Tip loss corrections for wind turbine computations, Wind Energy: An International Journal for Progress and Applications in Wind Power Conversion Technology 8 (4) (2005) 457–475.

[241] T. Sant, Improving bem-based aerodynamic models in wind turbine design codes, Tech. rep., ECN Renewable Energy, Petten (Netherlands) (2007).

[242] W. Z. Shen, W. J. Zhu, J. N. Sørensen, Study of tip loss corrections using cfd rotor computations, in: Journal of Physics: Conference Series, Vol. 555, IOP Publishing, 2014, p. 012094.

[243] J. G. Leishman, T. Beddoes, A semi-empirical model for dynamic stall, Journal of the American Helicopter society 34 (3) (1989) 3–17.

[244] L. Beaudet, Etude expérimentale et numérique du décrochage dynamique sur une éolienne à axe vertical de forte solidité, Ph.D. thesis, Université de Poitiers (2014).

[245] K.-J. Bathe, Computational fluid and solid mechanics, Elsevier, 2001.

[246] N. Troldborg, Actuator line modeling of wind turbine wakes, Ph.D. thesis, DTU (2009).

[247] H. Meng, F.-S. Lien, L. Li, Elastic actuator line modelling for wake-induced fatigue analysis of horizontal axis wind turbine blade, Renewable energy 116 (2018) 423–437.

[248] Z. Yu, Z. Hu, X. Zheng, Q. Ma, H. Hao, Aeroelastic performance analysis of wind turbine in the wake with a new elastic actuator line model, Water 12 (5) (2020) 1233.

[249] D. D. Gray, A. Giorgini, The validity of the boussinesq approximation for liquids and gases, International Journal of Heat and Mass Transfer 19 (5) (1976) 545–551.

[250] Y. Tominaga, T. Stathopoulos, Turbulent schmidt numbers for cfd analysis with various types of flowfield, Atmospheric Environment 41 (37) (2007) 8091–8099.

[251] C. Gualtieri, A. Angeloudis, F. Bombardelli, S. Jha, T. Stoesser, On the values for the turbulent schmidt number in environmental flows, Fluids 2 (2) (2017) 17.

[252] A. Reynolds, The prediction of turbulent prandtl and schmidt numbers, International Journal of heat and mass transfer 18 (9) (1975) 1055–1069.

[253] C. Gorlé, J. van Beeck, P. Rambaud, Dispersion in the wake of a rectangular building: validation of two reynolds-averaged navier–stokes modelling approaches, Boundary-layer meteorology 137 (2010) 115–133.

[254] R. Longo, A. Bellemans, M. Derudi, A. Parente, A multi-fidelity framework for the estimation of the turbulent schmidt number in the simulation of atmospheric dispersion, Building and Environment 185 (2020) 107066.

[255] J. C. Kaimal, J. J. Finnigan, Atmospheric boundary layer flows: their structure and measurement, Oxford university press, 1994.

[256] T. J. Ypma, Historical development of the newton–raphson method, SIAM review 37 (4) (1995) 531–551.

[257] A. Andren, A. R. Brown, P. J. Mason, J. Graf, U. Schumann, C.-H. Moeng, F. T. Nieuwstadt, Large-eddy simulation of a neutrally stratified boundary layer: A comparison of four computer codes, Quarterly Journal of the Royal Meteorological Society 120 (520) (1994) 1457–1484.

[258] F. K. Chow, R. L. Street, M. Xue, J. H. Ferziger, Explicit filtering and reconstruction turbulence modeling for large-eddy simulation of neutral boundary layer flow, Journal of the atmospheric sciences 62 (7) (2005) 2058–2077.

[259] M. Xue, K. K. Droegemeier, V. Wong, The advanced regional prediction system (arps)–a multi-scale nonhydrostatic atmospheric simulation and prediction model. part i: Model dynamics and verification, Meteorology and atmospheric physics 75 (2000) 161–193.

[260] I. Senocak, A. S. Ackerman, M. P. Kirkpatrick, D. E. Stevens, N. N. Mansour, Study of near-surface models for large-eddy simulations of a neutrally stratified atmospheric boundary layer, Boundary-layer meteorology 124 (2007) 405–424.

[261] D. E. Stevens, S. Bretherton, A forward-in-time advection scheme and adaptive multilevel flow solver for nearly incompressible atmospheric flow, Journal of Computational Physics 129 (2) (1996) 284–295.

[262] Y. Feng, J. Miranda-Fuentes, S. Guo, J. Jacob, P. Sagaut, Prolb: A lattice boltzmann solver of large-eddy simulation for atmospheric boundary layer flows, Journal of Advances in Modeling Earth Systems 13 (3) (2021) e2020MS002107.

[263] G. Willis, J. Deardorff, A laboratory model of the unstable planetary boundary layer, Journal of Atmospheric Sciences 31 (5) (1974) 1297–1307.

[264] J. Deardorff, G. Willis, Further results from a laboratory model of the convective plane-

tary boundary layer, Boundary-Layer Meteorology 32 (3) (1985) 205–236.

[265] H. Schmidt, U. Schumann, Coherent structure of the convective boundary layer derived from large-eddy simulations, Journal of Fluid Mechanics 200 (1989) 511–562.

[266] M. Lejeune, G. Winckelmans, M. Duponcheel, P. Chatelain, Large eddy simulation of a convective atmospheric boundary layer, Ph.D. thesis, PhD thesis, Université Catholique de Louvain (2018).

[267] J. Sanz Rodrigo, M. Churchfield, B. Kosovic, A methodology for the design and testing of atmospheric boundary layer models for wind energy applications, Wind Energy Science 2 (1) (2017) 35–54.

[268] P. P. Sullivan, J. C. Weil, E. G. Patton, H. J. Jonker, D. V. Mironov, Turbulent winds and temperature fronts in large-eddy simulations of the stable atmospheric boundary layer, Journal of the Atmospheric Sciences 73 (4) (2016) 1815–1840.

[269] M. Min, A. Tombouldies, Simulating atmospheric boundary layer turbulence with nek5000/rs, Tech. rep., Argonne National Laboratory (ANL), Argonne, IL (United States) (2022).

[270] V. Kumar, G. Svensson, A. Holtslag, C. Meneveau, M. B. Parlange, Impact of surface flux formulations and geostrophic forcing on large-eddy simulations of diurnal atmospheric boundary layer flow, Journal of Applied Meteorology and Climatology 49 (7) (2010) 1496–1516.

[271] J. Huang, E. Bou-Zeid, Turbulence and vertical fluxes in the stable atmospheric boundary layer. part i: A large-eddy simulation study, Journal of the Atmospheric Sciences 70 (6) (2013) 1513–1527.

[272] G. Matheou, D. Chung, Large-eddy simulation of stratified turbulence. part ii: Application of the stretched-vortex model to the atmospheric boundary layer, Journal of the Atmospheric Sciences 71 (12) (2014) 4439–4460.

[273] N. S. Ghaisas, C. L. Archer, S. Xie, S. Wu, E. Maguire, Evaluation of layout and atmospheric stability effects in wind farms using large-eddy simulation, Wind Energy 20 (7) (2017) 1227–1240.

[274] W. Lazeroms, Turbulence modelling applied to the atmospheric boundary layer, Ph.D. thesis, KTH Royal Institute of Technology (2015).

[275] Y. Dai, S. Basu, B. Maronga, S. R. de Roode, Addressing the grid-size sensitivity issue in large-eddy simulations of stable boundary layers, Boundary-Layer Meteorology 178 (2021) 63–89.

[276] E. Audusse, M. H. Do, P. Omnes, Y. Penel, Analysis of modified godunov type schemes for

the two-dimensional linear wave equation with coriolis source term on cartesian meshes, Journal of Computational Physics 373 (2018) 91–129.

[277] J. Cuxart, A. A. Holtslag, R. J. Beare, E. Bazile, A. Beljaars, A. Cheng, L. Conangla, M. Ek, F. Freedman, R. Hamdi, et al., Single-column model intercomparison for a stably stratified atmospheric boundary layer, Boundary-Layer Meteorology 118 (2006) 273–303.

[278] R. Stoll, F. Porté-Agel, Large-eddy simulation of the stable atmospheric boundary layer using dynamic models with different averaging schemes, Boundary-layer meteorology 126 (2008) 1–28.

[279] M. J. Berger, P. Colella, Local adaptive mesh refinement for shock hydrodynamics, Journal of computational Physics 82 (1) (1989) 64–84.

[280] D. Rossinelli, B. Hejazialhosseini, W. van Rees, M. Gazzola, M. Bergdorf, P. Koumoutsakos, Mrag-i2d: Multi-resolution adapted grids for remeshed vortex methods on multicore architectures, Journal of Computational Physics 288 (2015) 1–18.

[281] D. Fuster, G. Agbaglah, C. Josserand, S. Popinet, S. Zaleski, Numerical simulation of droplets, bubbles and waves: state of the art, Fluid dynamics research 41 (6) (2009) 065001.

[282] D. Angelidis, F. Sotiropoulos, Simulation of wind turbine wakes on locally refined cartesian grids, in: 33rd Wind Energy Symposium, 2015, p. 1471.

[283] R. Deiterding, S. L. Wood, Predictive wind turbine simulation with an adaptive lattice boltzmann method for moving boundaries, in: Journal of Physics: Conference Series, Vol. 753, IOP Publishing, 2016, p. 082005.

[284] A. C. Kirby, M. J. Brazell, Z. Yang, R. Roy, B. R. Ahrabi, M. K. Stoellinger, J. Sitaraman, D. J. Mavriplis, Wind farm simulations using an overset hp-adaptive approach with blade-resolved turbine models, The International Journal of High Performance Computing Applications 33 (5) (2019) 897–923.

[285] S. Zeoli, G. Balarac, P. Bénard, G. Georis, F. Houtin-Mongrolle, L. Bricteux, Large eddy simulation of wind turbine wakes using adaptative mesh refinement, Journal of Physics: Conference Series 1618 (2020) 062056.

[286] M. Oberlack, J. Peinke, A. Talamelli, L. Castillo, M. Hölling, Progress in turbulence and wind energy IV: proceedings of the iTi conference in Turbulence 2010, Springer, 2012.

[287] L. Vollmer, G. Steinfeld, D. Heinemann, M. Kühn, Estimating the wake deflection downstream of a wind turbine in different atmospheric stabilities: an les study, Wind Energy Science 1 (2) (2016) 129–141. doi:10.5194/wes-1-129-2016.
URL https://wes.copernicus.org/articles/1/129/2016/

[288] M. F. Howland, J. Bossuyt, L. A. Martínez-Tossas, J. Meyers, C. Meneveau, Wake structure in actuator disk models of wind turbines in yaw under uniform inflow conditions, Journal of Renewable and Sustainable Energy 8 (4) (2016) 043301.

[289] N. Coudou, M. Moens, Y. Marichal, J. Van Beeck, L. Bricteux, P. Chatelain, Development of wake meandering detection algorithms and their application to large eddy simulations of an isolated wind turbine and a wind farm, in: Journal of Physics: Conference Series, Vol. 1037, IOP Publishing, 2018, p. 072024.

[290] C. Bak, F. Zahle, R. Bitsche, T. Kim, A. Yde, L. C. Henriksen, M. H. Hansen, J. P. A. A. Blasques, M. Gaunaa, A. Natarajan, The dtu 10-mw reference wind turbine, Tech. rep., Danish Wind Power Research 2013 (2013).

[291] M. Moens, M. Duponcheel, G. Winckelmans, P. Chatelain, An actuator disk method with tip-loss correction based on local effective upstream velocities, Wind Energy 21 (9) (2018) 766–782.

[292] F. Houtin—Mongrolle, P. Bénard, G. Lartigue, V. Moureau, A level-set framework for the wind turbine wake analysis: from high-fidelity unsteady simulations to 1d momentum theory, in: Journal of Physics: Conference Series, Vol. 1934, IOP Publishing, 2021, p. 012011.

[293] C. L. Kelley, B. L. Ennis, Swift site atmospheric characterization, Tech. rep., Sandia National Lab.(SNL-NM), Albuquerque, NM (United States) (2016).

[294] E. Jézéquel, M. Cathelain, V. Masson, F. Blondel, Validation of wind turbine wakes modelled by the meso-nh les solver under different cases of stability, in: Journal of Physics: Conference Series, Vol. 1934, IOP Publishing, 2021, p. 012003.

[295] positioning paper, Sustaining a cost-efficient energy transition in europe, Tech. rep., Wind Europe (2018).

[296] S. Meynet, Simulation aux grandes échelles des transferts thermiques dans les échangeurs de chaleur en fabrication additive, Ph.D. thesis, Normandie (2023).

[297] R. J. Stevens, J. Graham, C. Meneveau, A concurrent precursor inflow method for large eddy simulations and applications to finite length wind farms, Renewable energy 68 (2014) 46–50.

[298] M. Garciá, Méthodes numériques pour la simulation aux grandes échelles de la combustion gazeuse et diphasique, Ph.D. thesis, institut national polytechnique de Toulouse (2008).